



HAL
open science

Plasma etching of high- χ block copolymers

Maria Gusmao Cacho

► **To cite this version:**

Maria Gusmao Cacho. Plasma etching of high- χ block copolymers. Micro and nanotechnologies/Microelectronics. Université Grenoble Alpes [2020-..], 2021. English. NNT : 2021GRALT056 . tel-03524057

HAL Id: tel-03524057

<https://theses.hal.science/tel-03524057v1>

Submitted on 13 Jan 2022

HAL is a multi-disciplinary open access archive for the deposit and dissemination of scientific research documents, whether they are published or not. The documents may come from teaching and research institutions in France or abroad, or from public or private research centers.

L'archive ouverte pluridisciplinaire **HAL**, est destinée au dépôt et à la diffusion de documents scientifiques de niveau recherche, publiés ou non, émanant des établissements d'enseignement et de recherche français ou étrangers, des laboratoires publics ou privés.

THÈSE

Pour obtenir le grade de

DOCTEUR DE L'UNIVERSITÉ GRENOBLE ALPES

Spécialité : NANO ELECTRONIQUE ET NANO TECHNOLOGIES

Arrêté ministériel : 25 mai 2016

Présentée par

Maria Gabriela GUSMAO CACHO

Thèse dirigée par **Nicolas POSSEME**, Ingénieur de recherche, **CEA-Leti**, et encadrée par **Patricia PIMENTA-BARROS** et **Khatia BENOTMANE**, Ingénieures de recherche, **CEA-Leti**

préparée au sein du **Laboratoire CEA-Leti**
dans l'**École Doctorale Electronique, Electrotechnique,
Automatique et Traitement du Signal (EEATS)**

Gravure plasma de copolymères à blocs dits « high- χ »

Plasma etching of « high- χ » block copolymers

Thèse soutenue publiquement le **24 septembre 2021**,
devant le jury composé de :

Monsieur Christophe CARDINAUD

Directeur de recherche, CNRS-IMN, Nantes, Rapporteur (Président de jury)

Monsieur Laurent LE BRIZOUAL

Professeur des Universités, Université de Rennes 1, Rapporteur

Monsieur Christophe VALLEE

Professeur des Universités, SUNY Poly, New York, Examineur

Monsieur Pascal GOURAUD

Ingénieur de recherche, ST Microelectronics, Examineur

Monsieur Nicolas POSSEME

Ingénieur de recherche HDR, CEA-Leti, Directeur de thèse

Madame Patricia PIMENTA-BARROS

Ingénieure de recherche, CEA-Leti, Invitée, Co-encadrante de thèse

Madame Khatia BENOTMANE

Ingénieure de recherche, CEA-Leti, Invitée, Co-encadrante de thèse



À mes bassoures

Remerciements

Difficile de résumer en quelques mots ma reconnaissance à toutes les personnes qui ont contribué à l'accomplissement de cette thèse, que ça soit directement ou indirectement.

Tout d'abord, je remercie les membres du jury pour avoir accepté d'évaluer mes travaux de thèse. M. Christophe Cardinaud, M. Laurent Le Brizoual, M. Christophe Vallée et M. Pascal Gouraud, merci pour votre bienveillance et pour nos échanges très intéressants lors de la soutenance.

Je tiens à exprimer ma profonde gratitude et reconnaissance à mon équipe encadrante. Je remercie mon directeur de thèse, Nicolas Possémé, pour son encadrement et ses conseils. J'ai beaucoup apprécié nos discussions scientifiques et la confiance que tu m'as accordée. Patricia, je savais que cette thèse serait une super expérience dès le début grâce à toi. Merci de m'avoir (re)confié le sujet de la gravure DSA et pour le temps que tu as pris pour m'expliquer la gravure, les équipements, les copolymères à blocs, et tout ce qui va avec. Khatia, merci d'avoir accepté le défi d'attraper le train en mouvement ! J'ai beaucoup apprécié nos discussions allant des copolymères à blocs aux voyages en Italie, en passant par nos plaintes à propos du froid alors que presque tout le monde semblait trop heureux de voir de la neige (et geler). A tous, je ne vous remercierai jamais assez pour votre écoute, votre encouragement, votre bienveillance, votre réactivité et vos conseils au long de ces 3 années de thèse au CEA.

Je souhaite aussi remercier mes co-bureaux, anciens et nouveaux, pour la bonne ambiance dans le bureau et pour nos discussions (pas toujours très sérieuses...). Fred et Vincent, merci pour votre super accueil et pour avoir répondu toutes les (nombreuses) questions que j'avais au début. Val, mon co-bureau devenu pseudo-coloc, merci pour nos discussions sur tout et n'importe quoi (d'expressions françaises à astrophysique, passant par les nourritures brésiliennes, les araignées géantes, l'origami et le street art, pour en citer une très petite partie). Courage pour la fin, ne changes jamais et prends bien soin de No-Speak ! Max, les nombreuses cuillères de confiture de lait entre deux chapitres ont rendu la rédaction de ce manuscrit beaucoup plus facile. Profite bien de la vue des montagnes depuis mon bureau !

Un merci tout particulier pour mes autres « bassoures », qui n'étaient pas officiellement des co-bureaux mais qui passaient presque autant de temps que moi dans la pièce 306 : Saïmone l'anémone, le roi des astuces Excel, clivage et MEB, entre autres ; Mathieu, qui a certainement oublié encore quelque chose chez nous ; Antoine, mon digne successeur malgré ses 15 ans seulement ; et Benjamin, le maître des incertitudes et des bonnes idées. Merci également aux « bassourettes » qui n'étaient pas au CEA, mais qu'ont rendu nos soirées et weekends encore plus funs : Emilie Scoundrel-Plague-Ours Marotte et Lila(s) Kada(s). Vous me manquez tous ! Vivement la prochaine après-midi jeux.

Je remercie également tous les collègues du Leti qui ont contribué à la réussite de cette thèse. L'équipe de gravure pour nos interactions quotidiennes, vos conseils et pour les bons moments partagés au H3 (et le bar à vin... et le Carré...) : Christelle B., Ludivine, Aurélien T., Aurélien S., Sana, Yann, Hanh, Pauline, François, Romain, Yohan, Carole, Latifa, Christian, Christelle A., Sébastien, Alain, Coline et Baptiste. Le groupe DSA pour tout votre support et votre aide dans la compréhension de la litho des copolymères à blocs : Aurélie, Max, Guido, Charlotte, Marie-Line, Anne et Raluca. Les personnes de caractérisation de la PFNC et en salle pour votre expertise : Dédé, Névine, Bernard, Nicolas, Christophe, Denis. Et finalement les personnes en

Remerciements

salle qui m'ont aidé quand j'en avais besoin pour les campagnes HF, les plaques ou la maintenance : Raphy, Zouhir, Jean-Marc, Karine, Corinne, Maxime, Michael.

Petit mot également pour mes nouveaux collègues de l'atelier gravure R&D de ST : merci pour votre accueil, vos conseils et votre encouragement lors de la préparation de la soutenance.

Malgré les 8000 km qui me séparent de l'océan à 28 degrés, mon accueil en France a été très chaleureux (pour compenser l'hiver et la pluie). C'est en partie grâce à ma belle-famille : merci à Cécile, Pascal, Jérôme, Nico, Juju et Elisa. Vous n' imaginez pas à quel point j'apprécie d'avoir une deuxième famille en France !

A mes parents et ma petite sœur (et Dobby, l'amour de ma vie sous forme canine) au Brésil, je ne serais pas ici sans vous. Ma liste de remerciements est infinie et ne rentrerait jamais dans ce manuscrit (même avec ces 230 pages). Surtout, je vous remercie pour votre amour, votre soutien inconditionnel et pour m'avoir encouragé à poursuivre mes rêves, peu importe à quelle distance ils m'emmènent. Je compte les jours jusqu'à ce que je puisse vous serrer fort dans mes bras et fêter ce diplôme avec vous. Amo muito vocês.

Je finis mes remerciements par la personne qui m'a permis d'arriver jusqu'au bout de cette aventure tout en gardant le sourire. Guigui, le roi des « barroues », heureusement que tu as le don pour inventer des mots qui veulent tout dire et ne rien dire en même temps, car aucune langue ne pourra vraiment traduire ma gratitude pour ton soutien au quotidien. Tu as su me motiver quand j'avais des doutes, m'encourager quand j'avais des idées et célébrer avec moi quand ça marchait. Si notre vie était un jeu, ça serait une campagne deck-building coopérative avec plein de scénarios qu'on vient à peine de commencer.

TABLE OF CONTENTS

TABLE OF CONTENTS	7
LIST OF ABBREVIATIONS	11
I. INTRODUCTION AND GENERAL CONTEXT OF THE STUDY	15
I.1 Microelectronics: origins and evolution.....	16
I.1.1 History of microelectronics	16
I.1.2 Evolution of microelectronics	16
I.2 Lithography	19
I.2.1 Optical lithography	19
I.2.2 New lithography techniques to continue pattern scaling.....	23
I.3 Directed Self-Assembly of Block Copolymers.....	27
I.3.1 Block copolymers definition	27
I.3.2 Obtaining a block copolymer thin film.....	31
I.3.3 Obtaining patterns by directed self-assembly (DSA).....	32
I.4 Etching	40
I.4.1 Principles of plasma etching	41
I.4.2 Etching characteristics and criteria.....	43
I.5 Etching for the DSA: state of the art	45
I.5.1 State of the art of PS- <i>b</i> -PMMA etching	45
I.5.2 State of the art of silicon-containing high- χ BCP etching.....	46
I.6 Thesis objectives	47
II. EXPERIMENTAL SETUP	52
II.1 Materials	52
II.1.1 Polymer and copolymer materials.....	52
II.1.2 Obtaining thin films of block copolymers.....	56
II.2 Etching tools	59
II.2.1 Dry etching.....	59
II.2.2 Wet etching	66
II.3 Characterization methods.....	67
II.3.1 Physicochemical characterization	67
II.3.2 Morphological characterization.....	81
III. ETCHING IMPACT ON THE ACE CHEMO-EPITAXY FLOW FOR DIRECTED SELF-ASSEMBLY	86
III.1 ACE chemo-epitaxy flow	86
III.2 Understanding the effect of etching on the block copolymer's alignment.....	92

Table of contents

III.2.1 Effect of the sequence of etching and deposition steps on the TiN surface	92
III.2.2 Effect of each etching step on the TiN surface	97
III.2.3 Understanding the effect of the SO ₂ /O ₂ /He plasma on the TiN surface and neutral layer deposition	100
III.2.4 Understanding the interaction mechanism between SO ₂ /TiN/xNL/HF that leads to the neutral layer lift-off	104
III.3 Alternatives for the SOC removal step	114
III.3.1 First approach: replace the SOC removal step	114
III.3.2 Second approach: two-step SOC removal	120
III.4 Conclusions	124
IV. ETCHING AND PATTERN TRANSFER OF PURELY ORGANIC HIGH-χ BLOCK COPOLYMER	128
IV.1 Modified Polystyrene (PS) and Polymethyl methacrylate (PMMA) homopolymer results	129
IV.1.1 Characterization of modified PS and PMMA homopolymers	129
IV.1.2 Evaluation of different plasma chemistries for PMMA removal selectively to the PS	130
IV.2 Application to high- χ PS- <i>b</i> -PMMA films with lamellar morphology	133
IV.2.1 Impact of high- χ modified PS- <i>b</i> -PMMA chemistry for same pitch and plasma chemistry	133
IV.2.2 Impact of pitch and film thickness on the etching of high- χ modified PS- <i>b</i> -PMMA	135
IV.3 Alternatives for the etching of high- χ PS- <i>b</i> -PMMA films with 18-nm pitch	138
IV.3.1 First approach: argon-based PMMA removal	138
IV.3.2 Second approach: UV exposure followed by plasma etching	145
IV.3.3 Third approach: oxygen-free PMMA removal	149
IV.3.4 Fourth approach: mixed wet and dry etching	159
IV.4 Conclusions	164
V. ETCHING AND PATTERN TRANSFER OF SILICON-BASED HIGH-χ BLOCK COPOLYMER	168
V.1 Characterization of pristine top coat and PS- <i>b</i> -PDMSB	169
V.2 Top coat removal selectively to PS- <i>b</i> -PDMSB	171
V.2.1 Development of a top coat removal plasma etching process	172
V.2.2 Development of PS removal step selectively to PDMSB	175
V.3 One step top coat and PS removal selectively to PDMSB	182
V.3.1 Comparison between oxidizing and reducing plasma chemistries for top coat and PS removal	182

Table of contents

V.3.2 Understanding the etching and passivation mechanisms	188
V.3.3 Pattern transfer of the 18-nm pitch high- χ PS- <i>b</i> -PDMSB.....	193
V.4 Conclusions.....	197
VI. CONCLUSION AND PERSPECTIVES	202
BIBLIOGRAPHY	212
RÉSUMÉ EN FRANÇAIS.....	225

LIST OF ABBREVIATIONS

AFM – Atomic Force Microscopy
ALE – Atomic Layer Etching
ArF – Argon Fluoride
BCP – Block copolymer
BEOL – Back-End of Line
BKM – Best-Known Method
BSE – Backscattered Electrons
CA – Contact Angle
CARs – Chemically Amplified Resists
CCD – Charge-Coupled Device
CCP – Capacitively Coupled Plasma
CD – Critical Dimension
CD-SEM – Critical Dimension Scanning Electron Microscopy
CDU – Critical Dimension Uniformity
DIBL - Drain-Induced Barrier Lowering
DSA – Directed Self-Assembly
EBL – Electron-beam Lithography
EDP – End Point
EPE – Edge Placement Error
ER – Etch Rate
EUV – Extreme Ultraviolet
FEOL – Front-End of Line
FinFET – Fin Field-Effect Transistor
FTIR – Fourier-Transform Infrared
GAAFET – Gate-All-Around Field-Effect Transistor
H₂SO₄ – Sulfuric Acid
HF – Hydrofluoric Acid
hPMMA – Poly(methyl methacrylate) homopolymer
hPS – Polystyrene homopolymer
HSQ – Hydrogen Silsesquioxane
IC – Integrated Circuit
ICP – Inductively Coupled Plasma
IPA – Isopropyl Alcohol
IRDS – International Roadmap for Devices and Systems
ISR – Intermediate Segregation Regime

List of abbreviations

ITRS – International Technology Roadmap of Semiconductors
LELE – Litho-Etch-Litho-Etch
LER – Line-Edge Roughness
LWR – Line-Width Roughness
ME – Main Etch
MEOL – Middle-End of Line
MF – Multiplication Factor
MIBK – Methyl Isobutyl Ketone
MOSFET – Metal–Oxide–Semiconductor Field-Effect Transistor
MPL – Multiple Patterning Lithography
NBA – N-Butyl Acetate
NIL – Nanoimprint Lithography
NL – Neutral Layer
NTD – Negative Development Resist
ODT – Order-Disorder Transition
OE – Overetch
OES – Optical Emission Spectroscopy
OPL – Organic Planarizing Layer
PDMSB - Polydimethylsilacyclobutane
PECVD – Plasma-Enhanced Chemical Vapor Deposition
PEHMA – Poly(2-ethylhexyl methacrylate)
PGMEA – Propylene glycol methyl ether acetate
PMMA – Polymethyl methacrylate
PS – Polystyrene
PVD – Physical Vapor Deposition
PW – Process Window
RF – Radio-frequency
RIE – Reactive Ion Etching
rpm – Revolutions per Minute
SADP – Self-Aligned Double Patterning
SAOP – Self-Aligned Octuplet Patterning
SAQP – Self-Aligned Quadruple Patterning
sccm - Standard Cubic Centimeters per Minute
SCE – Short Channel Effect
SE – Secondary Electrons
SEM – Scanning Electron Microscopy

List of abbreviations

SiN or Si₃N₄ – Silicon Nitride

SiARC – Silicon-containing Anti-Reflective Coating

SiO₂ – Silicon Oxide

SMART – Surface Modification for Advanced Resolution Technology

SOC – Spin-On Carbon

SOI – Silicon on Insulator

SSL – Strong Segregation Limit

TC – Top coat

TEM – Transmission Electron Microscopy

TiGeR – Tone-inverted Grapho-epitaxy Resolution Enhancement

TiN – Titanium Nitride

T_g – Glass Transition Temperature

T_{ODT} – Order-Disorder Temperature

ToF-SIMS – Time-of-Flight Secondary Ion Mass Spectrometry

UV – Ultraviolet

WCA – Water Contact Angle

WSL – Weak Segregation Limit

xNL – Cross-linkable Neutral Layer

XPS – X-ray Photoelectron Spectroscopy

CHAPTER I:

INTRODUCTION AND GENERAL CONTEXT OF THE STUDY

I. INTRODUCTION AND GENERAL CONTEXT OF THE STUDY

I.1 Microelectronics: origins and evolution

Microelectronics corresponds to the field that studies and manufactures small electronic devices and components. This industry is ever growing and, nowadays, it has been integrated into nearly every aspect of our daily lives. Some fields of activity that heavily depend on the microelectronics industry include transports, communication, aerospace, medical, and others.

The transistor is the basic component of microelectronics. In 2014, it was estimated that 2.9 sextillion transistors had been manufactured since the first one was created in 1947 [**Handy 2014**]. This number has only grown ever since and shows the ubiquity of microelectronics in our daily lives.

I.1.1 History of microelectronics

The first major event in microelectronics history dates back to 1948, when physicists John Bardeen, Walter Brattain and William Shockley of Bell Telephone Laboratories built the first working transistor on a germanium substrate [**Bardeen 1948**]. These three scientists were awarded the Nobel Prize in Physics in 1956 “for their researches on semiconductors and their discovery of the transistor effect” [**Nobel Prize 1956**].

The second turning point for the industry took place in 1954, when scientists at Texas Instruments demonstrated the first transistor on a silicon substrate [**Adcock 1954**]. In 1958, Jack Kilby from Texas Instruments successfully demonstrated the first hybrid integrated circuit (IC) based on germanium [**Kilby 1964**], which earned him the Nobel Prize in Physics in 2000 [**Nobel Prize 2000**]. Half a year later, Robert Noyce from Fairchild Semiconductor demonstrated the first monolithic integrated circuit, which was based on silicon [**Noyce 1961**].

Finally, the MOSFET (metal–oxide–semiconductor field-effect transistor), which has been the most commonly used type of transistor ever since, was invented by Mohamed Atalla and Dawon Kahng at Bell Telephone Laboratories in 1959 [**Kahng 1963**].

I.1.2 Evolution of microelectronics

I.1.2.1 Moore’s Law

Since the introduction of integrated circuits, there has always been a great interest, driven by both economic and performance aspects, to increase the number of transistors on the surface of a wafer. Indeed, in 1965, Gordon E. Moore – then director of research and development (R&D) at Fairchild Semiconductor – observed the importance of increasing the integration density to reduce the production cost, since it allows manufacturing more chips on a single wafer. He also observed that the number of components in a dense integrated circuit had doubled approximately every year, and speculated that this trend would continue for the next ten years [**Moore 1965**]. Then, in 1975, already as co-founder of Intel Corporation, Moore revised his forecast rate to doubling every two years [**Moore 1975**], therefore creating what would be known as “Moore’s Law”.

placed between the source and the drain and isolated from the substrate by an insulator called a gate oxide. When a certain voltage is applied to the gate, the potential difference between the substrate and the gate attracts the few electrons present in the substrate to the positively polarized gate. Due to the insulating layer between the gate and the substrate, these electrons are blocked just below the gate oxide. These electrons thus brought to the surface of the substrate allow the electrons from the source to flow towards the drain, forming a conduction channel.

Ideally, this means that the voltage applied to the gate will only have an electric field effect on the channel, thus enabling a control over the current: when the voltage applied to the gate is superior to the threshold voltage, the current is on; otherwise, the current is off. This gives the MOSFET transistor the ability to produce the electrical signals necessary for the operation of digital electronic devices.

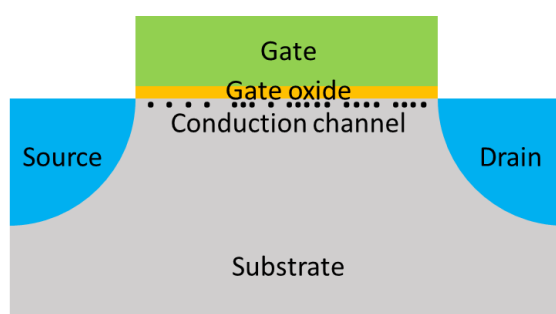


Figure I-2: Simplified MOSFET structure representing the gate, the source, the drain and the gate oxide.

As the transistor scaling continued, however, the reduction of the gate length lead to limitations on the operation of the transistors. For the more recent nodes, difficulties arise due to the MOSFET size reduction, like current leakage and subthreshold conduction, Short Channel Effects (SCEs), Drain-Induced Barrier Lowering (DIBL) and others.

I.1.2.3 Evolution of transistor architecture

In order to overcome these problems for the current nodes, new architectures have been investigated to replace the common MOSFET planar structure. Planar devices are limited in terms of scaling, performance and power consumption to reach the 10 nm node, so technologies exploiting novel degrees of freedom at physical and architectural level are the most promising candidates to continue pattern scaling according to Moore's Law. This has led to the introduction of three dimensional (3D) multigate structures, such as the Fin-FET, two-gate, Ω -gate, and Gate-All-Around (GAAFET) transistors. These increasingly sophisticated architectures enhance the electrostatic control of the gate over the device channel, reducing short channel effects (SCEs), and allowing more aggressive scaling of the device dimensions [De Marchi 2014].

The FinFET (Fin Field-Effect Transistor) basic structure is presented in Figure I-3(a). The main difference between the FinFET and the common MOSFET structure presented in Figure I-2 is that the body of the FinFET device is formed by 3D conducting channels with a fin-like structure. They are covered by the gate in order to increase their contact surface by 3D effect.

When their number is multiplied, a multi-channel structure such as the one presented in Figure I-3(b) is obtained and allow us to maximize the contact when covered by the gate. This gate structure provides a better electrical control over the channel and thus helps in reducing the leakage current and overcoming other SCEs [Chevillon 2012].

Finally, Figure I-3(c) presents the GAAFET structure, which is obtained by stacking nanowires and then wrapping them with the gate from all sides. This structure maximizes the channel density on the chip as much as possible while reducing the space occupied and providing for the greatest capacitive coupling between the gate and the channel.

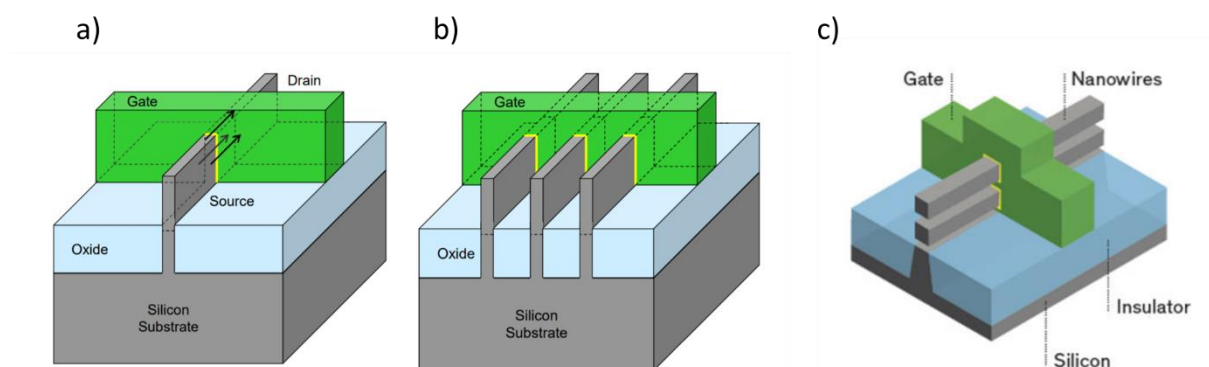


Figure I-3: Schematics for (a) a single-channel FinFET structure; (b) a multi-channel FinFET structure; and (c) a gate-all-around structure [Intel 2011] [Courtland 2016].

Moreover, in order to improve device performance, other alternatives include materials replacement, such as the use of the Silicon On Insulator (SOI) substrate and new materials for the gate and insulating layer. However, we will not go into detail for these alternatives, since this thesis will focus on pattern scaling and densification thanks to new lithography techniques that are able to continue enabling Moore’s Law by reducing the critical dimension (CD) and pitch of the transistors.

I.2 Lithography

Lithography is the technique used to define the nanoscale patterns that will later be transferred into the different stack layers in order to manufacture the transistor. The miniaturization of the transistor’s dimensions has been made possible by the evolution of lithography techniques.

I.2.1 Optical lithography

Optical lithography is the most commonly used lithography technique. It consists of three main elements: source, mask and lens. The patterns from an optical mask are transferred to a photosensitive polymer (also known as “photoresist”) through exposure to photons emitted by a light source.

I.2.1.1 Principle of optical lithography

Figure I-4 explains the principle of this technique: the source emits a light with a fixed wavelength. The light then crosses the optical mask on which are defined the desired patterns and the opaque patterns of the mask form a grating diffracting the incident light. In order to reduce the resolution even more, the light now made up of the mask patterns arrives on the

converging lens, which reduces the size of the patterns. Finally, the photoresist is exposed to light in certain zones corresponding to the patterns of the mask with reduced sizes thanks to the passage through the lens. Due to the light radiation received, a chemical reaction takes place within the photoresist, inducing a difference in solubility between the exposed and unexposed areas.

Two types of photoresists are used in microelectronics: positive and negative. If they are exposed under the same conditions through the same mask, in the case of a positive photoresist, the exposed part becomes soluble in the developer solution, while the non-exposed part remains insoluble. In the case of a negative photoresist, it is the unexposed area which is soluble in the developer. The patterns formed correspond to the non-soluble part. Both cases are represented in the bottom of Figure I-4. Finally, the resultant photoresist pattern is used as an etch mask during the pattern transfer steps in order to define small features on the wafer.

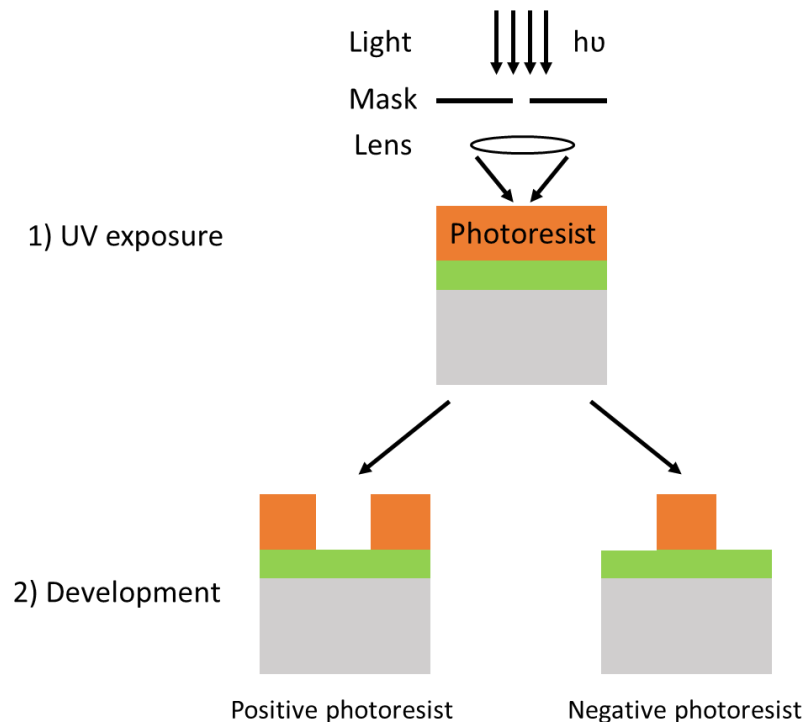


Figure I-4: Principle of optical lithography for positive and negative photoresists.

I.2.1.2 Evolution of optical lithography

As we have seen, optical lithography is a technique based on light diffraction, for which the achievable resolution is determined by Rayleigh's law:

$$R = k \times \frac{\lambda_0}{NA}$$

Equation I-1: Rayleigh's law.

In which:

- R is the resolution, which corresponds to the minimum achievable dimension or CD;
- k is the Rayleigh coefficient of resolution, an empirical factor smaller than 1, which depends on the optical devices, the photoresist and the type of mask used;
- λ_0 corresponds to the vacuum wavelength of the light source.

- NA is the numerical aperture of the imaging system, with $NA = n \cdot \sin\theta$; where n is the refractive index of the incident medium and θ is the angular aperture of the lens.

In order to increase the resolution and, consequently, decrease the size of the obtained patterns, the different parameters present in Rayleigh's law have been modified over the years.

The first parameter to be explored was the vacuum wavelength λ_0 of the light source, which has been gradually decreased over the last 30 years, from 436 nm in the 1980s using a mercury source to 193 nm since the 2000s using an argon fluoride (ArF) laser. The 193 nm ArF lithography is currently used in manufacturing and is capable of obtaining patterns whose pitch reaches minimum values of 160-180 nm, with CDs of 80-90 nm. Reducing the wavelength from 193 nm to 157 nm was abandoned, due to the rapid increase of technological challenges and costs associated with developing new exposure tools and imaging materials [Sanders 2010].

Another parameter to be explored was the photoresist's sensitivity to the light exposure. Increasing this sensitivity made it possible to decrease the k parameter, thus maximizing the resolution and the definition of the patterns. Chemically Amplified Resists (CARs) are an example of innovation linked to this parameter.

Finally, the third parameter to be optimized was the numerical aperture (NA) of the imaging system, which has been increased over the years in order to increase the resolution. Its angular opening θ cannot be infinitely increased. Due to the geometry of the lens and the fact that light travels in a straight line through homogeneous media, θ is limited to 90° and therefore $\sin\theta$ is limited to 1.0. This leaves the refractive index n of the medium in which the lithography takes place to be optimized. Traditionally, optical lithography is performed in air, which has a refractive index of $n_{\text{air}} = 1.00$. However, by changing to a medium with a higher refractive index, such as water ($n_{\text{water}} = 1.44$), it is possible to further increase the resolution by reducing the effective wavelength λ_{eff} :

$$\lambda_{\text{eff}} = \frac{\lambda_0}{n_{\text{medium}}}$$

Equation I-2: Effective wavelength.

From this equation, we can see that using water as an immersion fluid leads to a reduction of around 30% in the effective wavelength of 193 nm lithography, which is more than would be obtained by changing to 157 nm wavelength. This led to the creation of 193 nm immersion lithography, which is capable of attaining CDs of around 40 nm and was introduced to industrial manufacturing in 2005.

Another important advantage of 193 nm immersion lithography is that, since reducing λ_{eff} does not change the frequency of the incident radiation, this technique is able to use much of the already existing technology used in 193 nm dry lithography in terms of materials (mask, lens, photoresist, and antireflective coating, for example) [Sanders 2010].

However, nowadays this method has reached its limits in terms of pattern scaling. With its minimum CD of 30-40 nm for line/space applications, optical immersion lithography no longer meets the expectations of manufacturers for technological nodes of 10 nm and beyond.

I.2.1.3 Multiple patterning: extending optical lithography limits

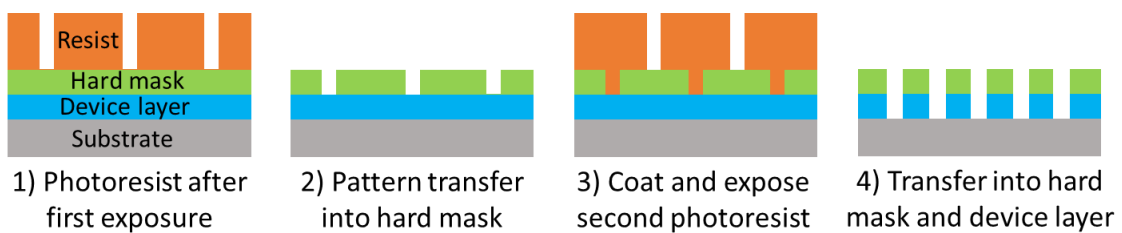
Among the techniques investigated to continue extending the optical lithography limits while also retaining its equipment and methods for as long as possible, there is one known as Multiple

Patterning Lithography (MPL), which consists of obtaining patterns through several steps. MPL has been gradually developed over the last few years, until finally being used in production to complement traditional optical immersion lithography.

The first example of a multiple patterning technique is the double patterning process, also known as LELE (Litho-Etch-Litho-Etch), which is represented by the schematics in Figure I-5(a). This technique consists of carrying out a first lithography, transferring the patterns into a hardmask through etching, then carrying out a second lithography over the first one by shifting the patterns by half a step in order to expose the new patterns in the middle of the previous ones, and finally etching the hardmask using the newly-shifted patterns. For example, if we consider that lines with 40 nm CD and 160 nm pitch are exposed and etched, each line is then 120 nm apart. The second lithography is shifted by half a step compared to the previous one, i.e. 80 nm: the new printed lines are located between the previous ones at a distance of 40 nm. A network of lines of 40-nm CD which are 40 nm apart – obtaining a period of 80 nm – is then obtained, making it possible to halve the lithography pitch. This means that, by shifting the second exposure compared to the first, we are able to double the pattern density on our wafer. The major advantage of this technique lies in the use of optical lithography and, therefore, it does not require the development of new tools and materials.

However, when approaching the smaller nodes, even more Litho-Etch steps are necessary, which not only significantly increases the cost but also highlights the main challenge of this technique: the mask overlay problem, which is represented in Figure I-5(b). Indeed, the second mask must be perfectly aligned with respect to the first level in order to avoid any overlapping of patterns with respect to each other. The smaller the target dimensions, the more precise this alignment must be [Levinson 2010]. For critical dimensions smaller than 20 nm, the cost and overlay limitations are considered too critical for integration to be possible and, therefore, other MPL approaches become more attractive.

a) LELE process



b) Overlay problem

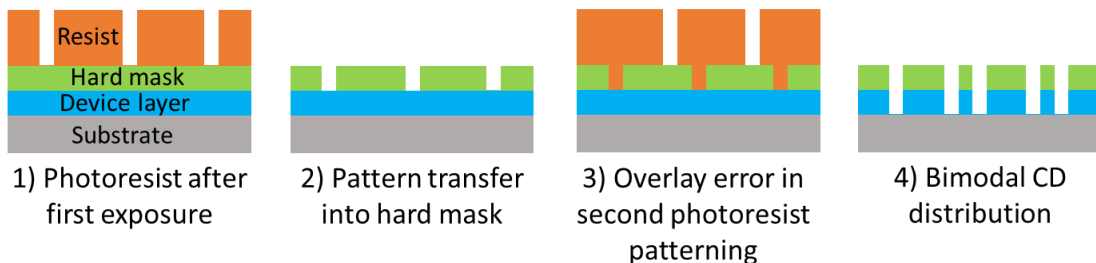


Figure I-5: Schematic representation of the (a) LELE process and (b) the overlay problem.

The most used MPL approach is the Self-Aligned Double Patterning (SADP), represented in Figure I-6. In this approach, the first step consists of a standard 193 nm optical lithography process to form patterns with a loose pitch. These patterns form the core material, known as “mandrel”. The mandrel is then coated with a conformal thin film, known as “spacer”, which is usually composed of silicon oxide (SiO₂) or silicon nitride (SiN). Next, the spacer material is anisotropically plasma etched in order to remove the thin film on the substrate and on the top of the mandrel patterns, while leaving it intact on the sides. Afterwards, the mandrel is removed by either plasma or wet etching, which must be very selective to both the spacer and the substrate materials. At this stage, only the spacers remain and form a network of lines whose pitch is equal to half the initial pitch and whose width is defined by the thickness of the spacer deposited on the sides. Finally, we use the spacers created as a mask to transfer the patterns into the subjacent layer.

With this technique, very uniform and resolved structures are thus obtained without the need for multiple Litho-Etch type steps and, more importantly, by eliminating the need for alignment methodology [Levinson 2010]. By repeating these steps, it is therefore possible to double, quadruple (known as SAQP, for Self-Aligned Quadruple Patterning) and even octuplet (SAOP, for Self-Aligned Octuplet Patterning) the density of 193 nm immersion lithography. Nowadays, spacers offering guide widths up to 7 nm and obtaining dense line and space patterns with 5-nm CDs have been demonstrated [Oyama 2014].

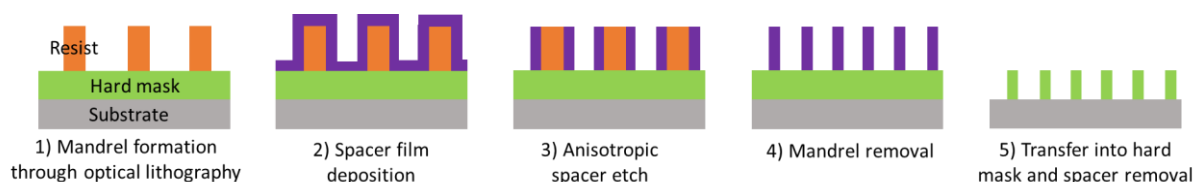


Figure I-6: Schematic representation of the SADP process using spacer patterning.

I.2.2 New lithography techniques to continue pattern scaling

As we have seen before, until around 2015 the ITRS determined which techniques had a better chance of attaining the necessary pattern dimensions for the next technological nodes. In 2016, the ITRS was replaced by the IRDS (International Roadmap for Devices and Systems) in order to address “a much broader approach to system integration, including, for example, topics of communications spanning from conductors to wireless to fiber optics and exploring non-electron-based technologies” [IRDS 2016]. Defined by the leading experts in microelectronics, the IRDS is a roadmap to follow in order to allow the microelectronics industry to evolve and meet economic criteria, becoming ever more competitive. It is updated regularly and defines the next technological nodes, when they should be reached and also through which means it should be made possible. The IRDS includes several different reports, each one presenting a roadmap in terms of lithography techniques, transistor architecture, number of metal levels, evolution of materials, and so on. Within the framework of this thesis, we will focus on the IRDS recommendations for the evolution of the lithography techniques. In this case, the IRDS proposes in particular to favor certain lithography techniques for the various technological nodes according to their maturity.

Figure I-7 presents the lithography roadmap taken from the 2020 IRDS Lithography Report [IRDS 2020]. It shows that optical immersion lithography no longer meets the demands of

industry for the next technological nodes. Even though SAQP and SAOP using 193 nm immersion lithography might be able to produce very small features, the complexity and the rising costs of the associated processes make these techniques a short-term alternative while a new, more resolving lithography technique makes the transition from lab to fab. This means that, in order to continue pattern scaling, it is necessary to develop new lithography methods, some of which are presented in Figure 1-7 either by themselves or associated with multiple patterning techniques. The next sections will present some of these new techniques.

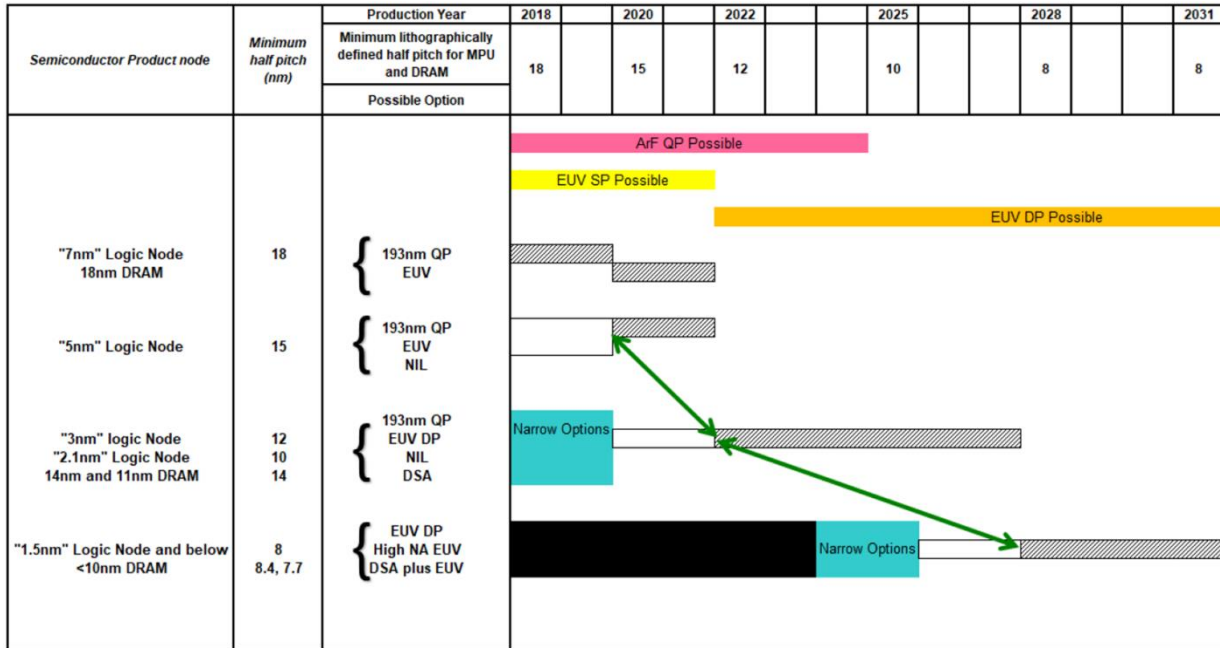


Figure I-7: The 2020 IRDS Lithography Report presented this roadmap for the line/space potential solutions in lithography for the next 10 years. Adapted from [IRDS 2020].

I.2.2.1 Extreme Ultraviolet (EUV) lithography

Today the most developed and best placed solution to continue pattern scaling is the Extreme Ultraviolet (EUV) lithography, as we can see in Figure I-7. This technology uses significantly shorter wavelengths when compared to immersion lithography, which leads to better resolution. The source used is a high-power laser striking a tin (Sn) droplet, forming a plasma emitting radiation at a wavelength of 13.5 nm. In this range of extreme UV rays, also called soft X-rays, the material strongly absorbs radiation. All the optical projection system based on focal lens used by the 193 nm immersion lithography becomes therefore unusable for EUV. They are replaced by a Molybdenum-Silicon (Mo-Si) multi-layer sheet mirror system which allows, by multiple reflections, to conserve approximately 70% of the original signal. However, mirrors present a low numerical aperture, introducing the need to use several of them in order to achieve the desired resolution according to the Rayleigh criteria (equation I-1). There are four mirrors used for the illuminator optics and six mirrors for the projection optics. Since the EUV mask in itself counts as an additional mirror, there are at least eleven reflections, which means that only around 2% of the EUV source light actually reaches the wafer [Mizoguchi 2017]. The development of EUV sources powerful enough to compensate for these losses (and therefore allow sufficient exposure doses) concentrates a large part of the development efforts for this technology.

Nowadays, Samsung and TSMC are the only companies that use EUV in production, mainly targeting the 5 nm node [Samsung 2019] [Yeap 2019]. According to the IRDS 2020 Lithography roadmap, the implementation of EUV means that pattern scaling major challenges for this technique are no longer resolution, but are instead related to Edge Placement Error (EPE) effects, namely overlay, critical dimension uniformity (CDU) and line-edge roughness (LER) [IRDS 2020]. IRDS also announces that some of the defects in EUV lithography are due to random variations in light exposure and in resist chemistry, which are called stochastics. Some examples of stochastics are bridging between lines, line breaks, missing contact holes or merged contact holes. These stochastics defects only become more important as we reduce the pitch of the desired features. Another challenge related to EUV lithography is the tool cost, which can reach more than 100 million dollars per scanner [Shilov 2020]. Not all companies can withstand its extremely high cost, hence the pursuit of research and development on other techniques.

I.2.2.2 Nanoimprint lithography (NIL)

At the end of the 1990s, Nanoimprint Lithography (NIL) appeared as one of the alternative lithography techniques and immediately gained a lot of interest, mainly due to its low manufacturing cost and its high-resolution capability. NIL consists of replicating a predefined model in a soft material, such as a polymer resist, using a mold. Unlike photolithography, its resolution is not limited by the effects of wavelength diffraction, but depends mostly on the manufacturing method of the mold and on the resin used for the pattern transfer. The mold is usually manufactured by e-beam lithography on silicon or alumina substrates and then transferred, in the form of a flexible mold, into a silicone material.

Figure I-8 shows the basics of this method. The mold, which contains the reverse (or negative) of the desired patterns at a scale of 1:1, is brought into contact and pressed onto a resist previously coated on a chosen substrate. By mechanical action, the patterns are transferred into the resist. Two types of nanoimprint coexist: thermal and UV-assisted.

Thermal nanoimprint structures a thermoplastic resist by heating it beyond its glass transition temperature (T_g) when it is under pressure, then cooling it rapidly to freeze the transferred structure before removing the mold, thus avoiding pattern collapse [Chou 1995]. UV-assisted nanoimprint, on the other hand, directly structures a fluid resist with a mold that is transparent to UV radiation. By exposing the resist to UV, it undergoes cross-linking of its polymer chains and thus remains fixed in the shape imposed by the mold. The mold is then removed, leaving the patterns printed in the resist. This technique makes it possible to work at low temperatures and thus prevent any resist degradation [Haisma 1996].

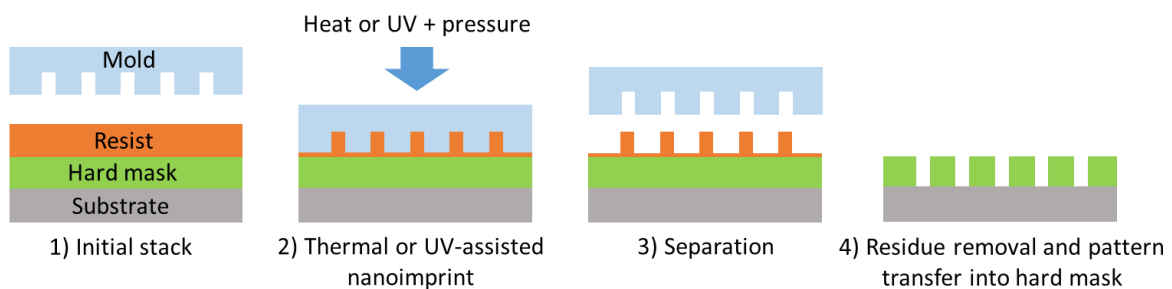


Figure I-8: Schematic representation of nanoimprint lithography.

The production of lines with 5-nm width and 14-nm pitch has been demonstrated using UV-assisted NIL [Austin 2004]. Nanoimprint patterning tools are considerably cheaper than high-performance optical lithography exposure tools because there is no high-resolution lens required. However, due to the mechanical nature of NIL, its tools present significantly less throughput than typical of optical lithography systems. Another advantage of this method is that the challenge of obtaining high resolution critical dimensions is carried over to the initial production of the mold alone. Even if the mold is complex and long to create, each nanoimpression made from it is then no more than a simple faithful reproduction.

However, for the future technological nodes with sub-20nm resolutions, since the mold presents a scale of 1:1, they become difficult to make for logic and DRAM leading edge feature sizes. The fabrication cost of the initial mold becomes not negligible, and the resist indentation mechanics become more complex at this nanometric scale, in particular because of the greater mold adhesion phenomena. Finally, the levels of defectivity achieved by this technique are still below the expectations of the logic industry. NIL is, therefore, used in applications which are defect tolerant [Takeishi 2015].

The IRDS Lithography report for 2020 announces that, since 3D flash memory has much larger feature sizes than 2D flash, manufacturing grade tools are in use for pilot production for this application, with high-volume manufacturing being possible in 2021 [IRDS 2020].

1.2.2.3 Electron-beam lithography

Electron-beam (or “e-beam”) lithography (EBL) is able to create patterns on wafers directly, without the use of a mask. Electrons have noticeably short wavelengths at the energies typically used for EBL (5–100 keV). Therefore, this technique has potential for extremely high resolution, producing features 10 nm and smaller [Craighead 1984].

In the same way as photolithography, the e-beam irradiates a resist sensitive to this energy range, which will modify its solubility in the development solvent used: either by becoming more soluble (positive EBL) or by cross-linking, rendering it less soluble (negative EBL). The application of its solvent will then selectively remove (for positive EBL) or leave (for negative EBL) the exposed areas on the surface. The limit of resolution is therefore more dependent on the chemical sensitivity of the resist to the electron than on the size of the beam itself. Nevertheless, it has drawbacks, such as the emission of backscattered electrons at a short distance by the very energetic beams, which are capable in turn of modifying the resist and therefore enlarging the printed pattern.

Unlike photolithography, which simultaneously insulates the entire surface of wafer, EBL produces continuous writing, pattern by pattern. Therefore, it has great flexibility in its drawing rules, but on the other hand, its yield is extremely low and incompatible with high-volume manufacturing. This is why its use is currently limited to mask manufacturing, low volume production and R&D.

In order to achieve throughputs superior to 10 wafers per hour, an alternative method known as Massively Parallel-Electron Beam Direct Write (or “multi-beam”) has been proposed by some companies. Based on the same principle as the e-beam, it combines several electron beams in parallel, each working on nearby areas to decrease writing time [Pourteau 2016]. For example, MAPPER systems with tens of thousands of beams have been proposed. However, increased number of beams means increased currents, which will then heat the wafers, and the

resulting thermal expansion will cause overlay errors. Even with beam energies as low as 5 keV, such as proposed by MAPPER, overlay errors greater than 2 nm can result from EBL-induced heating. These overlay errors become too important for sub-20 nm nodes and, along with low throughput, have removed EBL from the list of possible lithography approaches to continue pattern scaling in high-volume manufacturing [Levinson 2010].

I.2.2.4 Directed Self-Assembly (DSA) of block copolymers

The previous methods presented follow the "top-down" principle, in which the morphological and dimensional information of nanoscale patterns are created by larger, externally controlled sources such as photons or electrons. The technique that has been studied in the framework of this thesis, however, follows a "bottom-up" strategy, which assembles atoms and molecules in structures of shape and dimensions determined by the physical-chemical nature of the material used: the Directed Self-assembly (DSA) of block copolymers (BCPs). The next section will go into detail of this technique, showing its potential to complement and improve the performance of already existing lithography methods, such as immersion photolithography, multiple patterning and EUV lithography.

I.3 Directed Self-Assembly of Block Copolymers

DSA is one of the low-cost solutions proposed by the IRDS to obtain small and dense patterns for the sub-10 nm nodes. This technique is based on the self-assembling property of block copolymers, which are able to microphase separate, spontaneously forming a dense array of different ordered nanostructures, like cylinders or lamellae, with domain dimensions of around 5 to 50 nm [Lane 2017] [Isono 2018].

The idea of using these structures in microelectronics was first introduced in 1996 by P. Mansky *et al.* [Mansky 1996]. Since then, research activity on block copolymers made a real leap forward. This approach has many promising points: the cost of polymer materials is low compared to lithography industry standards; the process is relatively simple and fast since it consists of coating and annealing polymeric materials; and the resolution and density achieved are equal to or greater than that of the other alternatives presented so far.

I.3.1 Block copolymers definition

A copolymer is a polymer derived from more than one species of monomer. There are different types of linear copolymers, depending on the way that the monomers polymerize:

- Alternating copolymers: the monomers are regularly alternating, like A-B-A-B-A-B-A-B
- Random copolymers: the monomers are arranged in any order, like A-A-B-A-B-B-A-B
- Block copolymers: composed of two or more homopolymers linked by covalent bonds, like A-A-A-A-B-B-B-B.

In this thesis, we will focus on diblock copolymers since they are the ones that present an interest for the microelectronics industry due to their ability to self-assemble at the nanoscale. Moreover, the structures formed are inherently periodic, uniform and reproducible.

If the two blocks have different solubility parameters, they tend to minimize their free energy (and therefore their contact surface) by repelling each other, which induces a separation between them. The advantage of using block copolymers, instead of a mixture of two

homopolymers, lies in the covalent bond which binds them to each other. Because of this bond, the phase separation takes place only on a scale similar in size to that of the copolymer, meaning the nanoscale [Morris 2015]. The micro domains obtained have a size which can range from 5 to 100 nm depending on the properties of the polymers constituting it [Stoykovich 2006].

The Flory-Huggins interaction parameter, also known as “chi” or χ , represents the strength of repulsive interaction between two blocks. This parameter is defined by Equation I-3 for the copolymer blocks A and B. ϵ_{XY} represents the interaction energy per monomer between X and Y monomers, k_B represents the Boltzmann constant, T represents the temperature and Z represents the coordination number, that is, the number of nearest neighbor monomers for a lattice site:

$$\chi_{AB} = \frac{Z}{k_B T} [\epsilon_{AB} - \frac{1}{2}(\epsilon_{AA} + \epsilon_{BB})]$$

Equation I-3: Flory-Huggins interaction parameter χ for two copolymer blocks A and B [Bates 1999].

A positive value of the Flory-Huggins parameter χ corresponds to a net repulsion between the two blocks present, generally causing phase separation, while a negative value indicates a free-energy drive towards mixing. As we can see from Equation I-3, the Flory-Huggins interaction parameter is inversely proportional to the temperature, which means that the more the temperature increases, the lower χ will be, favoring mixing.

When the χ between the two blocks is positive, obtaining microphase structures with a block copolymer is possible depending on the degree of polymerization (N) of the block copolymer and on process temperature. The strength of the repulsive interaction is characterized by the product χN . A product $\chi N = 10.5$ has been calculated as the location of the order-disorder transition (ODT). Thus, diblock copolymers of high molecular weight or with strongly incompatible blocks ($\chi N > 10.5$) are predicted to be microphase separated, whereas smaller copolymers with more compatible blocks ($\chi N < 10.5$) are predicted to show no microphase separation [Bates 1999].

The morphology of the structures formed after microphase separation depend on the volume fraction (f) of each phase and on the product χN . Figure I-9 shows the typical phase diagram for a diblock copolymer as well as the different morphologies that might be obtained depending on the volume fraction of each phase. We note that the parameter χN has little influence on the morphology except when $\chi N < 10.5$ (represented as DIS in the phase diagram), because in this case the phases do not segregate and therefore no pattern is formed. For $\chi N > 10.5$, the volume fraction of each phase determines the corresponding structure: lamellar (LAM) when $f_A = f_B = 0.5$, followed by gyroidal (GYR), cylindrical in hexagonal (HEX) structure and spherical in body-centered cubic (BCC) structure, respectively, as the volume fraction of one of the blocks increases. A rarer cubic close-packed structure (CPS) is also possible [Cochran 2006] [Kim 2010].

Amongst these structures, two have been investigated the most for microelectronic applications: cylinders and lamellae structures. Once one phase has been selectively removed from the other in order to obtain an etch mask, cylinders allow for contact hole patterning while lamellae are used for line/space patterning [Kim 2010].

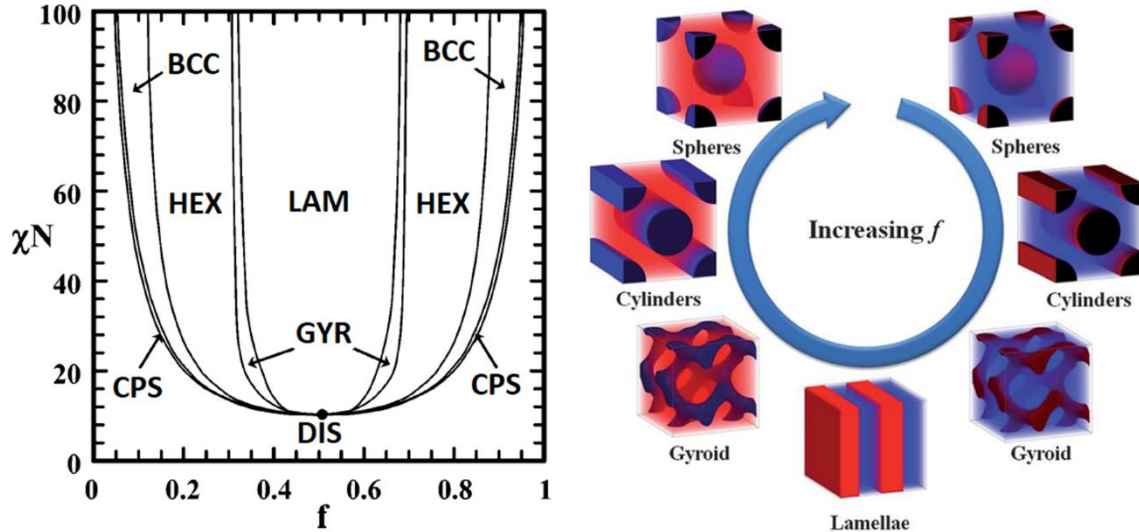


Figure I-9: On the left, a typical phase diagram for a diblock copolymer adapted from [Cochran 2006]. On the right, the possible morphologies for the diblock copolymer depending on the volume fraction (f) of the red phase [Koo 2013].

The Flory Huggins interaction parameter χ also has a very important role in the definition of the block copolymer's intrinsic period (L_0), which corresponds to a repeating unit of the block copolymer (one A block and one B block) and is equivalent to the pitch of the nanostructures obtained. The period of the block copolymer is a key parameter for the semiconductor industry, since it determines the size of the patterns obtained.

In order to determine L_0 , different proportionality laws have been established over the years by research groups [Sivaniah 2008] [Matsushita 1990]. All of them agree on the proportionality between the period and the degree of polymerization of the polymer:

$$L_0 \propto N^\alpha$$

Equation I-4: Proportionality law for determining the intrinsic period L_0 of the block copolymer.

The exponent α varies depending on the degree of phase separation. The phase diagram presented in Figure I-9 can be divided into three horizontal segments defining segregation zones characteristic of three different values of the product χN :

- **Strong Segregation Limit (SSL)**: this segment is not represented on the phase diagram, but corresponds to the product $\chi N \gg 100$. In this zone, the coefficient α has been demonstrated to be $2/3$ [Hashimoto 1980]. For the SSL, a more precise law of proportionality also involves the Flory-Huggins parameter χ , with a representing the statistical length of the monomer:

$$L_0 \sim a \chi^{\frac{1}{6}} N^{\frac{2}{3}}$$

Equation I-5: Proportionality law for the intrinsic period L_0 of the block copolymer in the strong segregation limit.

- **Weak Segregation Limit (WSL)**: this segment is located in the lower part of the phase diagram, where the product $\chi N < 40$. In this segment, the coefficient α is close to $1/2$.

- **Intermediate Segregation Regime (ISR)**: this segment constitutes the heart of the diagram, where $40 < \chi N < 100$. In this zone, the value of α varies between 0.72 and 1.017 (theoretical) or 0.80 and 0.83 (experimental) [Sivaniah 2008].

In order to have stable structures which are better suited to the lithography requirements, it is preferable to be in the regime of strong segregation (SSL). In the SSL, the well-defined interface width leads to lower pattern roughness. Moreover, the fact that the transitions between morphologies are independent of χ and of N ensures better reproducibility of the results. Finally, since Equation I-5 establishes that the period L_0 is defined by intrinsic parameters of the material, full control over all dimensions of the nanostructures is possible.

The most commonly studied block copolymer for the DSA application is the polystyrene-*b*-poly(methyl methacrylate), also known as PS-*b*-PMMA, due to its easy synthesis and well-known properties [Argoud 2014]. However, PS-*b*-PMMA presents a relatively low Flory-Huggins parameter ($\chi \approx 0.06$ at 298K [Girardot 2014]). In order to satisfy the condition for the order-disorder transition ($\chi N > 10.5$), the minimum pitch for the PS-*b*-PMMA system is limited to around 24 nm for minimum degrees of polymerization $N \approx 500$.

Therefore, in order to obtain resolutions lower than that of PS-*b*-PMMA and remain attractive for the smaller technological nodes, the most common strategy consists in increasing the value of χ . Doing so allows us to reduce the value of N – and thus also reduce the BCP's period – without violating the condition of the order-disorder transition. This “strong χ / weak N ” approach has given rise to the development of so-called “high- χ ” block copolymer systems over the past years [Feng 2017]. Moreover, the increase in χ leads to an increase in repulsion between the blocks: the domains are thus better defined and present better Line-Edge Roughness (LER) and Line-Width Roughness (LWR) compared to PS-*b*-PMMA [Tsai 2016]. The high- χ BCP systems currently under investigation can be divided into two main groups: organic and inorganic high- χ block copolymers.

Purely organic high- χ block copolymers are developed based on monomers of very different polarity (such as PS-*b*-P2VP with $\chi \approx 0.18$ [Gu 2012]) or hydrophobicity (PCHE-*b*-PMMA [Kennemur 2014] with $\chi \approx 0.32$ and capable of producing sub-8 nm lamellae). Using highly hydrophobic blocks like polylactic acid in a PS-*b*-PLA also increases incompatibility and results in $\chi \approx 0.23$ [Zalusky 2002]. Another example of purely organic high- χ BCPs includes the “HC series” developed by EMD Performance Materials with pitch of 17 to 26 nm [Hirahara 2016]. Other authors have started from the structure of PS-*b*-PMMA by adding a third monomer. This is the case, for example, of Zhou *et al.* who introduce vinylnaphthalene into the chain of the PS block to form a poly((styrene-*random*-vinylnaphthalene)-*block*-methyl methacrylate) (PSVN-*b*-PMMA) BCP and double the χ parameter of PS-*b*-PMMA [Zhou 2016].

Inorganic high- χ block copolymers usually consists of one organic phase (for example, PS or PMMA) covalently bound to one phase containing an inorganic element, such as silicon or iron. The use of inorganic blocks makes it possible to increase the χ parameter while also significantly increasing the etching contrast. Most of the inorganic high- χ BCPs present a silicon-containing phase such as polydimethylsiloxane (PDMS) as one of the blocks. Poly(styrene-*block*-dimethylsiloxane) (PS-*b*-PDMS) ($\chi = 0.26$ at 300K and pitch of 14 nm) [Girardot 2014] and poly(lactic acid-*block*-dimethylsiloxane) (PLA-*b*-PDMS) ($\chi = 1.41$ at 300K) are some of the examples found in the literature. K. Aissou *et al.* demonstrated a templated semicrystalline poly(1,1-dimethylsilacyclobutane-*block*-methyl methacrylate) (PDMSB-*b*-PMMA) thin film enabling the production of highly ordered cylinders of 9-nm diameter [Aissou 2015]. Luo *et al.* studied a PDMS-*b*-PMMA with $\chi = 0.24$ at 300K, demonstrating well-ordered sub-10 nm line and sphere features under either thermal or solvent

annealing conditions [Luo 2015]. Durand *et al.* demonstrated a poly(4-methoxystyrene-*block*-4-trimethylsilylstyrene) (PMOST-*b*-PTMSS) with 20-nm and 14-nm pitch [Durand 2015]. Finally, Rodwogin *et al.* reported on the assembly of a PLA-*b*-PDMS-*b*-PLA triblock copolymer which presents a $\chi = 1.4$ at 298K and is able to form lamellar, cylindrical and spherical morphologies with sub-20 nm pitch [Rodwogin 2010]. Iron-based block copolymers such as poly(nonafluorohexyl methacrylate-*block*-ferrocenylmethyl methacrylate) (PF9MA-*b*-PFMMA) have also been demonstrated [Chernyy 2017].

Organic and inorganic high- χ block copolymers present both advantages and limitations when it comes to their application in lithography. Organic block copolymers usually present an easier synthesis, while inorganic BCPs most of the times demand additional processing, such as solvent annealing, addition of a top coat, and others. Inorganic BCPs are considered better options for etching, since it is easier to obtain a good etching selectivity between inorganic and organic phases. However, a higher incompatibility between the two blocks also presents some drawbacks: these BCPs usually have a high diffusive energy barrier and slow kinetics as well as a preferential wetting of one of the blocks to the air interface [Mokarian-Tabari 2014]. Organic BCPs, on the other hand, are known for having lower etching selectivity between the two organic phases which, combined with the smaller dimensions (thickness and pitch), renders the pattern transfer into the subjacent layers more challenging. Furthermore, other advantages and challenges related to each type of high- χ BCP will be presented in the next section, when we explain the procedure for obtaining a BCP film.

1.3.2 Obtaining a block copolymer thin film

The block copolymers are often supplied in solution, which is then deposited by spin-coating on the wafers. The speed of rotation of the spinner as well as the viscosity and concentration of the solution determine the thickness of the copolymer film obtained.

As deposited in a thin film on a wafer, block copolymers are in a disordered state, where the domains between each block are not defined. The different film deposition parameters (speed of rotation, evaporation of the solvent, etc.) can slightly influence the shape of the polymer chains on the wafer. However, the domains are not defined at this stage due to the low self-assembly kinetics of the chains. Micro-phase separation is above all a thermodynamic phenomenon, requiring an input of energy into the system to separate the different phases. The most widely used method is thermal annealing. The wafer is placed in an oven heated to a temperature above both the glass transition temperature (T_g) and the order-disorder temperature (T_{ODT}) of the two blocks and below their degradation temperature. The kinetics of the micro-phase separation are increased due to the increased mobility of the chains and, therefore, the domains between the blocks are formed. The ideal annealing time and temperature are different depending on the thickness and the morphology of the film, but also the length of the copolymer chains [Choi 2010] [Tseng 2010].

Obtaining microphase separation and forming the desired nanostructure (lamellae or cylinders, for example), however, is often not enough to use these block copolymers in lithography. The two blocks should be oriented on the substrate in such a way that the patterns defined by it can be transferred through etching to the substrate or to the underlying materials. Therefore, they must have a perpendicular orientation, meaning that the two blocks of the copolymer must be in contact with the surface of the substrate. Indeed, in order to incorporate the DSA into the microelectronics industry, one of the most important aspects is controlling the

block copolymer's orientation. Such orientation is defined by surface properties, particularly the affinity between the two blocks and the surfaces they are in contact with, like the substrate and the air [Han 2008]. For example, if a PS-*b*-PMMA with lamellar morphology is spin-coated directly onto a silicon (Si) substrate, the PS block will occupy the interface Si/BCP since it has more affinity with silicon, and the PS-*b*-PMMA BCP will therefore organize itself into horizontal lamellae, as illustrated in Figure I-10(a).

In order to obtain the vertical lamellae independently of the substrate's affinity to one of the blocks, a thin polymer layer is spin-coated on the substrate before the BCP deposition. This layer is commonly referred to as neutral layer because it has the same affinity for both phases of the block copolymer, and thus allows the formation of vertical morphologies [Mansky 1997], as illustrated in Figure I-10(b). This neutral layer is often composed of the same copolymer, but in random form (for example, PS-*r*-PMMA), along with other additives necessary to promote either the cross-linking or grafting of the neutral layer.

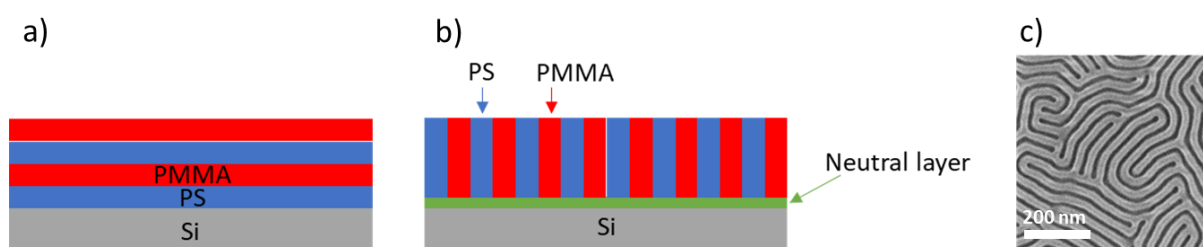


Figure I-10: (a) schema for the lamellar PS-*b*-PMMA deposited directly over the substrate, forming horizontal lamellae; (b) schema for the lamellar PS-*b*-PMMA deposited over a neutral layer, thus forming vertical lamellae; and (c) top-view SEM image of lamellar PS-*b*-PMMA assembled into a fingerprint-like vertical structure thanks to the neutral layer.

PS-*b*-PMMA presents the advantage of both phases having the same affinity for the air and, therefore, they only need a neutral layer at the bottom to obtain a vertical orientation. Most high- χ BCPs, however, do not present the same affinity for air: the strong repulsion between the two blocks often means that one phase (often the inorganic one, when applicable) has a stronger affinity to air than the other. Therefore, in order to obtain vertical lamellar morphologies with most high- χ BCPs, control of surface affinities and wetting is mandatory. The most common solution is the addition of a top coat (TC) layer with neutral affinity to both phases of the BCP at the interface between BCP and air [Bezard 2018].

The top coat can be either another copolymer spin-coated and annealed on top of the block copolymer [Bates 2012] [Kim 2014] or it can be integrated into the composition of the BCP [Zhang 2016] [Vora 2016]. The top coat's solvent must also be optimized: if the block copolymer is soluble in this solvent, it will not be possible to deposit the top coat over the BCP.

The addition of a neutral layer and a top coat (when needed) allows us to obtain a block copolymer assembled on a free surface. For a lamellar block copolymer, Figure I-10(c) shows a top-view scanning electron microscopy (SEM) image of the fingerprint-like structure that is formed once the appropriate neutral layer and/or top coat is used.

I.3.3 Obtaining patterns by directed self-assembly (DSA)

At this point of the integration, we have seen how to obtain the desired morphology and how to control the pattern orientation on the substrate. However, we are still not able to control the position of the patterns on the wafer to obtain lines or cylinders parallel to each other with long-

range order. Obtaining a three-dimensional control of the two phases requires a new constraint to be imposed on the block copolymer. The ensemble of guiding methods is referred to as Directed Self-Assembly, or DSA, and differ in the way they enforce the orientation control. Their common philosophy is to use the perfect alignment of well-established conventional lithography (top-down approach) so that the phase microseparation of the block copolymer (bottom-up approach) reproduces it at smaller resolution and higher density.

Two main approaches have been developed over the years: chemo-epitaxy and grapho-epitaxy. In both cases, the block copolymer is constrained in order to organize itself and form the desired line/space or contact holes pattern. The grapho-epitaxy is mainly based on mechanical constraints while the chemo-epitaxy is mainly based on chemical affinity constraints [Ji 2016].

I.3.3.1 Grapho-epitaxy

Segalman *et al.* first demonstrated the grapho-epitaxy technique back in 2001, using sphere-forming PS-*b*-P2VP block copolymers [Segalman 2001]. This guiding method uses mechanical constraints, such as topographical features obtained by conventional lithography, to act as guide-patterns for the block copolymer's self-assembly. The BCP is coated and annealed in the space between the guides. For lamellar BCPs, the sidewalls of the guide-patterns preferentially attract one domain of the BCP, allowing lamellar line/space patterns to form parallel to the sidewalls of the guide, as we can see in Figure I-11.

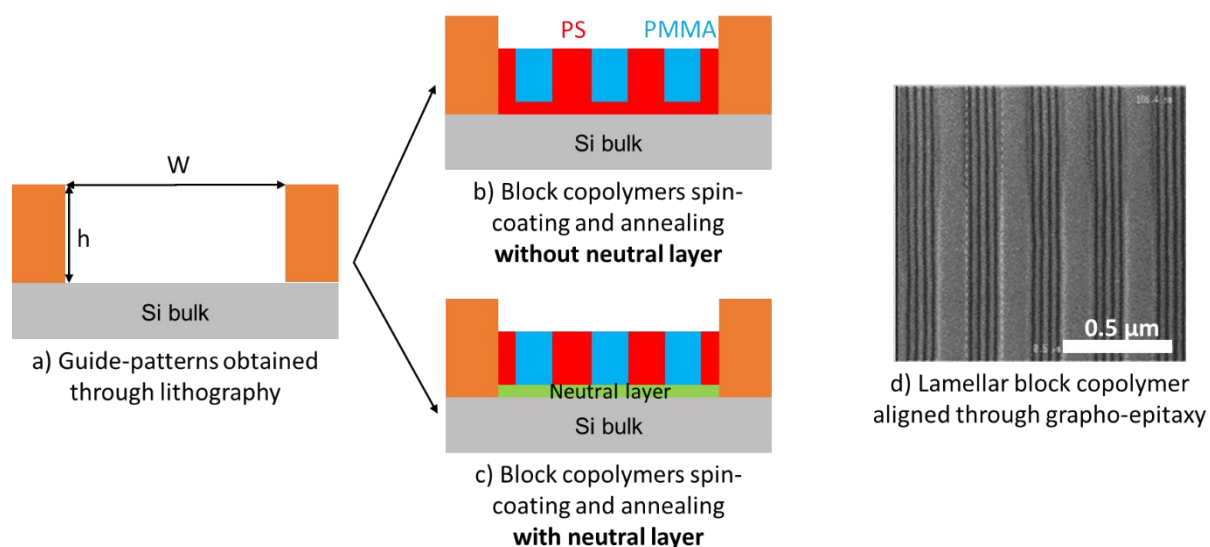


Figure I-11: Principle of grapho-epitaxy guiding method: (a) topographical features obtained by conventional lithography, which act as guide-patterns for the block copolymer's self-assembly (b) without or (c) with neutral layer, leading to the results observed in (d) the top-view SEM image of a lamellar PS-*b*-PMMA aligned using grapho-epitaxy [Claveau 2016].

The commensurability between the width of the trench guide structure (W) and the period L_0 of the block copolymer used must be respected for the good organization of the BCP within the guide. Different studies have shown that good organization is obtained when this width is proportional to the period of the block copolymer ($W = n * L_0$), which favors the formation of an exact number of n domains. Conversely, approaching $W = (n + 0.5) * L_0$, a coexistence between two favorable states (n and $n + 1$) is preferred [Claveau 2016] [Cheng 2004].

Therefore, the trench guide width is equally chosen according to the multiplication factor (n) that we want to achieve. For a lamellar BCP, this factor qualifies the number of lamellae obtained (by one of the two polymers) within a guide.

The height of the trench guide structure (h) is also a parameter to be taken into account during grapho-epitaxy. For the topography confinement effect to prevail over the other interfaces, h must be at least equal to the intrinsic period L_0 of the BCP used. Several works have shown that the ratio between the thickness of the deposited copolymer (t) and the trench height (h) plays a determining role in the orientation and the level of defects of the final assembly [Yang 2009]. The results of Park *et al.* show that for a lamellar PS-*b*-PMMA, when the t/h ratio > 1 , the material present above the trenches is no longer confined and adopts a fingerprint structure [Park 2009].

Despite the stress applied to the block copolymer by the topological guide, it is also necessary to control the affinity of the copolymer with the walls and the bottom of the trenches [Koo 2013]. Indeed, Figure I-11(b) shows that, for line/space applications using a PS-*b*-PMMA lamellar block copolymer aligned by grapho-epitaxy, a wetting layer composed of the block that has the most affinity for the substrate is formed on the interface between the BCP film and the substrate, which renders pattern transfer more difficult [Claveau 2017]. Therefore, a neutral layer may be deposited only at the bottom of the trenches to eliminate the wetting layer, as shown in Figure I-11(c). Several solutions to obtain different affinities at the walls and the bottom of the trenches have been developed by CEA Leti through the use of a sacrificial layer [Delachat 2018] or UV exposition [Pimenta-Barros 2018], and also by Imec through preferential grafting of two different polymeric layers [Doise 2017].

IBM, CEA-Leti and others have demonstrated different grapho-epitaxy approaches applied to an integration. There are two main types of applications for which grapho-epitaxy has been demonstrated: contact hole shrink for vertical connections and line multiplication for interconnections, gates and active areas of transistors [Cheng 2010] [Black 2005].

For line/space applications, IBM reported on the first DSA-patterned FinFET fabricated using the tone-inverted grapho-epitaxy resolution enhancement (TiGeR) technique with a 29-nm pitch PS-*b*-PMMA. A schematic representation of the TiGeR process can be found in Figure I-12. The BCP is oriented by SiO_x guiding patterns formed by e-beam lithography of hydrogen silsesquioxane (HSQ) resist, which converts the HSQ into a low quality SiO_x . After forming the DSA patterns, the PMMA domains are selectively removed from the BCP, except for the PMMA half-domains formed between the PS and the SiO_x guide. The lines pattern is then transferred into the silicon nitride (SiN) hard mask and the organic planarizing layer (OPL). A tone-inversion process is then applied in the OPL layer by spin-coating a spin-on dielectric material, etching back to reveal the OPL, followed by removal of the OPL. Finally, the tone inverted image is transferred into a thin SiN hard mask layer and into the silicon on insulator (SOI) underneath [Tsai 2014].

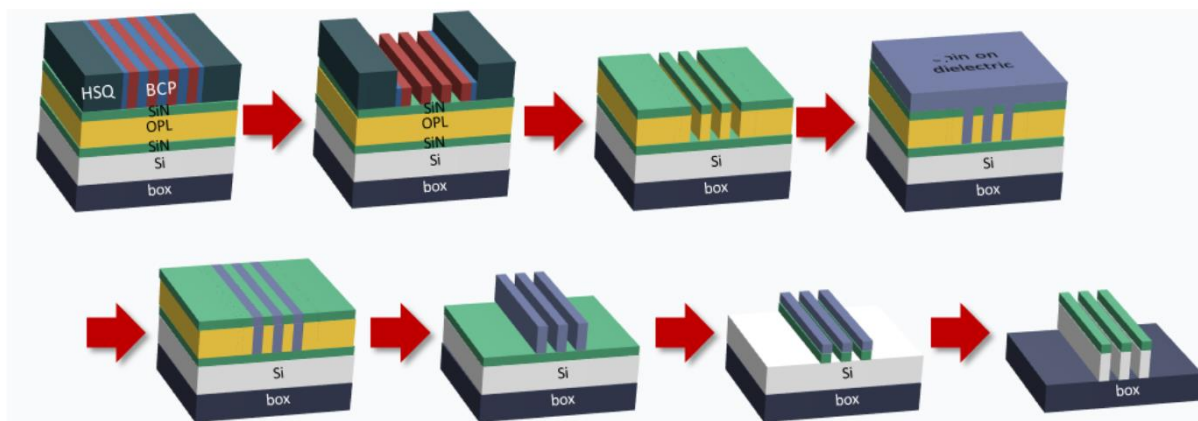


Figure I-12: Schematics for the tone-inverted grapho-epitaxy resolution enhancement (TIGeR) technique used by IBM to obtain 29-nm pitch DSA-patterned FinFETs [Tsai 2014].

Grapho-epitaxy has also been used in contact shrink applications, making it possible to obtain contacts with dimensions not attainable by conventional lithography (around 20 nm) and with very good alignment. Chang *et al.* have shown that the use of block copolymers organized by grapho-epitaxy can meet the requirements in terms of electrical results for obtaining devices for sub-20 nm technological nodes. They have demonstrated top gated FETs and CMOS inverters featuring 20-nm contact holes defined by PS-*b*-PMMA using guide trenches with a width of 60 nm obtained by optical lithography in order to obtain a row of contacts of 20 nm with the BCP [Chang 2009] [Wong 2012].

Through these examples, we can see the different possibilities available for microelectronics thanks to the organization of block copolymers by grapho-epitaxy. Nevertheless, this technique presents some limitations. Since the topographical features occupy some space on the wafer surface, grapho-epitaxy presents a lower pattern density when compared to the other DSA approach (chemo-epitaxy). In addition, all defects of the guiding topographical prepattern (for example, the line-edge roughness of its sidewalls) may propagate into the adjacent self-assembled domains and cause additional CD variation and placement error [Cheng 2010].

While the use of grapho-epitaxy for contact hole shrink is validated, when it comes to obtaining line/space patterns, chemo-epitaxy is often preferred.

I.3.3.2 Chemo-epitaxy

Chemo-epitaxy consists of a guiding method by surface property change of the substrate that is to receive the block copolymer. Overall, the principle of chemo-epitaxy is based on the long-range alignment of a block copolymer thanks to the presence of narrow guiding stripes that present a chemical affinity to one of the blocks. These guiding stripes present a CD corresponding to half the period of the block copolymer (L_0) and are interlaced with wide neutral layer stripes on the substrate surface. If the distance between each guide follows the commensurability rules, when the BCP is coated and annealed over the surface, the guiding stripes will attract one of the blocks and induce the BCP to organize itself in the desired patterns (usually line/space) over long distances. For this, the distance between each guide (W) must be proportional to the BCP's period: $W = n * L_0$, where n is once again the multiplication factor (MF) [Hu 2014].

Different chemo-epitaxy processes have been developed over the last few years, like LiNe [Liu 2011], Lift-off [Cheng 2010], and SMART [Kim 2013], amongst others. With the current chemo-epitaxy methods, it is possible to achieve multiplication factors of two or three, and sometimes even four. Beyond this, the higher multiplication factors generate high defectivity, which no longer allows the block copolymer to be integrated in a manufacturing process.

The LiNe integration, named after the two inventors Liu and Nealey, is the most popular one. Figure I-13 presents the principles of this technique. To direct the self-assembly of PS-*b*-PMMA, for example, a cross-linkable polystyrene (X-PS) layer is deposited over silicon. This layer is identified as “mat” in Figure I-13. Then 193nm immersion lithography, consisting of deposition of the photoresist and definition of the patterns, is carried out so that the pitch of the patterns created is an integer number of times greater than the period of the copolymer (L_0). The resulting structures are treated with an oxygen-based plasma trim etch that laterally shrinks the photoresist lines and removes X-PS in the spaces between them. When the line/space patterns transferred to the X-PS have been reduced to a CD_{guide} of approximately $0.5 * L_0$, the remaining photoresist is stripped. Next, a PS-*r*-PMMA designed to be non-preferential to the two blocks, identified as “brush” in Figure I-13, is grafted between the remaining XPS structures. This results in a two-tone pattern of sparse X-PS guide stripes and background brush regions. Finally, the block copolymer is deposited and, because of the chemical affinity, the X-PS structures attract the PS block. Annealing then allows the block copolymer to organize itself [Liu 2013]. This flow has been generalized for use with many different BCP systems by changing the guiding mat and background materials [Bates 2014] [Khaira 2014].

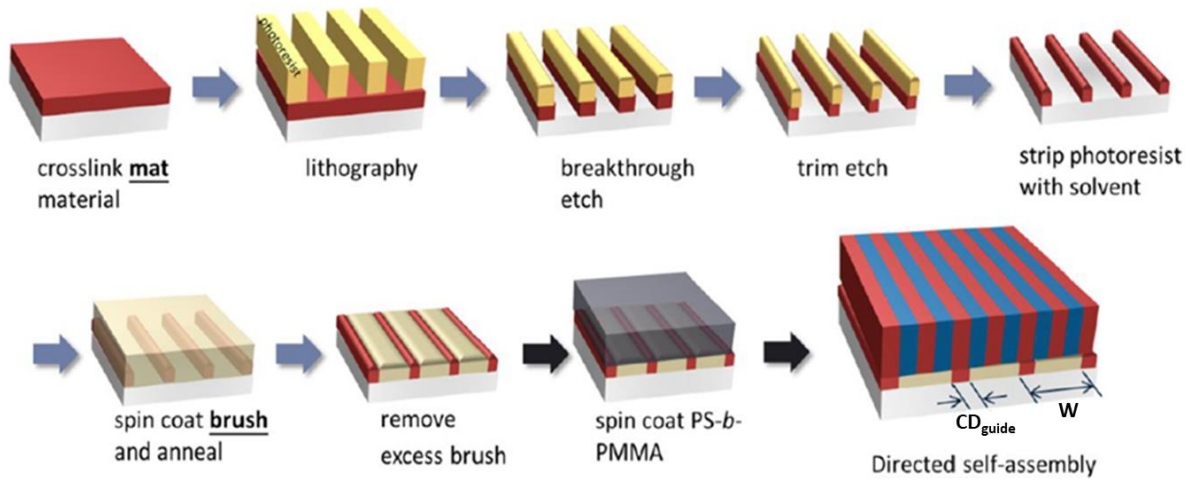


Figure I-13: Schematics for the LiNe chemo-epitaxy integration. Adapted from [Liu 2013].

A few years later, studies by Williamson *et al.* demonstrated the critical importance of oxidized X-PS sidewalls during oxygen plasma breakthrough and trimming for the success of the LiNe integration. These highly hydrophilic areas, which are PMMA-attractive, create additional chemical contrast and contribute just as much for self-assembly guiding as intact X-PS. Unlike the IBM or AZ methods, LiNe chemo-epitaxy is therefore generated by a constraint of not only two but rather three tone zones (PS-attractive, PMMA-attractive and neutral) [Williamson 2016]. This three-tone chemical contrast could explain why the defectivity of LiNe is much better than that of the other two processes [Somervell 2012].

IBM developed an integration called “Lift-off”, shown in Figure I-14, which consists of a pattern-first, neutralize-last process to fabricate chemical prepatters. First, polarity-switched

photoresist prepatterns consisting of around 30-nm lines and 100-nm pitch are formed using 193 nm immersion lithography. These prepatterns mask some areas of the substrate while a neutral layer is grafted over the whole surface. Subsequent selective lift-off of the photoresist using standard TMAH developer generates sparse chemical patterns suitable for DSA. Finally, the block copolymer is spin-coated and annealed in order to obtain straight lines. This integration allows for a more relaxed resist lithography at $CD_{\text{guide}} = 2 * L_0$ or $3 * L_0$. Also, since the neutral layer is applied last in this process, the photoresist pattern can be trimmed to overcome the restrictions of the optical lithography tool without any damage to the surface properties of the underlayers [Cheng 2010]. This process has been shown to be fully compatible with industry 300 mm tools on the Imec pilot line [Somervell 2012].

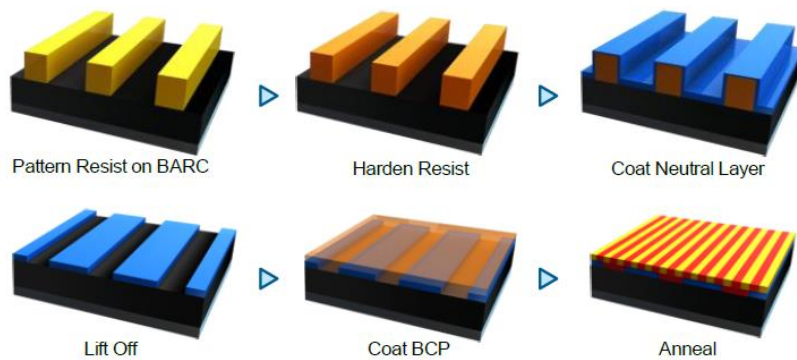


Figure I-14: Schematics for the Lift-off chemo-epitaxy integration developed by IBM [Somervell 2012].

AZ's SMART™ (Surface Modification for Advanced Resolution Technology) integration is presented in Figure I-15. It follows the same relaxed lithography principle as IBM except that it starts with a cross-linkable PS-*r*-PMMA neutral layer, identified as NLD-175, deposited over the substrate. Then the photoresist is spin-coated on top of the neutral layer and 193 nm immersion lithography is carried out to obtain the resist prepatterns. An oxygen-based Reactive Ion Etching (RIE) is performed to remove the neutral layer at the bottom of the resist trenches. The remaining resist is then stripped and a substrate alternating PS-*r*-PMMA neutral layer and vacant areas is obtained. In some cases, this chemical contrast is enough to align the BCP. However, for a more stable performance, a thin layer with affinity to one of the blocks (identified as NLD-226) is spin-coated and grafted. This layer presents high reactivity to the substrate (SiARC in this case) and low reactivity to the neutral layer (NLD-175), ensuring that the NLD-226 that is deposited over the NLD-175 does not graft to it and is therefore removed during rinse. This way, only a monolayer of NLD-226 is left in the trenches, increasing the chemical contrast and leading to the alignment of the block copolymer [Kim 2013]. A step of a few nanometers is present at the interface between NLD-175 and NLD-226: due to the introduction of topography, the stresses brought to the copolymer are greater and thus offer better alignment of the BCP [Kim 2015].

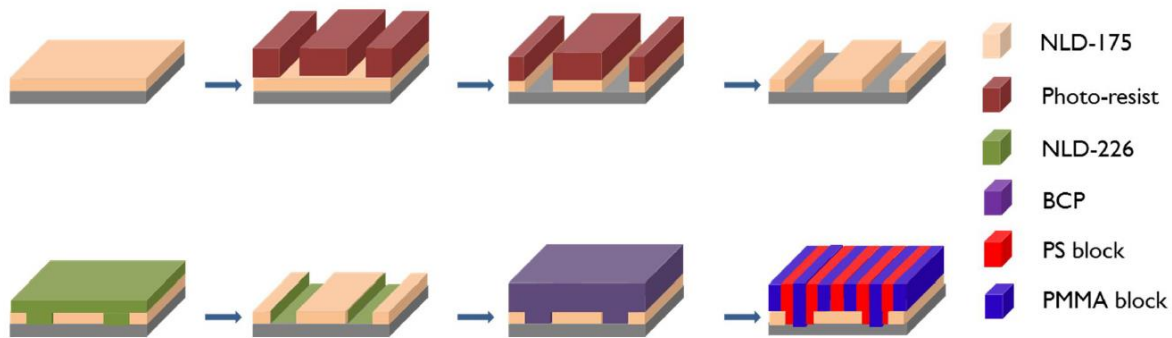


Figure I-15: Schematics for the SMART™ chemo-epitaxy integration developed by AZ [Kim 2015].

As we have seen, one of the advantages of chemo-epitaxy is its long-range order compared to grapho-epitaxy, meaning it is possible to obtain lines of the same dimensions on a larger scale since there are no half-lamellae or guide hindering this organization. However, the absence of lateral mechanical stress means that, theoretically, the attainable multiplication factor is less important than for grapho-epitaxy.

Several studies applied to the LiNe, Lift-off and SMART™ integrations have highlighted the importance of introducing a physical stress on the substrate by having a difference between the thickness of the guide and neutral layers. This has been shown to promote a better alignment of the block copolymer and reduce defectivity by increasing the guiding strength of the prepattern. Blachut *et al.* studied the impact of the guide thickness on the alignment of the block copolymer through the development of a hybrid chemo/grapho-epitaxy process. Two different guide step thicknesses were evaluated: 0 nm (in the case where guide and neutral layers present the same thickness, meaning a purely chemo-epitaxy integration) and 11 nm. The results attest to better alignment if a step of noticeable thickness is present, leading to the development of so-called “hybrid” chemo/grapho-epitaxy approaches [Blachut 2016].

I.3.3.3 ACE chemo-epitaxy process

As part of this thesis, we have focused on the chemo-epitaxy process developed by the CEA-Leti and Arkema, which is known as “ACE” for Arkema-CEA [Paquet 2019].

Figure I-16 presents the schematics for the ACE flow. The first part of the process is equivalent to a Self-Aligned Double Patterning (SADP) process. 193 nm immersion lithography is performed on a standard trilayer stack which consists of, from bottom to top: Spin-On Carbon (SOC), Silicon-containing Anti-Reflective Coating (SiARC) and photoresist. The trilayer stack is plasma etched in order to transfer the lithography patterns into the SiARC and SOC layers and then the SiARC is wet removed to conserve only the SOC mandrel. Afterwards, a thin silicon nitride (SiN) layer is deposited over the SOC mandrel and anisotropically etched in order to form the spacers. The SOC mandrel is removed through plasma etching, forming spacers with a CD corresponding to half the pitch of the BCP, which will later be replaced by the guide patterns for the BCP’s self-assembly.

The directed self-assembly part of the ACE flow begins by spin-coating and annealing the neutral layer, thus filling the area between the spacers to create a neutral surface. Next, the SiN

spacers are removed. In the space left by the spacers that were removed, a guiding layer is then selectively grafted, therefore obtaining the guiding template for the BCP alignment. Finally, the block copolymer is spin-coated and annealed to obtain guided line/space patterns.

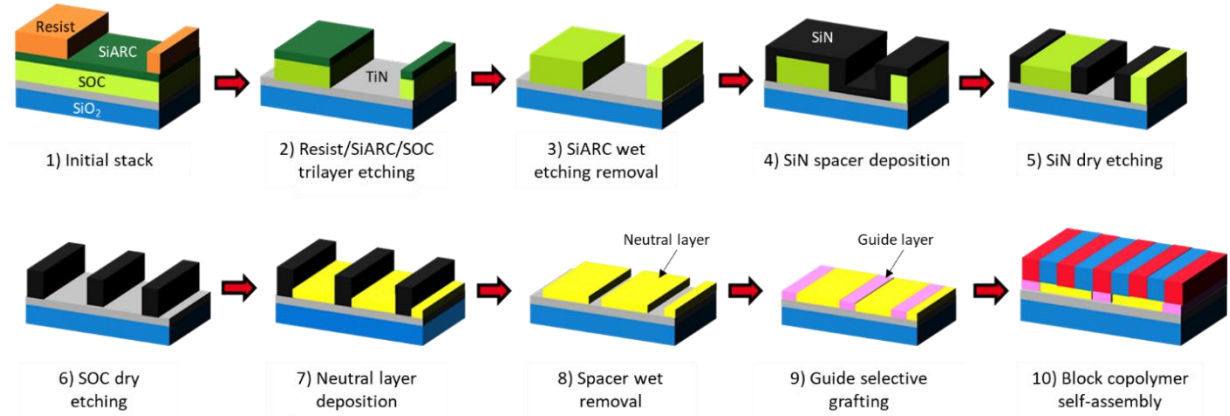


Figure I-16: ACE process flow schematics, consisting of a conventional Self-Aligned Double Patterning (SADP) process (steps 1 to 6), followed by the DSA process (steps 7 to 10).

In order to integrate the high- χ block copolymers in chemo-epitaxy, the main difficulty comes from the first lithography step. Two key parameters are limiting, namely the minimum pitch and the guide CDs accessible by the lithography technique used, in particular 193 nm immersion lithography. Although the LiNe process trims the resist guides to reduce their CD, this etching step adds new constraints: the chemical modification of the lithography resist used, which might make its stripping difficult; the affinity modification of the underlying surface; and an increased roughness (LER/LWR) of the guides.

Figure I-17 presents the guide period necessary for directed self-assembly of block copolymers with different multiplication factors (MF) according to their intrinsic period (L_0). The need for 193 nm immersion (in blue) or EUV lithography (in violet) is indicated for the LiNe, SMART™ and ACE integrations. For the LiNe flow, beyond a BCP period of 28 nm, the definition of the guides by 193 nm immersion lithography and the trimming of the photoresist brings too much defectivity and roughness to the process. Therefore, the LiNe process using a guide with $CD = 0.5 L_0$ can no longer respond to the periods defined by the high- χ block copolymers with $L_0 < 20$ nm without the use of EUV.

In the ACE flow, however, the spacers form a network of lines whose pitch is equal to half the initial pitch of the lithography patterns and whose width is defined by the thickness of the spacer deposited on the sides. Therefore, we can see in Figure I-17 that ACE is able to relax the lithography constraints and obtain a MF of three or four for high- χ block copolymers without the need for EUV patterning.

Process	BCP L_0 (nm)	Lithography pitch by MF (nm)			CD guide (nm)	
		2	3	4		
LiNe & SMART	30	60	90	120	15	
	18	36	54	72	9	
	14	28	42	56	7	
ACE	30	120	180	240	15	193i
	18	72	108	144	9	
	14	56	84	112	7	EUV

Figure I-17: The lithography pitch necessary for directed self-assembly of block copolymers with different multiplication factors (MF) according to their intrinsic period (L_0). The need for 193 nm immersion (in blue) or EUV lithography (in violet) is indicated for the LiNe, SMART™ and ACE integrations [Rademaker 2020].

We have seen how to direct the self-assembly of block copolymers in order to obtain long-range order and dense patterns. Another critical step for the integration of DSA in the microelectronics industry is to selectively remove one block while conserving enough of the other block to transfer the line or hole pattern into the underlayers (usually a hard mask). This is achieved through etching. Furthermore, other important steps present in the chemo-epitaxy integrations that we have presented also consist of etching steps: trimming and stripping of the resist, spacer formation, amongst others.

The next section will present the principles of wet and dry etching and their role in microelectronics.

I.4 Etching

Etching, in microelectronics, is the act of removing material from a wafer's surface in order to transfer patterns from one layer to another, and therefore create the desired microelectronic components. As we have seen before, it usually follows a lithography step that creates the patterns on a photoresist. Etching is then responsible for transferring said patterns into a hard mask or the desired subjacent layer, therefore helping define the different parts of the integrated circuits (ICs).

In the early days of microelectronics, the first etching processes consisted of chemically attacking the wafer with either acid or basic solutions. This type of etching is called "wet etching" and it can be very selective, fast and relatively simple. However, it presents one important disadvantage for the smaller nodes: it is isotropic, that is, the etching rate of the material is the same in all directions, as we can see in Figure I-18(a). This means there is usually an undercutting phenomenon under the mask that alters the desired CD of the patterns since it does not allow the conservation of their dimensions during their transfer.

That is why, from the late 1970s, another type of etching was introduced into semiconductor manufacturing: the plasma etching, also known as dry etching. It was first introduced in a Capacitively Coupled Plasma (CCP) plasma reactor with mainly Oxygen and Fluor-based chemistries [Coburn 2002]. As we can see in Figure I-18(b), plasma etching usually presents an anisotropic aspect, meaning the etching rates vary for each direction through directional acceleration of the ions. Over the years, plasma etching has replaced most selective wet etching

processes in IC manufacturing because of its cleanliness, uniformity, ease of automation and ability to allow faithful transfer of submicron circuit patterns [Hoffman 1998].

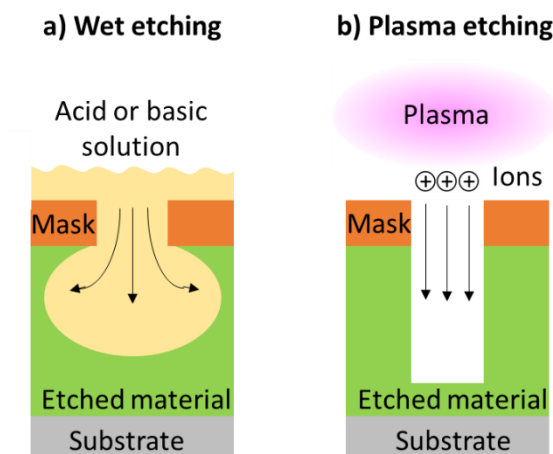


Figure I-18: Example of (a) wet etching with isotropic aspect and (b) plasma etching with anisotropic aspect.

Since then, plasma etching has been changing and improving in order to meet manufacturing demands. This includes the introduction of other types of reactors, such as the Inductively Coupled Plasma (ICP) reactor, which allows to separate the plasma generation from the wafer bias; and different approaches, such as Atomic Layer Etching (ALE), which allows for plasma etching with atomic-scale precision [Kanarik 2015]. Each wafer is exposed to a plasma etching environment between 10 and 20 times during its manufacture and without the highly anisotropic etching provided by this critical process, high density IC manufacturing would not be possible [Coburn 2002].

It should be noticed that anisotropic wet etching exists due to some wet etchants being capable of etching crystalline materials at different etch rates depending on the crystal plane [Kelly 2005]. Plasma etching can also be isotropic depending on the material being etched and on the plasma parameters, as is the case for photoresist stripping under oxygen-based plasma.

In this PhD thesis, we have focused on plasma etching due to its ability to conserve pattern dimension, which is necessary for the etching of high- χ block copolymers. In order to understand the challenges related to the etching of block copolymers encountered during this PhD, as well as the results obtained, we shall briefly present what is a plasma and the important parameters related to plasma etching in microelectronics.

I.4.1 Principles of plasma etching

In physics, plasma is considered as the fourth state of the matter. Phase transformations of different materials usually occur through heating because the thermal agitation (that is, the kinetic energy) of the particles increases with temperature. Therefore, by increasing even more the temperature of a gas, the thermal agitation becomes so energetic that when the particles collide, they ionize. That is the plasma state, which may be defined as a partially ionized gas composed of positive (and sometimes negative) ions, electrons, and neutral species in molecular or atomic form. The proportion of these elements is such that the medium is globally neutral, meaning the density of electrons (n_e) is equal to the density of ions (n_i).

In the hot plasmas – the natural plasmas that form the stars, for example, and those obtained by nuclear fusion – all the species present in the plasma are in thermodynamic equilibrium, in very high temperatures (normally higher than 10^6 K). That means the hot plasma cannot be used in microelectronics.

For that reason, another type of plasma was developed, known as the “cold” plasma. In this case, the ionization of the gas is not caused by heating, but through electrical excitement by applying an electric field, generated by a radiofrequency (RF) power, on a low pressure gas (between 1 mTorr and 1 Torr) confined in a reactor chamber. Free electrons will then be accelerated and will ionize the other species when they collide. This plasma is not in thermodynamic equilibrium and is said to be “cold” because of the low electronic temperature ($T_e \sim 2\text{-}3$ eV). Therefore, it can be used in microelectronics, especially for the etching step [Hoffman 1998].

In the plasma phase, the only interaction between atoms and molecules are the collisions, namely the inelastic collisions involving the electrons. From these collisions, several different mechanisms can occur [Nojiri 2015]. The main mechanisms are:

- Ionization: $A + e^- \rightarrow A^+ + 2e^-$, in which an electron can ionize an atom or a molecule when it has an energy superior to the species ionization potential. This reaction represents the physical aspect of the etching and maintains the plasma.

- Dissociation: $AB + e^- \rightarrow A + B + e^-$, in which an electron can dissociate a molecule if its energy is larger than the binding energy of the molecule. This reaction creates the free radicals, which are the reactive agents in the plasma, responsible for its chemical aspect.

- Electronic excitation and relaxation: $e^- + A \rightarrow A^* + e^- \rightarrow A + e^- + h\nu$, in which an atom or a molecule at rest may be excited by absorbing energy, that is, an electron goes from an energy level to another. This excitation is always followed by the inverse phenomenon, the relaxation, in which the molecule or atom returns to its energy level at rest with the emission of a photon. h represents Planck’s constant while ν is the frequency of the emitted light.

- Electron attachment: $A + e^- \rightarrow A^-$, in which the colliding electron attaches to the atom and turns it into a negative ion. This reaction occurs more rarely than the others.

The plasma etching normally used in microelectronics is actually a synergetic mixture of two different types of etching: the chemical etching, responsible for the selective etching; and the physical etching, responsible for the anisotropy.

The **chemical etching**, also known as spontaneous etching, comes from the interaction between the thin film exposed to the plasma and the reactive species generated in the plasma by dissociation, such as the free radicals. These reactive species react with the target film and form volatile products, which are then desorbed and pumped out of the reactor. The chemical etching is isotropic and selective. The choice of the gases used is defined by the reaction products, which must usually be volatile and stable.

The **physical etching**, also known as sputtering, consists on the pulverization of the thin film when it is bombarded by highly energetic ions. The ion flux is created by the electric field present near the surface of the wafer, which vertically accelerates the ions, making them collide with the target film. Due to that vertical acceleration, the physical etching has a strong anisotropic aspect.

When we combine these two types of etching, we have a chemical etching assisted by ion bombardment, also known as Reactive Ion Etching (RIE) [Karouta 2014]. This mixture allows the combination, and even improvement, of the better aspects of each type of etching. For example, the ion bombardment improves the absorption of the reactive species in the material's surface by creating defects and breaking bonds. Also, the high energy from the ions accelerates the chemical reactions, by raising the temperature locally and improving the migration of the reactive species. Finally, the ion bombardment also stimulates the desorption of the reaction products.

The chemical etching assisted by ion bombardment is mainly anisotropic, thanks to the physical aspect. However, the chemical etching of the sidewalls is still present, as well as the loss of selectivity due to the ion bombardment. For the smaller patterns, in order to ensure that pattern transfer is perfectly anisotropic and selective, another mechanism has been introduced to plasma etching, known as **passivation**. Passivation is the phenomenon through which species resistant to etching, called passivating species, are deposited on the sidewalls of the thin film in order to inhibit the lateral component of the chemical etching. These passivating species come mainly from two different sources:

- From the gas phase: the passivating species is one of the gases injected in the chamber;
- From the pulverization of the mask: the passivating species can be generated by the ion bombardment of the material that forms the mask, which reacts with one of the gases in the plasma to form a passivation layer on the sidewalls of the subjacent layer.

I.4.2 Etching characteristics and criteria

In order to characterize the pattern transfer into the subjacent layers, some etching criteria must be taken into consideration and optimized. Some of the criteria that are considered important for the understanding of the results obtained in the framework of this PhD are presented below.

1) Etching rate (ER):

$$ER_A = \frac{\text{thickness of etched material } A}{\text{duration of the etching process}}$$

Equation I-6: Etching rate (ER) equation, defined by the thickness of etched material divided by the etching time.

The etching rate, defined in Equation I-6, is one of the most important parameters, since it defines the duration of the plasma etching process. An optimized etching rate usually means the equilibrium between high etching rate, which improves the productivity by allowing the processing of a higher number of wafers per hour, and an etching rate low enough so that the etching is still reproducible, since etching processes of only a few seconds tend to be more instable.

The etching rate is usually higher on the top of the patterns in comparison to the bottom. It can be influenced by several parameters, such as the geometry of the stack (for example, holes or lines), and the mask opening rate and material. The etching rate is usually estimated with the help of blanket wafers, which are silicon wafers with a homogeneous layer of a specific material on top, and ellipsometry measurements. However, the etching rate on blanket wafers is usually different from that on the patterned wafer, serving only as an estimate value for the later.

2) Selectivity:

In order to transfer the patterns into the subjacent layers, it is necessary to etch this layer without completely consuming the mask that determines the patterns. That means the etching step has to eliminate one material selectively to the other. The selectivity is described as the ratio between the etch rates of the two different materials, that is:

$$\text{Selectivity } A:B = \frac{\text{thickness of etched material } A}{\text{thickness of etched mask } B} = \frac{ER_A}{ER_B}$$

Equation I-7: Selectivity between materials A (subjacent layer) and B (mask), defined by the thickness of etched material A divided by the thickness of etched mask B, for the same etching time.

Therefore, the maximum thickness that can be etched from the material A corresponds to the product between the selectivity A:B and the initial thickness of the mask B. The selectivity between two materials is mainly determined by the choice of the etching gases, which define the reactive species present in the plasma.

3) CD/CD Bias:

The Critical Dimension (CD) refers to the minimal feature size on a transistor. It is a measure of the resolution of a lithography process. The CD Bias is the difference between the CD post-etch and the CD pre-etch. For block copolymers, the CD represents the width of the lines created by one of the blocks and corresponds to half the intrinsic period (L_0) of the BCP.

Finally, CD control refers to the set of methods and requirements to be respected in order to correctly transfer the CD of a mask (such as the remaining block from the block copolymer) into the subjacent layers on the stack. The thickness of the passivation layer formed on the sidewalls, for example, is a deviation of the desired CD size. By finding an equilibrium between etch and deposition rates within each step of the etching process, the passivation layer thickness can be controlled in order not to surpass the desired CD size.

4) LWR/LER:

With lamellar block copolymers, the main goal is to achieve straight lines by transferring the remaining block's lines into the desired stack. However, in reality, a perfectly straight line is hardly achievable, because there is always a variation on the profile of the line, defined by the Line-Edge Roughness (LER) and the Line-Width Roughness (LWR).

The Line-Edge Roughness refers to the fluctuation of edges along patterned lines while the Line-Width Roughness (LWR) represents the fluctuation in both edges, which induces a variation in the width of these narrow lines. The LER/LWR mainly originates from the fabrication process, such as lithography and etching [Jiang 2013].

For the DSA of block copolymers, LER/LWR normally comes from the guides used for grapho or chemo-epitaxy, as well as the dry etching removal of one of the blocks, which degrades the lines sides. For very small features, such as those obtained through high- χ block copolymers, the amplitude of LER/LWR is becoming comparable with the dimension of devices. Furthermore, LER/LWR has a more important impact in 3D multigate devices, such as stacked nanowires, where both gate and channel roughness exist. LER-induced variation is largely responsible for overall static variation, which cannot be neglected for multigate devices [Wang 2011]. Thus, minimizing LER/LWR is one of the priorities for the smaller technological nodes.

The LWR can be mathematically defined using the standard deviation 3σ for the pattern CD, as seen in Equation I-8, where w_i is the line width (CD) measured at the point i :

$$LWR = 3\sigma = 3 \sqrt{\frac{1}{N-1} \sum_{i=0}^N (w_i - \langle w \rangle_N)^2}$$

Equation I-8: Definition of LWR, based on the standard deviation 3σ for the pattern CD, where w_i is the line width (CD) measured at the point i .

The LER is the equivalent of the LWR for only one edge. Thus, we can define two different LER for a single line: the LER of the right edge and the LER of the left one. It can be mathematically defined by the same equation than the LWR one but using the line-edge position (x_i) instead of the width (w_i). Figure I-19 presents a top-view SEM image of a polysilicon line showing both the LWR and the LER, as well as a schema illustrating the difference between LER and LWR.

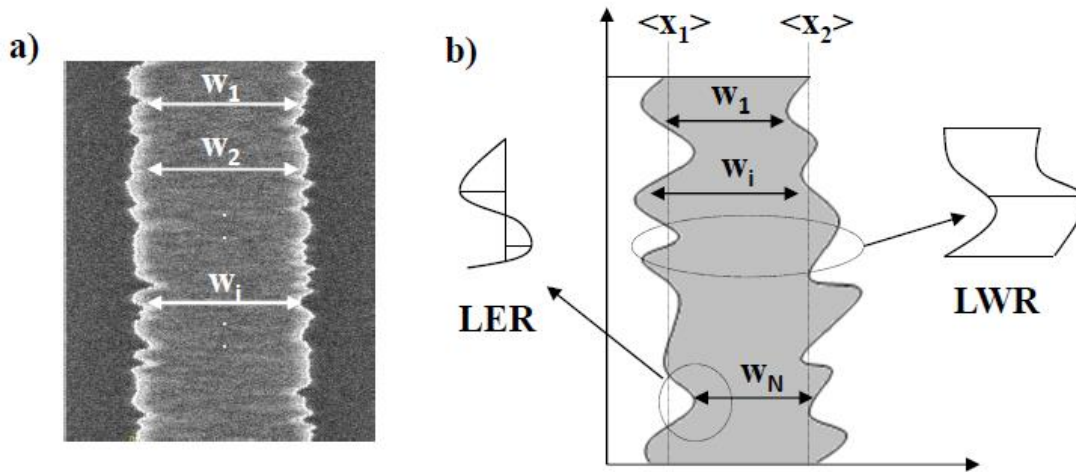


Figure I-19: (a) top-view SEM image of a polysilicon line showing both the LWR and the LER and (b) a schema illustrating the difference between LER and LWR. Adapted from [Azarnouche 2012].

I.5 Etching for the DSA: state of the art

As we have mentioned before, the main etching step for the DSA integration is the selective removal of one block, while conserving enough of the other block to be able to obtain and correctly transfer the line/space patterns into the subjacent layers. Over the last few years, several approaches for selectively removing one block have been developed for different block copolymers. This next section will focus on the state of the art for PS-*b*-PMMA and silicon-containing high- χ block copolymers etching, since these are the types of BCPs studied during this PhD.

I.5.1 State of the art of PS-*b*-PMMA etching

As the block copolymer that has been most widely studied for the DSA application, a major etching challenge for DSA integration into the microelectronics industry has always concerned the PMMA removal selectively to PS. To transfer the line/space pattern into the subjacent

layers, we must completely remove the PMMA and conserve enough PS budget. This can be achieved by either wet or dry etching. Wet etching allows for quasi-infinite selectivity between both blocks, but presents a pattern collapse risk due to capillary forces [Gharbi 2015]. Plasma etching is more compatible with narrow lines, thus limiting the risk of pattern collapse. However, the main difficulty with this approach is to obtain high selectivity between PMMA and PS films, since both are organic blocks.

For the traditional PS-*b*-PMMA system, PS has an aromatic backbone, whereas the PMMA structure is linear and oxygen-containing. Since it presents a higher oxygen content when compared to PS, which is oxygen-free, PMMA presents a higher plasma etching rate according to the Ohnishi parameter, which is based on the observation that materials containing a high concentration of C–O and C=O groups exhibit much higher sputter yields than pure carbon materials [Ohnishi 1983]. This difference in molecular structures can be expected to achieve a certain degree of etch selectivity.

The most common plasma etching used for the selective PMMA removal are based on O₂ [Tsai 2014] [Tsai 2016], Ar/O₂ [Ting 2008] [Yamashita 2012] and CO/H₂ [Sarrazin 2016] plasmas. Cyclic approaches based on CO + CO/H₂ [Miyazoe 2017] [Sarrazin 2018] or Ar/O₂ + Ar [Chan 2014] have also been studied. The O₂-based chemistries are very reactive and present low PMMA:PS selectivity (around 2.0). The CO + CO/H₂ plasma cycles were shown to be suitable for the cylindrical application, but present limitations for lamellar application: higher PS consumption due to a higher amount of oxygen (coming from PMMA) released during etching leads to lower selectivity (around 6.0) [Sarrazin 2017]. Therefore, an oxygen-free chemistry based on CH₄/N₂ was developed by Sarrazin *et al.* to obtain high selectivity with line/space patterns for standard PS-*b*-PMMA with a 38-nm pitch [Sarrazin 2019]. However, as the size of the features decrease, the thickness of the BCP film also decreases and any steps that can be taken to enhance the etching selectivity will soon be a necessity to achieve pattern transfer with high fidelity.

I.5.2 State of the art of silicon-containing high- χ BCP etching

As stated before, silicon-containing block copolymers reportedly present a better selectivity between the two phases, since one of them is purely organic while the other contains silicon in its composition. One of the most studied silicon-containing high- χ BCPs is the PS-*b*-PDMS. For the PS removal selectively to a silicon-containing phase such as PDMS, the most commonly used approaches are oxygen-based plasmas. Oxygen is known to etch the organic block by forming a volatile CO_x product, while oxidizing the silicon-containing block, replacing Si-CH₃ bonds by Si-O_x bonds, with good selectivity. SiO_x being resistant to oxygen-based etching, the fidelity of the original pattern is thus well-preserved during the transfer [Zhang 2014] [Girardot 2014] [Aissou 2015].

Furthermore, the top coat material necessary for vertical assembly of the block copolymers is usually composed of purely organic monomers, and therefore it should present etching mechanisms and selectivity similar to the PS-*b*-PMMA with oxygen-based chemistries.

Bezard *et al.* demonstrated a grapho-epitaxy approach for directing a PS-*b*-PDMSB BCP without top coat. Because of PDMSB's higher affinity to the air than PS, a wetting layer of horizontal PDMSB and PS lamellae is formed on top of the thin film, while the bottom of the film aligns into vertical lamellae due to the influence of the topographical guides. To improve

the mechanical stability of the lamellae, a VUV exposure through the entire film is performed before etching. Then, a planarization process based on CF_4/O_2 is applied in order to non-selectively remove the horizontal lamellae formed on top of the film. This planarization process is also important to adjust the thickness of the perpendicular lamellas in the trenches, since too high PDMSB lamellae would be mechanically unstable once the PS block is removed. According to Bezard *et al.*, the best results in terms of LER and mechanical stability are achieved for a 25 nm-thick planarized film while remaining sufficiently robust to withstand a transfer etching of the patterns into silicon [Bezard 2018].

I.6 Thesis objectives

Throughout this chapter, we have seen how the transistors have evolved to continue improving their performance through constant miniaturization and new three-dimensional architectures. This evolution has been mainly supported by the development of new generation lithography. We have presented some of these new approaches, highlighting the Directed Self-Assembly of block copolymers as a low-cost alternative investigated to obtain small and dense patterns for the sub-10 nm nodes.

We then presented the block copolymers and their significant self-assembly property, which allows them to be considered as an alternative technique for obtaining patterns. In particular, they can form lamellar and cylindrical morphologies for line/space and contact hole shrink applications in microelectronics, respectively. Next, we saw the influence of surface affinity on the orientation of the block copolymers. This usually leads to the addition of a layer with no affinity to either of the blocks on the bottom and/or top of the thin film in order to obtain a neutral surface and thus guarantee the orientation of the patterns. However, the block copolymers also have to be laterally guided to finally obtain the line/space or localized contacts patterns. For this, two main approaches have been developed over the years: the grapho-epitaxy, based on mechanical constraints, and the chemo-epitaxy, based on chemical affinity constraints. The ensemble of guiding techniques is known as Directed Self-Assembly or DSA.

Finally, we have presented the importance of etching for the microelectronics industry. We then focused on another important step in the integration of block copolymers, which consists on removing one phase of the block copolymer selectively to the other, while conserving enough of the remaining block to correctly transfer the patterns into the subjacent layers.

This PhD focused on the etching of both purely organic and silicon-containing high- χ lamellar block copolymers, having as goal to successfully remove one block and transfer the line/space patterns into the desired subjacent layers. It also investigated the impact of plasma etching on the ACE process in order to optimize the flow for a PS-*b*-PMMA BCP and a future application with high- χ block copolymers.

This thesis objectives can be separated into three main parts:

1) First part: etching impact on the ACE flow.

Figure I-20 presents the top-view SEM image obtained after the non-optimized ACE flow has been applied to a PS-*b*-PMMA block copolymer with 32-nm pitch. The PMMA phase is removed through dry etching to enhance the contrast and facilitate the image capture. Different types of defects can be seen in this image, like dark spots and BCP alignment defects. These results indicate that the surface properties of the titanium nitride (TiN) hard mask are modified

during the different etching steps and, therefore, become less favorable to the alignment of the block copolymer.

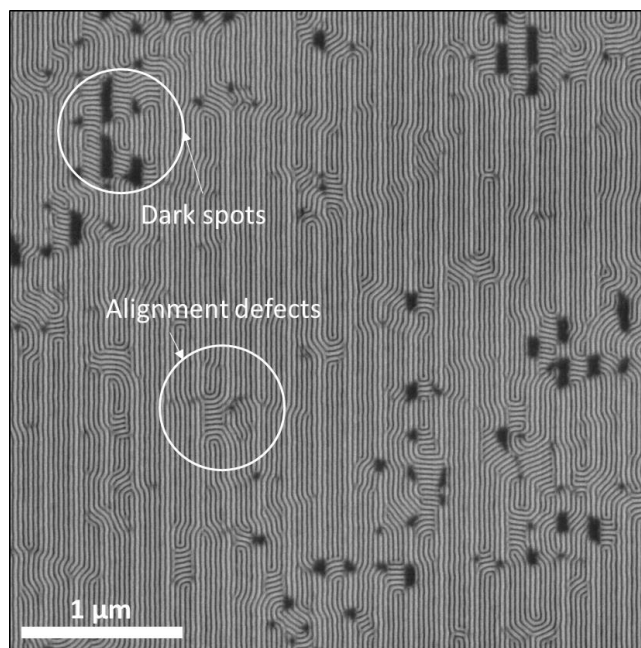


Figure I-20: Top-view SEM image of the PS-*b*-PMMA block copolymer with 32 nm pitch partially aligned by the ACE flow, highlighting the alignment defects and dark spots.

Therefore, the main objective for the first part of this PhD is to investigate and understand the origin of these defects and the impact that the different etching steps of the ACE flow have on the surface properties of the TiN hard mask, and thus on the final self-assembly of the BCP over it. Their effect on the neutral layer adherence and therefore its resistance to the hydrofluoric acid (HF) wet etching step is also evaluated.

The results obtained shall be used to optimize the different etching steps, thus validating the chemo-epitaxy ACE flow for a PS-*b*-PMMA BCP without defects.

2) Second part: etching of a purely organic high- χ block copolymer.

During this PhD thesis, the organic high- χ block copolymer system studied is a **modified PS-*b*-PMMA** with a pitch of 18 nm and lamellar morphology. It was developed by Brewer Science Inc. and Arkema. The modifications done to the standard PS-*b*-PMMA in order to obtain this modified version with smaller pitch are confidential.

The main goal of this study is to develop a PMMA removal process selective to the PS and adapted to the 18-nm pitch on 300 mm wafers by exploring different chemistries and approaches, such as cyclic etching and UV exposure.

We estimate that there should be at least 15 nm of PS plus neutral layer left after PMMA removal to ensure the correct pattern transfer into the subjacent silicon oxide (SiO₂) layer, which means that the high- χ BCP requires a PMMA:PS selectivity > 3.5 due to its reduced initial thickness (around 16 nm). Once the PMMA has been completely removed, the pattern transfer into the SiO₂ subjacent layer is used to validate the etching approach developed. Figure I-21 shows the etching flow for this high- χ PS-*b*-PMMA.

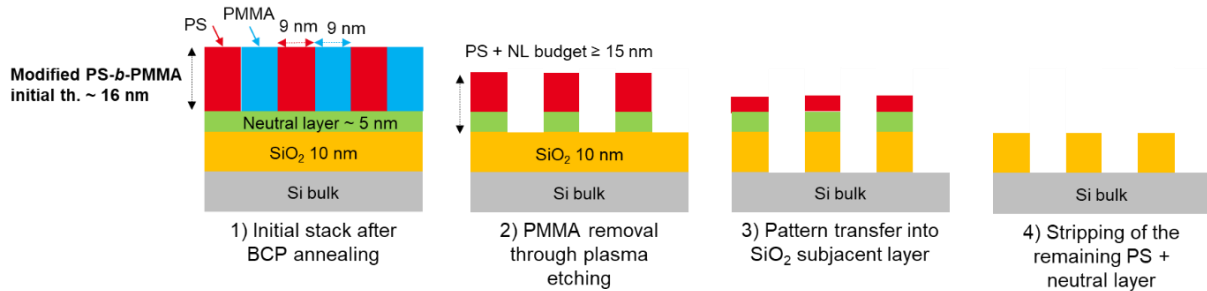


Figure I-21: Schematics for the flow used in the study of high- χ PS-*b*-PMMA etching.

Other objectives include:

- Good dimensional control during removal, that is, limiting the variation in CD of the lines (CD Bias < 2 nm);
- Comparing the high- χ modified PS-*b*-PMMA with 18 nm pitch and the standard PS-*b*-PMMA with 32 nm pitch regarding the impact of the chemistry change (modified vs standard PS-*b*-PMMA), of pitch and of film thickness on the etching;
- Establishing a methodology for chemical and morphological characterization of the high- χ BCP, since one of the main difficulties come from the characterization of complete PMMA removal due to charging effects on cross-section SEM.

3) Third part: etching of a silicon-containing high- χ block copolymer.

During this PhD thesis, the silicon-containing high- χ system investigated is a poly(styrene-*b*-1,1-dimethylsilacyclobutane) (**PS-*b*-PDMSB**) developed by Arkema. It presents a pitch of 18 nm, lamellar morphology and a Flory-Huggins parameter χ in the range 0.08-0.1 at room temperature. The PDMSB block presents a low glass transition temperature (T_g) in order to improve the self-assembly kinetics.

Our goal is to remove the top coat and PS selectively to the PDMSB, conserving enough PDMSB budget to then transfer the line/space pattern into the 18-nm hard mask (15 nm of TiN and around 3 nm of native titanium oxide, TiO_x). In order to do so, different chemistries are evaluated to obtain high selectivity and good dimension control (CD Bias < 2 nm). Figure I-22 shows the etching flow for the PS-*b*-PDMSB block copolymer.

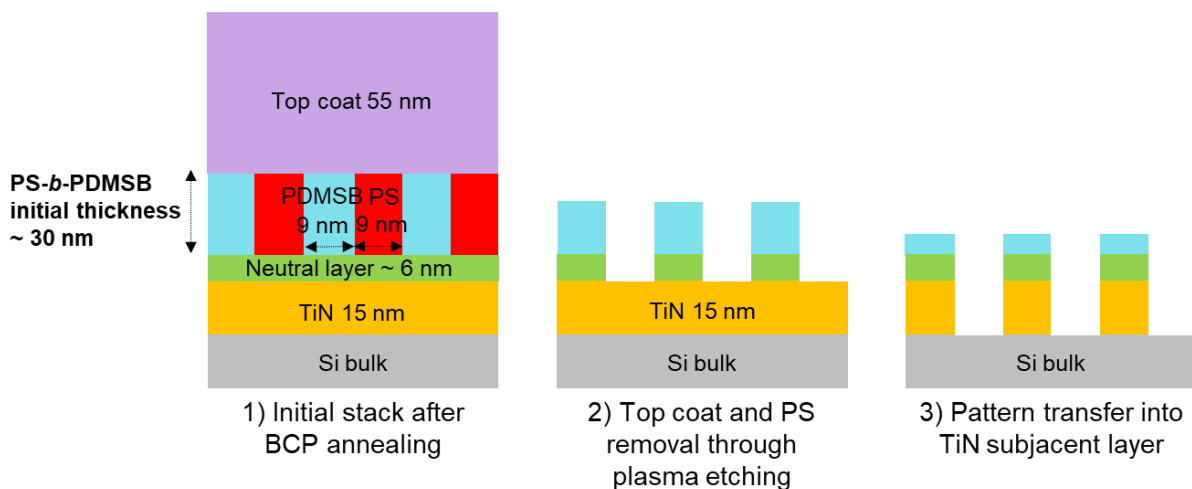


Figure I-22: Schematics for the flow used in the study of high- χ PS-*b*-PDMSB etching.

Now that we have established the main objectives of this PhD thesis, **Chapter 2** will be devoted to the experimental setup used during the thesis. Next, **Chapter 3** will present the results relating to the ACE flow, highlighting the effect of the etching steps on the TiN surface and on the adherence of the neutral layer. Then, **Chapter 4** will focus on the results for the etching of the high- χ modified PS-*b*-PMMA and its pattern transfer into the subjacent layers, presenting the challenges related to the etching of very small and dense patterns. Likewise, **Chapter 5** will present the etching of high- χ PS-*b*-PDMSB, focusing on the trade-off between obtaining high selectivity and avoiding bridge formation and pattern collapse. Finally, **Chapter 6** shall present the conclusions and perspectives to this work.

CHAPTER II:

EXPERIMENTAL SETUP

II. EXPERIMENTAL SETUP

In the experimental setup chapter, we shall start by presenting the different polymeric materials used throughout this PhD thesis as well as the procedure to obtain thin films of block copolymers. Next, we shall detail the different tools used for both plasma and wet etching. Finally, we shall present the different characterization methods used to determine the physicochemical and morphological properties of the materials studied before and after etching.

II.1 Materials

In Chapter I, we have presented the definition of block copolymers and the reasons that make them an interesting choice to continue pattern scaling. We have also presented some of the different block copolymer systems studied over the years, namely PS-*b*-PMMA as well as purely organic or silicon-containing high- χ block copolymers. Thus, in this first part of the chapter, we shall start by detailing the composition and other characteristics of the different types of polymers used within the framework of this thesis (homopolymers, statistical and block copolymers) as well as their interest for our studies. Then, we will explain the general procedure for obtaining thin films of block copolymers.

II.1.1 Polymer and copolymer materials

II.1.1.1 PS-*b*-PMMA block copolymer

One of the block copolymers investigated during this thesis was the polystyrene-*b*-poly(methyl methacrylate) diblock copolymer, also known as **PS-*b*-PMMA**, which is composed of repeating units of PMMA and PS linked by a covalent bond. The PS-*b*-PMMA block copolymer general structure is presented in Figure II-1. We observe that PS has an aromatic backbone, whereas the PMMA structure is linear and oxygen-containing.

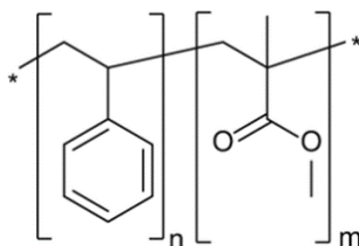


Figure II-1: PS-*b*-PMMA formula.

We have studied two types of PS-*b*-PMMA block copolymers throughout this PhD: a standard PS-*b*-PMMA, whose minimum pitch is limited to 32 nm in our case, and a modified high- χ PS-*b*-PMMA, which is able to reach a pitch of 18 nm.

The standard PS-*b*-PMMA is used to validate the ACE chemoepitaxy process in Chapter III, due to its well-known properties. It was provided by Arkema under the trade name Nanostrength® EO with an intrinsic period $L_0 = 32$ nm and a lamellar morphology. Due to its 32-nm pitch, it shall be represented hereafter as L32. The block copolymer is received at CEA Leti's clean room already decontaminated and in solution in propylene glycol methyl ether acetate (PGMEA). In addition to good solubility of the two blocks (PS and PMMA), this solvent is also commonly used in lithography for many photoresists. Thus, the use of these products on 300-mm lithography tools does not involve modifying the deposition, rinsing or cleaning

parameters. The block copolymer is received at a mass concentration between 0.75 and 1.5%, making it possible to obtain films ranging from a thickness of 22 to 43 nm depending on the rotational speed of the spin coating plate during deposition. The composition of the L32 block copolymer used in this thesis is presented in Table II-1.

Table II-1. Properties of the L32 standard PS-*b*-PMMA block copolymer.

	PMMA	PS	L32 BCP
Molecular weight (kg/mol)	35	35	70
Composition (%weight)	50	50	/
Homopolymer composition (%weight)	<1	<1	/
Polydispersity index (PDI)	/	/	<1.08

The standard PS-*b*-PMMA block copolymer was also supplied by Arkema with a pitch of 38 nm, which was used in Chapter IV.3.3.2 for comparison purposes with the high- χ L18 modified PS-*b*-PMMA. It presents similar properties to the ones presented in Table II-1, except for the molecular weight, which is respectively 39.5 kg/mol for the PS and 39.7 kg/mol for the PMMA, leading to a total molecular weight of 79.2 kg/mol.

The high- χ block copolymer composed of modified PS and PMMA blocks with a period of 18 nm shall be referred to as high- χ L18 hereafter. It was developed by Brewer Science Inc. and Arkema and presents a lamellar morphology [Guerrero 2017]. The modifications done to the standard PS-*b*-PMMA in order to obtain this modified version with smaller pitch are confidential. A modified PS-*b*-PMMA with pitch 32 nm and the same composition as the high- χ L18 was also supplied by Brewer Science Inc. for comparison studies with the standard PS-*b*-PMMA L32 in Chapter IV.

II.1.1.2 PS-*b*-PDMSB block copolymer

During this PhD thesis, the silicon-containing high- χ system investigated was a poly(styrene-*b*-1,1-dimethylsilacyclobutane) (**PS-*b*-PDMSB**) developed by Arkema under the trade name Nanostrength® EO Xn with an intrinsic period $L_0 = 18$ nm. Its Flory-Huggins parameter χ is 0.13 ± 0.06 at room temperature. The PS-*b*-PDMSB block copolymer general structure is presented in Figure II-2. We observe that PS is purely organic while PDMSB contains silicon atoms bound to carbon.

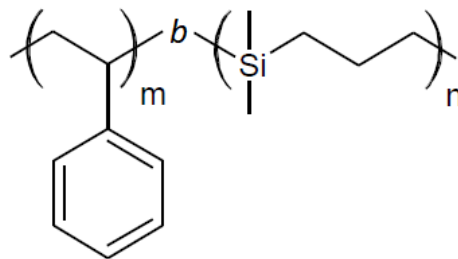


Figure II-2: PS-*b*-PDMSB formula.

The block copolymer is received at CEA Leti's clean room already decontaminated and in solution in methyl isobutyl ketone (MIBK) at a mass concentration of approximately 0.75%. The PDMSB block presents a low glass transition temperature ($T_g \sim -62^\circ\text{C}$) in order to improve the self-assembly kinetics. The composition of the PS-*b*-PDMSB block copolymer used in this thesis is presented in Table II-2. Since it is composed of approximately 49% PDMSB and 51% PS, it presents a lamellar morphology [Correia 2019].

Table II-2. Properties of the high- χ L18 PS-*b*-PDMSB block copolymer.

	PDMSB	PS	PS- <i>b</i> -PDMSB
Molecular weight (kg/mol)	8.40	8.74	17.14
Composition (%weight)	49	51	/
Polydispersity index (PDI)	/	/	~ 1.09

II.1.1.3 Neutral layers

In Chapter I, we have seen that the organization of the lamellar block copolymers into vertical lamellae was possible thanks to the addition of a neutral layer, which presents the same (or no) affinity with respect to both phases of the block copolymer. Different statistical copolymers are used as neutral layers for the different block copolymers studied during this PhD thesis. The neutral layers can be divided into two main types: graftable and crosslinkable.

The graftable layers are deposited in excess thickness, which may correspond to 2 to 10 times thicker than their intended final thickness. A grafting annealing takes place to graft the chains to the substrate. The grafting process is shown in Figure II-3 and works as follows: during annealing, the hydroxyl (-OH) endings of the graftable neutral layer allow the creation – which is thermally activated – of covalent bonds with the reactive silanol (Si-OH) sites on the oxidized surface of the silicon substrate. Then, the ungrafted chains are removed by rinsing with PGMEA, thus leaving a neutral layer thickness on the substrate which is a function of the molar mass of the chains.

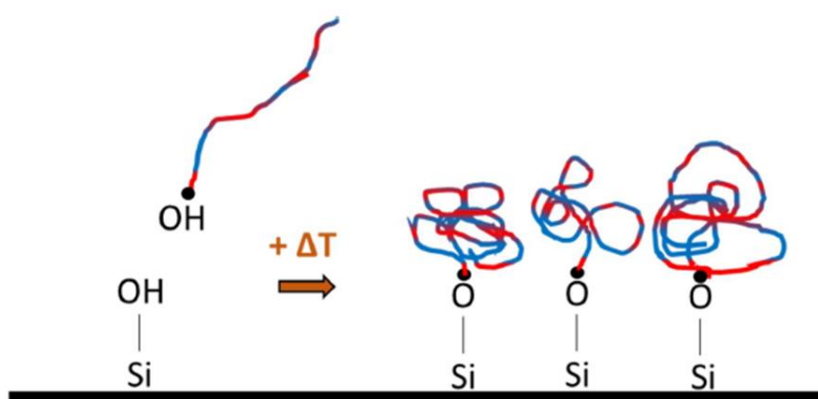


Figure II-3: Schematics for the grafting process of a neutral layer [Claveau 2017].

The crosslinkable neutral layers, on the other hand, are deposited at their final thickness. The crosslinking annealing binds the polymer chains together, making the structure insoluble in solvents. Subsequent rinsing with PGMEA is conducted to remove unreacted crosslinking agents and polymer chains.

Different neutral layers are used for the different block copolymers and stacks studied during this PhD. A list of the neutral layers, as well as their type and composition, used for the standard PS-*b*-PMMA block copolymer is presented in Table II-3. The neutral layers are random copolymers composed of PS and PMMA chains (PS-*r*-PMMA). For the standard PS-*b*-PMMA with pitch 32 nm, the crosslinkable neutral layer identified as “xNL” was used, while for the PS-*b*-PMMA with pitch 38 nm a graftable neutral layer identified as “NL2” was used. The composition of the graftable neutral layer used for the modified PS-*b*-PMMA with pitch 18 nm is confidential, but it has been adapted to remain neutral to the modified PS and PMMA structures.

Table II-3. Different neutral layers used throughout this PhD thesis for the standard PS-*b*-PMMA block copolymer with pitch 32 nm and 38 nm.

Block copolymer's L ₀	NL's name	Type	%w PS	%w PMMA
32 nm	xNL	Crosslinkable	50	50
38 nm	NL2	Graftable	60	40

As for the PS-*b*-PDMSB block copolymer, the neutral layer deposited between the block copolymer and the substrate consists of a poly(2-ethylhexyl methacrylate) (PEHMA) graftable homopolymer. It is provided by Arkema already dissolved in PGMEA with a mass concentration of 2%. The general structure of the neutral layer is presented in Figure II-4.

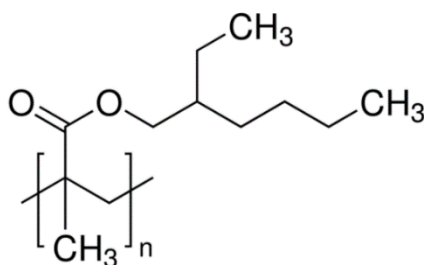


Figure II-4: Formula for the neutral layer used for the PS-*b*-PDMSB block copolymer, which consists of poly(2-ethylhexyl methacrylate) (PEHMA).

Furthermore, we have seen in Chapter I.3.2 that, in order to obtain a vertical orientation for the lamellae with silicon-containing block copolymer's, it is necessary to create a neutral surface regarding the air interface. For that, a neutral layer denoted as “top coat” is added on top of the block copolymer. For the PS-*b*-PDMSB BCP studied in Chapter V, the top coat is a crosslinkable polymer obtained by adding 0.2%w of ammonium triflate to the solution of poly(2,2,2-trifluoroethylmethacrylate-*r*-glycidylmethacrylate-*r*-2-hydroxyethylmethacrylate) statistical terpolymer (with 37%, 26% and 37% w, respectively) [Chevalier 2021]. It is provided by Arkema under the trade name Nanostrength[®] EO TC4. The general structure of the top coat is presented in Figure II-5.

For the top coat, the solvent must be different from the solvent used for the block copolymer to avoid the dissolution of the BCP during top coat deposition. It is preferably alcohol-based, for example ethanol.

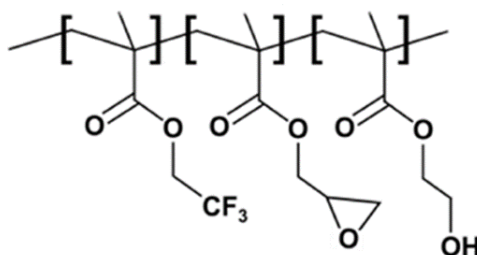


Figure II-5: Formula for the top coat layer deposited on top of the PS-*b*-PDMSB block copolymer. It consists of poly(2,2,2-trifluoroethylmethacrylate-*r*-glycidylmethacrylate-*r*-2-hydroxyethylmethacrylate) statistical terpolymer. Adapted from [Chevalier 2021].

II.1.1.4 PS and PMMA homopolymers

PS and PMMA homopolymers which present the same structure of the modified PS-*b*-PMMA block copolymer were also used during this thesis. The homopolymer films were used to study PS and PMMA polymers separately, thus making it possible to estimate each phase's etch rates and the selectivity between the two materials, thanks to ellipsometry measurements before and after etching. The homopolymers were also used to understand the etching mechanisms taking place for each of the two polymers through different characterization methods such as X-ray Photoelectron Spectroscopy (XPS) and Fourier-Transform Infrared Spectroscopy (FTIR), which shall be presented in further detail in sections II.3.1.2 and II.3.1.4, respectively. Both homopolymers were provided by Brewer Science Inc. already dissolved in PGMEA with a mass concentration of 2%.

II.1.2 Obtaining thin films of block copolymers

The different steps necessary to obtain a block copolymer film oriented perpendicularly to the substrate are shown in Figures II-6(a) and (b) for the high- χ PS-*b*-PMMA and PS-*b*-PDMSB, respectively.

For the high- χ PS-*b*-PMMA with pitch 18 nm, the process is as follows: (1) the graftable neutral layer is spin-coated with excess thickness and annealed in order to graft the polymer chains to the substrate. Then, (2) the non-grafted chains are removed through a PGMEA rinsing, leaving a neutral layer with the desired final thickness. Finally, the block copolymer solution is (3) spin-coated and (4) annealed to obtain the self-assembled vertical lamellae structure. For the high- χ PS-*b*-PDMSB with pitch 18 nm, the first steps (1-2) of the process are similar to the PS-*b*-PMMA. However, once the block copolymer is spin-coated (3), only a very short annealing step is conducted in order to evaporate the solvent. Then, (4) the top coat is spin-coated and annealed in order to crosslink its chains. Finally, (5) a final longer annealing step is conducted in order to self-assemble the block copolymer into vertical lamellae.

The different BCP processes presented in this thesis – both aligned by chemo-epitaxy and self-assembled in fingerprint-like free surface – are implemented on automated machines similar to those used in industry, thus all the samples are prepared on 300 mm silicon wafers. The main tool used for the BCP deposition steps presented in Figure II-6 is a DSA-dedicated 300 mm SOKUDO DUO track from SCREEN. Thanks to dedicated modules, this track is able to carry out the spin-coating, annealing and rinsing steps for the different neutral layer, block copolymer and top coat solutions.

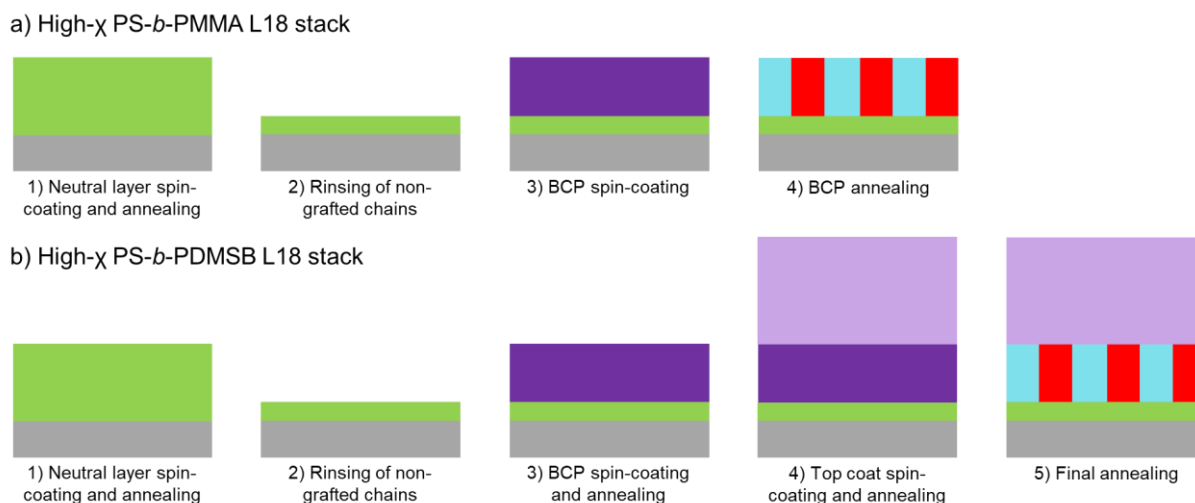


Figure II-6: Process for obtaining a block copolymer film perpendicular to the substrate with (a) modified high- χ PS-*b*-PMMA with pitch of 18 nm. For this BCP, no top coat is necessary; and (b) high- χ PS-*b*-PDMSB with pitch of 18 nm. For this BCP, a top coat is necessary in order to obtain vertical lamellae.

We shall now detail the different deposition steps for the polymeric materials.

Spin-coating

The different polymeric materials presented so far are deposited in the form of thin films on the substrate by centrifugal coating, better known as “spin-coating”. This technique is the most widely used in lithography to deposit thin polymer films, which range from a few nanometers to a few micrometers thick, on different substrates. Its main advantages are its speed and reproducibility.

As we have seen in the previous sections, the polymeric materials are provided by Arkema or Brewer Science Inc. already dissolved in their respective solvents (PGMEA, MIBK or ethanol) at low mass concentrations ranging from 0.75 to 2%. The schematics in Figure II-7 describe this technique. A few milliliters of the solution containing the polymer to be spread in a thin film are deposited on the substrate (1). The substrate then rotates at high speed (from 700 to 2500 rpm), thus allowing the polymeric solution to be spread (2). During this step, much of the solution is ejected out of the substrate. At the end of the spin-coating step, only a few % weight of residual solvent is present in the film (3) [Zhang 2010]. Finally, an extraction system placed above the plate removes the solvent by suction to avoid obtaining a saturated atmosphere (4).

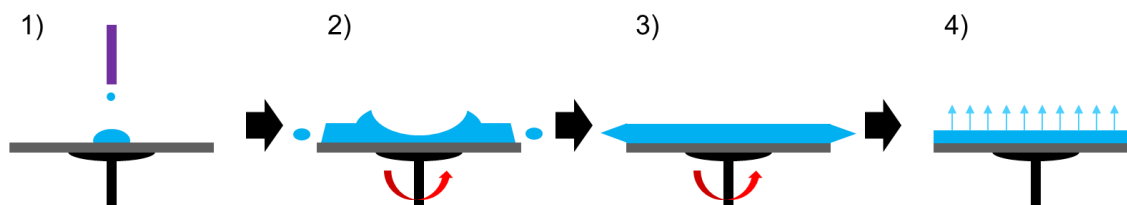


Figure II-7: Schematics for the spin-coating process.

Film thickness is mostly a function of the polymer concentration in the solution and of the rotational speed of the plate. The viscosity of the solution, the temperature and the vapor pressure are also parameters that can influence the thickness of the film [Danglad-Flores 2018].

Besides the solution concentration, which can be changed by dilutions, the speed can also be changed to achieve the desired thickness. The speed range used in this thesis varies from 700 to 2000 revolutions per minute (rpm). To know the spin-coating rotational speed necessary to achieve the target thickness, different equations have been formulated over the years [Emslie 1958] [Danglad-Flores 2018]. A simplified version of these equations is presented in Equation II-1, in which the film thickness (e) is directly proportional to the polymer concentration in the solution (c) and inversely proportional to the square root of the spin-coating rotational speed (w).

$$e \propto \frac{c}{\sqrt{w}}$$

Equation II-1: Thickness (e) of the film deposited by spin-coating as a function of the polymer concentration in the solution (c) and of the rotational speed (w).

Equation II-1 indicates that, at the same rotational speed (w), the higher the polymer concentration in the solution (c) and the higher the film thickness (e) due to the higher solution viscosity. Likewise, the higher the rotational speed of the plate and the thinner the film, due to the increase in centrifugal force. Furthermore, under identical spin-coating conditions, a modification of the solvent used changes the film thickness due to the difference in the evaporation rate and viscosity of the solvent [Wadley 2012].

Annealing

After spin-coating to obtain thin films, the polymeric materials are thermal-annealed in order to provide sufficient energy for their self-assembly (for the block copolymers), crosslinking or grafting (for the neutral layers). The annealing is carried out on the SOKUDO DUO track in a dedicated oven under a flow of nitrogen. The oven is configured in such a way that the temperature received by each zone of the wafer (edge, center, etc.) is identical. As soon as the annealing time is over, the wafer is automatically removed from the oven to be placed in a cooling module at approximately 23 °C, thus “fixing” the self-assembled structure.

Rinsing

The rinsing step is included for the graftable neutral layers after spin-coating and grafting annealing. Its goal is to remove the non-grafted polymeric chains, thus obtaining a thin neutral layer film with the desired final thickness. For all the neutral layers used during this PhD, the rinsing step was conducted using PGMEA.

For the crosslinkable neutral layers, the PGMEA rinsing is optional after crosslinking annealing. In the case of the xNL, which is the neutral layer used for the standard PS-*b*-PMMA with 32 nm pitch, the PGMEA rinsing is conducted to possibly remove any excess crosslinking agents or non-crosslinked polymer chains.

The spin-coating, annealing and rinsing conditions for the different polymers used throughout this PhD are presented in Tables II-4 and II-5 for the PS-*b*-PMMA and PS-*b*-PDMSB block copolymers, respectively.

Table II-4. Spin-coating, annealing and rinsing conditions for the different polymers used during the study of both the standard and modified PS-*b*-PMMA block copolymers.

	Spin-coating	Annealing	Rinsing	Thickness
Standard PS- <i>b</i> -PMMA $L_0 = 32$ nm	1500 rpm	15 minutes @ 240°C	/	33 nm
xNL (crosslinkable)	1500 rpm	5 minutes @ 250°C	PGMEA	7 nm
Standard PS- <i>b</i> -PMMA $L_0 = 38$ nm	1500 rpm	5 minutes @ 250°C	/	52 nm
NL2 (graftable)	1500 rpm	75 seconds @ 250°C	PGMEA	8 nm
Modified PS- <i>b</i> -PMMA $L_0 = 18$ nm	1500 rpm	5 minutes @ 180°C	/	16 nm
NL for high- χ L18 (graftable)	1500 rpm	10 minutes @ 250°C	PGMEA	5 nm
PS homopolymer	1500 rpm	5 minutes @ 180°C	/	50 nm
PMMA homopolymer	1500 rpm	5 minutes @ 180°C	/	50 nm

Table II-5. Spin-coating, annealing and rinsing conditions for the different polymers used during the study of the high- χ PS-*b*-PDMSB block copolymer.

	Spin-coating	Annealing	Rinsing	Thickness
Neutral layer	700 rpm	75 seconds @ 200°C	PGMEA	6 nm
PS- <i>b</i> -PDMSB	2000 rpm	60 seconds @ 60°C	/	30 nm
Top coat	2000 rpm	3 minutes @ 90°C	/	55 nm
Final annealing	/	5 minutes @ 200°C	/	/

II.2 Etching tools

II.2.1 Dry etching

In Chapter I, we saw that the evolution of etching in order to continue pattern scaling led to the use of plasma etching instead of wet etching. Indeed, one of the main advantages of plasma etching is its capability to privilege the etching in one direction (namely, vertical) while conserving the pattern in the other direction (lateral), also known as anisotropic etching. This characteristic makes it possible to pursue pattern scaling for features with critical dimensions of less than 20 nm.

Within plasma etching tools, different types of plasma reactors exist. They are classified according to the coupling mode of the RF (radio-frequency) power, and are divided in two main types: the Capacitively Coupled Plasma (CCP) and the Inductively Coupled Plasma (ICP). These two types of reactors have different applications. Capacitively coupled plasmas are

considered “Low Density Plasma”, since they generally deal with an ion bombardment of high energy and low density (10^9 - 10^{10} cm⁻³). Inductively coupled plasmas, on the other hand, are considered “High Density Plasma”, since they normally present an ion bombardment of low energy and high density (10^{10} - 10^{12} cm⁻³).

During this thesis, three different plasma etching reactors were used. All of them were integrated into a 300 mm LAM Versys™ platform from LamResearch®, which is one of the main providers of plasma etching tools in the microelectronics industry.

As illustrated in Figure II-8, the LAM Versys™ platform consists of:

- Three loading ports that can each load and unload up to 25 silicon wafers with 300-mm diameter.
- An atmospheric transfer module, comprising a robotic arm and a wafer orientation system. The robotic arm retrieves the wafer from the loading port and brings it to the orientation system, which locates the wafer’s notch using a laser. The objective is to orient the wafer so that it is always introduced in the chamber with the same orientation.
- Two loading docks allow the wafer to pass from atmospheric pressure to a primary vacuum pressure (around 50 mTorr) before being introduced into the transfer chamber.
- A vacuum transfer chamber, comprising a robot consisting of two arms, which allows the introduction of the wafer into the appropriate etching chamber.
- Three etching chambers: an ICP Kiyoo FX™, a CCP Flex CFET™ and an ICP Kiyoo CX™, which are identified as PM4, PM3 and PM2, respectively. They shall be detailed in the next sections.
- One vacuum loading port connected to the transfer chamber, which can receive a wafer from one of the etching reactors. This port, identified as PM1, is connected to a platform made up of an Adixen™ transfer case, which allows for the etched wafer to be transferred under vacuum (~ 30 mTorr) to other characterization tools equipped with the same Adixen™ platform, such as the X-ray Photoelectron Spectroscopy (XPS) tool used throughout this PhD thesis.

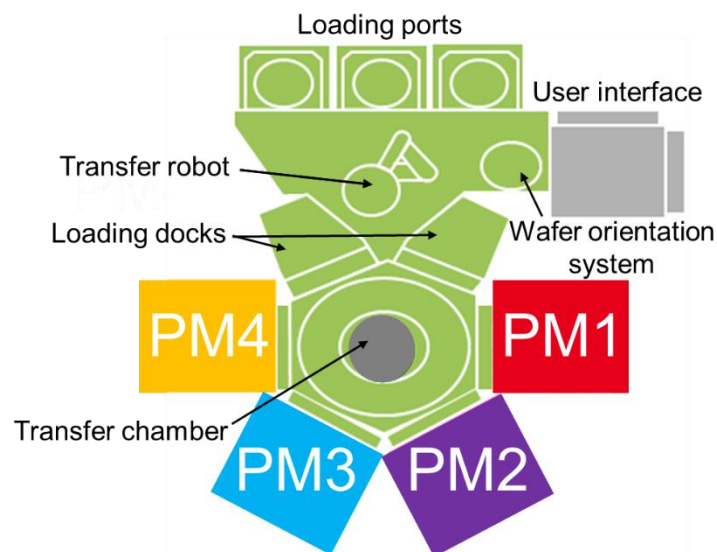


Figure II-8: Schematics for the LAM Versys™ etching platform.

Several parameters may influence the plasma inside the reactor, which will present different etching properties depending on these parameters. Therefore, the importance of the plasma chamber is the ability to control them. Six main parameters define the plasma inside the reactors and all of them can be directly modified when creating a plasma etching recipe:

- The choice of the **gases** used makes it possible to manage the nature of the plasma (mostly chemical or physical) and to adapt it to the different types of materials to be etched.
- **Source power**, also known as RF power, is the power injected by the RF power source. Thus, it corresponds to the energy applied to ionize the gas and to initiate the plasma. The larger it is, the denser the plasma and the more electrons, ions and radicals it contains.
- The **pressure** inside the reactor will influence the number of molecules present in the chamber. Low pressure increases the mean free path of electrons, giving them time to acquire more energy before colliding with another species in the plasma. The collisions are thus more energetic, promoting ionization and dissociation reactions.
- The **flux** is the quantity of each gas introduced into the chamber, influencing the density of the plasma. It is measured in standard cubic centimeters per minute (sccm).
- **Bias**, also known as bias voltage or RF bias, is the voltage applied to the substrate during etching. Indeed, by polarizing the surface to be etched, we can control the acceleration of positive ions towards that surface, and thus control the physical aspect of the etching. This mechanism is very important in the anisotropic plasma etching processes.
- The **temperature** of the substrate makes it possible to influence the kinetics of the etching reaction, the selectivity between materials and the anisotropy of the etching.

The next two sections shall detail the two types of plasma etching reactors used throughout this PhD: Capacitively Coupled Plasma (CCP) and Inductively Coupled Plasma (ICP) reactors.

II.2.1.1 Capacitively coupled plasma (CCP) reactor

Capacitively coupled reactors were the first type of reactors to be used in the microelectronics field. They consist of one or several RF power sources coupled to two electrodes inside a vacuum chamber. The capacitive current created between the top electrode (anode) and bottom electrode (cathode) – over which the substrate holder is positioned – generates an electromagnetic field that allows the plasma to be initiated and then maintained. The various gases used are injected through the upper electrode of the reactor.

The CCP reactor used during this PhD was the Flex CFE™ reactor from Lam Research®, identified as “PM3” in Figure II-8. This reactor has two RF generators with different frequencies connected to the bottom electrode: one of 2 MHz and another of 27 MHz, as shown in Figure II-9. The wafer is placed on the electrostatic substrate holder positioned on the bottom electrode of the chamber. A temperature control system allows the wafer to have a controlled temperature between 20 and 80°C while a flow of helium gas promotes thermal contact between the bottom electrode and the substrate. The top electrode is at 120 °C while the chamber walls are at room temperature. Containment rings are placed between the two electrodes in order to confine the plasma. The gases available on this reactor are Ar, CF₄, CH₃F, CH₂F₂, C₄F₈, C₄F₆, O₂, CO, N₂, Xe, He, H₂ and CHF₃. The pressure inside the reactor chamber can be regulated up to 1000 mTorr. The RF generator of 2 MHz can deliver power from zero to 4500W, while the 27 MHz generator varies between zero and 2800W.

In order to guarantee that all the wafers are etched under the same conditions, cleaning using an oxygen plasma is carried out between the passage of two wafers in the etching chamber.

This equipment was developed for Middle-End of Line (MEOL) applications, which comprises the different steps between the fabrication of the first transistors (Front-End of Line, or FEOL) and the fabrication of the first metallic levels of interconnects (Back-End of Line, or BEOL). This chamber is used in particular for the contact manufacture.

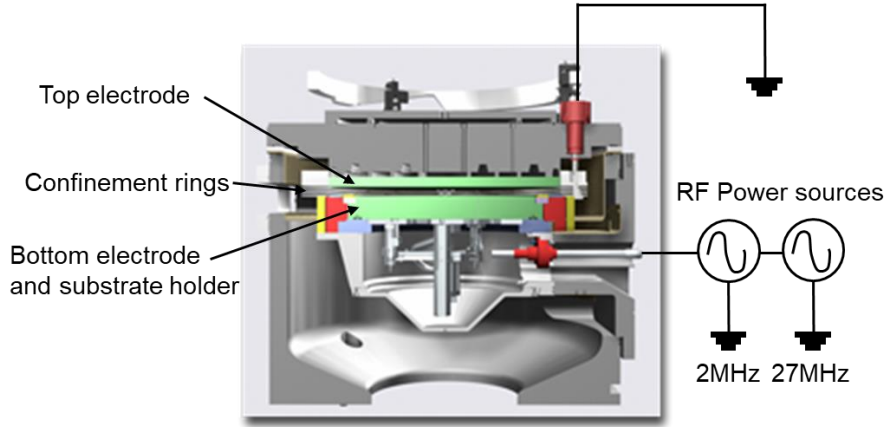


Figure II-9: Schematics for the CCP reactor Flex CFE™ used during this PhD thesis.

The use of generators of different RF frequencies makes it possible to partially dissociate the ion energy from the plasma density. LamResearch® evaluated the impact of the generator’s RF frequencies used alone or at the same time on the ion energy, the plasma density as well as the degree of plasma fragmentation (that is, the degree of molecule dissociation inside the plasma). The results are shown in Table II-6 for two RF frequencies: 2 MHz and 27 MHz [Dhindsa 2008]. Based on these results, we observe that the ion energy is mainly determined by the low frequency (2 MHz) while the plasma density and the molecule dissociation are favored by the higher frequency (27 MHz).

Table II-6. Influence of RF source frequency on plasma parameters. Adapted from [Dhindsa 2008].

2MHz	27MHz	Ion Energy	Plasma Density	Degree of Plasma Fragmentation
X	X	High	Medium	Medium
X		High	Low	Low
	X	Medium	Medium	Medium

These results can be explained by the Langmuir frequency – also known as plasma frequency – for a species (electron or ion) in the plasma, which corresponds to the maximum frequency that this species can follow. It is given by the following equation:

$$v = \frac{1}{2\pi} \sqrt{\frac{q^2 n}{\epsilon_0 m}}$$

Equation II-2: Definition of the Langmuir frequency of a species in the plasma.

Where q , n and m are the charge, density and mass of the considered species, respectively, and ϵ_0 is the dielectric permittivity of vacuum. Since the mass of the ionic species in the plasma is much greater than that of the electrons, the ions cannot follow high frequencies (typically > 3 MHz) while the electrons can. By introducing into the plasma a high frequency (27 MHz) that only electrons can follow and a lower frequency (2 MHz) whose energy can be transmitted to both electrons and ions in the plasma, it becomes theoretically possible to separately control the plasma density and the ion energy which, in general, is impossible in a capacitive plasma. Therefore, by combining the two frequencies, we have better control of the various plasma parameters, even though the complete dissociation of the two effects is not possible.

II.2.1.2 Inductively coupled plasma (ICP) reactors

The Inductively Coupled Plasma (ICP) reactor consists of a 13.56 MHz RF power source coupled to a coil or antenna placed in the exterior of the chamber, as seen in the schematic representation of the Kiyotm series ICP reactor from LamResearch® presented in Figure II-10. An alternating current flows through the coil, which induces a magnetic field inside the chamber where the gas mixture is injected. The variations in this magnetic flux inductively generate an RF electric field, thus creating the electromagnetic field responsible for the initiation and maintenance of the plasma in the chamber. The plasma density and the dissociation coefficient are controlled by the RF power injected in the coil.

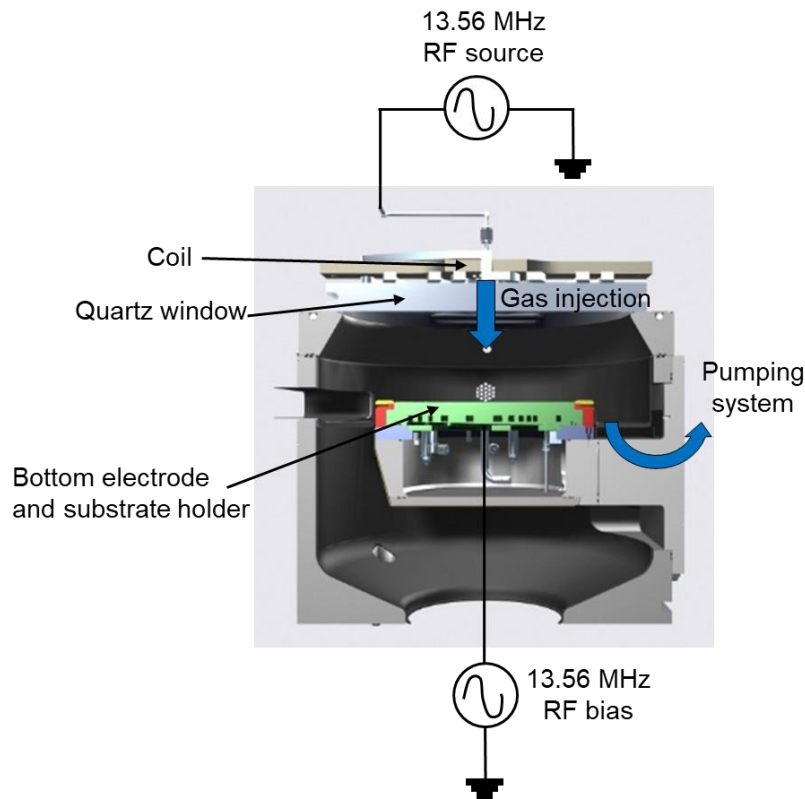


Figure II-10: Schematics for the Kiyotm ICP reactor.

In the ICP reactor, the electromagnetic field is generated close to the coil and sufficiently far from the bottom electrode, where the substrate is located. That means the plasma source does not interact with the different potentials at the wafer surface, and thus there is no current to induce the self-polarization of the electrodes. Therefore, to create the bias voltage, another 13.56 MHz generator is placed on the lower electrode, which controls the ion energy and

directionality. That means that, for ICP reactors, the ion bombardment energy and the plasma density can be independently controlled, which represents an advantage for more complex etching processes, in comparison with the CCP chamber.

As is the case with CCP reactors, the temperature of the wafer, deposited on the bottom electrode, is controlled by the electrostatic substrate holder and a helium injection system on the backside of the wafer ensures good heat transfer between the substrate holder and the wafer.

ICP reactors are generally used for the etching of trenches, gate-electrodes and high-k dielectrics, as well as aluminum and its alloys. Two ICP reactors were used during this thesis, both from the Kiyotm series by LamResearch®: a Kiyotm FX and a Kiyotm CX, identified as “PM4” and “PM2”, respectively, in Figure II-8. Most of the experiences were carried out on the Kiyotm FX reactor, since it is the latest generation reactor from this series. It was developed to meet the ITRS requirements for the next technological nodes and thus make it possible to obtain sub-10 nm patterns by offering good control of the polymerization and etching steps. In order to achieve that, a “Mixed Mode Pulsing” option is available, which makes it possible to pulse (turn either on or off with high frequency) the gas injection or the bias voltage. Thanks to this option, the chemisorption step and the etching step can be decorrelated and atomic precision can be achieved.

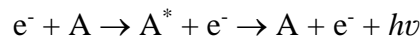
The available gases in the Kiyotm FX chamber are Cl₂, HBr, CH₄, O₂, CF₄, CHF₃, CH₃F, CH₂F₂, SF₆, N₂, He, Ar, BCl₃, SO₂, SiCl₄ and NF₃. The 13.56 MHz RF power source coupled to the coil can deliver power from zero to 2000W. Furthermore, the RF bias voltage applied to the wafer can be varied from zero to 1000 V, while the pressure can be regulated up to 100 mTorr. This chamber also presents the option of a RF bias pulsing mode. It consists of alternating two cycles during a single step, according to the specified pulsing frequency: one cycle of RF Bias ON and one cycle of RF Bias OFF. As we have seen in section II.2.1, the RF Bias in an ICP reactor is the parameter that allows us to have a strong ion bombardment and thus increase the anisotropic aspect of the etching. The pulsing mode usually allows for better profile and selectivity, since it increases the uniformity of the passivation layer [Agarwal 2009]. Indeed, during RF bias OFF, the passivation layer is deposited on the sidewalls without the effect of ion bombardment, which may consume the mask through sputtering and lead to a faceted profile. The parameters that define the RF bias pulsing mode are duty cycle, which corresponds to the percentage of ON time during one pulse and can be set between 3 to 90%; and pulse frequency, which corresponds to the duration of one pulse (ON + OFF time) and can be set between 100 and 1000 Hz. These two parameters must be set in order to respect a minimum pulse ON time of 300 μs (e.g. 3% duty cycle at 100 Hz).

The Kiyotm CX chamber was designed for etching isolation trenches, transistor gates and other components integrated into 65-nm technologies. During this PhD, it shall be used as an alternative for the Kiyotm FX chamber when the wafer has already seen other etching steps in the CCP Flex CFEtm chamber. Indeed, due to the different applications of each etching reactor and the different materials that are etched within them, it is not recommended to process a wafer in the Kiyotm FX chamber after it has been through one of the other two chambers. The gases available in this chamber are Cl₂, HBr, O₂, CF₄, CH₂F₂, CH₃F, CH₄, H₂, NF₃, N₂, Ar, He, BCl₃ and SiCl₄. The pressure can be regulated up to 400 mTorr. The bias voltage may be varied between zero and 1500V, while the RF source power varies from zero to 2000W.

Finally, both ICP etching chambers, in the absence of a wafer, are subjected to three cleaning steps and a pre-coating step between each wafer. The latter allows the deposition of a SiOCl-type film on the chamber walls before each etching to ensure good wafer-to-wafer reproducibility for the different processes.

II.2.1.3 Optical emission spectroscopy (OES)

In Chapter I.4.1, we have seen that one of the phenomena that takes place in the plasma is the electronic excitation and relaxation. During excitation, an atom or a molecule at rest (A) is brought to an excited state (A*) by absorbing energy, that is, an electron goes from an energy level to another. This excitation is always followed by the inverse phenomenon, the relaxation, in which the molecule or atom returns to its energy level at rest with the emission of light in the form of a photon of energy $h\nu$. Both phenomena are represented below, in which h represents Planck's constant while ν is the frequency of the emitted light:



Each excited state emits light at a specific wavelength (λ). Therefore, Optical Emission Spectroscopy (OES) can be used to identify the molecules present in the gas phase. Indeed, OES is a real-time plasma diagnosis that does not disturb the environment in which the measurement is made. This technique is based on the spectral analysis of the light emitted by the species present in the plasma.

The previously presented plasma etching chambers all offered this optical emission characterization technique. During this PhD, this technique was used to assess the etching progress. Indeed, by analyzing the plasma composition, it is possible to determine the end of the etching of a specific layer, also known as "end point (EDP) detection". The strategy consists in detecting the wavelength of the emission line of one of the constituents of the material to be etched. By following the change in intensity of this line during etching, we indirectly measure the amount of volatile etch products from the material that are excited in the plasma. Therefore, a drop in the emission line's intensity coincides with a net decrease in the amount of etching products, and is thus representative of the end of the etching of the material. By creating an algorithm based on the detection, evolution or disappearance of a characteristic emission line of the material that we want to detect or etch, we are able to determine the end of the etching of a material.

Connected directly to the interior of the etching chamber, the OES device consists of an optical fiber to collect the light emitted by the plasma. Through an array of mirrors internal to the spectrometer, the collected light is diffracted and then detected by a charge-coupled device (CCD) sensor. By exploiting the 2048 pixels of the sensor, the optical processing makes it possible to cover the entire spectral range from 200 to 850 nm with a dispersion of 0.3 nm per pixel and a resolution of 2 nm.

Figure II-11 shows an example of end point detection during trilayer etching, more precisely the SOC etching step, in which the patterns are transferred to the SOC layer using a HBr/O₂ plasma. For this plasma, the end point detection is based on the 520 nm emission line, shown in pink in Figure II-11, which is characteristic of CO species. By following the intensity of the CO emission line, we are able to determine the moment when these species will no longer be formed. Since CO species are the product formed by the etching of the SOC, once it is no longer detected, it means the patterns have been completely transferred into the SOC layer.

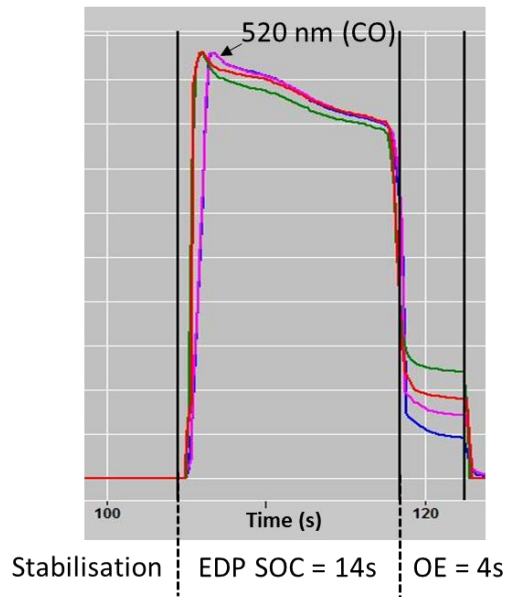


Figure II-11: Example of end point (EDP) detection obtained by OES during trilayer etching.

II.2.2 Wet etching

In Chapter I, we saw that the first etching processes consisted of chemically attacking the wafer with either acid or basic solutions, also known as wet etching. This type of etching is very selective, fast and relatively simple. However, it is isotropic, that is, the etching rate of the material is the same in all directions. This means that, for pattern transfer, there is usually an undercutting phenomenon under the mask that alters the desired CD of the patterns due to the isotropic aspect.

The wet etching, therefore, is ideal for stripping applications, in which high selectivity is necessary and there is no pattern transfer. For the ACE process, wet etching by hydrofluoric (HF) acid diluted at 1% is used for both the SiARC removal after trilayer etching and for the spacers removal once the neutral layer has been deposited, which corresponds to steps 3 and 8, respectively, of the ACE schematics presented in Chapter I.3.3.3.

Knotter and Denteneer have studied the silicon nitride etching mechanism by HF. Silicon nitride films or spacers are not completely pure, and have, on the surface, SiNH₂ groups, which are more numerous when the deposition temperature is low. Depending on the pH of the HF solution, these groups protonate to form SiNH₃⁺ groups. They have shown that the silicon atom at the Si-N bond is strongly electrophilic, and thus a nucleophilic substitution takes place when reacting with F⁻ ions in the HF solution, allowing the formation of a Si-F bond. The Si-N bonds are then gradually replaced by the Si-F bonds until a water-soluble SiF₄ compound is formed. The silicon nitride is thus etched layer by layer by the HF [Knotter 2001].

As for the SiARC removal, without a previous plasma treatment, it has been shown that the HF wet etching does not consume the SiARC [Sarrazin 2017]. However, after a plasma treatment containing oxygen, the SiARC is modified and becomes more SiO₂-like, that is, it presents a similar composition to SiO₂ [Fitrianto 2011]. Such is the case for the ACE flow, in which the SiARC wet removal step takes place after the trilayer plasma etching, which contains O₂. Once modified, the SiARC can be removed through HF following the same principle as the SiO₂ wet etching: to participate in the hydroxyl group (-OH) removal, a proton is added by reaction with H⁺ ions to form the protonated SiOH₂⁺ group. The second step is the nucleophilic

attack of HF_2^- or H_2F_2 on the electrophilic silicon atom, thus forming a Si-F bond. Once the SiF unit is formed, the reaction can proceed very quickly. Three subsequent nucleophilic substitution reactions will form a water-soluble SiF_4 compound and will bring the surface back into its initial form, where a SiOH unit has to be replaced by a SiF unit to continue the etching process [Knotter 2000].

During this PhD, the HF wet etching was conducted on a Raider tool from Semitool®. Inside this tool, the wafer is turned over and the etching is done by spraying the wafer with HF droplets diluted in water to obtain the desired concentration of 1%. Once the defined etching time ends, the wafer is again turned over, then dried by isopropanol (IPA) and N_2 vapor. The respective times used for SiARC stripping and spacer removal are 15 and 60 seconds.

II.3 Characterization methods

During this thesis, in order to understand the impact of etching on the different materials studied, several characterization techniques were used. This section shall present the techniques, tools and methods used to carry out these characterizations. It will be divided into two main classes: physicochemical and morphological characterization.

II.3.1 Physicochemical characterization

This section shall focus on physicochemical characterization techniques. These characterization methods make it possible to define the properties of a thin film, such as its thickness, which is determined by spectroscopic ellipsometry, and its composition, which may be determined by X-ray Photoelectron Spectroscopy (XPS), Fourier-Transform Infrared Spectroscopy (FTIR) or Time-of-Flight Secondary Ion Mass Spectrometry (ToF-SIMS). In Chapter 3, we are also interested in the surface energy of certain materials, which is determined by contact angle measurements.

II.3.1.1 Spectroscopic ellipsometry

The thickness of deposited films is measured by **spectroscopic ellipsometry**. This non-destructive, noncontact measurement technique uses a model-based approach to obtain information on the material's thickness and/or optical constants. It could also be used to characterize the composition, crystallinity, roughness, or any other phenomenon associated with a change in the material's optical constants.

Principle

A material's optical properties are comprised of two components: the refractive index (n), and the extinction coefficient (k). The refractive index is the ratio of the speed of light in a vacuum (c) to the speed of light in the material (v), so that:

$$n = \frac{c}{v}$$

Equation II-3: Definition of refractive index (n).

The extinction coefficient is related to the absorption loss in the material. Indeed, light slows as it enters a material with higher index. Because the frequency of light waves remains constant, the wavelength (λ) will shorten. Thus, the extinction coefficient describes the loss of wave

energy to the material and can be related to the absorption coefficient (α) according to the Equation II-4:

$$k = \frac{\alpha\lambda}{4\pi}$$

Equation II-4: Definition of extinction coefficient (k).

Together, these two components make up the complex refractive index (N), which describes electromagnetic radiation's interaction with materials (speed change and absorption loss), according to the Equation II-5:

$$N = n - ik$$

Equation II-5: Definition of complex refractive index (N).

When light interacts with a material, incident light will reflect and refract at the interface, as shown in Figure II-12. The angle between the incident ray and sample normal (θ_i) will be equal to the reflected angle (θ_r). Thus, according to Snell's law, represented in Equation II-6, the light entering the material is refracted at an angle θ_t given by:

$$n_i \sin \theta_i = n_t \sin \theta_t$$

Equation II-6: Snell's law.

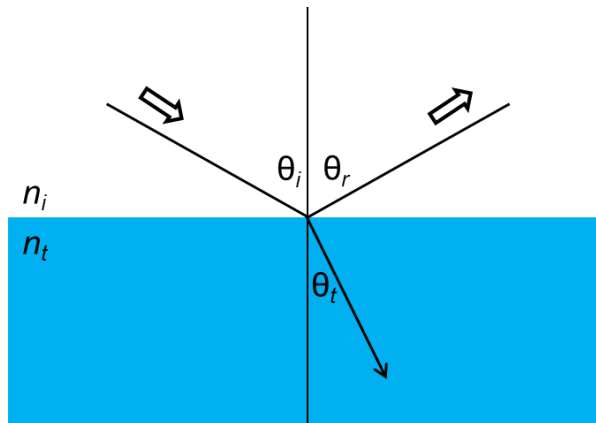


Figure II-12: Reflection and refraction of light according to Snell's law.

The same occurs at each interface where a portion of light reflects and the remainder transmits at the refracted angle. If we consider E_i the incident magnetic field, it can be separated into two components: a field parallel (p) to the surface ($E_{p,i}$) and a field perpendicular (s) to the surface ($E_{s,i}$). After reflection on the analyzed sample, these two components are modified. The boundary conditions determined by Snell's law provide different solutions for the electric fields parallel ($E_{p,r}$) and perpendicular ($E_{s,r}$) to the sample surface after reflection. It is possible to describe these modifications by the following reflection coefficients, determined by Fresnel equations:

$$r_p \equiv \frac{E_{p,r}}{E_{p,i}} = \frac{n_t \cos \theta_i - n_i \cos \theta_t}{n_t \cos \theta_i + n_i \cos \theta_t}$$

Equation II-7: Definition of the reflection coefficient of the sample for a polarization parallel to the plane of incidence (r_p).

$$r_s \equiv \frac{E_{s,r}}{E_{s,i}} = \frac{n_i \cos \theta_i - n_t \cos \theta_t}{n_i \cos \theta_i + n_t \cos \theta_t}$$

Equation II-8: Definition of the reflection coefficient of the sample for a polarization perpendicular to the plane of incidence (r_s).

In practice, the change in polarization is characterized by the complex reflectance (ρ), which is a function of the amplitude ratio (ψ) and of the phase difference introduced by the reflection (Δ), according to Equation II-9:

$$\rho = \frac{r_p}{r_s} = \tan(\psi)e^{i\Delta}$$

Equation II-9: Definition of the change in polarization.

The state of polarization after reflection is therefore reflected by these two quantities Delta (Δ) and Psi (ψ), also called ellipsometric angles, which are accessible by the measurement.

Data analysis

As we have seen, the principle of this technique is based on measuring the change in the polarization state of light as it is reflected or transmitted from a thin film sample. The schematics for the tool setup are presented in Figure II-13. A light source produces unpolarized light which is then sent through a polarizer in order to determine the incident beam, whose polarization values are known and defined by parallel (p) and perpendicular (s) components. The incident beam interacts with the sample, becomes elliptically polarized, and goes through the analyzer. Finally, the detector converts light to electronic signal to determine the reflected polarization. This information is compared to the known input polarization to determine the change of the polarization ellipse's p- and s- components, depending on the transmission or reflection of light from the sample. The polarization change is represented as an amplitude ratio, Psi (ψ), and the phase difference, Delta (Δ).

It is thus possible to determine both the thickness of the thin film layer and the optical index of this material. For this to be possible, the material must be transparent at certain wavelengths so that incident light rays can pass through the material.

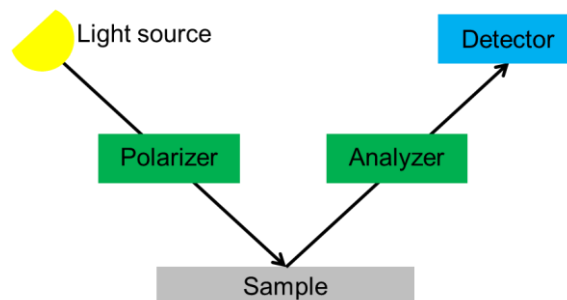


Figure I-13: Simplified schematics for the setup of an ellipsometry tool.

Application

Spectroscopic ellipsometry is used to determine the etch rate of the chemistries developed on our materials. For this, the material is measured before etching and then after etching. By subtracting the value obtained after etching by the value obtained before, we obtain the consumed or deposited thickness of the material. Moreover, by dividing the consumed thickness

by the etching time, we determine the etch rate, which is most often expressed in nanometers per second (nm/s).

Within the framework of this PhD, two ellipsometers were used. The first one, used for the 300 mm wafers, is the Atlas[®] XP+ from Nanometrics. This ellipsometer can emit a light spectrum between 300 nm and 1000 nm with an incident angle of 65°.

The second ellipsometer is the M-2000 model from J. A. Woollam[®]. It allows the analysis of both 300 mm wafers and smaller samples with spectra with wavelengths between 190 nm and 1800 nm, that is, a spectrum covering the infrared, visible and ultraviolet ranges. The results are obtained for incident angles of 55°, 65° and 75°.

In both cases, a spectrum corresponding to the material's response to the incident beams is obtained. To determine the thickness or refractive index of the materials, a model is compared to the experimental spectrum regarding the values of Psi (ψ) and Delta (Δ). For polymeric materials, the Cauchy model is the most used for measurements from wavelengths (λ) between 500 and 1000 nm, since these materials exhibit no absorption ($k = 0$) in this wavelength range. The Cauchy transparent model is presented in Equation II-10, where A, B and C are coefficients that can be determined for a material by fitting the equation to measured refractive indices at known wavelengths:

$$n(\lambda) = A + \frac{B}{\lambda^2} + \frac{C}{\lambda^4}$$

Equation II-10: Definition of the Cauchy transparent model for polymeric materials.

Ellipsometric porosimetry

Ellipsometric porosimetry measures the change of the optical properties and thickness of the materials during adsorption of a defined volatile solvent either under vacuum or at atmospheric pressure. This technique is used to measure porosity of very thin films, such as low-k materials and encapsulated organic light-emitting diodes (OLEDs).

In Chapter III, ellipsometric porosimetry is conducted to verify the presence of pores in the neutral layer. This experiment was conducted in a RC2 tool from J. A. Woollam[®]. The samples were placed under 90% humidity and then the neutral layer's thickness and refractive index were measured as a function of time (between zero and 60 minutes).

II.3.1.2 X-ray Photoelectron Spectroscopy (XPS)

X-ray Photoelectron Spectroscopy (XPS) is a surface analysis method developed in the 1960s by Kai Siegbahn, which earned him the Nobel Prize in Physics in 1981 [**Nobel Prize 1981**]. XPS is a non-destructive characterization technique that investigates the surface layers of all solid materials, thus characterizing the chemical state and composition of said material. Its ability to discriminate between the different chemical environments of an element makes it particularly well suited to the study of plasma-material interactions. The analysis depth of XPS is in the range of 5-10 nm and can detect all elements, except hydrogen and helium since they only have one energy level (1s).

Principle

The principle of XPS is based on the photoelectric effect, which was discovered by Heinrich Rudolf Hertz in 1887 and then explained by Albert Einstein in 1905 (which earned him the Nobel Prize in Physics in 1921). As shown in Figure II-14, when the surface of the sample is

bombarded with an X-ray photon with a known energy $h\nu$, all the energy of the photon is transferred to an electron from the core level of the atom. This electron is then ejected from its orbital with a given kinetic energy (E_K).

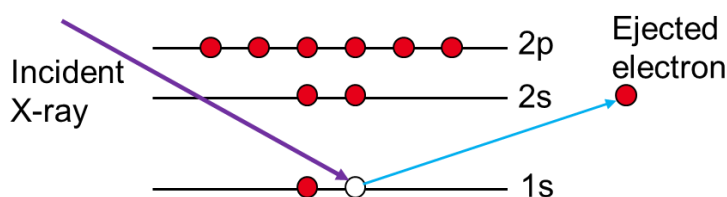


Figure II-14: Principle of the photoelectric effect.

Thus, during the analysis, the electrons emitted by the sample reach the detector and are separated based on their kinetic energy. This kinetic energy is representative of the binding energy (E_B) of the electron at the atom's core, which is the energy required to remove the electron from its orbital, thus also known as ionization energy. Therefore, the measured kinetic energy can be used to calculate the binding energy, according to the following energy conservation equation:

$$E_B = h\nu - E_K - \phi$$

Equation II-11: Definition of the electron's binding energy (E_B).

Where $h\nu$ is the energy of the X-ray photons being used and ϕ is the work function for the specific surface of the material, which in real measurements includes a small instrumental correction factor that accounts for the few eV of kinetic energy given up by the photoelectron as it gets emitted from the bulk and absorbed by the detector.

Therefore, XPS analysis allows us to identify the energy levels for all surface elements. Indeed, binding energies are specific to each chemical element and are sensitive to the chemical environment, that is, to the bonds that the element makes with its neighbors. As each chemical species has different binding energies with its core atoms, these species are easily identified on an XPS spectrum by well-known peaks, as shown in Figure II-15. Indeed, when the chemical species are detected with high resolution (0.1 eV), these main peaks can be decomposed into multiple peaks. This separation into several components may have two origins:

- Spin-orbit interaction: an orbital is defined by the principal quantum number n , which corresponds to the shells K, L, M, etc.; the secondary quantum number l , also known as orbital angular momentum, corresponding to the subshells s, p, d, etc.; and also the electron spin quantum number $m_s = \pm 1/2$, which corresponds to the two spins that can be obtained for each electron. Finally, the total angular momentum of the electron is given by $\vec{J} = \vec{L} + \vec{S}$. Depending on the electron spin, the angular momentum norm can take the two values $J = l + 1/2$ or $J = l - 1/2$. Therefore, apart from subshell s (for which $l = 0$), all orbitals have two possible states with two different binding energies, resulting in what is known as a doublet peak. An example of doublet peak is shown in Figure II-15 for the silicon 2p spectrum. For this spectrum, the angular momentum can have either of the two values ($J = 1/2$ or $3/2$), thus leading to the doublet Si2p_{3/2} and Si2p_{1/2} peaks separated by 0.6 eV. It should be noticed that, for the same electronic level of an element, the energy shift between the two components of the doublet peaks is constant and characteristic of the emitting atom. The ratio of their areas under the curve is also fixed.

- Chemical bonds: the other phenomenon behind the multitude of peaks measured for a species at a given orbital is the change in binding energy due to the chemical environment of that species. Indeed, depending on the bonds that the atom makes with its close neighbors, a shift of several eV can be observed, which is known as chemical shift. This energy shift depends on the electronegativity of the two species present. For example, if we take two elements A and B with the element B being more electronegative than the element A, the A-B bond will have a higher binding energy than the A-A bond. In the case where element A is linked with several elements B, the binding energy is even higher. A representative example of this effect is shown in Figure II-15, in which silicon is element A and oxygen is element B. Indeed, we observe that the Si-Si doublet peak is around 99.4 eV while the Si-O peak is around 103.6 eV.

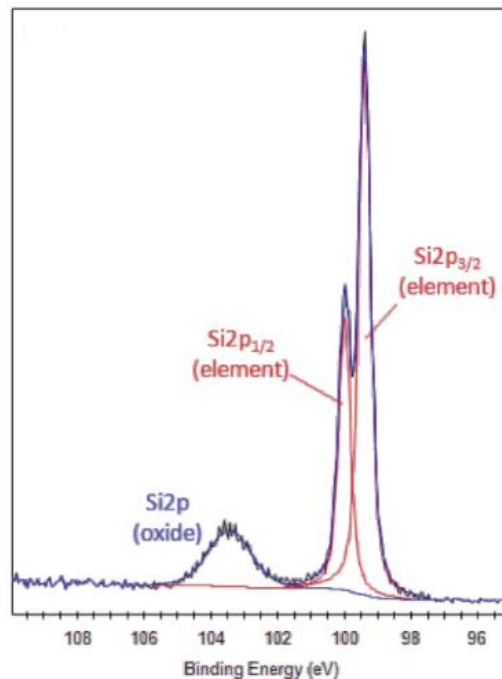


Figure II-15: Example of XPS spectra for the silicon 2p orbital, highlighting the effect of both spin-orbit interaction (with the presence of doublet peaks) and of the chemical shift due to the presence of electronegative species. Adapted from [Thermo 2021].

Data analysis

After subtraction of the continuous background by the semi-empirical method of Shirley, each XPS peak is deconvoluted into different components (corresponding to the different chemical environments). The profile of each component is established using the Voigt function, which combines the Gaussian and Lorentzian form functions. The area under the deconvoluted peak is then proportional to the intensity of the photoelectrons collected, which is directly representative of the quantity of elements detected in the volume analyzed. Thus, it is possible to quantify the concentration of each element because the intensity of a photoelectric peak for an element A (I_A) is proportional to its concentration (n_A), according to the following equation:

$$I_A = n_A \times S_A$$

Equation II-12: Relation between the peak intensity for an element A (I_A) and the element's concentration (n_A) and Scofield factor (S_A).

Where S_A is the Scofield factor for element A. This parameter was evaluated by Scofield in 1976. It is based on the photoemission yields obtained for various elements when they are excited by the $K\alpha$ line of aluminum [Scofield 1976]. Thus, based on the intensity and Scofield factor of each peak, we can determine the concentration of an element or a bond in the layer of material analyzed. However, the absolute concentrations of the species present at the analyzed surface are difficult to determine. Indeed, parameters such as the mean free path of an electron in a material or the photon flow are not known. It is nevertheless possible to determine the composition in terms of relative concentration of all the elements by atomic percentages P_A :

$$P_A = \frac{(I_A/S_A)}{\sum_i(I_i/S_i)}$$

Equation II-13: Definition of the relative atomic percentage of each element.

The sum of the relative concentrations of the species detected must be equal to 100%. The accuracy of XPS measurements is of the order of $\pm 5\%$.

Tool setup

X-ray photoelectron spectroscopy analysis are conducted using a Thermo Fisher Scientific® Theta300™ spectrometer. The analysis chamber is composed of an X-ray source, a monochromator, and an analyzer. The tool also includes a microscope and a camera to help identify the sample's position; an ion gun which allows the abrasion of the upper layers and was not used during our studies; and an electron gun (also known as flood gun) to prevent electron charging on the surface of insulating materials. A pressure inferior to 2.10^{-8} Torr must be attained before starting the x-ray gun in order not to damage it.

Furthermore, this XPS tool presents an angular-resolved mode, also known as AR-XPS, which consists of an angular analysis of the sample in order to have a more precise characterization in case of non-homogeneous surface layers. Throughout this PhD, all the analyzes were carried out using 8 take-off angles between 23.75° and 76.25° to the normal. The 76.25° angle corresponds to the most grazing incidence, which will analyze approximately the upper 3 nm of the material surface, while the 23.75° corresponds to the most in-depth analysis, which analysis around 10 nm of the surface.

The XPS Theta300™ uses a monochromatic Al $K\alpha$ X-ray source with an energy $h\nu = 1486.6$ eV. This line is produced by X-ray bombardment on an aluminum anode, which removes core electrons from Al atoms. By filling in the gaps thus created, electrons from the outer layers are de-excited by emitting photons. The X-ray beam is then filtered in the monochromator, thus obtaining a single emission line. During an analysis, the size of the X-ray beam determines the area and therefore the volume probed by XPS. In our study, the size of the X-ray beam, also known as spot size, is 400 μm in diameter.

Finally, the analyzer selects the energy of the emitted photoelectrons. It consists of two hemispherical electrodes of 150 mm of average radius. The potential difference between these two electrodes defines the pass energy of the electrons. Only the electrons having a kinetic energy included in an energy interval centered on this pass energy will arrive at the detector.

As part of this thesis, two types of spectra are obtained during a XPS analysis. First, an integral spectrum for binding energies between 0 and 1000 eV is carried out in order to determine the elements present in the material. This survey is conducted in a single scan, with

a pass energy of 200 eV, a dwell time of 200 ms and an energy step size of 1 eV. Through this survey, we can determine which elements are present in order to analyze them more precisely with longer, element-specific scans. An example of survey is presented in Figure II-16 for the PS-*b*-PDMSB high- χ block copolymer. In this survey, we identify the presence of a peak around 285 eV, which corresponds to the carbon C1s peak, and two others at 100 and 150 eV, which correspond to silicon's Si2p and Si2s peaks, respectively.

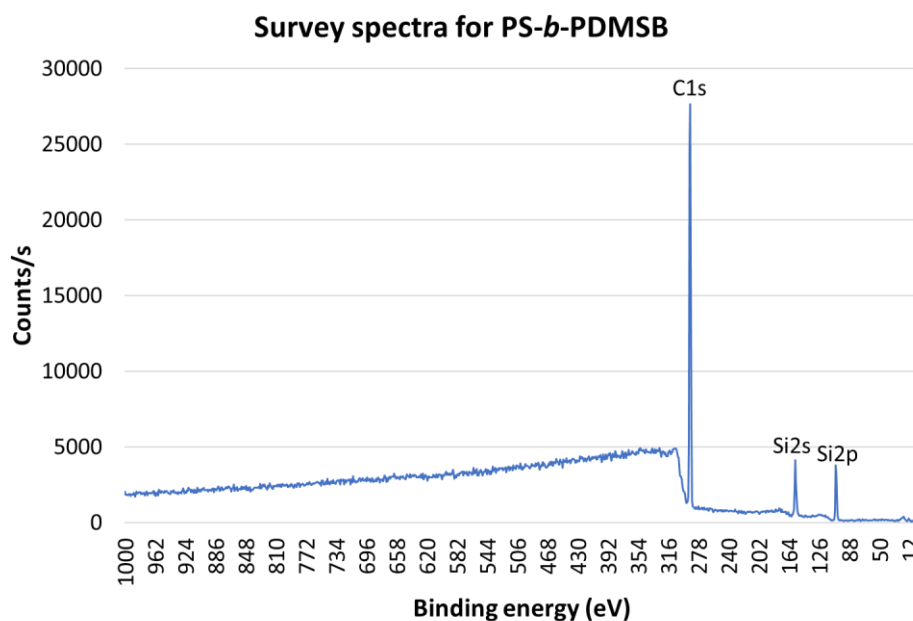


Figure II-16: Example of survey spectra for the high- χ PS-*b*-PDMSB block copolymer.

Once the elements present in the sample are detected, a window centered on the peak binding energy that we want to detect is defined in order to have a more precise analysis of the bonds composing the target peak. For this type of scan, the pass energy is 100 eV, the dwell time is 500 ms and the energy step size is 0.1 eV. Also, 5 scans are performed for each element.

The relative concentrations of Carbon, Oxygen, Nitrogen, Fluorine, Titanium, Sulfur, Silicon and Chlorine atoms are extracted from the C1s, O1s, N1s, F1s, Ti2p, S2p, Si2p and Cl2p core-level energy regions, respectively. Binding energies in all XPS spectra are calibrated using the C1s C-C peak (285 eV). All peaks are de-convoluted by a fitting routine consisting of a combination of Lorentzian and Gaussian functions using the Avantage™ software from Thermo Fisher Scientific®. Each element concentration is obtained by dividing the calculated peak areas by the corresponding Scofield factors, which are presented in Table II-7 for the different elements investigated throughout this PhD.

Therefore, we have seen that XPS allows us to analyze the first few nanometers of a material's surface. This technique will be used to investigate the plasma-material interactions after etching, thus helping us propose etching and passivation mechanisms for the different materials investigated.

Finally, as mentioned in section II.2.1, an Adixen™ transfer case is available for both the LamVersys etching tool and the Theta300™ spectrometer, which allows for the etched wafer to be transferred under vacuum (~ 30 mTorr) to the XPS tool. This *quasi in-situ* analysis allows us to avoid the effects of air exposure, which may impact the XPS results after etching, for example due to oxidation of the surface.

Table II-7. Scofield factors for different elements studied during this PhD, given by the Avantage™ software.

Element and spectra	Scofield factor
Oxygen O1s	2.88
Carbon C1s	1.00
Nitrogen N1s	1.68
Fluorine F1s	4.12
Titanium Ti2p	4.42 (2p _{3/2}) and 2.06 (2p _{1/2})
Sulfur S2p	1.25 (2p _{3/2}) and 0.64 (2p _{1/2})
Silicon Si2p	0.60 (2p _{3/2}) and 0.30 (2p _{1/2})
Chlorine Cl2p	1.78 (2p _{3/2}) and 0.96 (2p _{1/2})

II.3.1.3 Surface energy by contact angle measurements

In Chapter III, we investigate the adherence of the neutral layer to the TiN hard mask to predict their resistance to HF wet treatments. To do this, we estimate the TiN surface energy through contact angle measurements.

Principle

Surface energy is the work that would be necessary to increase the surface area of a solid phase. The surface energy of a film is estimated by measuring the contact angle in a three-component system, as shown in Figure II-17: drop, substrate and air. During a contact angle measurement experiment, a drop of liquid is deposited on the surface of the material being studied. The angle made by the intersection of the liquid/solid interface and the liquid/air interface is called the contact angle and is noted θ in Figure II-17. It can also be described as the angle between the solid surface (sample) and the tangent of the drop surface at the edge of the drop. If the contact angle is high, the substrate presents a low surface energy or chemical affinity to the drop, and thus a low degree of wetting. On the other hand, if the contact angle is low, the substrate presents a high surface energy or chemical affinity to the drop, and thus a high or sometimes complete (if $\theta = 0$) degree of wetting.

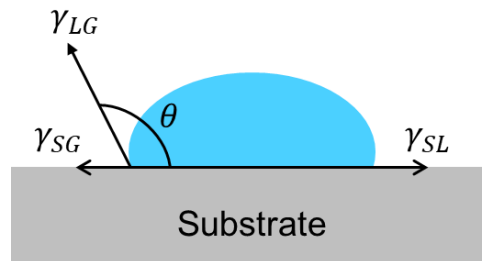


Figure II-17: Principle of contact angle measurements.

The contact angle makes it possible to characterize the affinity of the substrate's material to the liquid. In the case of water, there are 2 possibilities for the contact angle: when $\theta < 90^\circ$, the

material is hydrophilic, and when $\theta > 90^\circ$, the substrate is hydrophobic. In order to estimate the surface energy of the substrate, however, it is necessary to evaluate the contact angle for liquids with different densities and viscosities.

To determine the surface energy, we use Young's equation, which relates the interfacial tensions to each other and to the contact angle θ , according to the following equation:

$$\gamma_{SG} = \gamma_{SL} + \gamma_{LG} \times \cos(\theta)$$

Equation II-14: Young's equation to obtain the surface energy of a solid.

Where γ_{SG} is the solid-air interfacial tension; γ_{SL} is the solid-liquid interfacial tension and γ_{LG} is the liquid-air interfacial tension, as shown in Figure II-17. Only γ_{LG} is known and θ is measurable, and thus can be determined during the contact angle measurements. Therefore, in order to estimate the two unknowns, which are the interfacial tension γ_{SL} and the surface tension of the material γ_{SG} , many models have been proposed throughout the years. Some examples of well-known models are the OWRK (Owens, Wendt, Rabel and Kaelble), Fowkes and Zisman [OWRK 1969] [Fowkes 1964] [Zisman 1964].

Tool setup

The experimental setup for measuring the contact angles consists of a light source, a camera (connected to a computer) and a syringe to dispense the drops, as shown in Figure II-18. The tool used is the drop shape analyzer DSA100 from Krüss. The contact angle measurements were carried out on small samples of 5 cm x 7 cm.

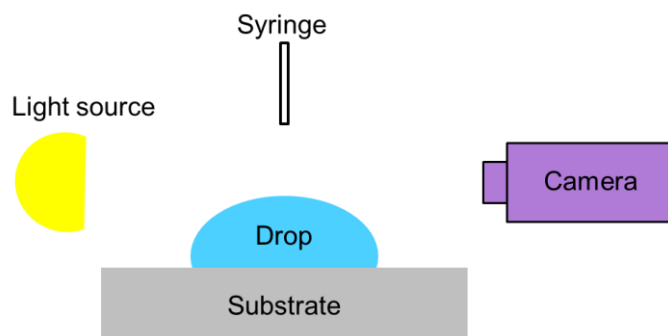


Figure II-18: Tool setup for contact angle measurements.

Three liquids were used to determine the surface energy of the substrate: water ($d = 1 \text{ g/cm}^3$); ethylene glycol ($d = 1.1 \text{ g/cm}^3$); and diiodomethane ($d = 3.3 \text{ g/cm}^3$). The use of these three liquids makes it possible to estimate the surface energy (γ) of the substrate, as well as its dispersive (γ^d) and polar (γ^p) components. For each liquid, 10 drops are deposited and measured to ensure the reproducibility of the measurement. The drop deposition conditions for each solvent are presented in Table II-8.

Table II-8. Deposition parameters of the liquids used for the contact angle measurements.

Solvent	Flow ($\mu\text{L/s}$)	Volume (μL)
Water	3	2
Ethylene glycol	4	3
Diiodomethane	2	1.5

Data analysis

Based on the measured contact angles obtained for each liquid, it is possible to determine the surface energy of the substrate. For this, the OWRK method is retained, since it allows obtaining a total surface energy value, as a function of polar and dispersive components, via a linear regression on the polar and dispersive energy values obtained for the three liquids. The OWRK method is represented by Equation II-15:

$$(1 + \cos \theta) \times \gamma_{LG} = 2 \times (\sqrt{\gamma_{SG}^d \gamma_{LG}^d} + \sqrt{\gamma_{SG}^p \gamma_{LG}^p})$$

Equation II-15: Owens, Wendt, Rabel and Kaelble (OWRK) equation for the surface energy.

Where γ^d and γ^p , respectively, represent the dispersive component and the polar component of the material or liquid. These values are given by the literature for the three liquids (Table II-9) and can be determined for the solid thanks to a linear regression, which represents the OWRK function in the form $y = ax + b$:

$$\underbrace{\frac{\gamma_{LG} \times (1 + \cos \theta)}{2 \times \sqrt{\gamma_{LG}^d}}}_y = \underbrace{\sqrt{\gamma_{SG}^p}}_a \times \underbrace{\sqrt{\frac{\gamma_{LG}^p}{\gamma_{LG}^d}}}_x + \underbrace{\sqrt{\gamma_{SG}^d}}_b$$

Equation II-16: Owens, Wendt, Rabel and Kaelble (OWRK) equation in the linear form.

Since γ_{LG} , γ_{LG}^d and γ_{LG}^p are known for each liquid and θ is the measured contact angle, the polar and dispersive components of the substrate's surface energy are determined by $a^2 = \gamma_{SG}^p$ and $b^2 = \gamma_{SG}^d$. Finally, the surface energy of the material is given by the sum of both components, so that $\gamma_{SG}^p + \gamma_{SG}^d = \gamma_{SG}$.

The surface energy measurement is commonly used in the microelectronics field, although it may be considered less reliable than other characterization techniques due to the many uncertainties that can accompany the result, such as a change in manipulator, device, or surface preparation. The tool used during this PhD gives a measurement uncertainty of the surface energy varying, depending on the materials, from 1 to more than 10 mN/m.

Table II-9. Surface energy, as well as its dispersive and polar components, of different liquids.

Solvent	Surface energy γ (mN/m)	Polar component γ^p (mN/m)	Dispersive component γ^d (mN/m)
Water	72.8	46.4	26.4
Ethylene glycol	47.7	21.3	26.4
Diiodomethane	50.8	2.3	48.5

II.3.1.4 Fourier-Transform Infrared (FTIR) Spectroscopy

Fourier-transform infrared (FTIR) spectroscopy is a chemical characterization technique for both organic and inorganic materials. It is based on measuring the absorption of infrared radiation by the sample. Once the raw data is obtained, a Fourier transform is necessary to convert them into spectral results [Griffiths 2007].

All molecules are made up of atoms linked by chemical bonds. The movement of these atoms can be regarded as being composed of two components: the stretching and bending vibrations. Similarly to what we have seen for XPS, the frequencies of these atomic vibrations depend on the nature of the bonds and also on their chemical environment (interaction with neighboring atoms). If an electromagnetic wave (infrared beam) strikes the bonds, their vibrations will increase in amplitude. During FTIR analysis, the sample is illuminated by an infrared beam with wavenumbers between 400 and 5000 cm^{-1} and the detector measures how much of that beam is absorbed by the sample. Since the vibrational energy levels of a molecule are quantized, only the infrared beam with a frequency exactly corresponding to that required to raise the energy level of a bond will be absorbed, so the amplitude of that particular vibration is increased by a certain amount and not gradually. Next, the infrared beam is modified to contain a different combination of frequencies. This process is rapidly repeated many times over a short time span. When the sample is irradiated by an infrared beam whose frequency is changed continuously, the molecule will absorb certain frequencies as the energy is consumed in stretching or bending different bonds. Then, a computer takes all this data and uses Fourier transforms to determine the absorption at each wavelength. The transmitted beam corresponding to the region of absorption will be weakened, and thus a recording of the intensity of the transmitted infrared beam versus wavenumbers will give a curve showing absorption bands. This is the infrared spectrum [Nakanishi 1977].

Therefore, by analyzing the beam transmitted through the sample with a spectrometer, the nature of the chemical bonds can be determined. The recorded signal is the transmittance (T), that is, the intensity of the transmitted beam (I) divided by the intensity of the incident beam (I_0) as a function of the wavenumber (λ). The absorbance spectrum (A) is then calculated by the formula $A = -\log T$. According to the Beer-Lambert law, the areas of the absorbance peaks are proportional to the concentration of the corresponding bonds. Figure II-19 shows an example of absorbance spectrum obtained through FTIR for a PS homopolymer, as well as a table detailing the corresponding bonds for each peak observed.

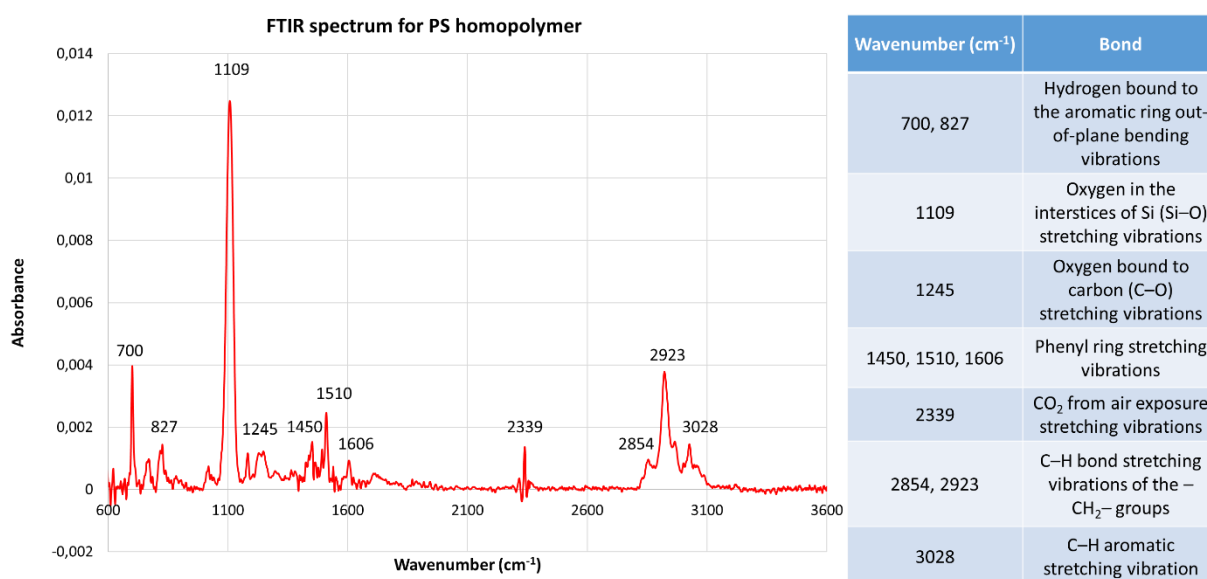


Figure II-19: Example of FTIR spectrum for a PS homopolymer and table with the corresponding bonds for each peak observed.

For the PS homopolymer, the absorption bands from 700 to 827 cm^{-1} correspond to out-of-plane bending vibrations of the hydrogen atoms bound to the aromatic ring. The band at 1109 cm^{-1} corresponds to the stretching vibrations of the oxygen in the interstices of Si (Si–O bonds), which is characteristic of the silicon substrate and unrelated to the PS. The band at 1245 cm^{-1} might correspond to the stretching vibrations of oxygen bound to carbon (C–O), which probably comes from air exposure. Next, the absorption band from 1450 to 1606 cm^{-1} corresponds to the phenyl ring stretching vibrations. The band at 2339 cm^{-1} is characteristic of the CO_2 from air exposure. The bands at 2854 and 2923 cm^{-1} characterize the C–H bond stretching vibrations of the $-\text{CH}_2-$ groups. Finally, the band at 3028 cm^{-1} represents the C–H aromatic stretching vibration ($\text{HC}=\text{CH}$) [Nakanishi 1977].

In Chapter IV, FTIR analysis are carried out on PS and PMMA homopolymers to determine the influence of UV exposure on their chemical structure. The FTIR measurements were conducted on a Vertex 70v spectrometer from Bruker. A reference silicon sample is used to create the background spectra. Finally, all spectra are normalized based on the thickness of the samples.

II.3.1.5 Time-of-Flight Secondary Ion Mass Spectrometry (ToF-SIMS)

Time-of-Flight Secondary Ion Mass Spectroscopy (SIMS) is a surface analytical technique which allows us to trace the concentration profile of different species in thin films with thickness ranging from 0.5 nm to around 100 nm. This technique combines the analytical technique SIMS (Secondary Ion Mass Spectrometry) with Time-of-Flight mass analysis (TOF). It provides detailed elemental and molecular information about the sample's surface, thin layers and interfaces. It is a very sensitive technique, for which lateral resolution can reach 50 nm, depth resolution is around 1 nm and mass detection limit is of the order of 1 $\text{ppm}/\mu\text{m}^3$ [Vickerman 2001].

During analysis, primary ions are produced by an ion source before being accelerated towards the sample with a known energy (in keV). Thus, the sample is bombarded by these primary ions, which then transfer their energy to the sample's atoms via atomic collisions, generating a collision cascade, as shown in Figure II-20(a). This energy allows surface atoms and molecular compounds to overcome the surface binding energy. It should be noticed that the ion dose is kept low to minimize chemical damage to the sample. Thus, the interaction of the collision cascade with the surface molecules is soft enough to allow even large and non-volatile molecules to escape without or with little fragmentation.

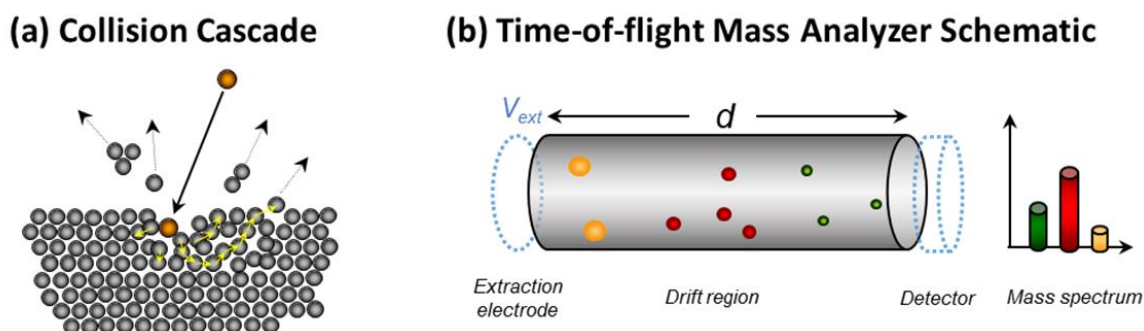


Figure II-20: (a) Schematic of the collision cascade, showing the desorption of atoms and molecules due to primary ion bombardment; and (b) schematic of the time-of-flight mass analyzer, which separates the secondary ions based on their mass determined by their time-of-flight. Adapted from [NIST 2021].

Due to the collision cascade, the ejected matter is composed of atoms, emitted ions, and neutral and ionic clusters. However, only the emitted ions – also known as secondary ions – are analyzed in this technique. A time-of-flight analyzer is then used. ToF mass spectrometry is based on the fact that ions with the same energy but different masses travel with different speed. An electrostatic field accelerates the generated ions to a common energy. Thus, the secondary ions are extracted from the surface of the sample with a known extraction potential, represented as V_{ext} in Figure II-20(b). The secondary ions are therefore accelerated towards a mass analyzer, traveling over a drift path with a speed (v) obtained according to the following equation, where q is the ion charge and m is the ion mass:

$$q \times V_{ext} = \frac{m \times v^2}{2}$$

Equation II-17: Conservation of energy of the secondary ions.

By replacing the ion speed (v) by the ratio between the distance traveled by the ions (d) and the time-of-flight (t), so that $v = \frac{d}{t}$, we obtain the following equation for the time-of-flight as a function of the ion's mass:

$$t = d \times \sqrt{\frac{m}{2qV_{ext}}} \Rightarrow t \propto \sqrt{m}$$

Equation II-18: Time-of-flight (t) as a function of the secondary ion's mass (m).

From Equations II-17 and II-18, we observe that lighter ions fly with a higher speed and arrive at the detector before the heavier ions. Measuring the time-of-flight for each ion allows the determination of its mass, thus making it possible to distinguish the different ions according to their masses in order to then obtain the mass spectrum. This cycle is repeated with a repetition rate of up to 50 kHz.

Furthermore, the time during which the extraction field is switched off can be used to apply a low energy secondary ion beam for sample erosion. This analysis mode is known as “dual beam depth profiling”, since the low energy secondary beam forms a sputter crater, and the center of this crater is analyzed by the pulsed primary ion beam. During the analysis, the evolution of the signal is followed according to the penetration depth into the substrate by alternating erosion and analysis phases. It is therefore possible to obtain several types of information:

- A mass spectrum, presenting the different chemical elements contained in the layer.
- A depth profile, which gives an evolution of the species according to the depth (the mass of the species is fixed in this case).
- A 2D map, which shows the mass distribution by rastering a fine-focused ion beam over the surface of the sample (the mass and the depth are fixed in this case).

In Chapter III, ToF-SIMS analysis are used to complement the results obtained through XPS and to identify light ions (hydrogen and helium). They were carried out on a ToF-SIMS5 tool from the company Ion-TOF. The dual beam depth profiling mode was used. Sample erosion was carried out by a low energy (500 eV) Cs^+ ion beam with a raster size of 300 μm . The analysis beam used is made up of Bi^+ ions with an energy of 25 keV, a frame size of 90 x 90 μm^2 and an ion dose of 3.87×10^{13} ions/cm².

II.3.2 Morphological characterization

This section shall focus on morphological characterization techniques. These characterization methods, namely the Scanning Electron Microscopy (SEM) and the Transmission Electron Microscopy (TEM), were used to observe the profile of different materials after etching. They allow us to measure the thickness and critical dimension (CD) of the patterns, as well as evaluate the quality of the slope, the roughness, and the presence of defects.

II.3.2.1 Scanning electron microscopy (SEM)

Throughout this thesis, two types of Scanning Electron Microscopes were used: a SEM allowing top-view imaging, also known as CD-SEM for Critical Dimension-SEM, and another allowing cross-sectional imaging. Scanning Electron Microscopy provides information on the dimensions of the structures observed and, in the case of cross-section images, on the thicknesses of the different layers of a sample.

Principle

The scanning electron microscopy is based on the following principle: an electronic probe emits an electron beam, which is strongly accelerated with an energy between 0.1 and 30 kV. Thanks to an array of electromagnetic lenses, this beam is focused on the sample, and scans the surface to be observed. During the interaction between the incident electrons and the sample, elastic and inelastic collisions take place. These interactions lead to different types of emission, namely the emission of secondary and backscattered electrons, which can give a certain amount of information on the sample, in the form of images.

- The emission of secondary electrons (SE) comes from the inelastic collisions between the primary electron (from the incident beam) and the electrons of the valence shells of the atoms present in the sample, as shown in Figure II-21(a). During the collision, the primary electron loses energy and its trajectory can be modified. Moreover, this inelastic collision gives little energy (between 0 and 50 eV) to the secondary electrons to extract themselves from the surface. Thus, only the secondary electrons emitted by atoms present in the superficial layers close to the surface can be collected by the detector. This means SE imaging is very sensitive to variations in the surface morphology and topography of the sample, and the slightest surface defect will have an impact on the quantity of electrons collected. By scanning the surface, an electron detector transcribes the electron flux into luminosity and the signal is collected and synchronized to reconstruct an image faithful to the surface with a topographical effect.

- The emission of backscattered electrons (BSE) is based on the elastic interaction of the primary electrons of the incident beam with the nuclei of atoms in the sample, as shown in Figure II-21(b). This results in a random deviation from its initial path, without loss of energy, also known as elastic diffusion. Since there is no energy loss, the backscattered electrons have a high energy and can be detected at a much greater depth in the sample, compared to secondary electrons. Therefore, backscattered electrons are very sensitive to the atomic number (Z) of the atoms they pass through, which gives an image of the observed surface based on chemical contrast instead of topography. The higher the atomic number of the atom observed, the more its number of protons gives it the ability to re-emit electrons in large quantities. Thus, regions composed of atoms with a high atomic number will appear brighter than others with lower atomic numbers.

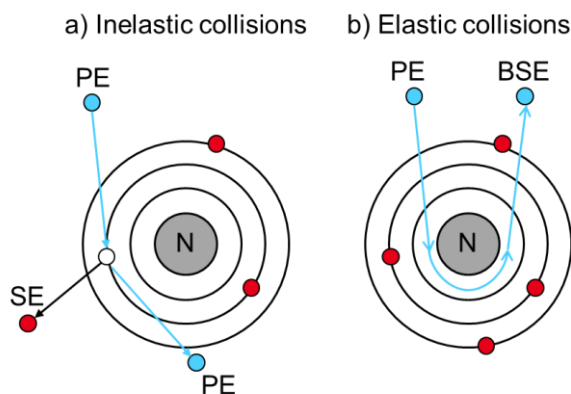


Figure II-21: Schematic representation of the interaction between the primary electron (PE) and the sample, leading to (a) inelastic collisions that generate the secondary electrons (SE) and (b) elastic collisions that generate the backscattered electrons (BSE).

Tool setup

Two different SEM tools were used for morphological observations during this PhD. The critical dimension SEM (CD-SEM) used for top-view observation is the VeritySEM 6i™ tool from Applied Materials®. SEM images are acquired with an accelerating voltage of 800V and a probe current of 10 pA. The CD-SEM observation is non-destructive, and no sample preparation is required. An example of top-view SEM image of a block copolymer assembled on free surface is shown in Figure II-22(a).

After top-view observations, the cross-section SEM tool used is a Hitachi® S5500™ microscope. It complements the information provided by the top-view observation, since it consists of obtaining cross-sectional images of the sample, allowing us to measure the CD, the slope of the sidewalls, the thickness of the stack after etching and the remaining materials at the bottom of the wafer (if they exist), for example. However, this technique is destructive, since the wafer must be cleaved to prepare the samples.

Furthermore, cross-sectional samples of polymeric materials are precoated with a platinum metallization for 30 seconds to reduce charging effects characteristic of the polymer reaction to the electron beam. All cross-section images are acquired with an accelerating voltage of 5.0 kV, a probe current of 15 μ A and using a tilt of -20° . An example of cross-section SEM image after removal of one of the blocks of the PS-*b*-PMMA block copolymer is shown in Figure II-22(b).

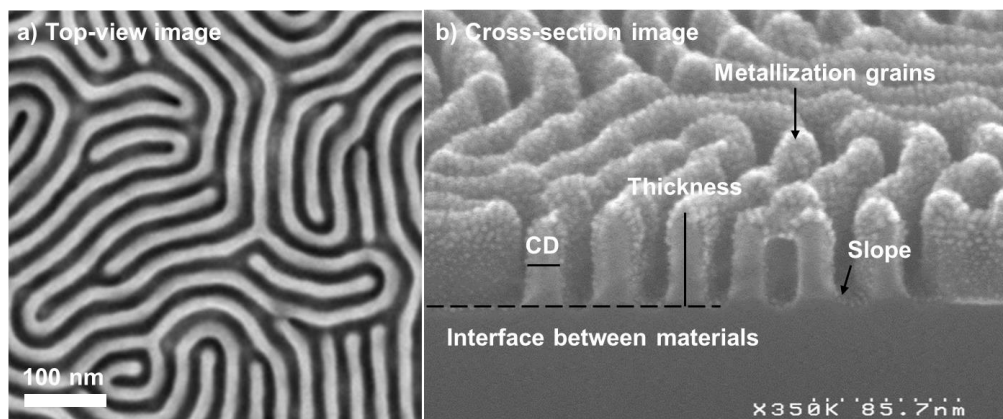


Figure II-22: Examples of (a) top-view and (b) cross-section SEM images of a PS-*b*-PMMA block copolymer after PMMA removal.

II.3.2.2 Transmission electron microscopy (TEM)

Transmission Electron Microscopy (TEM) is a morphological characterization technique that gives better resolution than SEM. In fact, the latest generation tools can achieve resolutions of the order of 90 to 200 pm.

Prior to imaging, samples are prepared using a Focused Ion Beam (FIB). This micromachining technique etches the material due to high energy ion bombardment (usually Gallium, Ga^+), thus creating cross-sections of approximately $1\mu\text{m}$ in a specific area of a pattern. In addition, the sample is thinned to less than 100 nm and a gas, such as tungsten hexacarbonyl [$\text{W}(\text{CO})_6$], is introduced to the vacuum chamber and allowed to chemisorb onto the sample. Next, the thinned sample is scanned by an electron beam. When scanning the sample with the beam, the precursor gas is decomposed into volatile and non-volatile components. Since it is a non-volatile component, the tungsten remains on the surface, thus forming a protection layer to reduce the impact of the imaging beam on the sample.

The electrons transmitted through the sample are analyzed by various detectors, allowing the formation of an image. The sample image is projected onto a fluorescent screen that transforms the electronic image, sensitive to transmission contrast, into an optical image. The contrast obtained gives information on both the atoms of the sample and the structural defects in the lattice:

- When the transmitted electrons are collected without diffraction, there is a bright field. Indeed, electrons that undergo elastic collisions when passing through the sample are deflected at large angles and are therefore not detected. As the probability of undergoing an elastic collision increases with the atomic number (Z) of the atoms analyzed, heavier elements appear darker.
- When the transmitted electrons are collected with diffraction, there is a dark field. This happens because, when structural defects are present in the lattice, they modify the diffraction angle.

FIB sample preparation was conducted on a FIB Helios 3 tool from FEI, while TEM analyzes were performed on a Tecnai Osiris tool, also from FEI, with an electron acceleration voltage of 200 kV. It should be noticed, however, that sample preparation and TEM analysis heavily impact polymeric materials, such as the block copolymers, leading to shrinkage. Furthermore, it is also long. Therefore, this technique shall be used sparingly during this PhD, namely to characterize the pattern profile after spacer etching and SOC removal for the ACE chemo-epitaxy flow.

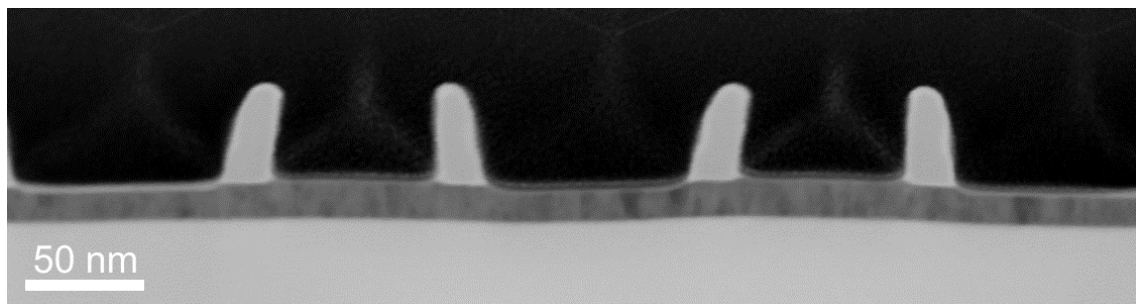


Figure II-23: Example of TEM image of a patterned wafer after spacer etching and SOC removal for the ACE chemo-epitaxy flow.

In this chapter, we have detailed the characteristics of the different polymeric materials studied throughout this PhD, namely their composition and deposition parameters. We have also presented the properties of the different etching reactors, both ICP and CCP, used to study the plasma etching of the high- χ block copolymers; as well as the wet etching tool used for understanding the interaction between plasma etching, the hard mask and the neutral layer during the ACE chemo-epitaxy process. Finally, we have explained the principle of several characterization tools used during this thesis to evaluate and understand the results obtained in the next three chapters, detailing the experimental setup and data analysis when applicable.

CHAPTER III:

ETCHING IMPACT ON THE ACE CHEMO-EPITAXY FLOW FOR DIRECTED SELF-ASSEMBLY

III. ETCHING IMPACT ON THE ACE CHEMO-EPITAXY FLOW FOR DIRECTED SELF-ASSEMBLY

We have seen in the introduction chapter that the Directed Self-Assembly of block copolymers is one of the advanced patterning techniques being considered for obtaining small and dense patterns with dimensions inferior to 20 nm. This choice is particularly motivated by the use of well-known lithography steps and by its low cost compared to other solutions. Different integrations have been proposed to obtain patterns by guiding the self-assembly of the block copolymers, as shown in Chapter I.3.3. The main difference between them was the use of either topographical (grapho-epitaxy) or chemical affinity (chemo-epitaxy) constraints, as well as the commensurability rules for each integration flow presented. In the introduction, we also outlined the chemo-epitaxy integration developed at CEA Leti, known as “ACE” for Arkema-CEA, which shall serve as the basis for this chapter.

The ACE flow includes several wet and plasma etching steps. The purpose of this chapter is therefore to investigate and understand the impact that the different etching steps of the ACE flow have on the assembly of the block copolymer. Indeed, through its chemistry or other parameters, the etching steps may modify the surface properties of the hard mask or the neutral layer, therefore having an effect on the block copolymer’s alignment, notably in terms of defectivity.

Part of the work presented in this Chapter has been published in the *Journal of Vacuum Science & Technology A* [Gusmão 2021].

III.1 ACE chemo-epitaxy flow

In this part, we will present in more detail the ACE integration flow, which was discussed in the introduction and used as the process of reference at the beginning of this PhD. As we can see in Figure III-1, this integration starts with an immersion lithography on a trilayer composed of a photoresist, an anti-reflective layer and a spin-on carbon layer (1-2). The spin-on carbon serves as a mandrel (3), over which a silicon nitride film is deposited (4) in a conformal manner and then etched to define the spacers (5-6). The neutral layer is deposited between the spacers (7) before they are removed to form the narrow guiding stripes (8). Finally, the guiding layer is grafted to the TiN surface where the spacers are no longer present (9) and the block copolymer is self-assembled and directed by one of the block’s affinity to the guiding layer (10).

Table III-1 shows the plasma parameters for the different dry etching steps of the flow. All plasma etching steps correspond to the best chemistries developed at CEA Leti and have been carried out on a 300 mm Kiyō FX® inductively coupled plasma (ICP) reactor from LamResearch®, which has been presented in Chapter II.2.1.2.

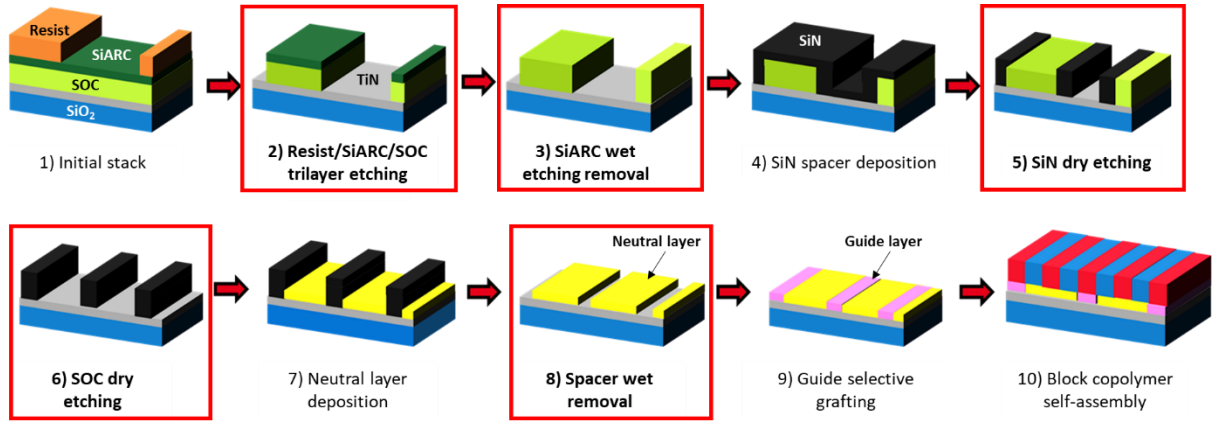


Figure III-1: ACE process flow schematics, consisting of a conventional Self-Aligned Double Patterning (SADP) process (steps 1 to 6), followed by the DSA process (steps 7 to 10). The different etching steps have been highlighted by red squares.

Table III-1: Plasma parameters for the different plasma etching steps of the ACE flow. The etching times correspond to approximately 50% overetch.

Step	Chemistry	Pressure (mTorr)	Power (W)	Bias (V)	Flow (ratio)	Time (s)
2a: SiARC opening	CH ₂ F ₂ /SF ₆ /N ₂ /He	5	450	-70	1.5:1:1.5:3	40
2b: SOC opening	ME: SO ₂ /O ₂ /He	10	950	-250	3:0.6:1	8
	OE: SO ₂ /He	10	950	-250	3:1	17
5: SiN etching	CH ₂ F ₂ /CF ₄ /O ₂	15	500	-400	3:1.5:1	25
6: SOC removal	SO ₂ /O ₂ /He	10	950	-250	3:0.6:1	25

The ACE flow consists of the following steps:

(1) Stack preparation

A 100-nm layer of silicon oxide (SiO₂) is obtained by thermal oxidation, carried out at 950°C. A 15-nm layer of titanium nitride (TiN) is then deposited over the SiO₂ by Physical Vapor Deposition (PVD) at room temperature under a pressure of 25 mTorr in an ENDURA 300A tool from Applied Materials.

Then, 193 nm immersion lithography is performed on a standard trilayer stack which consists of, from bottom to top: 73 nm of Spin-On Carbon (SOC), 35 nm of Silicon-containing Anti-Reflective Coating (SiARC) and 100 nm of lithography photoresist. The SOC and SiARC are provided by JSR under the trade names HM-8102-9 and ISX534, respectively. The lithography photoresist used is a negative development resist (NTD) provided by JSR under the trade name AEX2039, which is annealed at 120°C for 60 seconds before exposure.

Within the framework of the ACE process, the multiplication factor (MF) will be determined by the lithography pitch (represented only by “Pitch” hereafter) and the intrinsic period of the BCP (L_0). Thus, the notation MF_n will be used in the remainder of this manuscript, with $n = \frac{\text{Pitch}}{L_0}$. Figure III-2 shows an example of MF with $n = 4$ and $n = 6$.

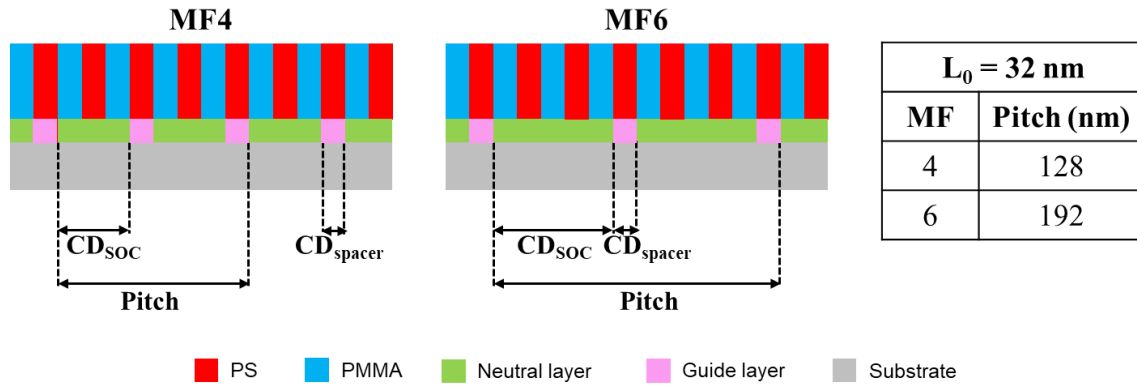


Figure III-2: Schematics for the block copolymer alignment with MF with $n = 4$ and $n = 6$. The table indicates the lithography pitch corresponding to each MF for a block copolymer with $L_0 = 32 \text{ nm}$.

The 193 nm immersion exposure is carried out on a Twinscan NXT:1970Ci tool from ASML. The lithography exposure dose is varied for each column. Since the critical dimension (CD) resolved in the lithography step depends on the dose received by the resist during exposure, with the dose variation applied to ACE, it is possible to obtain up to 88 different CDs for a given pitch on the same wafer. After exposure, the substrate is annealed at 90°C for 60 seconds. Finally, the photoresist is developed with n-butyl acetate (NBA) to remove the parts that were not exposed. The CD of the line patterns obtained in the lithography step are measured using a CD-SEM before moving to the next step. All the chips in the same column are identical in terms of CD after lithography as they have been exposed with the same dose.

(2) Trilayer etching: pattern transfer into the SOC layer

The line/space patterns obtained in the previous step are transferred by plasma etching into the SiARC and SOC layers. As we can see in Table III-1, the SiARC opening step (2a) consists on a fluorocarbon-based plasma while the SOC opening step (2b) presents a short main etch (ME) consisting of $\text{SO}_2/\text{O}_2/\text{He}$ followed by a SO_2/He overetch (OE).

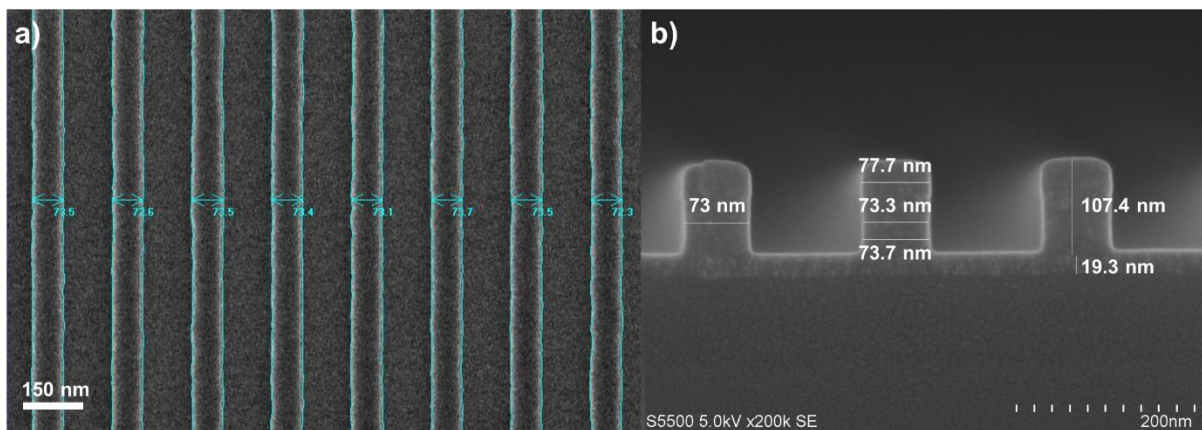


Figure III-3: (a) Top-view and (b) cross-section SEM images of the patterns corresponding to a lithography pitch of 190 nm in the central chip of the wafer ($X = 0, Y = 0$) after trilayer etching.

During trilayer etching, a lateral reduction of the lithography CD is observed. For the ACE flow, this lateral consumption has been measured at approximately 10 nm. Figure III-3 shows both top-view (a) and cross-section (b) SEM images of the patterns for the central chip on the

wafer, with a lithography pitch of 190 nm and a CD of around 73 nm after trilayer etching. The thickness of the patterns (around 107 nm) corresponds to the SOC + SiARC total thickness. The profile of the lines is straight except for the SiARC on top of the patterns, which presents a larger CD (around 78 nm) than the SOC (around 73 nm). As the SiARC will be removed on the next step, the final CD to be taken into account will be the CD of the SOC mandrel.

(3) SiARC wet etching removal to obtain the SOC mandrel

After pattern transfer into the SOC layer, the SiARC is wet removed with hydrofluoric acid (HF) diluted to 1% during 15 seconds. The SiARC removal leads to the formation of the SOC mandrels. The wet removal is conducted on a Raider tool from Semitool®, which has also been presented in Chapter II.2.2.

(4) SiN spacer deposition

Once the mandrel is formed, a conformal 26-nm layer of silicon nitride (Si_3N_4 , referred to as SiN for the remainder of this manuscript) is deposited by Plasma-Enhanced Chemical Vapor Deposition (PECVD) at a temperature of 320°C on a Producer tool from Applied Materials. Since the SOC degradation temperature is approximately 350°C, the SiN deposition temperature has been selected in order to avoid the mandrel degradation.

(5) Anisotropic plasma etching of SiN spacer

The SiN layer is anisotropically dry etched in order to form the spacers on the sidewalls of the mandrel. The parameters for the SiN etching using a $\text{CH}_2\text{F}_2/\text{CF}_4/\text{O}_2$ plasma chemistry can be found in Table III-1 (5). Previous studies have shown that the fluorine-based SiN etching forms TiF_3 particles when left in contact with the TiN hard mask [Posseme 2010], which can be seen in Figure III-4. Therefore a very short queue time was established between the SiN etching (step 5) and the SOC removal (step 6), meaning both steps are performed in the same reactor without air exposure to limit the formation of TiF_3 particles.

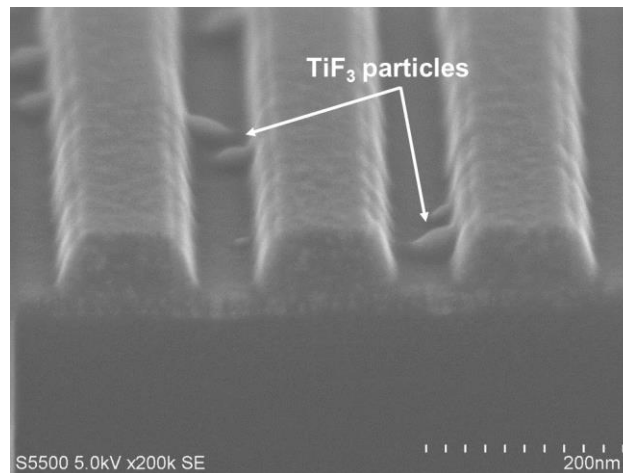


Figure III-4: Cross-section SEM image of the SOC mandrel and SiN spacers corresponding to a pitch of 190 nm in the central chip of the wafer ($X = 0$, $Y = 0$) after anisotropic SiN etching. The formation of TiF_3 particles on the TiN surface is highlighted.

(6) SOC mandrel removal

The SOC mandrel is removed by $\text{SO}_2/\text{O}_2/\text{He}$ plasma etching selectively to the SiN, forming spacers that will later be replaced by the guide patterns for the block copolymer's self-assembly. The parameters for the SOC removal can be found in Table III-1 (6).

Transmission electron microscopy (TEM) images of the SiN spacers after SOC removal are presented in Figure III-5. These images confirm the complete removal of the SOC mandrel and the formation of SiN spacers with CD around 14.5 nm. It should be noticed that the spacer CD at the interface with the substrate is around 6 nm larger than the top CD. This difference between top and bottom CD is known as spacer foot. Several solutions to reduce the spacer foot have been proposed, such as the implantation of light ions (for example, hydrogen or helium) to modify the SiN bottom layer and facilitate the foot removal [Posseme 2014]. However, they shall not be addressed during this PhD thesis.

Another important thing to notice is the difference in thickness between the TiN that has seen all the steps of the ACE flow until now (identified as “TiN A” in Figure III-4) and the TiN that has been protected by the SOC layer (identified as “TiN B”). This difference can be explained by the consumption of the TiO₂ layer on the “A” zone during steps 1 to 5, namely due to the ion bombardment of the plasma etching steps (2 and 5) and to the HF wet etching for SiARC removal (step 3).

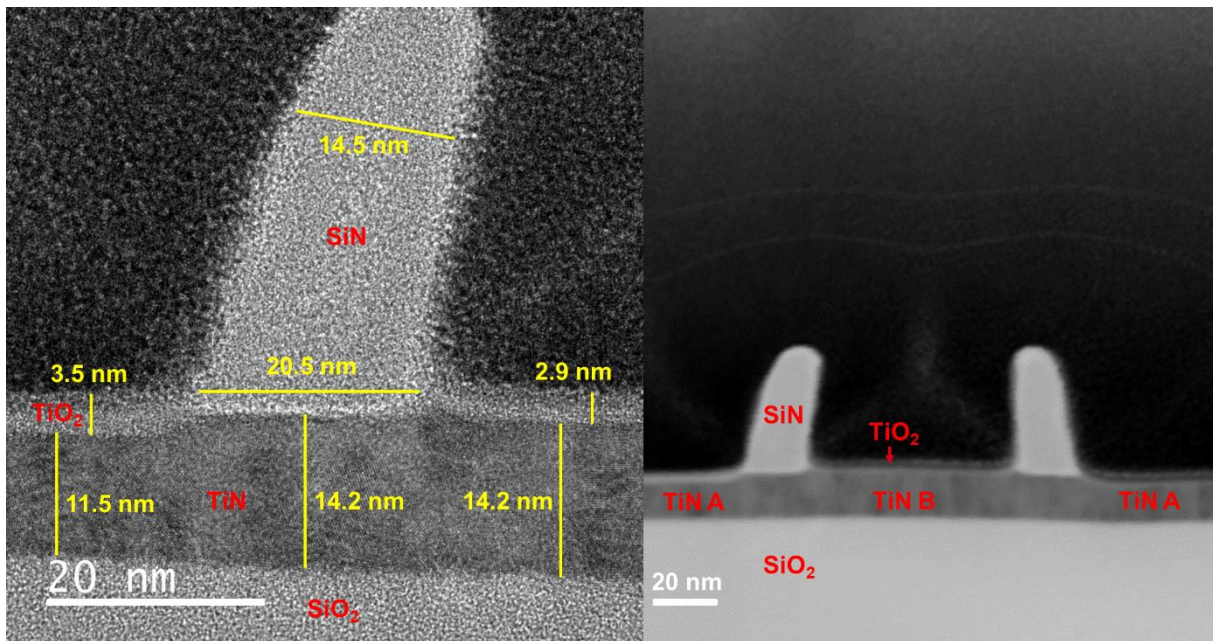


Figure III-5: TEM images of the SiN spacers corresponding to a lithography pitch of 190 nm in the central chip of the wafer ($X = 0$, $Y = 0$) after SOC mandrel removal.

(7) Deposition and cross-linking of the neutral layer

The directed self-assembly part of the ACE flow begins by depositing a cross-linkable neutral layer which will be referred to as “xNL”. This neutral layer is provided by Brewer Science Inc. and is composed of PS and PMMA. It is deposited by spin-coating in a 300 mm SCREEN SOKUDO Duo™ coat/develop track to obtain a thickness of around 7.5 nm. It is then annealed at 250°C for 5 minutes and rinsed using Propylene glycol methyl ether acetate (PGMEA) in the same track, thus filling the area between the spacers to create a neutral surface.

(8) SiN spacer wet removal

The SiN spacers are then removed by HF diluted to 1% for 60 seconds, creating a vacant space with a CD equal to half the pitch of the block copolymer, without modifying the physical-

chemical properties of the xNL. Once again, the wet removal is conducted on a Raider tool from Semitool®.

(9) Guide layer grafting

In the space left by the spacers that were removed, a guiding layer provided by Arkema® is then selectively grafted at 200°C for 75 seconds. A PGMEA rinse allows the removal of ungrafted polymer chains, thus obtaining the guiding template for the BCP alignment with a guide layer final thickness of around 7 nm. This grafting is selective, meaning the guide layer can be grafted onto the TiN hard mask, without grafting onto the xNL.

(10) DSA: block copolymer self-assembly

Finally, the block copolymer is spin-coated and annealed to obtain guided line/space patterns. The block copolymer used is a PS-*b*-PMMA provided by Arkema® under the trade name Nanostrength® EO with an intrinsic period $L_0 = 32$ nm and a lamellar morphology. The BCP solution is annealed at 240°C for 15 minutes to obtain a film with 33-nm thickness.

Figure III-6 represents the top-view SEM image obtained after the BCP self-assembly step for the PS-*b*-PMMA block copolymer with $L_0 = 32$ nm. The PMMA phase is removed through dry etching to enhance the contrast and facilitate the image capture. Different types of defects can be seen in this image, like dark spots and BCP alignment defects. These defects are probably caused by a change in surface properties of the TiN substrate, which is covered by either the neutral or guide layers. Therefore, the goal of our study shall be to identify the origin of these defects.

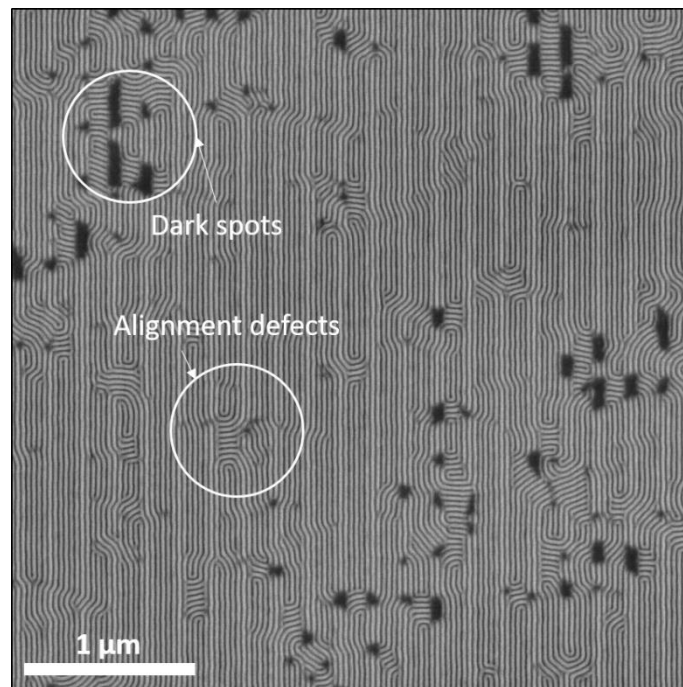


Figure III-6: Top-view SEM image of the PS-*b*-PMMA block copolymer with $L_0 = 32$ nm partially aligned by the ACE flow, highlighting the alignment defects and dark spots.

III.2 Understanding the effect of etching on the block copolymer's alignment

The results presented in Figure III-6 indicate that the surface properties of the TiN hard mask are not favorable to a perfect alignment of the block copolymer. The goal of this section is to understand the impact of the etching steps on the TiN surface and identify the ones that mostly affect its properties, especially regarding its composition and surface energy. We shall also evaluate the neutral layer's adherence to the TiN hard mask during HF wet etching as a function of the etching steps in order to pinpoint the source of the defects.

III.2.1 Effect of the sequence of etching and deposition steps on the TiN surface

In order to understand the origin of the different defects presented in Figure III-6, the effect of the sequence of etching and deposition steps on the TiN surface is investigated using TiN blanket wafers with a 73 nm SOC layer deposited on top, as seen in Figure III-7 (1). For the trilayer etching, only the last step, corresponding to the SOC opening, is investigated, since it is the only one that affects the TiN surface. The trilayer etching is conducted using the parameters presented in Table III-1 (2b). Once the complete removal of the SOC layer is confirmed by ellipsometry, an HF dip of 15 seconds is also conducted to represent the SiARC removal. Then, a 26 nm SiN layer is deposited through PECVD as described in the previous section. Next, the SiN etching and SOC removal are performed using the parameters from Table III-1 (5, 6). Once again, ellipsometry is used to confirm the complete removal of the SiN layer. Finally, the TiN surface composition and energy are determined by *ex-situ* XPS and contact angle measurements, respectively.

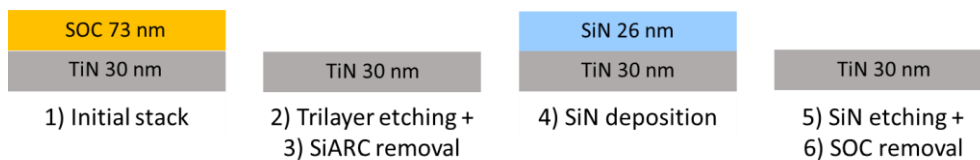


Figure III-7: Sequence of etching and deposition steps applied to TiN blanket wafers.

III.2.1.1 Study of etching steps impact on TiN surface composition

Figure III-8 presents the evolution of O1s (a), N1s (b) and Ti2p (c) *ex-situ* XPS spectra for the TiN surface before and after steps 1 to 6. Figure III-8 shows that the TiN surface after steps 1 to 6 presents a strong oxidation when compared to the as deposited TiN surface, with the increase of TiO₂ (Ti2p_{3/2} peak at around 458.7 eV and O1s peak at 531.6 eV) and decrease of TiN (Ti2p_{3/2} peak at around 454.7 eV and N1s peak at 396.9 eV) and Ti-O-N (Ti2p_{3/2} peak at around 456.3 eV, N1s peak at 399.6 eV and O1s peak at 530 eV) peaks [Oktay 2015] [Gonbeau 1991]. Figure III-9 summarizes the TiN surface composition determined by XPS before and after steps 1 to 6. Figure III-9(b) indicates that the TiN surface also presents around 13% of sulfur after steps 1 to 6, represented by TiO_xS_y and SO₄²⁻ with S2p_{3/2} peaks at 163.4 eV and 169.2 eV, respectively [Gonbeau 1991] [Wagner 1982]. Furthermore, the corresponding O1s peak at 532.4 eV in Figure III-8(a) also confirmed the presence of SO₄²⁻ [Salim 2011]. The presence of fluorine is due to the SiN etching and the presence of carbon is due to contamination from the reactor walls and to the air exposure between the etching and XPS analysis.

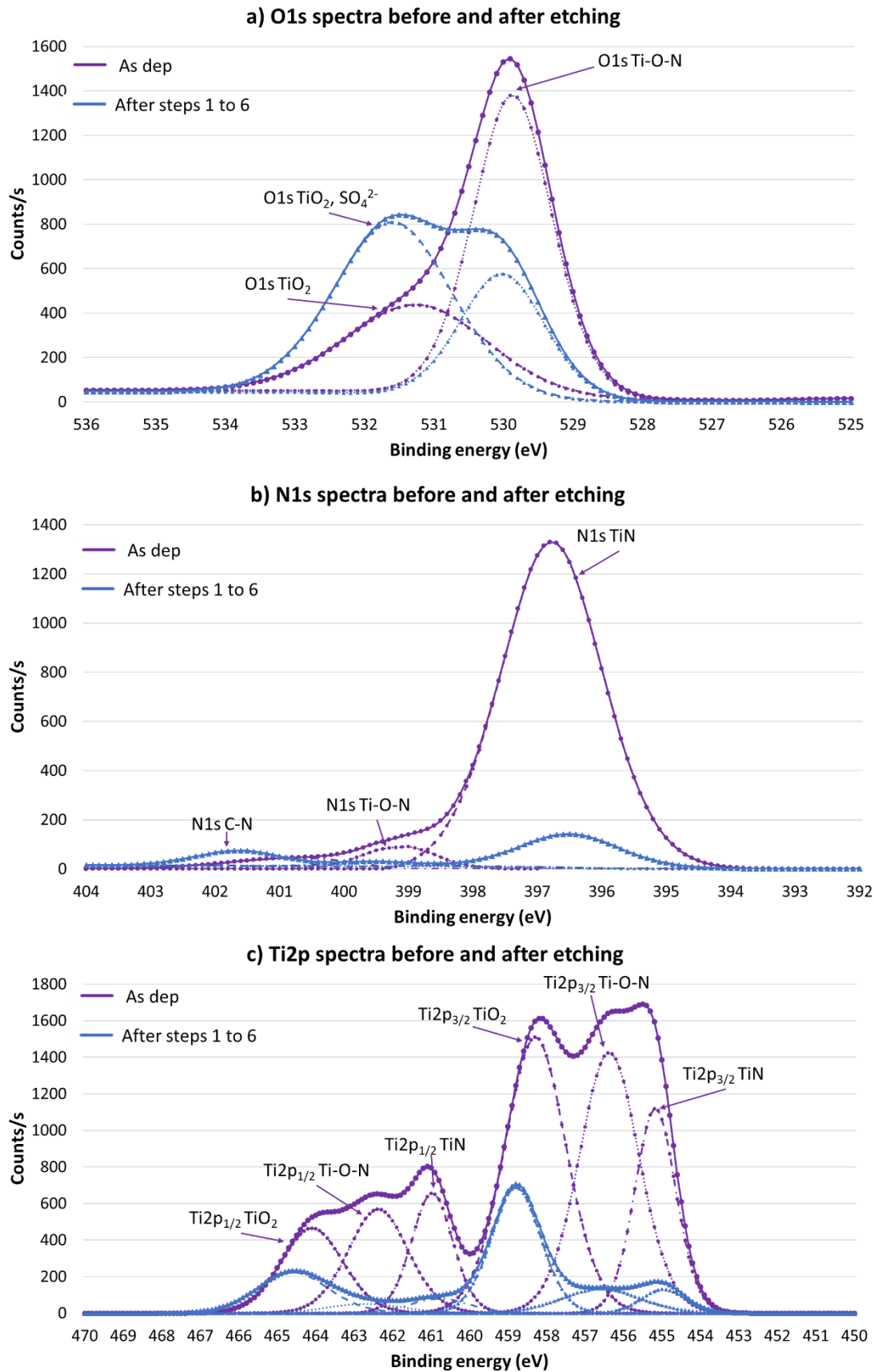


Figure III-8: (a) O1s, (b) N1s and (c) Ti2p *ex-situ* XPS spectra for the TiN surface before and after the sequence of etching and deposition steps 1 to 6 present on the ACE flow. The results correspond to an incident angle of 23.75°.

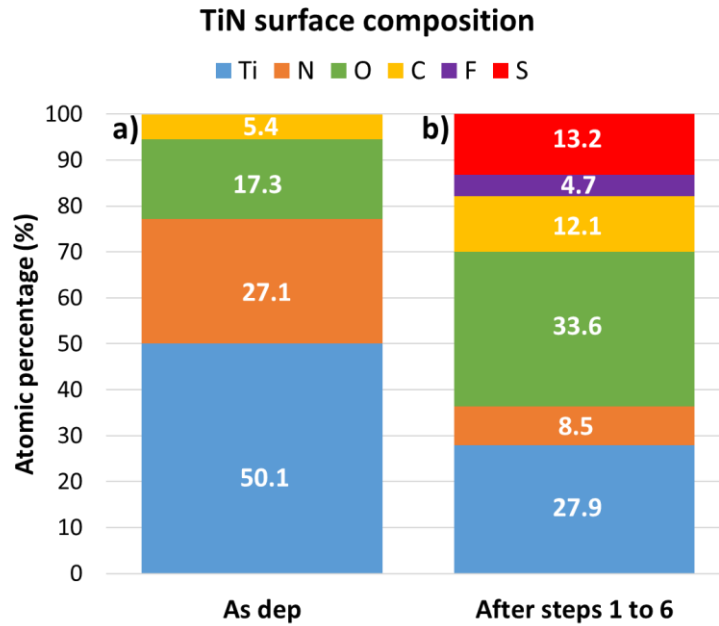


Figure III-9: TiN surface composition determined by *ex-situ* XPS (a) before and (b) after the sequence of etching and deposition steps 1 to 6 present on the ACE flow. The results correspond to an incident angle of 23.75°.

III.2.1.2 Contact angle and surface energy measurements

Contact angle measurements are performed on the TiN surface before and after the sequence of etching and deposition steps. The OWRK method described in Chapter II.3.1.3 is applied to calculate the surface energy of the TiN surface. The results for the surface energy γ and its dispersive (γ_d) and polar (γ_p) components are summarized in Table III-2, so that:

$$\gamma = \gamma_d + \gamma_p$$

Equation III-1: The surface energy (γ) corresponds to the sum of its dispersive (γ_d) and polar (γ_p) components.

Previous studies have shown that the surface energy's polar component is the one that best indicates the surface affinity between the neutral layer and the substrate [Claveau 2017]. These studies show that a substrate with a polar component close to 5 mN/m is attractive to the PS-*r*-PMMA, which composes the neutral layer used for the ACE process and presents a similar polar component.

Therefore, it is important to observe that the sequence of etching and deposition steps presented in Table III-2 induces a significant increase of the surface energy's polar component, which goes from 6.5 mN/m for the pristine TiN to approximately 33.5 mN/m for the TiN after steps 1 to 6. At first glance, this means that the TiN surface is probably not favorable to the adherence of the neutral layer after the sequence of etching and deposition steps.

Table III-2: TiN surface energy before and after the sequence of etching and deposition steps 1 to 6, calculated by contact angle measurements, as well as its dispersive and polar components.

Step	Surface energy γ (mN/m)	Dispersive component γ_d (mN/m)	Polar component γ_p (mN/m)
As deposited TiN	43.8	37.3	6.5
After steps 1 to 6	78.3	44.8	33.5

III.2.1.3 Effect of the wet spacer removal step on the neutral layer adherence

Following the ACE process flow, the next two steps after SOC removal are the neutral layer deposition (step 7) and spacer removal through HF wet etching (step 8). The neutral layer resistance to the HF wet etching is one of the most important parameters that must be verified in order for the ACE process to work. Failure to conserve the neutral layer after wet etching might induce various types of self-assembly defects of the block copolymer, such as the ones presented in Figure III-6.

Therefore, the goal is to verify the adherence of the neutral layer over the TiN surface modified by the sequence of etching and deposition steps. When the substrate presents the adequate surface conditions, the neutral layer adheres to the substrate and cannot be removed through HF dip. For this study, the xNL neutral layer is deposited over the TiN hard mask after steps 1 to 6, using the conditions described in section III.1(7). The neutral layer thickness after deposition is measured by ellipsometry. Finally, the 300 mm wafers are submitted to the HF dip with a 1% dilution using two different times in order to evaluate their impact: 15 and 60 seconds. The neutral layer thickness after HF dip is once again measured by ellipsometry.

Table III-3 presents the results obtained for the neutral layer thickness before and after HF wet etching for both the pristine TiN surface and the surface after steps 1 to 6 in order to be able to compare. For the pristine TiN surface, identified as “as deposited”, Table III-3 shows that the neutral layer thickness is the same before and after HF dip, regardless of its duration, which means that the surface state of the pristine TiN is favorable to the adherence of the neutral layer and allows the vertical alignment of the block copolymer during step 10. As shown in Table III-2, the pristine TiN surface presents a polar component of 6.5 mN/m. Therefore, this confirms what has been observed in previous studies and was presented in the previous section: a substrate with a polar component close to 5 mN/m is attractive to the PS-*r*-PMMA which composes the neutral layer [Claveau 2017].

Regarding the TiN surface after the sequence of etching and deposition steps 1 to 6, Table III-3 shows that the neutral layer thickness is reduced from 8.9 to 6.5 nm after HF dip for 15 seconds, meaning the xNL was partially removed during the wet etching. It also shows that after the longer HF dip of 60 seconds the xNL was completely removed, with its thickness reduced to zero. Figure III-10 presents cross-section SEM images of the surface after HF dip for 15 and 60 seconds. After 15 seconds, neutral layer lift-off spots are visible, while after 60 seconds these spots are no longer visible due to the xNL being completely removed. These results indicate that the TiN surface after the sequence of etching and deposition steps present in the ACE process is not favorable to the neutral layer’s adherence and, as a result, the neutral layer is removed through a lift-off process when exposed to a HF dip. Therefore, we can conclude that the defects observed in Figure III-6 are probably a consequence of the lift-off of

the neutral layer during HF dip (step 8). This means the actual sequence of etching steps is not adapted for the ACE integration flow.

Table III-3. Neutral layer thickness measured by ellipsometry before and after 15 and 60 seconds of HF dip when deposited over the TiN before and after steps 1 to 6.

Neutral layer thickness (nm)	Before HF (nm)	After HF for 15s (nm)	After HF for 60s (nm)
As deposited TiN	7.0 ± 0.3	7.0 ± 0.3	7.0 ± 0.3
TiN after steps 1 to 6	8.9 ± 1.0	6.5 ± 1.2	0.0 ± 0.0

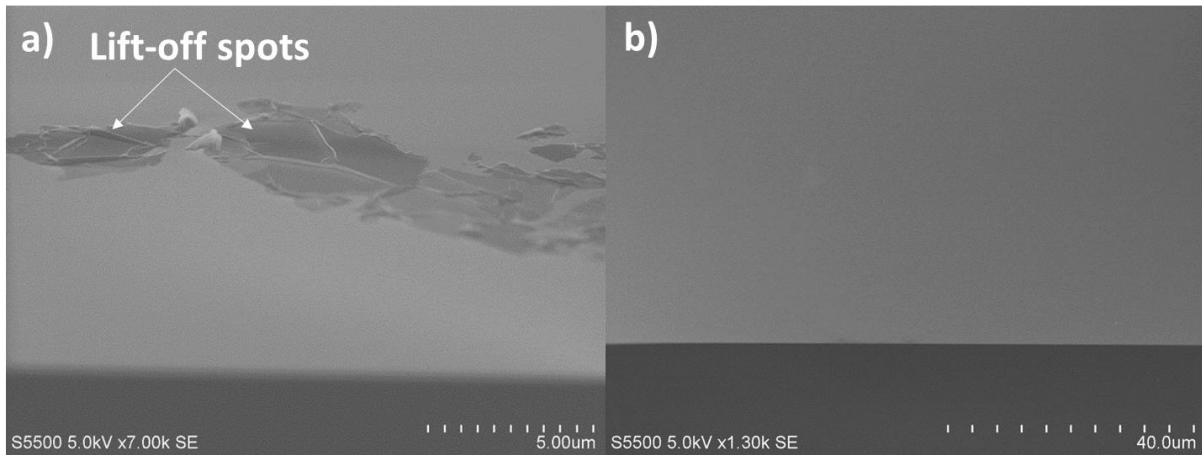


Figure III-10: Cross-section SEM image of the TiN + xNL surface after steps 1 to 6, neutral layer deposition and HF wet etching, indicating (a) the neutral layer lift-off spots after HF for 15 seconds and (b) the TiN surface after complete xNL removal using 60 seconds of HF.

In this section, we investigated the impact of the sequence of etching and deposition steps 1 to 6 of the ACE flow on the TiN surface using blanket wafers. XPS analysis showed that, after the sequence of etching and deposition steps, the TiN surface was highly oxidized and also presented around 13% of sulfur, represented by TiO_xS_y and SO_4^{2-} peaks. Contact angle measurements were performed to determine the surface energy of TiN. After steps 1 to 6, we observed that the polar component of the TiN surface energy is five times higher than the one for the as deposited TiN, which indicated that the TiN surface after the sequence of etching and deposition steps was probably not favorable to the adherence of the neutral layer.

The next experiment consisted in measuring the neutral layer thickness before and after HF wet etching. For the neutral layer deposited over non-modified TiN, there was no difference in thickness before and after HF. However, for the neutral layer deposited over the TiN after steps 1 to 6, depending on the duration of the HF dip, the neutral layer was either partially or completely removed. For the partially removed neutral layer, lift-off spots were observed on the TiN surface. Therefore, we concluded that the defects observed in the patterned wafer after ACE flow are probably a consequence of the lift-off of the neutral layer during HF dip. This means the actual sequence of etching steps is not adapted for the ACE integration flow.

III.2.2 Effect of each etching step on the TiN surface

In order to identify which etching step is not adequate for the ACE flow integration, the TiN blanket wafers have been exposed to each etching step, taken separately: trilayer plasma etching (step 2b), SiARC removal by HF wet etching (step 3), SiN spacer plasma etching (step 5) and SOC removal (step 6). Section III.1 already presented the chemistries and parameters used for each etching step. Figure III-11 presents the initial stack used for each of these studies, depending on the etching step that is being investigated. The complete removal of the SOC and SiN layers, when possible, is verified through ellipsometry measurements after etching.

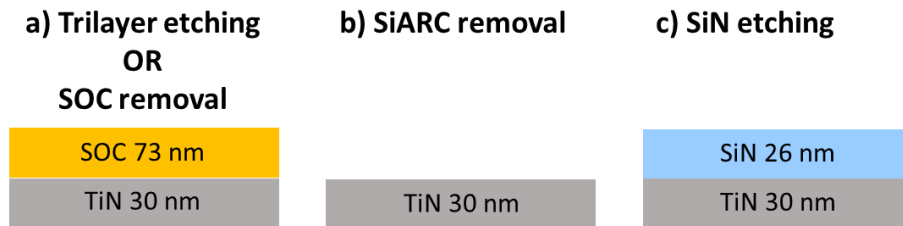


Figure III-11: TiN blanket wafers initial stack used to study each etching step, taken separately: (a) trilayer or SOC etching; (b) SiARC wet removal; and (c) SiN dry etching.

III.2.2.1 Effect of each etching step on the TiN surface composition

Figure III-12 presents the *ex-situ* XPS results obtained for the TiN surface before and after each etching step. Figures III-12(b) and III-12(e) show that the trilayer etching and the SOC removal present a similar result to the one presented in Figures III-8 and III-9 after the sequence of steps 1 to 6: strong increase in the oxygen percentage and decrease of the nitrogen percentage when compared to the pristine TiN surface in Figure III-12(a). This is characterized by the increase of TiO₂ and decrease of TiN and Ti-O-N bonds. They also present a considerable amount of sulfur, represented by TiO_xS_y, SO₄²⁻ and a new S2p_{3/2} peak at 167.2 eV, which might correspond to SO₂ [Salim 2011]. Together they represent around 12 to 15% of the TiN surface. As shown before, the presence of carbon and fluorine is due to contamination from the reactor walls and to the air exposure between the etching and XPS analysis.

Figure III-12 also shows the XPS results after wet etching with HF dip and after SiN spacer etching with CH₂F₂/CF₄/O₂. The surface composition after HF presented in Figure III-12(c) is quite similar to that of the pristine TiN, with only a very small amount of fluorine present, represented by a F1s peak at around 684.8 eV, characteristic of metal fluorides, such as TiF₃. Finally, after SiN spacer etching, even though it contains oxygen, the TiN surface was less oxidized. Indeed, Figure III-12(d) shows that TiN presented a small decrease of around 3 to 7% each for Ti, N and O percentages. This probably happens because the addition of oxygen to the fluorocarbon plasma makes it more energetically favorable to form volatile compounds, such as CO and CO₂, rather than a C_xF_y passivation layer [Mele 1984]. The addition of O₂ therefore increases the concentration of reactive fluorine on the surface of SiN, and thus the formation of volatile SiF₄ can continue without inhibition. The decrease in Ti, N and O percentages is also proportional to the considerable amount of fluorine (13.5%) present in this sample and consisting of TiF₃.

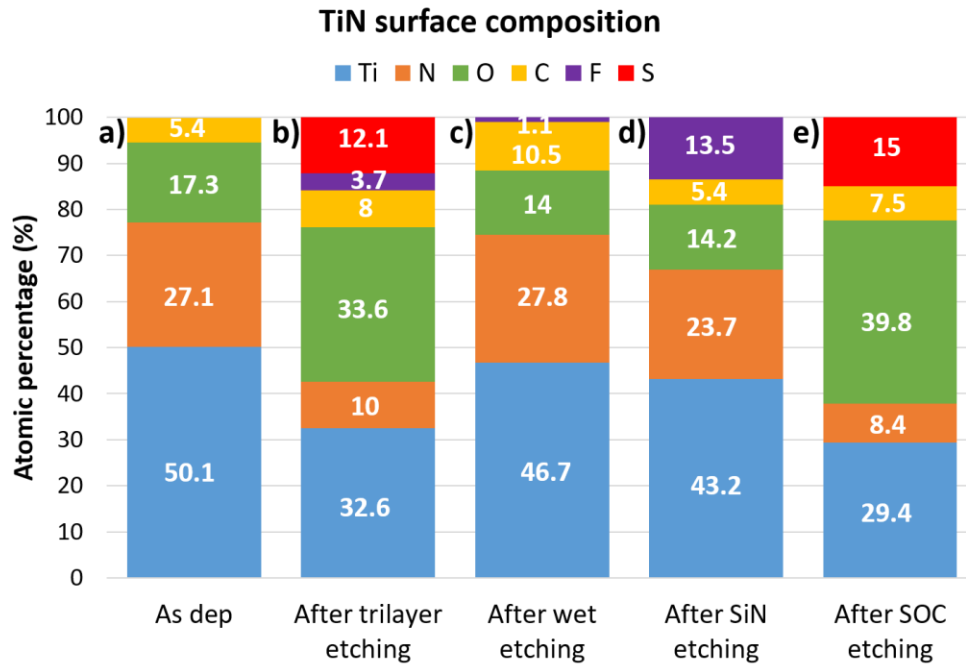


Figure III-12: TiN surface composition determined by *ex-situ* XPS before and after each etching step present on the ACE flow: (a) before etching; (b) after trilayer etching; (c) after SiARC wet etching; (d) after SiN etching; and (e) after SOC removal. The results correspond to an incident angle of 23.75°.

III.2.2.2 Contact angle and surface energy measurements

Like in section III.2.1.2, contact angle measurements are conducted on the TiN surface before and after each etching step. The results for the surface energy γ and its dispersive (γ_d) and polar (γ_p) components are presented in Table III-4. The results are once again similar to the ones observed in Table III-2 for the sequence of steps 1 to 6: every etching step induces a significant increase of the surface energy's polar component. The only exception is the SiN etching, which presents a smaller polar component compared to the other etching steps, but still 3 times higher than that of pristine TiN. This means that the surface energy measurements are not conclusive enough to indicate which etching steps are not adequate for the ACE integration.

Table III-4. TiN surface energy before and after each etching step, calculated by contact angle measurements, as well as its dispersive and polar components.

Step	Surface energy γ (mN/m)	Dispersive component γ_d (mN/m)	Polar component γ_p (mN/m)
As deposited TiN	43.8	37.3	6.5
2b: Trilayer etching	77.4	42.8	34.6
3: SiARC wet etching	77.0	46.0	31.0
5: SiN etching	57.2	36.8	20.4
6: SOC removal	77.3	43.1	34.2

III.2.2.3 Effect of the wet spacer removal step on the neutral layer adherence

As described in section III.2.1.3, the neutral layer is deposited over the TiN surface after each etching step and then submitted to a HF wet etching during 60 seconds in order to evaluate the TiN surface's compatibility to it. The neutral layer thickness is measured before and after HF for each case. The results are presented in Table III-5.

First, it is important to notice that the trilayer etching and the SOC removal, which are both based on SO₂/O₂/He plasma, are the only steps that present a complete removal of the neutral layer after HF wet etching. While for the SiARC wet removal by HF and the SiN etching using a fluorocarbon-based recipe, Table III-5 shows that these steps present the same neutral layer thickness before and after HF etching.

Table III-5. Neutral layer thickness measured by ellipsometry before and after HF wet etching for 60 seconds when deposited over the TiN surface after each etching step.

Neutral layer thickness (nm)	Before HF (nm)	After HF (nm)
TiN after trilayer etching	6.8 ± 0.4	0.0 ± 0.0
TiN after SiARC wet etching	5.8 ± 0.2	5.8 ± 0.2
TiN after SiN etching	5.9 ± 0.3	5.9 ± 0.3
TiN after SOC removal	7.1 ± 0.4	0.0 ± 0.0

The goal of this section was to identify which etching step was not adequate for the ACE flow integration. Thus, the TiN blanket wafers were exposed to each etching step, taken separately. The characterization procedure was similar to the one employed in section III.2.1.

The trilayer etching and the SOC removal, both based on a SO₂/O₂/He plasma, present similar results to the sequence of steps 1 to 6: the TiN surface was highly oxidized and around 14% of sulfur was observed. Moreover, the polar component of the surface energy was five times higher than the one for the as deposited TiN. Finally, the trilayer etching and the SOC removal were the only steps that led to a lift-off of the neutral layer during HF wet etching.

For the SiARC wet etching and the SiN etching, no difference was observed for the neutral layer thickness before and after HF.

Therefore, based on the different results obtained, we concluded that the neutral layer lift-off defects observed after the sequence of etching and deposition steps on both patterned and blanket wafers were most probably caused by the interaction of the SO₂/O₂/He plasma with the TiN surface.

III.2.3 Understanding the effect of the SO₂/O₂/He plasma on the TiN surface and neutral layer deposition

In order to understand the effect of the SO₂/O₂/He plasma on the TiN surface, each gas is applied separately to the TiN blanket wafers, using the same plasma parameters presented in Table III-1(6). Furthermore, the effect of ion bombardment has also been investigated by applying the SO₂/O₂/He plasma with zero RF Bias power and keeping the other parameters constant.

III.2.3.1 Effect of each gas on the TiN surface composition

The *ex-situ* XPS results for the TiN surface are presented in Figure III-13. First, when comparing the SO₂/O₂/He results with the results for each gas, the following is observed: for the SO₂ only presented in Figure III-13(b), the Ti and N percentages are similar to the reference in Figure III-13(a), while the oxygen content sees a decrease of about 4%, which is characterized by a slight reduction of the TiO₂ peak. The sulfur percentage is also slightly lower and the SO₂ peak at 167.2 eV is no longer present. As for the O₂ only, Figure III-13(c) shows a significant increase of the titanium percentage due to the increase of the TiO₂ peak intensity. There is also an important reduction of the nitrogen percentage, which is represented by the decrease of the TiN peak intensity. Finally, for the He only in Figure III-13(d), there is an increase of both Ti and N percentages, characterized by an augmentation of the TiN and Ti-O-N peaks intensity. It is also possible to observe a decrease of the oxygen percentage, consequence of the decrease of the TiO₂ peak intensity. As expected, sulfur is no longer present on the TiN surface after O₂ only and He only. For all conditions, the carbon, fluorine and chlorine contamination comes from the etching reactor walls.

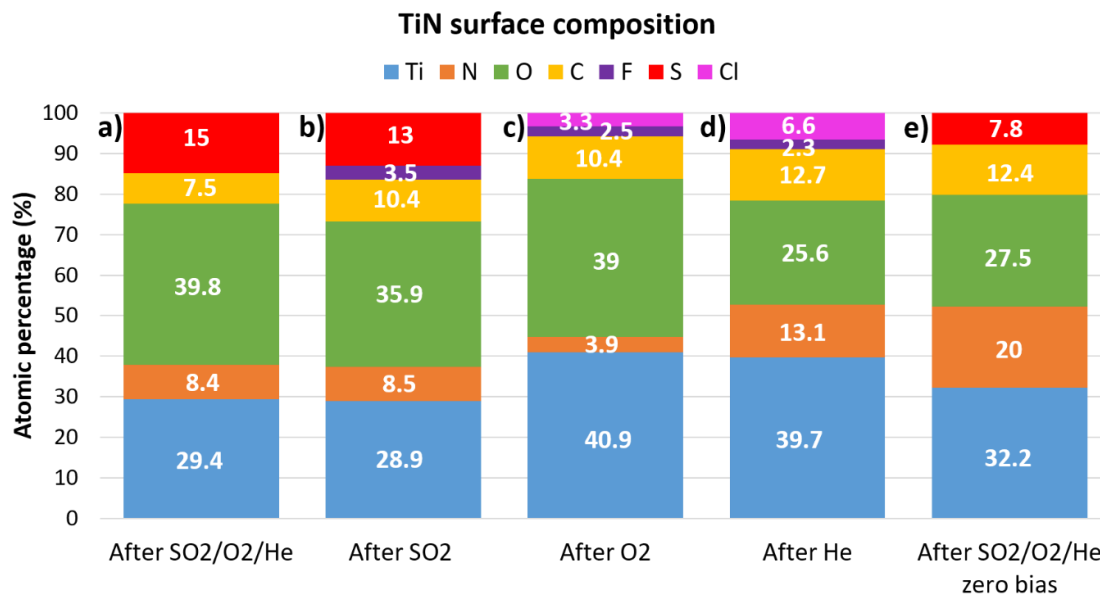


Figure III-13: TiN surface composition determined by *ex-situ* XPS: (a) after SO₂/O₂/He (reference); (b) after SO₂ only; (c) after O₂ only; (d) after He only; and (e) after SO₂/O₂/He without RF bias power. The results correspond to an incident angle of 23.75°.

Figure III-13(e) presents the results after etching using SO₂/O₂/He without RF bias power. When compared to the results with RF Bias in Figure III-13(a), several changes can be noticed: the nitrogen content is increased by about 11.6% compared to the same chemistry with bias,

which is characterized by an increase of the TiN peak. A significant decrease of the oxygen percentage of at least 12% is also observed, consequence of the decrease of the TiO₂ peak intensity. Moreover, it shows a slight increase of the Ti percentage, which is a combination of the TiN peak intensity augmentation and the TiO₂ peak intensity reduction. Finally, a sulfur percentage decrease of 7.2% is observed and the TiO_xS_y and SO₂ peaks are no longer present. This means that, for the zero bias etching, the thickness of the TiN layer modified by the plasma is smaller compared to that of the reference SO₂/O₂/He SOC removal process.

Ion implantation simulations using the software SRIM confirm this observation. For these simulations, the stack was defined as 150 Å of TiN with 30 Å of TiO₂ over it. The ion energy was varied between 10 and 500 eV, where 10 eV is an approximation for the zero RF bias condition and 250 eV is an approximation for the SO₂/O₂/He reference (RF bias = -250 V). For each condition, 100000 ions have been implanted. The graphs in Figure III-14 represent the number of sulfur (a) and helium (b) ions implanted for the different energies investigated as a function of the TiO₂ and TiN thickness. For the “zero bias” condition, both sulfur and helium ions are restrained to the first 10 to 20 Å of the TiO₂ layer. However, for the 250 eV condition, some sulfur ions reach the TiN layer and the total modified thickness is around 40 Å while most of the helium ions are present in the TiN layer and the total modified thickness corresponds to approximately 83 Å.

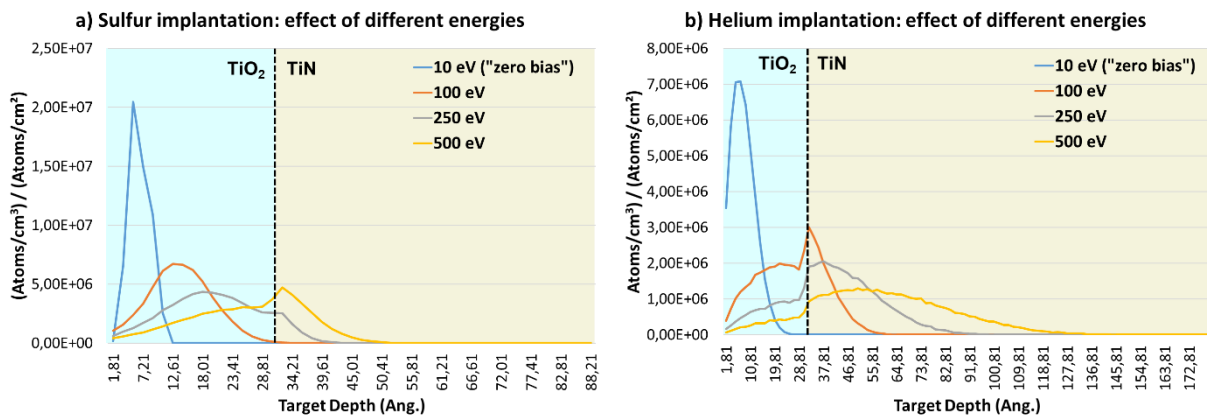


Figure III-14: Simulation showing the effect of different ion energies on the implanted thickness for (a) sulfur and (b) helium ions on a TiO₂ + TiN stack.

Furthermore, Time-of-Flight Secondary Ion Mass Spectrometry (ToF-SIMS) analysis have also been conducted on these samples to determine the concentration of sulfur, oxygen, fluorine and chlorine as a function of the sample thickness and compare the results to those obtained using XPS. Indeed, XPS analysis quantify an element on a larger volume (approximately 10 nm x π x 200 μm x 200 μm) than ToF-SIMS (1 nm x 90 μm x 90 μm). Therefore, XPS analysis average the signal over 10 nm while ToF-SIMS gives a value within 1-2nm. Moreover, ToF-SIMS is able to detect light elements, such as helium. However, during our analysis, no helium was detected, meaning it presented low ionization yield and probably little implantation into the TiN surface.

The ToF-SIMS results are presented in Figure III-15. The sulfur profile in Figure III-15(a) confirms what has been indicated by both the *ex-situ* XPS analysis and the ion implantation simulation: for the SO₂/O₂/He with zero bias, the thickness of the modified layer is thinner than for the same chemistry with -250 V bias.

For the oxygen profile presented in Figure III-15(b), due to the O^- saturation on the TiN extreme surface for every sample, we have chosen to use the molecular fragment OH^- instead, whose attribution is the most reliable and whose ionization yields are considered good. The results are as expected: the O_2 only sample presents a thicker TiO_2 layer (around 4 nm) compared to the other samples, followed by $SO_2/O_2/He$ and SO_2 only (around 2 nm). As has been shown before, the $SO_2/O_2/He$ without bias presents a thinner modified layer (around 1 nm). The He only sample, however, presents a higher oxygen content than expected based on the XPS results. One possible explanation for this difference between the two results is the air exposure duration. While XPS analysis were conducted at the most 5 hours after sample etching, ToF-SIMS samples waited 24 hours between etching and analysis, meaning they had more time to oxidize.

Finally, for the fluorine (c) and chlorine (d) profiles, it should be noticed that excess oxygen increases the ionization yield of Cl^- and F^- ions, which explains their significant presence in the O_2 only and He only samples. Fluorine and chlorine contamination is also more visible for these two samples due to the lower total flow when O_2 and He are taken separately (maximum 50 sccm). Therefore, the ToF-SIMS results confirm the observations made with XPS.

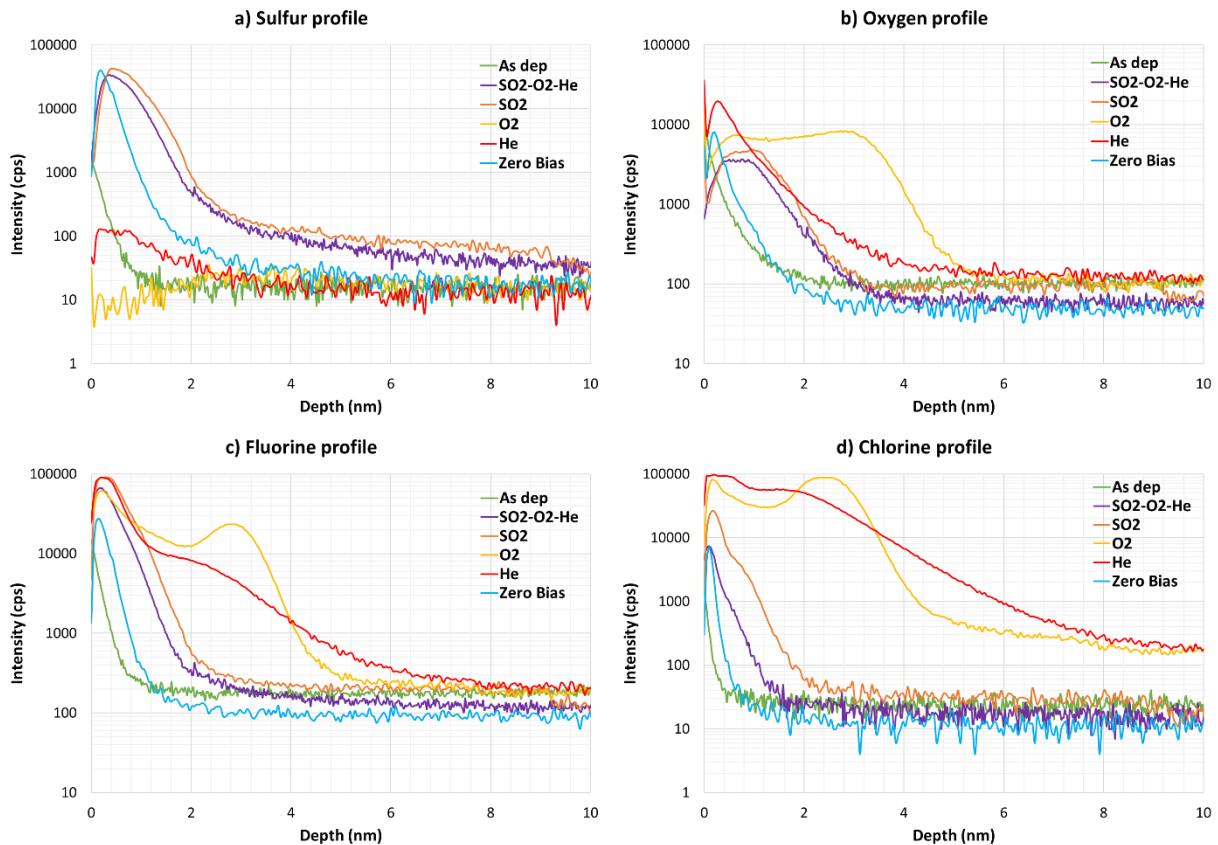


Figure III-15: ToF-SIMS analysis for (a) sulfur (S^-), (b) oxygen (OH^-), (c) fluorine (F^-) and (d) chlorine (Cl^-) concentration as a function of the sample thickness (depth).

III.2.3.2 Contact angle and surface energy measurements

Contact angle measurements have also been conducted for these samples. Table III-6 presents the surface energy results for the different gases applied individually and for the zero bias etching. All results are similar to the $SO_2/O_2/He$ SOC removal, with the surface energy

varying between 1 and 3% regarding the reference value (77.3 mN/m). Moreover, the polar component varies between 1.5 and 14% compared to the SO₂/O₂/He reference (34.2 mN/m) and is at least 4 times higher than the pristine TiN polar component (6.5 mN/m). Therefore, these measures are not conclusive enough for understanding the effect of each gas on the TiN surface and neutral layer adherence.

Table III-6. TiN surface energy as well as its dispersive and polar components calculated by contact angle measurement before and after SO₂/O₂/He, SO₂ only, O₂ only, He only and SO₂/O₂/He without RF bias power.

Etching	Surface energy γ (mN/m)	Dispersive component γ_d (mN/m)	Polar component γ_p (mN/m)
As deposited TiN	43.8	37.3	6.5
SO ₂ /O ₂ /He	77.3	43.1	34.2
SO ₂ only	78.4	44.7	33.7
O ₂ only	74.9	45.6	29.3
He only	79.0	47.2	31.8
SO ₂ /O ₂ /He zero bias	78.3	45.0	33.3

III.2.3.3 Effect of the wet spacer removal step on the neutral layer adherence.

Finally, in order to verify the adherence of the neutral layer over the TiN surface for the different conditions investigated, the neutral layer deposition and HF wet etching have been conducted following the same procedure described in the previous sections. The thickness measurement results are presented in Table III-7. After SO₂ only and SO₂/O₂/He with zero bias, the neutral layer is almost completely removed after wet etching. As for the O₂ only and He only samples, no significant thickness variation is observed after HF.

Table III-7. Neutral layer thickness measured by ellipsometry before and after 60 seconds of HF wet etching when deposited over the TiN surface etched using SO₂/O₂/He, SO₂ only, O₂ only, He only, and SO₂/O₂/He without RF bias power.

Neutral layer thickness (nm)	Before HF (nm)	After HF (nm)
SO ₂ /O ₂ /He	7.1 ± 0.4	0.0 ± 0.0
SO ₂ only	8.2 ± 0.5	0.5 ± 0.2
O ₂ only	9.2 ± 0.4	9.3 ± 0.5
He only	6.3 ± 0.6	6.5 ± 1.1
SO ₂ /O ₂ /He zero bias	7.0 ± 0.5	0.9 ± 0.2

In order to understand the effect of the SO₂/O₂/He plasma on the TiN surface, each gas was applied separately to the TiN blanket wafers, while keeping the other plasma parameters constant.

The results led us to conclude that, while the oxygen alone highly oxidizes the TiN surface and increases its surface energy, it did not have a significant negative effect on the neutral layer adherence, thus allowing this layer to resist the HF wet etching step. The same was observed for the helium: based on the ellipsometry measurements, it did not seem to prevent the adherence of the neutral layer.

The effect of ion bombardment was also investigated by applying the SO₂/O₂/He plasma with zero RF Bias power and keeping the other parameters constant. However, this parameter did not seem to be the most significant either. Without RF Bias, even though the TiN modified layer was thinner when compared to the same process with Bias, the neutral layer was still almost completely removed, which means the SO₂/O₂/He SOC removal chemistry is not adapted to the chemo-epitaxy application.

Finally, it was the SO₂ alone that presented the TiN surface composition the most similar to the TiN after SO₂/O₂/He. It also failed to conserve the neutral layer during HF wet etching, leading to its lift-off. Therefore, we concluded that the SO₂ molecule was the main responsible for this recipe's inadequacy to the ACE flow.

III.2.4 Understanding the interaction mechanism between SO₂/TiN/xNL/HF that leads to the neutral layer lift-off

Now that we have determined the SO₂ to be the main responsible for the xNL lift-off during HF wet etching, this section shall focus on understanding the interaction mechanisms between the SO₂ plasma, the TiN surface, the xNL deposition and the HF wet etching that ultimately leads to the lift-off of said neutral layer.

III.2.4.1 Impact of TiN modified layer

We first decided to verify the role of the modified layer that is formed on the TiN surface after SO₂/O₂/He SOC removal, which consists of TiO₂/TiO_xS_y/SO₄²⁻ according to XPS results previously shown. Our goal is to remove the modified layer before depositing the xNL and then evaluate the neutral layer adherence. Thus, before xNL deposition, we chose to perform an HF wet etching, which is known to remove the TiO₂ native oxide without removing the TiN, following the reaction [Lee 2017]:



The schematics for this experience can be found in Figure III-16. We used a TiN blanket wafer on which a 73-nm SOC layer was deposited. The SOC layer was then removed using the SO₂/O₂/He plasma. However, before depositing the neutral layer, an HF wet etching was conducted during 60 seconds to remove the modified TiO₂/TiO_xS_y/SO₄²⁻ layer on the TiN surface. The native TiO₂ layer was reformed on the TiN surface right after HF etching due to the air exposure. Then, the xNL was spin-coated and annealed over the TiN surface and another HF dip was conducted for 60 seconds after xNL deposition.

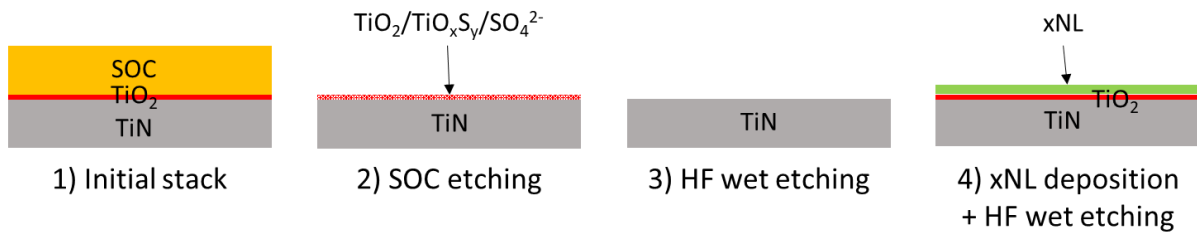


Figure III-16: Schematics for the experience conducted in order to verify the impact of the modified layer formed on the TiN surface after SOC etching.

Thickness measurements for the TiN, SOC and neutral layer after each step can be found in Table III-8. The SOC thickness measurement is used to confirm the complete SOC removal using the $\text{SO}_2/\text{O}_2/\text{He}$ plasma (step 2) before moving on to the first HF wet etching (step 3). The TiN ellipsometry measurements also include the native oxide layer on the TiN surface, as well as the modified layer after etching. This should explain the larger uncertainty in the measurements observed for TiN (between 1.0 and 1.2 nm) when compared to the SOC and xNL (around 0.2 nm). Considering the difficulty of fitting for metallic materials such as TiN, along with the probable change in refractive index of the surface layer before and after etching and the reduced thickness of the modified $\text{TiO}_2/\text{TiO}_x\text{S}_y/\text{SO}_4^{2-}$ layer estimated to be around 2 or 3 nm, the TiN thickness measurements shall only be used comparatively and cannot be considered quantitatively accurate.

Nevertheless, after step 3, we observe a decrease on TiN thickness of about 2.1 nm, which indicates that the $\text{TiO}_2/\text{TiO}_x\text{S}_y/\text{SO}_4^{2-}$ layer has been removed through HF wet etching. *Ex-situ* XPS analysis were conducted immediately after the first HF wet etching (step 3) to confirm this and the results are presented in Figure III-17. When comparing the XPS results after $\text{SO}_2/\text{O}_2/\text{He}$ plasma shown in Figure III-17(b) and the ones after the first HF treatment shown in Figure III-17(c), we are able to confirm the consumption of the modified $\text{TiO}_2/\text{TiO}_x\text{S}_y/\text{SO}_4^{2-}$ layer, since sulfur is no longer present and the oxygen percentage is decreased by around 30%.

Table III-8. TiN, SOC and neutral layer thicknesses measured by ellipsometry after each step presented in Figure III-16.

Step	TiN thickness (nm)	SOC thickness (nm)	xNL thickness (nm)
1: Initial stack	18.1 ± 1.0	72.4 ± 0.2	-
2: $\text{SO}_2/\text{O}_2/\text{He}$ etching	18.2 ± 1.2	0.0 ± 0.0	-
3: HF wet etching	16.1 ± 1.0	-	-
4: xNL deposition	17.1 ± 1.0	-	9.6 ± 0.2
5: HF wet etching	17.1 ± 1.0	-	9.7 ± 0.3

Finally, Table III-8 shows that, by introducing an HF wet etching step between the SOC removal and the xNL deposition, the xNL is not removed by the second HF treatment, which confirms the negative effect of the $\text{TiO}_2/\text{TiO}_x\text{S}_y/\text{SO}_4^{2-}$ layer on the adhesion of the neutral layer.

However, while the addition of an HF wet etching step is one solution to avoid the neutral layer lift-off issue, it cannot be applied to the ACE chemo-epitaxy flow. Indeed, along with the $\text{TiO}_2/\text{TiO}_x\text{S}_y/\text{SO}_4^{2-}$ layer, the HF would also remove the SiN spacers before the xNL could be deposited, thus going against the principles of the ACE integration. Other solutions to avoid lift-off which are compatible with the ACE flow shall be presented in section III.3.

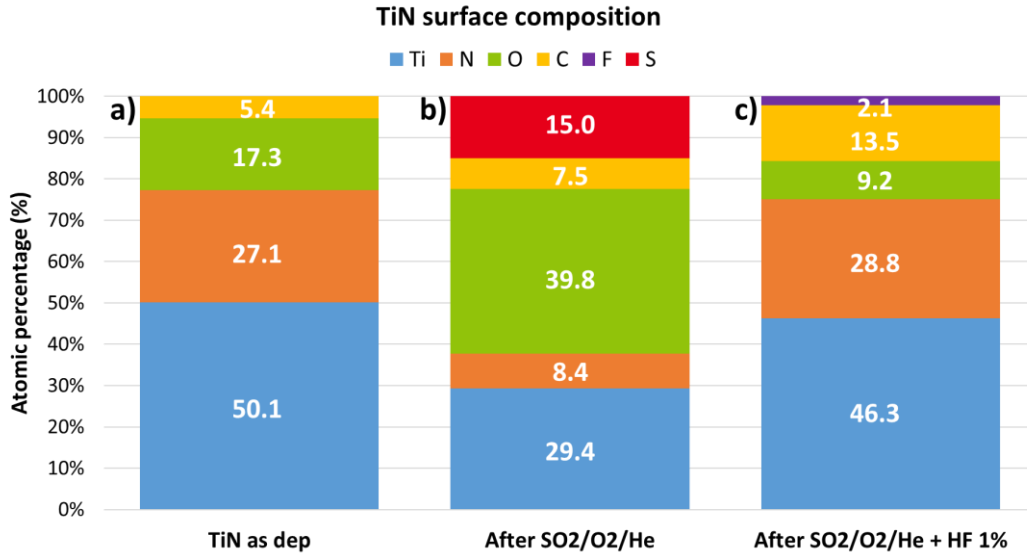


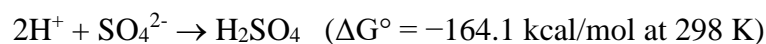
Figure III-17: TiN surface composition determined by *ex-situ* XPS: (a) before etching; (b) after $\text{SO}_2/\text{O}_2/\text{He}$ plasma; and (c) after $\text{SO}_2/\text{O}_2/\text{He}$ plasma and HF wet etching. The results correspond to an incident angle of 23.75° .

III.2.4.2 First hypothesis: H_2SO_4 formation on the TiN surface

Based on the results obtained until now, we have proposed some mechanism hypothesis for the neutral layer lift-off and we will verify then over the next three sections.

Hypothesis #1: SO_4^{2-} ions on the TiN surface recombine with the H^+ ions of the HF wet etching to form sulfuric acid (H_2SO_4), which removes the neutral layer.

The schematics for the first hypothesis are presented in Figure III-18. It is based on the recombination of the H^+ ions of the HF with the SO_4^{2-} ions observed on the surface of the TiN after any plasma etching based on SO_2 , therefore forming H_2SO_4 , which could then remove the neutral layer. The reaction for H_2SO_4 formation is:



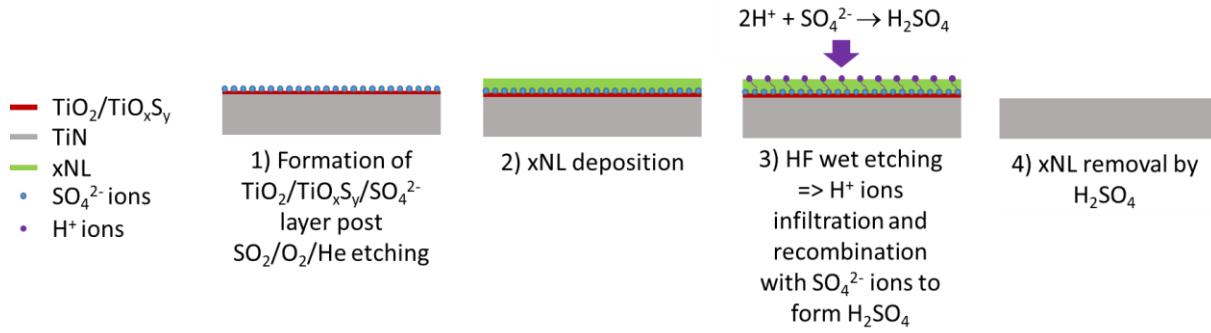


Figure III-18: Schematics for hypothesis #1, highlighting the infiltration of the H⁺ ions and recombination with SO₄²⁻ ions to form H₂SO₄ and remove the xNL.

In order to verify this theory, two experiences were conducted. The first one consisted on etching the SOC layer deposited over the TiN blanket wafer using SO₂/O₂/He, then deposit and anneal the neutral layer and, finally, rinse the wafer with demineralized water during 60 seconds. Demineralized water is known to dissociate into H⁺ and OH⁻, therefore, if this rinsing removes the neutral layer, it would indicate an ion recombination on the surface of the TiN. However, the results in Table III-9 show that the neutral layer thickness does not change after water rinsing.

Table III-9. Neutral layer thickness measured by ellipsometry before and after 60 seconds of rinsing using demineralized water.

Neutral layer thickness (nm)	Before water rinsing (nm)	After water rinsing (nm)
TiN after SO ₂ /O ₂ /He	7.2 ± 0.6	7.2 ± 0.6

The results from the first experience left us to wonder:

- 1) If the H⁺ ion concentration was insufficient to lead to recombination; or
- 2) If the H⁺ ions could not pass through the neutral layer; or
- 3) If the H₂SO₄ would even be able to remove the xNL in case it is formed.

Therefore, the goal of the second experience was to verify if the H₂SO₄ would be able to remove the neutral layer. The xNL was therefore deposited on two TiN blanket wafers: one before etching and the other after SO₂/O₂/He etching. Afterwards the wafers were cleaved to obtain 9 x 9 cm samples that were then dipped into an H₂SO₄ bath with concentration 96% at room temperature for 60 seconds. We have chosen to evaluate the effect of H₂SO₄ at room temperature in order to simulate the conditions during HF wet etching, which is also conducted at room temperature.

The results on Table III-10 show that the neutral layer thickness does not present a significant change after H₂SO₄. However, it should be noticed that its surface is still modified because the water contact angle (WCA) after H₂SO₄ is measured between 54.6 and 55.9°, which is different from the reference value for the xNL (WCA = 76.6° ± 0.3°).

Table III-10. Neutral layer thickness measured by ellipsometry before and after 60 seconds inside an H₂SO₄ bath at room temperature, as well as the water contact angle measured after H₂SO₄.

Neutral layer thickness (nm)	Before H ₂ SO ₄ (nm)	After H ₂ SO ₄ (nm)	WCA after H ₂ SO ₄
TiN as dep	7.1 ± 0.2	7.5 ± 0.4	55.9° ± 0.4°
TiN after SO ₂ /O ₂ /He	7.3 ± 0.5	7.7 ± 0.6	54.6° ± 0.2°

Figure III-19 shows the cross-section SEM images after H₂SO₄ during 60 seconds for both wafers. Due to the neutral layer's very small thickness and to its sensitivity to the electron beam from the SEM, it is not possible to measure its real thickness using these SEM images. Nevertheless, the cross-section images indicate that the xNL surface after H₂SO₄ is slightly rough, which may explain the slight increase in thickness (around 0.4 nm) measured by ellipsometry after H₂SO₄.

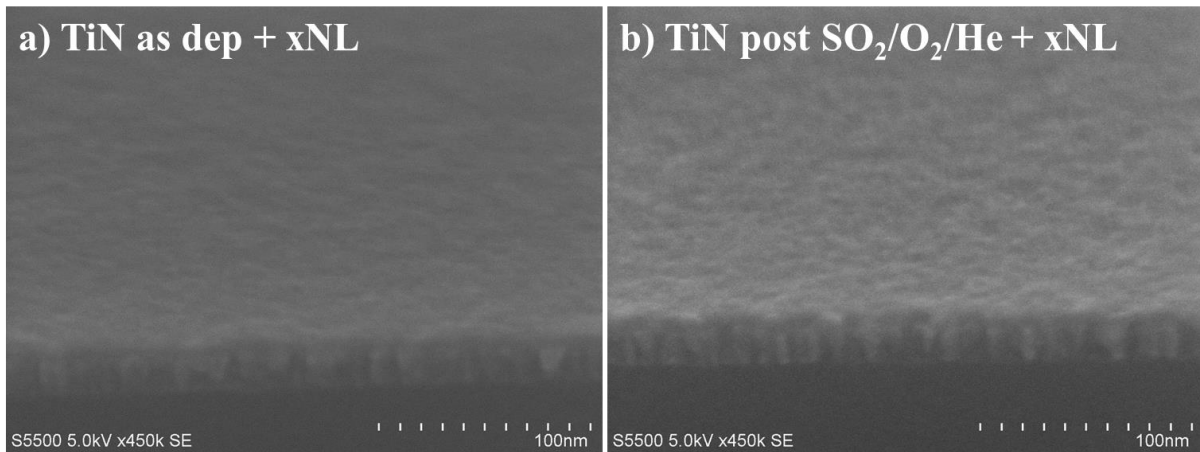


Figure III-19: Cross-section SEM images of the xNL surface after H₂SO₄ during 60 seconds for the xNL deposited over TiN (a) before etching; and (b) after SO₂/O₂/He plasma.

Moreover, we have also evaluated a longer H₂SO₄ exposure, leaving the wafer inside the bath for 5 minutes instead of 60 seconds, but the results were similar. These results allow us to conclude that the H₂SO₄ does not spontaneously remove the neutral layer at room temperature.

Finally, concerning observation 2 – “can the H⁺ ions pass through the neutral layer?” –, it should be noticed that if HF were capable of passing through the cross-linked neutral layer to interact with the TiN surface, it should remove the TiO₂ layer even for other plasma chemistries and for the pristine TiN. And if it did remove the TiO₂, then the xNL should also be removed through lift-off. However, we have seen in sections III.2.1.3 and III.2.2.3 that in most cases the xNL resists the HF wet etching, which indicates that the HF does not pass through the neutral layer in normal conditions. Therefore, based on all the results and observations presented, hypothesis #1 has been eliminated.

III.2.4.3 Second hypothesis: pore formation on the neutral layer

When Salim *et al.* studied the preparation of TiO₂ nanoparticles from hydrolysis reaction of TiOSO₄, they observed the adsorption of SO₄²⁻ ions on the surface of TiO₂ through XPS

analysis. They also observed that the intensity of the XPS peak corresponding to the SO_4^{2-} ions decreases with a post-treatment consisting of annealing during 1 hour at 600°C , indicating that the annealing provides the energy necessary not only for the growth of the grains but also for the desorption of the residual ions on the surface of the TiO_2 . Finally, due to this ionic desorption, internal pores are formed inside the TiO_2 nanoparticles [Salim 2011].

Hypothesis #2: desorption of SO_4^{2-} ions during annealing of the neutral layer could form pores inside the xNL, which would facilitate the infiltration of the HF. The HF would then remove the modified $\text{TiO}_2/\text{TiO}_x\text{S}_y$ layer formed on the TiN surface, thus reducing the neutral layer adherence to the TiN hard mask and allowing its consequent lift-off.

Therefore, our second hypothesis is based on the desorption of the SO_4^{2-} ions – which are observed on the surface of the TiN after SO_2 -based etching – during the annealing of the neutral layer at 250°C . This would form internal pores inside the xNL, thus allowing the HF to pass through and remove the modified $\text{TiO}_2/\text{TiO}_x\text{S}_y$ layer on the TiN surface. By removing this modified layer, the neutral layer adherence to the TiN hard mask is reduced, allowing its consequent lift-off. The schematics for this hypothesis can be found in Figure III-23.

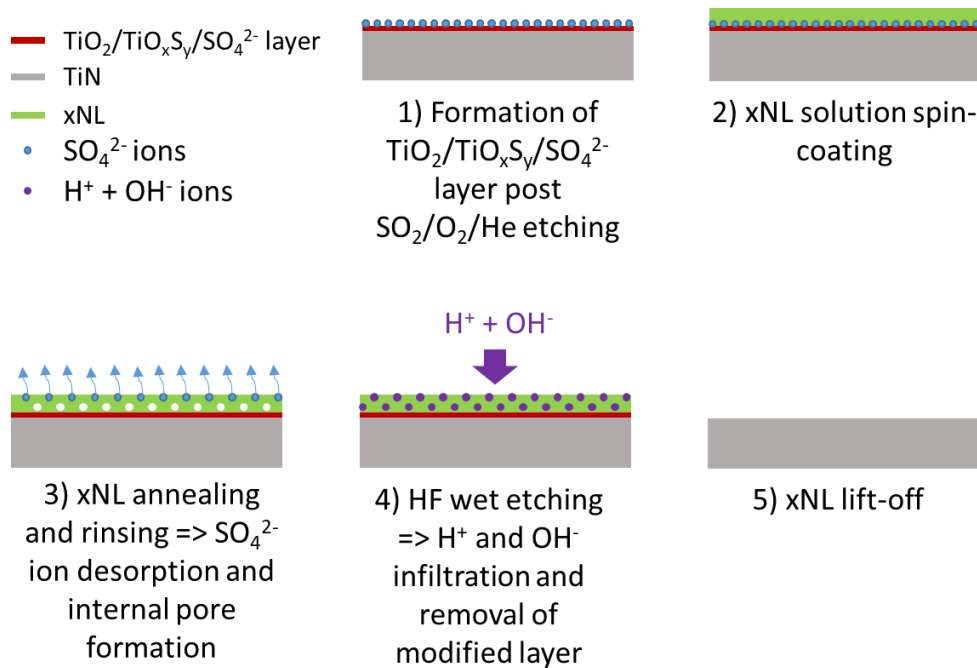


Figure III-20: Schematics for hypothesis #2, highlighting the desorption of SO_4^{2-} ions during annealing of the neutral layer and the consequent formation of internal pores inside the xNL. These pores facilitate the infiltration of the H^+ and OH^- ions and the removal of the modified $\text{TiO}_2/\text{TiO}_x\text{S}_y$ layer formed on the TiN surface, thus reducing the neutral layer adherence to the TiN hard mask and allowing its consequent lift-off.

In order to verify this hypothesis, TiN blanket wafers after SOC removal using $\text{SO}_2/\text{O}_2/\text{He}$ are introduced in the Sokudo DUO 300 mm track dedicated to xNL deposition. However, instead of depositing the neutral layer, one of the wafers goes through the annealing at 250°C for 5 minutes and is then removed from the track while the other wafer goes through the same annealing and also the PGMEA rinsing. The surface composition of these wafers is analyzed

through XPS to verify the presence of the SO_4^{2-} ions after annealing and annealing + rinsing. The distribution of sulfur S2p peaks on the TiN surface for each sample is shown in Figure III-21. By comparing the results after etching (a), after annealing (b) and after rinsing (c), there is no significant variation of the SO_4^{2-} and TiO_xS_y percentages while the SO_2 is slightly reduced after annealing and rinsing.

However, when the effect of each gas individually and of the RF bias was evaluated in section III.2.3, it was observed that for $\text{SO}_2/\text{O}_2/\text{He}$ without RF bias, the only peak present on the S2p XPS spectra is the SO_4^{2-} and still the xNL is partially removed after HF wet etching. Therefore, the SO_2 peak does not seem to be the main responsible for the lift-off of the neutral layer and its slight reduction in percentage after annealing and rinsing is probably not significant regarding the neutral layer lift-off.

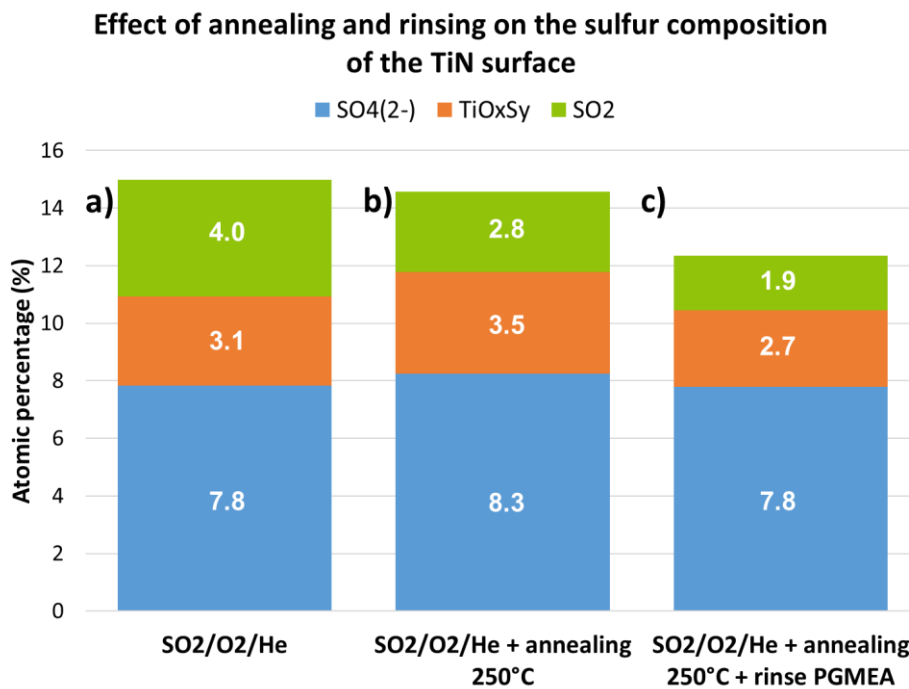


Figure III-21: Distribution of sulfur S2p peaks on the TiN surface determined by *ex-situ* XPS for each sample: (a) after $\text{SO}_2/\text{O}_2/\text{He}$ etching; (b) after $\text{SO}_2/\text{O}_2/\text{He}$ etching + annealing at 250°C for 5 minutes; and (c) after $\text{SO}_2/\text{O}_2/\text{He}$ etching + annealing at 250°C for 5 minutes + PGMEA rinsing. The results correspond to an incident angle of 23.75° .

Nevertheless, we decided to verify if pores are formed on the surface of the neutral layer by conducting ellipsometric porosimetry measurements on the xNL deposited over pristine TiN (identified as “as dep”) and over TiN after $\text{SO}_2/\text{O}_2/\text{He}$ SOC removal. The samples were placed under 90% humidity and then the xNL thickness and refractive index were measured as a function of time (between zero and 60 minutes). For the xNL thickness results presented in Figure III-22(a), a variation of about 0.15 nm for TiN as dep and 0.6 nm for TiN post $\text{SO}_2/\text{O}_2/\text{He}$ plasma is observed. However, measurement fitting turned out to be very complicated because the xNL and TiN layers are significantly thin and do not necessarily present the same refractive indices for both samples due to the impact of etching. Therefore, several “solutions” (thickness/refractive index pairs) were possible each time. Considering the difficulty of fit, it is hard to determine if the 0.6 nm thickness variation is significant.

As for the refractive index (n) measurements, usually if the material is porous, the average refractive index increases with the water infiltration because it presents a higher refractive index ($n_{\text{water}} = 1.3$) when compared to the air ($n_{\text{air}} = 1.0$). The refractive index results at a wavelength of 632.8 nm are presented in Figure III-22(b) for both samples. For the xNL deposited over pristine TiN, the refractive index does not vary significantly and the average index is around 1.51. As for the xNL over TiN after $\text{SO}_2/\text{O}_2/\text{He}$ plasma, the measurements are very noisy and the refractive index varies between 1.58 and 1.61, but this variation is not constant over time. Moreover, the average refractive index is at 1.59, which is higher compared to the xNL deposited over pristine TiN. This could indicate a difference in composition for the xNL deposited over the etched surface, but once again it is hard to determine if this difference is significant with the difficulty of fit and the many {thickness/refractive index} pairs possible.

Therefore, while the ellipsometric porosimetry measurements are not entirely conclusive, *a priori* they do not indicate the presence of pores on the surface of the xNL. Along with the XPS results in Figure III-21 that show no desorption of SO_4^{2-} ions after annealing and rinsing, hypothesis #2 does not seem to be the most likely explanation for the neutral layer lift-off.

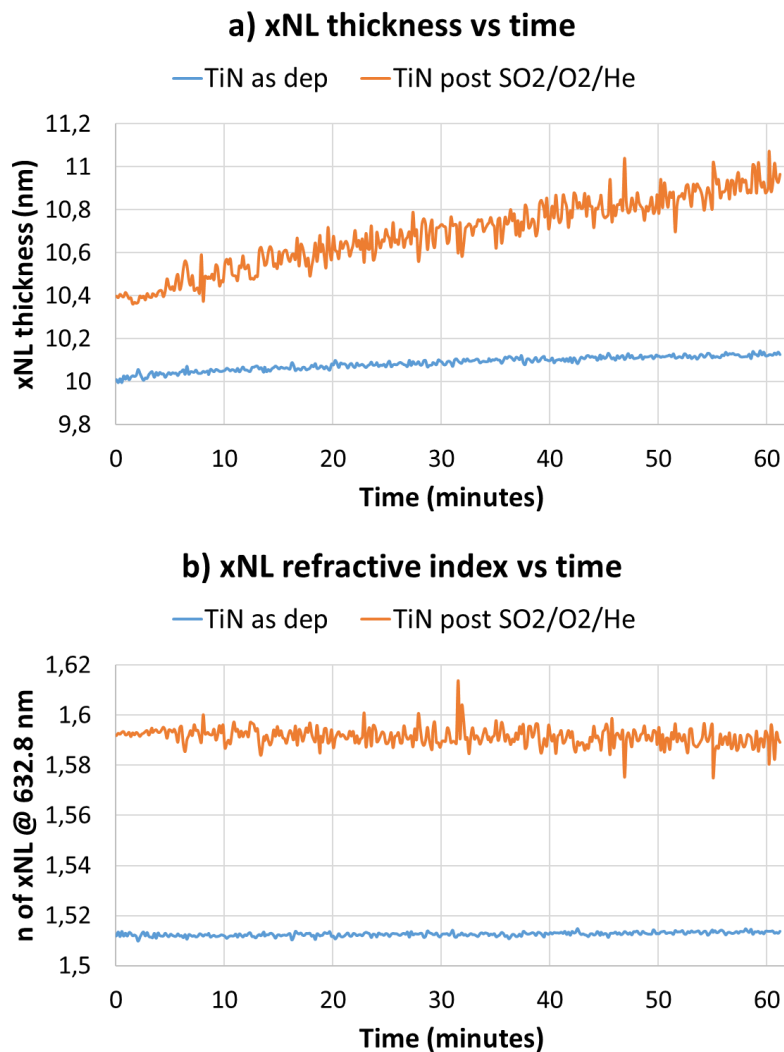


Figure III-22: (a) xNL thickness and (b) refractive index as a function of exposure time obtained through ellipsometric porosimetry for the xNL deposited over non-etched TiN (“as dep”) and TiN after $\text{SO}_2/\text{O}_2/\text{He}$ SOC removal.

III.2.4.4 Third hypothesis: disruption of the neutral layer's cross-linking

Hypothesis #3: SO_4^{2-} ions interact with the neutral layer's cross-linking agent, disrupting its complete cross-linking and allowing the HF to pass through. The HF then removes the modified $\text{TiO}_2/\text{TiO}_x\text{S}_y$ layer formed on the TiN surface, which reduces the neutral layer adherence to the TiN hard mask and allows its consequent lift-off.

Our third hypothesis is based on an interaction between the SO_4^{2-} ions and the cross-linking agent of the neutral layer. The SO_4^{2-} ions would disrupt the complete cross-linking of the xNL, allowing for a path to form, through which the HF would be able to cross and react with the modified $\text{TiO}_2/\text{TiO}_x\text{S}_y$ layer on the TiN surface. The HF would then remove the modified $\text{TiO}_2/\text{TiO}_x\text{S}_y$ layer, which would reduce the neutral layer adherence to the TiN hard mask and allow its consequent lift-off.

Since the cross-linking agent's composition and its cross-linking kinetics are not known due to confidentiality reasons, this hypothesis is harder to verify than the previous ones. Nevertheless, we have investigated the impact of the xNL deposition parameters, namely thickness and annealing time, on its adherence to the TiN surface after $\text{SO}_2/\text{O}_2/\text{He}$ SOC removal.

First, we decided to evaluate the influence of the TiN/xNL interface on the lift-off phenomenon. By increasing the xNL thickness, we are able to reduce the influence of the TiN/xNL interface on the bulk material and, therefore, possibly avoid the lift-off. To obtain a thicker xNL, we have to decrease the spin-coating speed. The reference spin-coating speed for the xNL is 1500 rpm (revolutions per minute), which leads to a thickness of around 7.5 nm. In order to increase the xNL thickness, the spin-coating speed was reduced to 700 rpm and the results can be found in Table III-11 for the xNL deposited over TiN after $\text{SO}_2/\text{O}_2/\text{He}$ plasma. The xNL thickness with lower spin-coating speed is around 13.4 nm, which represents an increase of approximately 6 nm compared to the reference speed. However, even though the xNL thickness was increased, Table III-11 shows that after HF wet etching the xNL is still completely removed.

This could either mean that the SO_4^{2-} ions are rapidly incorporated into the xNL no matter the thickness or that the 6-nm increase in thickness is simply not enough to evaluate the influence of the TiN/xNL interface. However, it is not possible to further increase the xNL thickness because of the solution concentration available and because spin-coating speeds below 700 rpm are not recommended. Therefore, we cannot draw definitive conclusions on the impact of the TiN/xNL interface on the lift-off of the neutral layer during HF wet etching.

The second parameter evaluated was the annealing time. Although the cross-linking agent kinetics is not known, it is safe to assume that the cross-linking is thermally activated during annealing. Assuming the SO_4^{2-} ions are able to disrupt or delay the cross-linking process, we have decided to evaluate the effect of a longer annealing time on the adherence of the neutral layer during HF wet etching. The results in Table III-11 show that, even for longer annealing time, the neutral layer is still completely removed during HF wet etching.

Table III-11. Neutral layer thickness deposited over the TiN surface after SO₂/O₂/He etching and measured by ellipsometry before and after 60 seconds of HF wet etching for two different deposition conditions: lower spin-coating speed and longer annealing time.

Neutral layer thickness (nm)	Before HF (nm)	After HF (nm)
@700 rpm, annealing 5 min	13.4 ± 0.5	0.0 ± 0.0
@1500 rpm, annealing 15 min	7.3 ± 0.5	0.0 ± 0.0

Therefore, even though the results are not entirely conclusive, hypothesis #3 remains the most probable. Knowledge of the cross-linking agent composition and kinetics would help on any further investigation of the neutral layer lift-off mechanism. The next sections shall focus on replacing the SOC etching chemistry in order to avoid the neutral layer lift-off.

Since the SO₂ was determined to be the main responsible for the xNL lift-off during HF wet etching, section III.2.4 focused on understanding the interaction mechanisms between the SO₂ plasma, the TiN surface, the xNL deposition and the HF wet etching that ultimately led to the lift-off of the neutral layer.

We first investigated the role of the TiO₂/TiO_xS_y/SO₄²⁻ modified layer that is formed on the TiN surface after SO₂/O₂/He SOC removal. By introducing an HF wet etching step between the SOC removal and the xNL deposition, we showed that the xNL is not removed by the second HF treatment, therefore confirming the negative effect of the TiO₂/TiO_xS_y/SO₄²⁻ layer on the adhesion of the neutral layer.

We then proposed different mechanism hypothesis for the neutral layer lift-off:

- 1) *Hypothesis #1*: SO₄²⁻ ions on the TiN surface recombine with the H⁺ ions of the HF wet etching to form sulfuric acid (H₂SO₄), which removes the neutral layer → The neutral layer thickness results before and after an H₂SO₄ bath allowed us to conclude that the H₂SO₄ does not spontaneously remove the neutral layer at room temperature, while the xNL thickness results before and after demineralized water did not indicate a recombination of H⁺ and SO₄²⁻ ions. Therefore, hypothesis #1 was eliminated.
- 2) *Hypothesis #2*: desorption of SO₄²⁻ ions during annealing of the neutral layer could form pores inside the xNL, which would facilitate the infiltration of the HF. The HF would then remove the modified TiO₂/TiO_xS_y layer formed on the TiN surface, thus reducing the neutral layer adherence to the TiN hard mask and allowing its consequent lift-off → The XPS results did not indicate a desorption of SO₄²⁻ ions, since there was no significant variation of the SO₄²⁻ percentage before and after annealing. Moreover, ellipsometric porosimetry measurements conducted on the xNL deposited over TiN after SO₂/O₂/He SOC removal did not indicate the presence of pores on the surface of the xNL. Therefore, hypothesis #2 was also eliminated.
- 3) *Hypothesis #3*: SO₄²⁻ ions interact with the neutral layer's cross-linking agent, disrupting its complete cross-linking and allowing the HF to pass through. The HF then removes the modified TiO₂/TiO_xS_y layer formed on the TiN surface, which reduces the neutral layer adherence to the TiN hard mask and allows its consequent lift-off → We investigated the impact of the xNL deposition parameters, namely

thickness and annealing time, on its adherence to the TiN surface after SO₂/O₂/He SOC removal. By increasing the xNL thickness, we hoped to reduce the influence of the TiN/xNL interface. However, we were limited to a 6-nm thickness increase, which was not significant enough to avoid the neutral layer lift-off during HF dip. By increasing the annealing time, we hoped to increase the cross-linking percentage because cross-linking is usually thermally activated during annealing. However, the results showed that xNL was still completely removed during HF dip even with longer annealing time. Since the cross-linking agent's composition and its cross-linking kinetics are not known, the results obtained were not entirely conclusive. Despite that, hypothesis #3 remains the most probable.

III.3 Alternatives for the SOC removal step

In this third part of the chapter, we propose different approaches to optimize the SOC removal step based on SO₂/O₂/He plasma, which is not favorable to the neutral layer adherence. We have chosen to optimize the SOC removal step instead of the trilayer etching, which are both based on SO₂/O₂/He, for a couple of reasons. The first one is related to a higher freedom of choice, because while the trilayer etching must be anisotropic in order to correctly transfer the lithography patterns into the SOC layer, the SOC mandrel removal step has no constraint tied to the anisotropy, only to the selectivity regarding the SiN spacers. The second reason is that the SOC mandrel removal is the last step before the neutral layer deposition and, therefore, probably the one whose impact on the TiN surface is the most important.

III.3.1 First approach: replace the SOC removal step

The first solution consists in replacing the SOC removal chemistry. Two different approaches have been explored: the first one is an oxygen only SOC removal, since it has been shown in section III.2.3.3 that the oxygen does not have a negative effect on the neutral layer adherence. The second approach is a reductive SOC removal based on H₂/N₂. Both approaches are well-known SOC and resist stripping chemistries and their plasma parameters were taken from already existing recipes used in other applications within CEA Leti. The oxygen only plasma is conducted on the Kiyoflex™ ICP reactor with 200 sccm of O₂ during 30 seconds, with a RF power of 1320 W, pressure of 10 mTorr and zero RF Bias. The H₂/N₂ reductive SOC removal, on the other hand, is conducted in a capacitively coupled plasma (CCP) reactor, known as Flex CFE™ from LamResearch®, due to the H₂ not being available in the ICP reactor. The details of the CCP reactor have been presented in Chapter II.2.1.1. The plasma parameters are H₂/N₂ 150/500 sccm, during 60 seconds with a pressure of 160 mTorr, RF 2 MHz power at zero and RF 27 MHz power at 1000 W.

III.3.1.1 Effect of the SOC removal alternatives on the TiN surface composition

The XPS results for both approaches are presented in Figure III-23, along with the results before etching for comparison purposes. For the oxygen only SOC removal presented in Figure III-23(b), as expected, it is possible to observe a significant increase of about 17.3% for the oxygen percentage, characterized by an intensity increase of the TiO₂ peak. Consequently, an equivalent decrease of around 17.8% is observed for the nitrogen content, indicating a reduction of the TiN peak intensity. As for the titanium percentage, a decrease of 6% is observed, which is a combination of both TiO₂ peak intensity augmentation and TiN peak intensity reduction.

As for the H₂/N₂ SOC removal presented in Figure III-23(c), the slight decrease of Ti and O percentages is explained by the increase of the carbon contamination, which comes from the reactor's chamber walls and the air exposure between etching and XPS analysis. Therefore, no significant changes are observed for the TiN surface composition after etching using H₂/N₂.

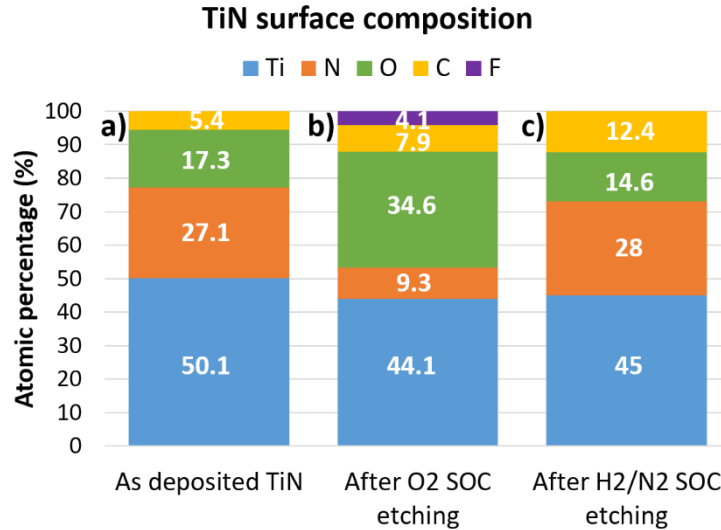


Figure III-23: TiN surface composition determined by *ex-situ* XPS: (a) before etching; (b) after O₂ only SOC removal; and (c) after H₂/N₂ SOC removal. The results correspond to an incident angle of 23.75°.

III.3.1.2 Contact angle and surface energy measurements

Contact angle measurements have also been conducted to obtain the surface energy of these samples after SOC removal and the results are presented in Table III-12. For the oxygen only plasma, the results obtained were similar to those seen in the previous sections for other oxidative chemistries: a significant increase of the surface energy and polar component after etching. As for the H₂/N₂ plasma, it is important to notice that the polar component is similar to that of the as deposited TiN, which indicates a natural compatibility with the neutral layer.

Table III-12. TiN surface energy before and after the alternative SOC removal approaches, calculated by contact angle measurements, as well as its dispersive and polar components.

	Surface energy γ (mN/m)	Dispersive component γ_d (mN/m)	Polar component γ_p (mN/m)
As deposited TiN	43.8	37.3	6.5
After O ₂ etching	76.1	42.9	33.2
After H ₂ /N ₂ etching	54.2	47.3	6.9

III.3.1.3 Effect of the wet spacer removal step on the neutral layer adherence

Like in the previous sections, the neutral layer deposition and HF wet etching have been conducted in order to verify the correct adherence of the neutral layer over the modified TiN surface after SOC removal. Table III-13 presents the thickness measurement results: for both SOC removal approaches, the neutral layer presents the same thickness before and after HF wet

etching. The TiN + xNL surface for both approaches has also been verified by cross-section SEM and, as expected based on the results from Table III-13, both surfaces are smooth and do not present lift-off spots. Therefore, both approaches present a favorable surface for the neutral layer adherence.

Table III-13. Neutral layer thickness measured by ellipsometry before and after 60 seconds of HF wet etching when deposited over the TiN surface after SOC removal using O₂ and H₂/N₂.

Neutral layer thickness (nm)	Before HF (nm)	After HF (nm)
O ₂ only etching	6.7 ± 0.3	6.8 ± 0.3
H ₂ /N ₂ etching	6.9 ± 0.1	7.0 ± 0.1

III.3.1.4 Application to patterned wafers using the ACE chemo-epitaxy flow

Finally, these alternative SOC removal steps have been applied to pattern wafers following the complete ACE flow presented in Section III.1. The work presented in this section was carried out in collaboration with a PhD student specializing in DSA lithography.

Figure III-24 represents the results obtained after the BCP self-assembly step for the PS-*b*-PMMA block copolymer with 32 nm pitch. The PMMA phase has been removed through dry etching to enhance the contrast and facilitate the image capture. For both processes, we observe a great improvement compared to the first result presented in Figure III-6 for the SO₂/O₂/He SOC removal. The top-view SEM image after oxygen only SOC etching in Figure III-24(a) corresponds to a measurement field of 4 x 4 μm and does not present lift-off spots, but it still presents very few BCP self-assembly defects, such as small dark spots and alignment defects. As for the H₂/N₂ SOC etching, Figure III-24(b) represents a 10 μm x 10 μm (the largest measurement field the CD-SEM tool used can obtain) top-view SEM image without any type of alignment or lift-off defects, which translates to 0 def/100 μm².

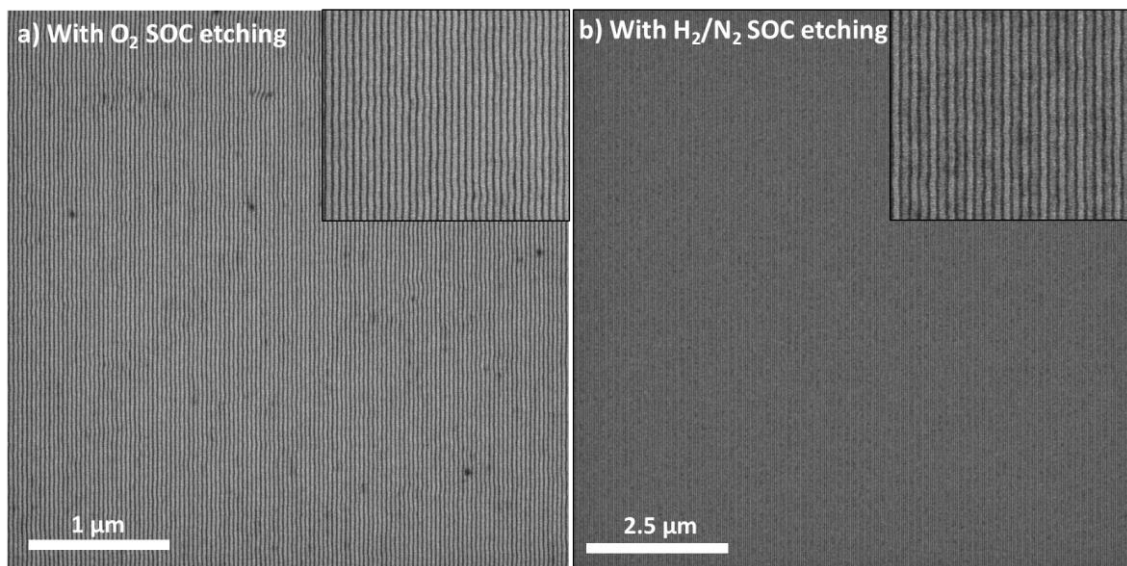


Figure III-24: Top-view SEM images of the PS-*b*-PMMA block copolymer with pitch 32 nm aligned by the ACE flow using: (a) O₂ SOC removal with a measurement field of 4 x 4 μm; (b) H₂/N₂ SOC removal with a measurement field of 10 x 10 μm. Both images correspond to a multiplication factor of 4 (lithography pitch = 128 nm) and present a zoomed view to highlight the good alignment obtained.

For further evaluation of the DSA alignment results as a function of the SOC removal etching chemistry, defectivity maps were obtained at the DSA step. To obtain these maps, an expo-dose per column was conducted on these wafers, which consists of varying the UV exposure dose per column during the immersion lithography step. The mask used and the expo-dose allow us to obtain up to 88 different CDSOC for a given pitch, as well as lithography pitches varying from 68 to 263 nanometers. These pitch and CDSOC variations allow us to determine the process window, that is, the ideal CDSOC and lithography pitch values that lead to the defect-free alignment of the block copolymer. Indeed, for the grapho-epitaxy or chemo-epitaxy approaches, there are commensurability rules which predict the values of the guide CD which will more likely induce the alignment of the copolymer. For grapho-epitaxy, the CDSOC is proportional to n times the period L_0 of the copolymer, n being an integer, while for chemo-epitaxy, the CDSOC is proportional to $n - 0.5$ times the period L_0 of the copolymer. These values will be represented by the red circle and orange cross symbols, respectively, in the defectivity maps.

Figure III-25 presents the results for the three SOC etching chemistries presented so far: $\text{SO}_2/\text{O}_2/\text{He}$, O_2 only and H_2/N_2 . To obtain these defectivity maps, several $1 \times 1 \mu\text{m}$ CD-SEM images were taken all over the wafer to cover most of the {CDSOC/pitch} pairs available, which are represented in the maps as a function of the block copolymer's intrinsic period L_0 . For each image, the number of defects on a $1\text{-}\mu\text{m}^2$ surface was counted using the Deboara software. The color scale in the map represents the ratio between the number of defects for each {CDSOC/pitch} pair of the patterned wafer and the number of defects on a free surface wafer with a fingerprint-like morphology. Therefore, the lower the defectivity ratio, the better the alignment of the block copolymer. The {CDSOC/pitch} pairs that present a fingerprint alignment are not represented. Thus, this color scale allows us to define the different process windows (PW) for the ACE chemo-epitaxy process as a function of each SOC etching chemistry. The experimental details for the image capture and defectivity analysis can be found in [Le Pennec 2021]. The defectivity results for the $\text{SO}_2/\text{O}_2/\text{He}$ SOC removal presented in Figure III-25(a) are as expected based on the results we have shown throughout this chapter: there is not a single $1\text{-}\mu\text{m}^2$ zone that presents a block copolymer alignment without defects, due to the neutral layer lift-off.

For the O_2 only SOC removal presented in Figure III-25(b), at least 11 process windows can be discerned, some better defined than others. It is important to notice that the PWs for multiplication factors ($\text{MF} = \text{Pitch}/L_0$) ≤ 6 are mainly located on red circles, which are characteristic of an alignment defined by grapho-epitaxy, while PWs for $\text{MF} \geq 7$ are mainly located between the red circles and orange crosses characteristic of a hybrid alignment. Therefore, the O_2 SOC removal leads to a hybrid chemo/grapho-epitaxy alignment depending on the ratio between the pitch and the block copolymer's intrinsic period L_0 .

Finally, the defectivity map obtained for the H_2/N_2 SOC removal chemistry presented in Figure III-25(c) shows the start of alignment for the patterns with $\text{MF} \leq 6$. At least 4 PWs can be discerned and most of them are located on the area between the orange crosses and red circles, characteristic of an hybrid chemo/grapho-epitaxy alignment.

These results allow us to confirm that the DSA alignment obtained for the ACE integration depends on the SOC removal chemistry used. While the H_2/N_2 SOC removal presents the best defectivity result for a single {CD_{SOC}/pitch} pair, as shown in Figure III-24(b) with 0 def/100 μm^2 , the O_2 SOC removal presents the best process window results, with 11 PWs

discerned instead of 4 for the H_2/N_2 . However, most of the process windows for the O_2 plasma are centered on grapho-epitaxy commensurability values instead of the chemo-epitaxy values expected for the ACE flow.

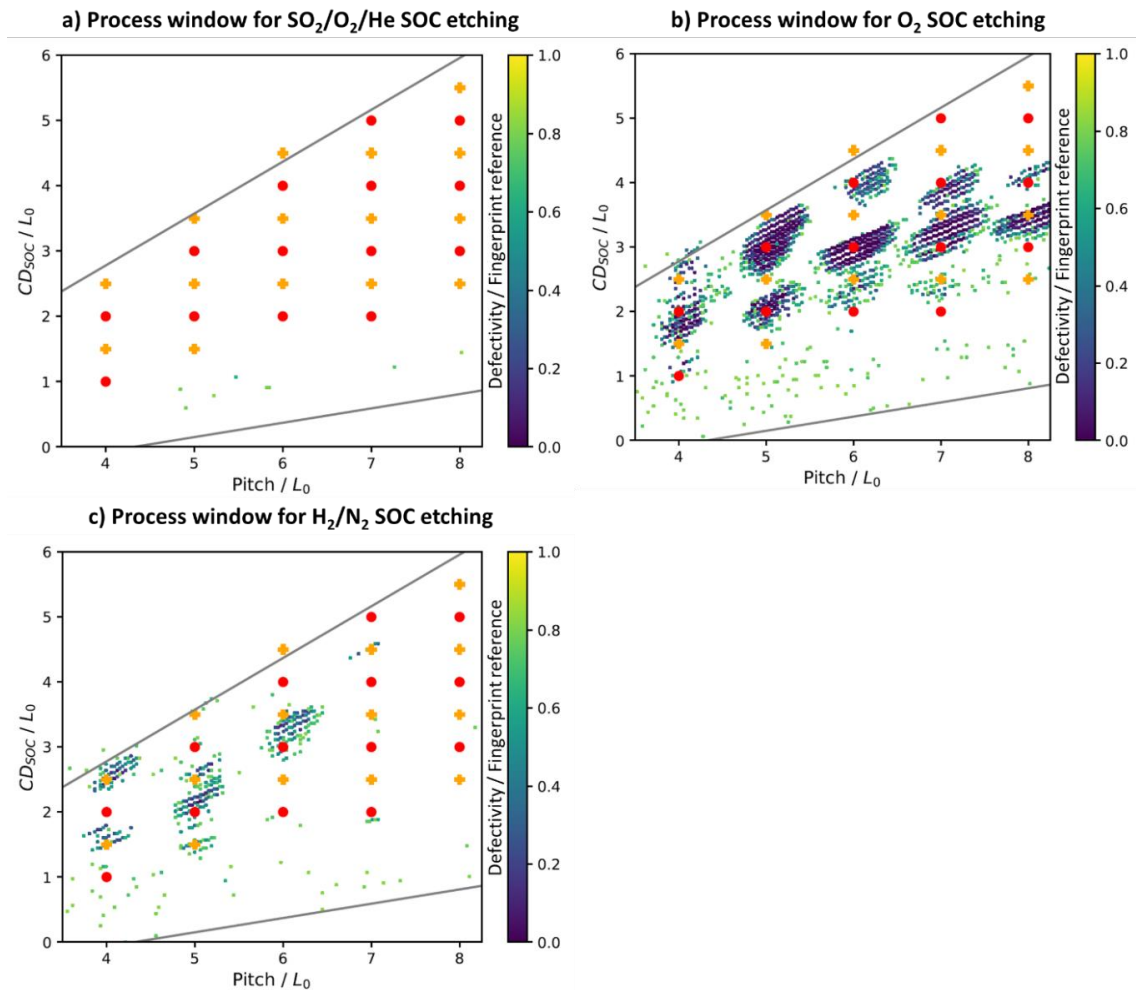


Figure III-25: Defectivity maps obtained for the ACE flow using different SOC removal chemistries: (a) $SO_2/O_2/He$; (b) O_2 only; and (c) H_2/N_2 . The orange cross and red circle symbols represent the theoretical commensurability values for chemo-epitaxy and grapho-epitaxy, respectively. Adapted from [Le Pennec 2021].

In order to understand the origin of this hybrid alignment, the complete SOC removal during step 6 was investigated on patterned wafers for the three different SOC removal chemistries using backscattered electrons (BSE) imaging and atomic force microscopy (AFM). The detailed experience can be found in [Le Pennec 2021]. Indeed, SOC residues were observed at the bottom of the patterns depending on the etching conditions, which can lead to defects or a shift in the process window. The different tables in Figure III-26 synthesize the results obtained. The ✓ symbol represents the presence of SOC residues after etching and the ✗ symbol represents the absence of SOC residues after etching.

From Figures III-26(a) and (b), we observed that after SOC removal carried out by either O_2 or H_2/N_2 plasma, the $\{Pitch/L_0, CD_{SOC}/L_0\}$ pairs that exhibit SOC residues are identical. The $SO_2/O_2/He$ SOC removal, on the other hand, allows for a complete removal of the SOC for all the patterns studied, as shown in Figure III-26(c). When increasing the etching time for O_2 or H_2/N_2 plasma to 60s and 120s, respectively, the same trend is still observed for smaller pitch

and CD_{SOC} : while the SOC residual thickness is reduced, the SOC is not completely removed. These SOC residues can be explained by the presence of patterns of different densities on the same wafer, represented by the pitch and CD_{SOC} variations. This leads to a local variation in the density of the reactive species present in the plasma, and therefore, a local variation in the etch rate. As we have seen in Figure III-26, the smaller the pitch and CD_{SOC} , the lower the etch rate and the more SOC residues are present. This phenomenon is known as ARDE, for Aspect Ratio Dependent Etching [Hedlund 1994].

It should also be noticed that, for the O_2 and H_2/N_2 SOC removal, the $\{Pitch/L_0, CD_{SOC}/L_0\}$ pairs that exhibit SOC residues are also the ones close to the process windows based on grapho-epitaxy and hybrid chemo/grapho-epitaxy alignment, respectively.

a) O_2 SOC etching					b) H_2/N_2 SOC etching					c) $SO_2/O_2/He$ SOC etching				
$\frac{Pitch}{L_0}$ & $\frac{CD_{SOC}}{L_0}$	2	3	4		$\frac{Pitch}{L_0}$ & $\frac{CD_{SOC}}{L_0}$	2	3	4		$\frac{Pitch}{L_0}$ & $\frac{CD_{SOC}}{L_0}$	2	3	4	
4	✓				4	✓				4	✗			
5	✓	✓	✗		5	✓	✓	✗		5	✗	✗	✗	
6	✓	✓	✗		6	✓	✓	✗		6	✗	✗	✗	
7	✗	✗	✗		7	✗	✗	✗		7	✗	✗	✗	
8		✗	✗		8		✗	✗		8		✗	✗	

Figure III-26: Summary tables for the presence of SOC residues after step 6 for the different SOC removal chemistries studied (a) O_2 , (b) H_2/N_2 and (c) $SO_2/O_2/He$ as a function of the different $\{Pitch/L_0, CD_{SOC}/L_0\}$ pairs. ✓ represents the presence of SOC residues and ✗ represents the absence of SOC residues. Adapted from [Le Pennec 2021].

In this section, we proposed alternatives to replace the SOC removal step based on $SO_2/O_2/He$ plasma, which was not favorable to the neutral layer adherence. The two chemistries proposed were O_2 and H_2/N_2 .

All the results presented allowed us to conclude that:

- 1) The $SO_2/O_2/He$ plasma allows the SOC to be removed for all the different multiplication factors, probably due to the presence of RF bias to accelerate the ions inside the plasma. However, the surface state of the TiN hard mask is modified and the interaction of the SO_2 with the xNL leads to the neutral layer lift-off during HF wet etching, and therefore no alignment zones without defects are observed.
- 2) The O_2 plasma modifies the surface composition and energy of the TiN hard mask, but allows the xNL to be conserved during HF wet etching and presents several different process windows for patterned wafers. However, due to an ARDE effect on patterned wafers, it does not allow complete removal of the SOC for smaller pitch and CD_{SOC} , leading to a hybrid chemo/grapho-epitaxy alignment as a function of the multiplication factor.
- 3) The H_2/N_2 plasma is capable of conserving the surface properties of the as deposited TiN, such as its surface energy and composition, and therefore allows the xNL to be conserved during HF wet etching. Similarly to the O_2 plasma, ARDE effects during etching of patterned wafers lead to SOC residues for smaller patterns and to a hybrid

chemo/grapho-epitaxy alignment. While this approach presents the best defectivity result for a single $\{CD_{SOC}/pitch\}$ pair, with 0 def/100 μm^2 for a lithography pitch of 128 nm, it presents fewer process windows compared to O₂ plasma.

III.3.2 Second approach: two-step SOC removal

In order to further optimize the block copolymer's alignment with the ACE flow, our second approach consists in a two-step SOC removal. It starts with the SO₂/O₂/He plasma to completely remove the SOC layer followed by the O₂ or H₂/N₂ plasma to recover a TiN surface state compatible with the xNL.

We have followed the same procedure as the previous studies: TiN blanket wafers with a 73-nm SOC layer were etched using the SO₂/O₂/He plasma, followed by either the O₂ plasma in the same ICP reactor or the H₂/N₂ in the CCP reactor of the same etching tool. Therefore, in both cases, no air exposure took place between the first and second steps. *Ex-situ* XPS analysis and contact angle measurements were conducted to evaluate the TiN surface properties after the two-step approach. Furthermore, the xNL was deposited and its thickness was measured before and after HF wet etching to evaluate its adherence to the TiN surface. And finally the results when applying the two-step approach to patterned wafers are also evaluated.

III.3.2.1 Effect of the SOC removal two-step approach on the TiN surface composition

The XPS results for both two-step approaches are presented in Figures III-27(e) and (f). The results before etching and after etching with each step separately are also included in Figures III-27(a) to (d) for comparison purposes. For the SO₂/O₂/He + O₂ SOC removal presented in Figure III-30(f), it should be noticed that about 5% of sulfur is still present after the O₂ post-treatment, corresponding to the SO₄²⁻ S2p peak at 169.2 eV. Therefore, this two-step approach with the oxidizing post-treatment has not been able to completely remove the sulfur from the TiN surface and, from the results presented throughout this chapter, should not be expected to preserve the neutral layer adherence during HF wet etching. As for the SO₂/O₂/He + H₂/N₂ SOC removal presented in Figure III-27(e), the TiN surface composition after the two-step approach is quite similar to the one after H₂/N₂ only, albeit a 4% decrease in the nitrogen percentage, characteristic of a decrease of the TiN peak, and 4% increase of the oxygen content, due to an increase of the TiO₂ peak. Most importantly, no sulfur is presented in Figure III-27(e). Therefore, this two-step approach with the reducing post-treatment is capable of completely removing the sulfur from the TiN surface and should be expected to preserve the neutral layer adherence during HF wet etching.

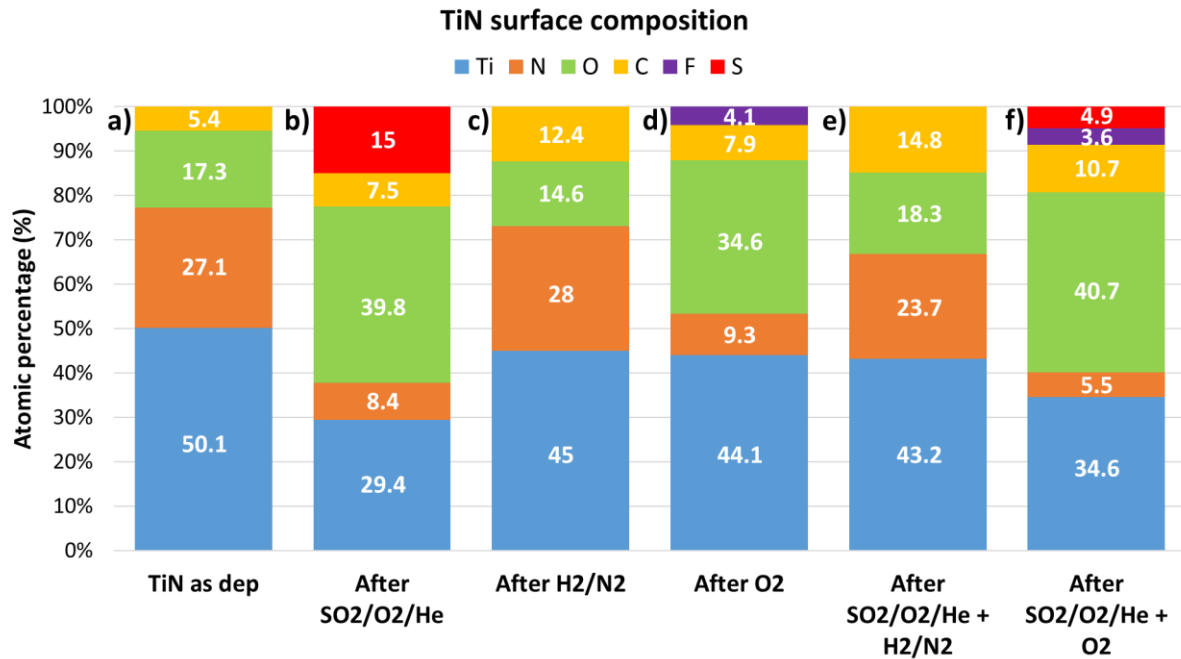


Figure III-27: TiN surface composition determined by *ex-situ* XPS: (a) before etching; (b) after SO₂/O₂/He SOC removal; (c) after H₂/N₂ SOC removal; (d) after O₂ SOC removal; (e) after SO₂/O₂/He + H₂/N₂ SOC removal; and (f) after SO₂/O₂/He + O₂ SOC removal. The results correspond to an incident angle of 23.75°.

III.3.2.2 Contact angle and surface energy measurements

Similarly to the previous sections, the contact angle measurements have also been conducted to obtain the surface energy of these samples after the two-step SOC removal and the results are presented in Table III-14. For the SO₂/O₂/He + O₂ SOC removal, the results obtained were similar to those seen in the previous sections for other oxidative chemistries: a significant increase of the surface energy and polar component after etching. As for the SO₂/O₂/He + H₂/N₂ removal, it is important to notice that the polar component is similar to that of the as deposited TiN and of the TiN after H₂/N₂ only, therefore confirming the results obtained from XPS: the reductive post-treatment is capable of recovering the TiN surface properties even after SO₂-based modification.

Table III-14. TiN surface energy before and after the alternative two-step SOC removal approaches, calculated by contact angle measurements, as well as its dispersive and polar components.

	Surface energy γ (mN/m)	Dispersive component γ_d (mN/m)	Polar component γ_p (mN/m)
As deposited TiN	43.8	37.3	6.5
After SO ₂ /O ₂ /He + H ₂ /N ₂	53.1	45.2	7.9
After SO ₂ /O ₂ /He + O ₂	76.9	41.3	35.6

III.3.2.3 Effect of the wet spacer removal step on the neutral layer adherence

The neutral layer deposition and HF wet etching have been conducted in order to verify the correct adherence of the neutral layer over the modified TiN surface after two-step SOC removal. Table III-15 presents the thickness measurement results for both two-step SOC removal approaches. As expected based on the XPS results for the SO₂/O₂/He + O₂ SOC removal, the neutral layer is removed after 60 seconds of HF wet etching. Thus, this approach is not adequate for the neutral layer adherence. The SO₂/O₂/He + H₂/N₂ SOC removal, on the other hand, presents the same xNL thickness before and after HF wet etching. Therefore, the reducing post-treatment presents a favorable surface for the neutral layer adherence.

Table III-15. Neutral layer thickness measured by ellipsometry before and after 60 seconds of HF wet etching when deposited over the TiN surface after the two-step SOC removal using SO₂/O₂/He + H₂/N₂ and SO₂/O₂/He + O₂.

Neutral layer thickness (nm)	Before HF (nm)	After HF (nm)
After SO ₂ /O ₂ /He + H ₂ /N ₂	8.0 ± 0.3	8.1 ± 0.3
After SO ₂ /O ₂ /He + O ₂	8.2 ± 0.3	0.0 ± 0.0

III.3.2.4 Application to patterned wafers using the ACE chemo-epitaxy flow

Finally, the SO₂/O₂/He + H₂/N₂ two-step SOC removal has been applied to patterned wafers following the complete ACE flow presented in Section III.1. Figure III-28 represents the results obtained for two different multiplication factors after the BCP self-assembly step for the PS-*b*-PMMA block copolymer with 32 nm pitch. The PMMA phase has been removed through dry etching to enhance the contrast and facilitate the image capture. For both MFs, the 1 x 1 μm top-view SEM images do not present any type of alignment or lift-off defects, which translates to 0 def/μm².

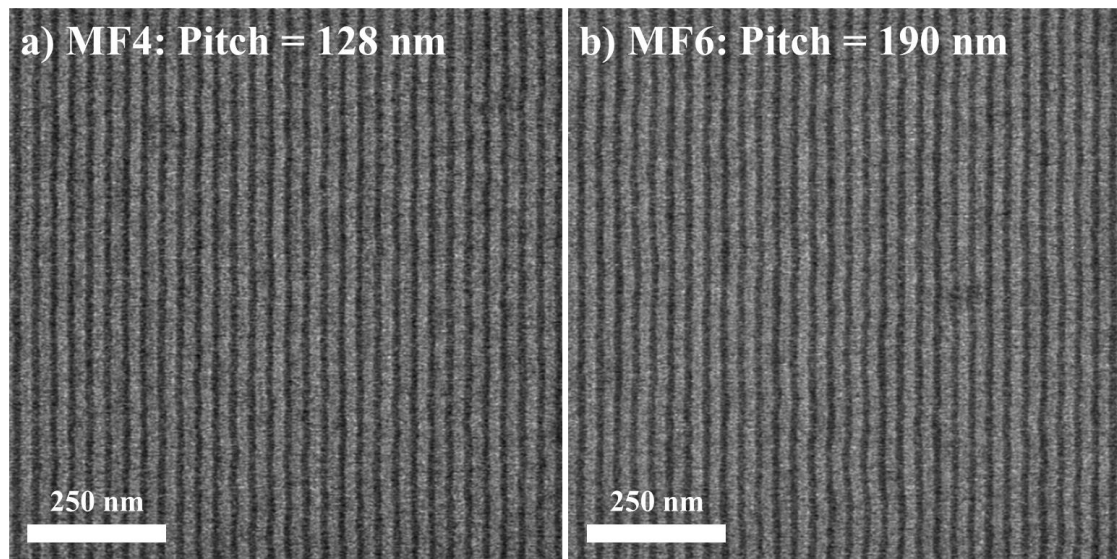


Figure III-28: 1 x 1 μm top-view SEM images of the PS-*b*-PMMA block copolymer with pitch 32 nm aligned by the ACE flow using the SO₂/O₂/He + H₂/N₂ two-step SOC removal approach. (a) corresponds to a multiplication factor of 4 and a lithography pitch of 128 nm, while (b) corresponds to a multiplication factor of 6 and a lithography pitch of 190 nm.

For further evaluation of the DSA alignment results as a function of the $\text{SO}_2/\text{O}_2/\text{He} + \text{H}_2/\text{N}_2$ two-step SOC removal, a defectivity map was obtained at the DSA step following the same procedure presented in section III.3.1.4. Figure III-29 presents the defectivity map obtained by compiling the defectivity results of several $1 \times 1 \mu\text{m}$ CD-SEM images, such as the ones presented in Figure III-28, taken all over the wafer to cover most of the $\{\text{CD}_{\text{SOC}}/\text{pitch}\}$ pairs available, which are represented in the map as a function of the block copolymer's intrinsic period L_0 .

For the defectivity map presented in Figure III-29, we can observe a large number of patterns presenting an alignment with $0 \text{ def}/\mu\text{m}^2$ (purple pixels) and at least 14 process windows can be discerned, which is greater than all the other processes presented previously. It is important to notice that the PWs are mainly centered around the orange crosses, significant of a commensurability for which $\text{CD}_{\text{SOC}} = (n - 0.5) L_0$. Therefore, the ACE integration with a $\text{SO}_2/\text{O}_2/\text{He} + \text{H}_2/\text{N}_2$ two-step SOC removal is determined mainly by chemo-epitaxy.

However, for the process windows with $(\text{MF} = \text{Pitch}/L_0) \geq 7$, at least 4 of them are located on the area between the orange crosses and red circles, characteristic of an hybrid chemo/grapho-epitaxy alignment. A. Le Pennec has proposed a mechanism to explain this hybrid alignment on higher MF, based on the difference in xNL thickness as a function of the lithography pitch. According to her observations, the xNL is thinner for larger lithography pitch, leading to a difference in height between the neutral layer and the guide layer and, therefore, a hybrid chemo/grapho-epitaxy process determined by both the difference in height and the difference in chemical affinity of the neutral layer and guiding layer [Le Pennec 2021].

These results allow us to conclude that the various etching steps preceding the deposition of the neutral layer have a significant impact on the block copolymer's alignment, as well as the type of alignment observed (chemo or grapho-epitaxy). Most importantly, the adherence of xNL is highly influenced by the surface properties of the TiN hard mask.

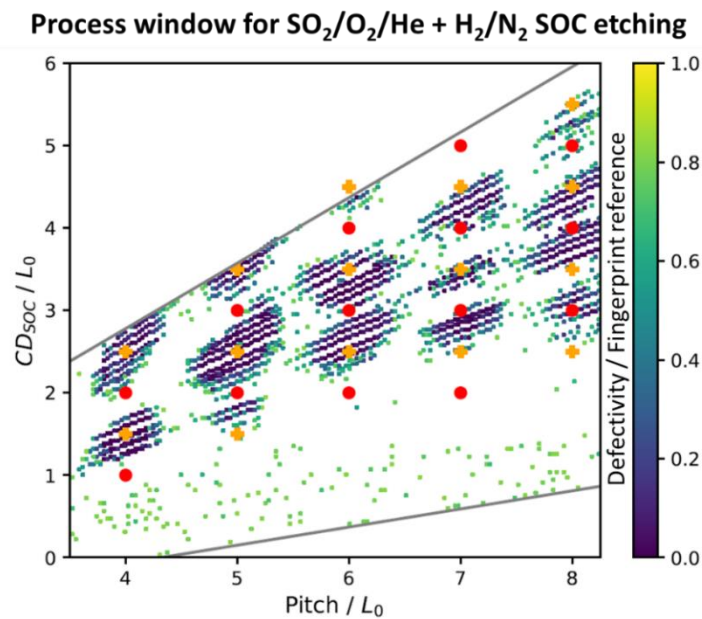


Figure III-29: Defectivity map obtained for the ACE flow using the $\text{SO}_2/\text{O}_2/\text{He} + \text{H}_2/\text{N}_2$ two-step SOC removal approach. The orange cross and red circle symbols represent the theoretical commensurability values for chemo-epitaxy and grapho-epitaxy, respectively. Adapted from [Le Pennec 2021].

In order to further optimize the block copolymer's alignment with the ACE flow, the second approach consisted in a two-step SOC removal. It starts with the SO₂/O₂/He plasma to completely remove the SOC layer followed by the O₂ or H₂/N₂ plasma to recover a TiN surface state compatible with the xNL.

The O₂ post-treatment after the SO₂/O₂/He plasma was not able to completely remove the modified TiO₂/TiO_xS_y/SO₄²⁻ layer from the TiN surface and, therefore, the neutral layer was removed during the HF dip.

Therefore, based on the work presented throughout this chapter, the SOC removal process that exhibited the best alignment was obtained using a SO₂/O₂/He plasma followed by a H₂/N₂ plasma. The combination of both plasmas allows for all of the prerequisites to be met: the SOC layer is completely removed, the TiN surface properties are conserved, the xNL adheres to the TiN surface throughout the HF wet etching step, and the ACE process is determined mainly by chemo-epitaxy.

III.4 Conclusions

In this chapter, we began by detailing and characterizing the Arkema-CEA (ACE) chemo-epitaxy process flow. However, when applying the non-optimized process of reference to patterned wafers, we realized that different types of defects could be seen in the CD-SEM image of the block copolymer's alignment after the DSA step, such as dark spots and BCP alignment defects.

This led us to study the impact of the different etching steps present on the ACE flow on the surface properties (composition and surface energy) of the TiN hard mask. The goal was to understand the origin of the defects and evaluate the hard mask's capability to align the block copolymer after the different etching and deposition steps. By studying the effect of the sequence of etching and deposition steps on the TiN surface and neutral layer adherence using blanket wafers, we concluded that the dark spots and BCP alignment defects were caused by a lift-off phenomenon, confirming the inadequacy of the non-optimized flow to align the block copolymer.

We then investigated the effect of each etching step on the TiN surface. We observed that all of them induced significant surface energy and composition modifications when compared to the pristine TiN hard mask. Next, to verify the adherence of the neutral layer to the TiN surface modified by the different etching steps, the neutral layer thickness was measured before and after HF wet etching. Ellipsometry measurements showed that the neutral layer is completely removed for the samples after trilayer etching and SOC removal, which were both based on SO₂/O₂/He. This led to the conclusion that the TiN surface after SO₂/O₂/He plasma was not favorable to the neutral layer adherence and, as a result, this layer could not resist the HF wet etching.

Further investigation on the effect of the RF bias and each gas (SO₂, O₂ and He) separately showed that, while O₂ highly oxidizes the TiN surface and increases its surface energy, it does not have a negative effect on the neutral layer adherence, thus allowing this layer to resist the HF wet etching step. The same was concluded for the helium, which does not prevent the adherence of the neutral layer. The RF Bias power also does not seem to be the most significant parameter. Indeed, without RF Bias, even though the TiN modified layer is thinner when

compared to the same process with Bias, the neutral layer is still almost completely removed, which means the $\text{SO}_2/\text{O}_2/\text{He}$ plasma etching chemistry was not adapted to the chemo-epitaxy application. Finally, this led to the conclusion that the SO_2 molecule was the main responsible for this recipe's inadequacy to the ACE flow.

Once the SO_2 was determined to be responsible for the lift-off, our goal was to understand the interaction mechanisms between the SO_2 plasma, the TiN surface, the xNL deposition and the HF wet etching that led to the lift-off of the neutral layer. Several hypotheses were proposed. Ultimately, hypothesis #3 was retained as the most probable: SO_4^{2-} ions interact with the neutral layer's cross-linking agent, disrupting its complete cross-linking and allowing the HF to pass through. The HF then removes the modified $\text{TiO}_2/\text{TiO}_x\text{S}_y$ layer formed on the TiN surface, which reduces the neutral layer adherence to the TiN hard mask and allows its consequent lift-off.

The third part of this chapter consisted in proposing two different alternatives for the SOC removal: replacing the $\text{SO}_2/\text{O}_2/\text{He}$ plasma or adding a post-treatment step. To replace the $\text{SO}_2/\text{O}_2/\text{He}$, two plasma chemistries were explored: O_2 and H_2/N_2 . The results showed that the O_2 etching modifies the surface composition and energy of the TiN hard mask, but allows the xNL to be conserved during HF wet etching and presents several different process windows for patterned wafers. However, due to a microloading effect on patterned wafers, it does not allow complete removal of the SOC for smaller pitch and CD_{SOC} , leading to a hybrid chemo/grapho-epitaxy alignment as a function of the multiplication factor. The H_2/N_2 etching, on the other hand, is capable of conserving the surface properties of the as deposited TiN, such as its surface energy and composition, and therefore allows the xNL to be conserved during HF wet etching. Similarly to the O_2 etching, microloading effects during etching of patterned wafers lead to SOC residues for smaller patterns and to a hybrid chemo/grapho-epitaxy alignment. While this approach presents the best defectivity result for a single $\{\text{CD}_{\text{SOC}}/\text{pitch}\}$ pair, with 0 def/100 μm^2 for a lithography pitch of 128 nm, it presents fewer process windows compared to O_2 etching.

In order to further optimize the block copolymer's alignment with the ACE flow, the second approach consisted in a two-step SOC removal: $\text{SO}_2/\text{O}_2/\text{He}$ plasma followed by the H_2/N_2 plasma. The different results led to the conclusion that this approach exhibits the best alignment results when compared to the other approaches investigated. Indeed, the combination of both plasmas allows for all of the prerequisites to be met: the SOC layer is completely removed, the TiN surface properties are conserved, the xNL adheres to the TiN surface throughout the HF wet etching step, and the ACE process is determined mainly by chemo-epitaxy.

CHAPTER IV:

ETCHING AND PATTERN TRANSFER OF PURELY ORGANIC HIGH- χ BLOCK COPOLYMER

IV. ETCHING AND PATTERN TRANSFER OF PURELY ORGANIC HIGH- χ BLOCK COPOLYMER

In Chapter I, we have described the different properties of the block copolymers that allow them to self-assemble into nanostructures with dimensions inferior to 20 nm. We have also seen that, once the domains have been aligned into long-range order nanostructures, the next challenge is to obtain a mask from the patterns formed. In order to do so, we must remove one of the blocks selectively to the other, as represented in Figure IV-1.

During this chapter, the organic high- χ block copolymer system studied is a modified PS-*b*-PMMA with a pitch of 18 nm and lamellar morphology, which was developed by Brewer Science Inc. and Arkema and shall be identified as “high- χ L18” throughout this chapter. The main goal of this study is to develop a PMMA removal process selective to the PS and adapted to the 18-nm pitch on 300 mm wafers.

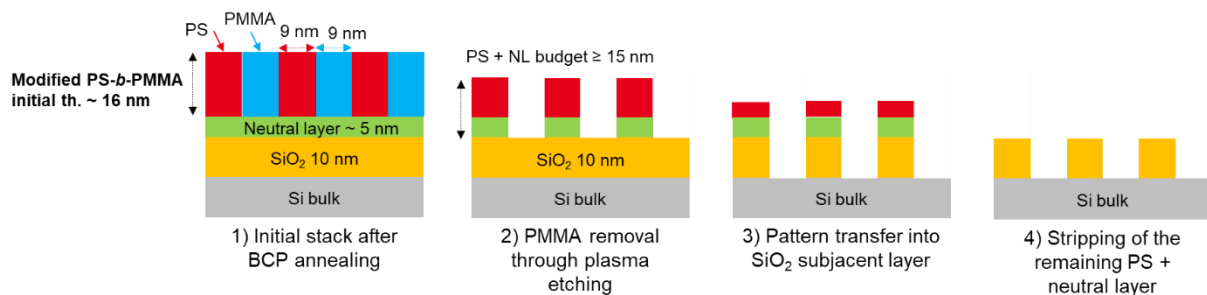


Figure IV-1: Schematics for the flow used in the etching study of the 18-nm pitch high- χ PS-*b*-PMMA block copolymer.

Figure IV-1 shows the etching flow for this high- χ PS-*b*-PMMA. The initial stack consists of a 10-nm silicon oxide (SiO₂) hard mask layer deposited over the silicon substrate. The neutral layer composed of PS-*r*-PMMA with a thickness of around 5 nm was deposited over the SiO₂ layer in order to self-assemble the modified PS-*b*-PMMA block copolymer into vertical lamellae with a thickness of around 16 nm. At this point of the thesis, the ACE chemo-epitaxy flow was not yet adapted to the 18-nm pitch and, therefore, all studies have been conducted on free surface wafers with the fingerprint-like morphology.

We estimate that there should be at least 15 nm of PS plus neutral layer left after PMMA removal to ensure the correct pattern transfer into the SiO₂ hard mask, which means that the high- χ BCP requires a PMMA:PS selectivity of at least 3.5 due to its reduced initial thickness (around 16 nm). Once a PMMA removal process that fits the desired selectivity criteria has been identified, the pattern transfer into the SiO₂ hard mask shall be used to validate the etching approach developed.

We have started by studying PS and PMMA homopolymers to characterize the modified high- χ PS-*b*-PMMA, as well as the PMMA:PS selectivity for different plasma etching chemistries. Once the plasma chemistries that achieve good selectivity between PS and PMMA have been identified, they shall be evaluated on high- χ PS-*b*-PMMA patterned wafers with fingerprint-like morphology.

Part of the work presented in this Chapter has been published in the journal *Microelectronic Engineering* [Gusmão 2020].

IV.1 Modified Polystyrene (PS) and Polymethyl methacrylate (PMMA) homopolymer results

The modifications done to the standard PS-*b*-PMMA in order to obtain the modified version with higher χ and smaller pitch were not detailed by Brewer Science Inc. and Arkema for confidentiality reasons. Therefore, it is important to characterize both materials and compare them to the standard PS and PMMA. This information should help us understand the etching mechanisms involved in order to obtain a good PMMA:PS selectivity for this BCP.

For the X-ray photoelectron spectroscopy (XPS) and etch rate results presented throughout this section, PS and PMMA homopolymer solutions with the modified high- χ chemistry were spin-coated on 300 mm silicon blanket wafers and then annealed to obtain 50-nm films. The procedure for obtaining polymer films has been detailed in Chapter II.1.2.

IV.1.1 Characterization of modified PS and PMMA homopolymers

The surface composition of modified PS and PMMA homopolymers, identified as “hPS” and “hPMMA” respectively, was characterized by XPS. Even though XPS only allows the analysis of the first 10 nm of the surface of these materials, we can consider that the results presented in Figure IV-2 represent the bulk of both the PS and PMMA films because they are homogeneous before etching.

Figure IV-2(a) shows a comparison of the full survey spectra (binding energies between 0 and 750 eV) for the two homopolymers. The first peak detected around 285 eV corresponds to the carbon C1s peak and is observed for both PMMA and PS. The second peak detected around 533 eV corresponds to the oxygen O1s peak and is only observed for PMMA [Beamson 1992]. It is important to notice that hydrogen cannot be detected by XPS. Therefore, we can conclude that PS consists only of carbon and hydrogen, while PMMA consists of carbon, oxygen and hydrogen. These observations correspond to the standard PS and PMMA structures presented in Figure II-1 of Chapter II.1.1.1.

From Figure IV-2(b), which represents the C1s spectra for both modified PS and PMMA, we notice that the XPS analysis for the PS presents two peaks: one around 284.8 eV and another around 291.5 eV. The peak at 284.8 eV is the sum of two contributions: the first at 284.7 eV, which corresponds to the aliphatic carbon (carbon bonds without an aromatic ring), and the second at 285 eV, which corresponds to the phenyl compound (C₆H₅-R). Due to the small difference in binding energy between both bonds, they cannot be dissociated with the spectral resolution used. Therefore, these peaks will be represented together as C-C/C=C. The other peak is observed at 291.5 eV and represents a shake-up peak characteristic of the aromatic cycle, represented as $\pi \rightarrow \pi^*$ [Beamson 1992].

As for PMMA, the C1s peaks are as follows: a peak at 285.0 eV represents both the carbon resulting from the methylene (-CH₂) and methyl (-CH₃) groups at 284.7 eV and the carbon from the acrylate compounds (CHCOOH) at 285.5 eV. The sum of both contributions will be represented as C-C/C=C in Figure IV-2(d), even though the PMMA does not present C=C double bonds, because it corresponds to the same binding energy value of the C-C/C=C PS peak. The second peak appears at 286.5 eV and represents the carbon in the methyl ester (C-O) bonds. The last one, located at 288.8 eV, corresponds to the carbon in the carboxyl group (C=O) [Beamson 1992].

The O1s peaks observed in Figure IV-2(c) confirm the observations already made. PS does not present any O1s peaks, while PMMA presents a first peak at 532.0 eV and the other one at 533.7 eV corresponding to O=C and O-C bonds, respectively [Beamson 1992].

Finally, following the analysis of the various contributions present in PS and PMMA, we can quantify each of them and thus define the composition of these two polymers. Figure IV-2(d) shows that the PS is only composed of carbon-carbon and carbon-hydrogen bonds, as expected by the known formula of the material presented in Figure II-1 of Chapter II.1.1.1. Regarding the PMMA, we observe a composition of 72.7% carbon and 27.3% oxygen since hydrogen cannot be detected by XPS. This result is consistent with the values that can be calculated from the mass of each element and the abbreviated formula of PMMA (C₆H₅O₂) [Beamson 1992].

Therefore, we can conclude that the modified high- χ PS and PMMA present a composition similar to that of the standard PS and PMMA.

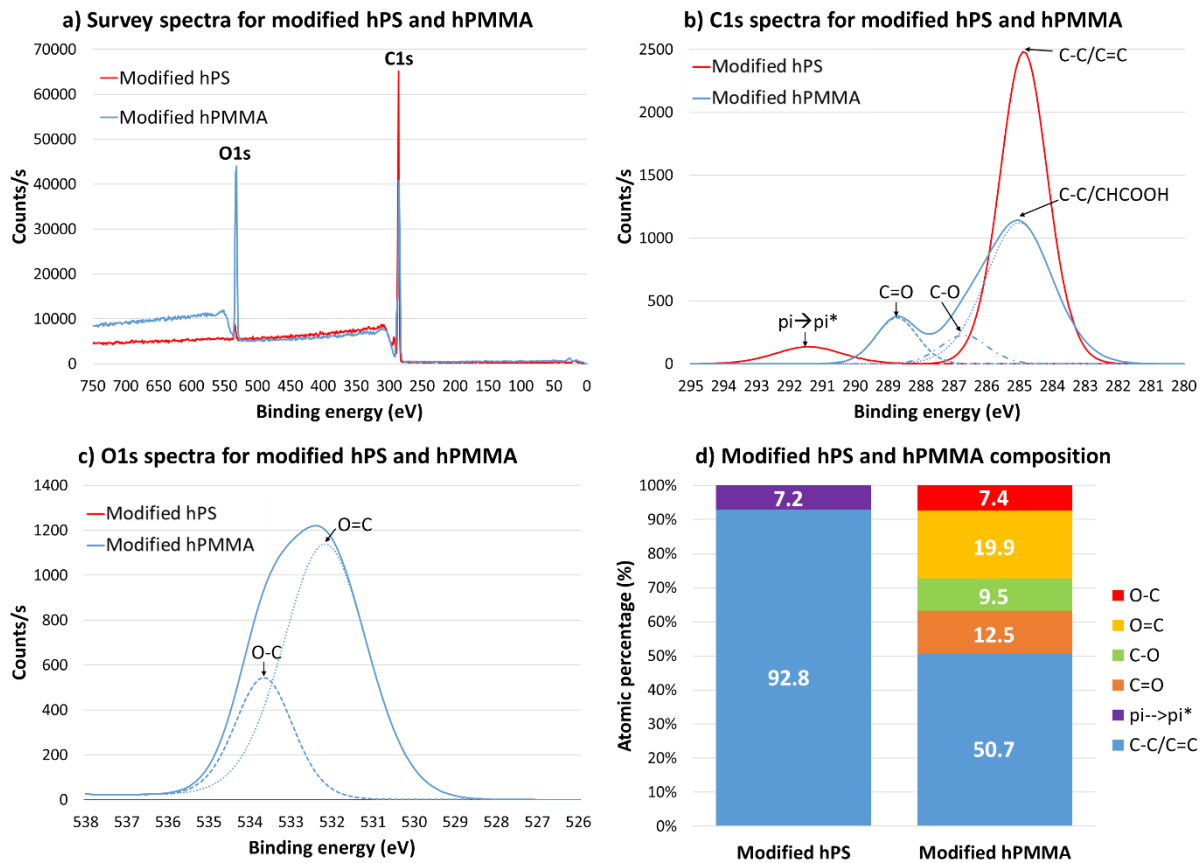


Figure IV-2: Surface composition of modified PS and PMMA homopolymers obtained by *ex-situ* XPS: (a) survey spectra; (b) C1s spectra; (c) O1s spectra; and (d) atomic percentage of each peak identified on the C1s and O1s spectra. The results correspond to an incident angle of 23.75°.

IV.1.2 Evaluation of different plasma chemistries for PMMA removal selectively to the PS

As we have seen in Chapter I.5.1, the main difficulty in the PS-*b*-PMMA etching is to obtain high selectivity between PMMA and PS films, since both are organic blocks. The PMMA removal selectively to PS is usually preferred, since PMMA presents a higher plasma etching

rate according to the Ohnishi parameter, which is based on the observation that materials containing a high concentration of C–O and C=O groups exhibit much higher sputter yields than pure carbon materials [Ohnishi 1983].

The first chemistries developed for the selective PMMA removal regarding the PS were based on O₂. However, this chemistry only achieves a selectivity of around 2.0 on homopolymer wafers [Liu 2007]. The other disadvantage of the O₂ only approach is the lack of dimensional control, since oxygen leads mainly to an isotropic etching, thus inducing a lateral consumption of the patterns. In order to increase the PMMA:PS selectivity and improve dimensional control, O₂ was then combined with a chemically inert gas, such as argon (Ar), which does not induce lateral etching. Ting *et al.* showed that adding argon to the O₂ plasma does not improve selectivity, which is still around 2.0, but it improves pattern roughness. They also showed that a PMMA:PS selectivity of around 3.6 can be achieved when argon is used on its own, because only the bonds resistance to ion bombardment determines the selectivity between the two materials, thus the PS is consumed very little by this plasma. However, the results obtained on lamellar patterns show that with a pure Ar plasma, the resulting PS domains have a rough surface and wider CD than expected. Indeed, the PS seems to deform and occupy the space left by the PMMA. Therefore, pure Ar does not allow the conservation of the patterns [Ting 2008]. Finally, based on these results, Chan *et al.* developed a cyclic Ar + Ar/O₂ approach, leading to a selectivity of around 3.0 [Chan 2014]. Despite these improvements, O₂-based chemistries are limited in terms of PMMA:PS selectivity and dimensional control.

One of the alternatives to O₂ is the use of carbon monoxide (CO), in which oxygen is responsible for etching while carbon allows for better selectivity between both blocks. Sarrazin *et al.* evaluated the behavior of CO etching on PS and PMMA homopolymers. They observed that while PMMA is etched, a deposit is created on the PS. However, after 10 seconds of CO plasma, an etch saturation is verified for the PMMA. In order to avoid an etch stop and completely remove the PMMA, a small amount of hydrogen (H₂) is added to control the polymerization, thus allowing a 50-nm PMMA film to be fully etched with a selectivity around 12.0. However, when applying this chemistry to PMMA cylinders, this selectivity decreases to around 3.5 [Sarrazin 2016]. To improve the selectivity, Sarrazin *et al.* developed a cyclic approach based on CO + CO/H₂ combining the higher selectivity of CO with the polymerization control of CO/H₂ [Sarrazin 2018]. The CO + CO/H₂ plasma cycles were shown to be suitable for the cylindrical application, with infinite PMMA:PS selectivity, but present limitations for lamellar application: higher PS consumption due to a higher amount of oxygen (coming from PMMA) released during etching leads to lower selectivity (around 6.0) [Sarrazin 2017]. Therefore, an oxygen-free chemistry based on CH₄/N₂ was developed by Sarrazin *et al.* to obtain infinite selectivity with lamellar PS-*b*-PMMA with a 38-nm pitch [Sarrazin 2019].

This section shall present an evaluation of the etch rate of different plasma etching chemistries applied to modified PS and PMMA homopolymers. The goal is to identify the chemistries that might be interesting for the 18-nm pitch high- χ PS-*b*-PMMA, namely regarding the PMMA:PS selectivity. The plasma parameters for the different chemistries tested are presented in Table IV-1. All of the experiments for this section were performed in the 300 mm Kiyoo FX® ICP reactor from LamResearch®, which was already presented in Chapter II.2.1.2.

Table IV-2 presents the PS and PMMA homopolymer etch rates, as well as the corresponding PMMA:PS selectivity, calculated by applying the different etching chemistries presented in Table IV-1 for 10 seconds.

The first chemistry evaluated was a CH₃F/Ar/SO₂ plasma proposed as a Best-Known Method (BKM) by LamResearch®. This recipe presents a RF bias pulsing mode, which consists of alternating two cycles during a single step, according to the specified pulsing frequency: one cycle of RF Bias ON and one cycle of RF Bias OFF. As we have seen in Chapter II.2.1.2, the RF Bias in an ICP reactor is the parameter that allows us to have a strong ion bombardment and thus increase the anisotropic aspect of the etching. The pulsing mode usually allows for better profile and selectivity, since it increases the uniformity of the passivation layer [Agarwal 2009]. Indeed, during RF bias OFF, the passivation layer is deposited on the sidewalls without the effect of ion bombardment, which may consume the mask through sputtering and also lead to a faceted profile. For this recipe, the RF bias pulsing conditions were: duty cycle, which corresponds to the percentage of ON time, at 31% and pulsing frequency at 300 Hz. These parameters shall not be varied during our studies. The CH₃F/Ar/SO₂ plasma presented a PMMA:PS selectivity of 3.5 on blanket homopolymers.

The second plasma evaluated was an Ar/O₂ plasma, which has been vastly studied in the literature and, for the parameters chosen, presented a selectivity of 3.4, superior to the results shown in the literature, but still inferior to the other plasma etching chemistries presented in Table IV-2. And the third one was the oxygen-free etching based on CH₄/N₂, which presents infinite PMMA:PS selectivity since no PS was consumed.

Table IV-1: Plasma parameters for the different chemistries tested on modified PS and PMMA homopolymers.

Chemistry	Pressure (mTorr)	Power (W)	Bias (V)	Flow (sccm)
CH ₃ F/Ar/SO ₂	10	250	-650 (pulsed)	30/200/150
Ar/O ₂	10	220	-100 (continuous)	50/5
CH ₄ /N ₂	10	500	-200 (continuous)	50/50

Table IV-2: Modified PS and PMMA homopolymer etch rates, as well as the corresponding PMMA:PS selectivity, calculated for the different etching chemistries. Etching duration was 10 seconds.

Chemistry	Etch rate modified hPS (nm/s)	Etch rate modified hPMMA (nm/s)	hPMMA:hPS selectivity
CH ₃ F/Ar/SO ₂	1.3	4.6	3.5
Ar/O ₂	0.8	2.7	3.4
CH ₄ /N ₂	0.0	1.1	∞

Based on these preliminary results, the $\text{CH}_3\text{F}/\text{Ar}/\text{SO}_2$ and CH_4/N_2 plasma chemistries, which fulfill our requirement by presenting a PMMA:PS selectivity ≥ 3.5 , have been selected for testing on the modified high- χ PS-*b*-PMMA and the results shall be presented throughout the next section.

In this section, we have characterized the composition of the modified PS and PMMA homopolymers that compose the high- χ modified PS-*b*-PMMA block copolymer. We have concluded that the modified PS-*b*-PMMA presents a composition similar to that of standard PS-*b*-PMMA: indeed, modified PS is composed of carbon and hydrogen with an aromatic ring, while modified PMMA is an aliphatic compound composed of carbon, hydrogen and oxygen.

We have also seen the evolution of the PMMA removal through plasma etching, which has seen an improvement on PMMA:PS selectivity throughout the years thanks to different gases used. Then, we selected some of these well-known plasma chemistries and we evaluated their etch rate, and consequent selectivity, on modified PS and PMMA homopolymers, therefore selecting two different chemistries that fulfill our selectivity requirement: $\text{CH}_3\text{F}/\text{Ar}/\text{SO}_2$ and CH_4/N_2 .

IV.2 Application to high- χ PS-*b*-PMMA films with lamellar morphology

In this section, we shall apply the selected plasma chemistries from the previous section to the high- χ modified PS-*b*-PMMA with two different pitch: the 18-nm pitch, also known as “high- χ L18”, and a 32-nm pitch modified PS-*b*-PMMA, which shall be referred to as “high- χ L32”. The high- χ L32 presents the same modified chemistry of the high- χ L18, but with a larger pitch (32 nm) and initial thickness (36 nm).

All high- χ PS-*b*-PMMA experiments were conducted on 300 mm silicon wafers with a 10-nm SiO_2 layer. A thin neutral layer composed of PS-*r*-PMMA random copolymer is spin-coated on the substrate before the BCP deposition in order to neutralize the surface. Then, the BCP solution is spin-coated and annealed to form the vertical lamellae morphology. The L18 BCP presents the dimensions shown in Figure IV-1(1). For the high- χ L32, the neutral and BCP layer thicknesses are around 8 and 36 nm, respectively.

IV.2.1 Impact of high- χ modified PS-*b*-PMMA chemistry for same pitch and plasma chemistry

In section IV.1.1, the XPS analysis of the modified PS and PMMA have shown no significant difference in composition between standard and modified PS-*b*-PMMA. In this section, our goal is to verify if the high- χ modified PS-*b*-PMMA chemistry has no impact on the etching of this BCP when applied to patterned wafers. In order to do so, the same PMMA removal process shall be applied to two block copolymers with same pitch and initial thickness: the high- χ L32 BCP and a standard PS-*b*-PMMA, also with 32-nm pitch, which we have already used throughout chapter III. The same neutral layer (NL) is used for both copolymers and the BCP's initial thickness is also the same (36 nm), leading to a BCP + NL initial thickness of 44 nm. The top-view and cross-section SEM images of the high- χ L32 and standard L32 PS-*b*-PMMA

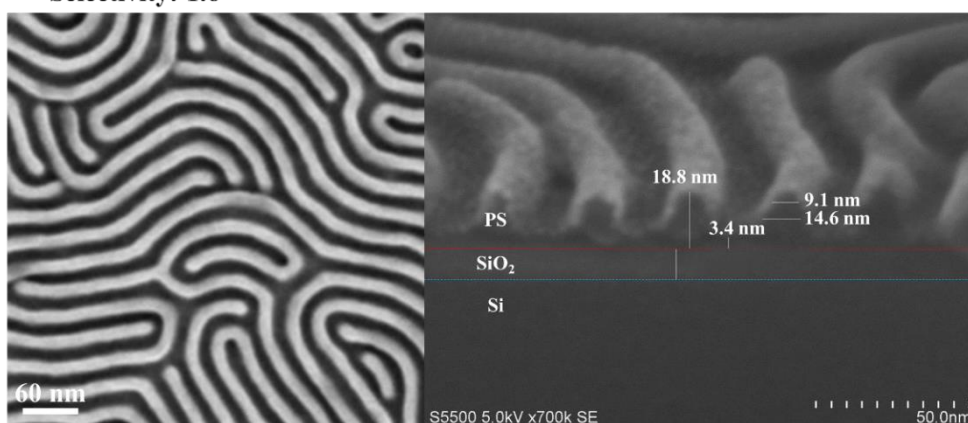
block copolymer after PMMA removal using the $\text{CH}_3\text{F}/\text{Ar}/\text{SO}_2$ plasma for 12 seconds are presented in Figure IV-3.

From Figure IV-3(a), we observe that after PMMA removal during 12 seconds, the PMMA has been completely removed and around 3.4 nm of neutral layer remain, which translates to a total PMMA + NL consumed thickness of 40.6 nm. Moreover, the PS + NL remaining thickness is around 18.8 nm, meaning 25.2 nm of PS have been consumed. Therefore, the PMMA:PS selectivity for the high- χ L32, determined by the ratio between consumed PMMA+NL (40.6 nm) and consumed PS (25.2 nm) is approximately 1.6.

The same calculation can be done for the standard L32, based on the results of Figure IV-3(b): after PMMA removal for the same duration, the PMMA has also been completely removed and around 2.7 nm of neutral layer remain, which translates to a PMMA + NL consumed thickness of 41.3 nm. Moreover, the PS + NL remaining thickness is around 18.5 nm, meaning 25.5 nm of PS have been consumed. Therefore, the PMMA:PS selectivity for the standard L32 is approximately 1.6, similar to the high- χ L32.

Furthermore, the CD measurements in Figures IV-3(a) and (b) are quite similar for both block copolymers and the line patterns present the same profile, with a difference of approximately 5.5 nm between the top CD (~ 9 nm) and the bottom CD (~ 14.5 nm).

a) $\text{CH}_3\text{F}/\text{Ar}/\text{SO}_2$ on high- χ L32
Selectivity: 1.6



b) $\text{CH}_3\text{F}/\text{Ar}/\text{SO}_2$ on standard L32
Selectivity: 1.6

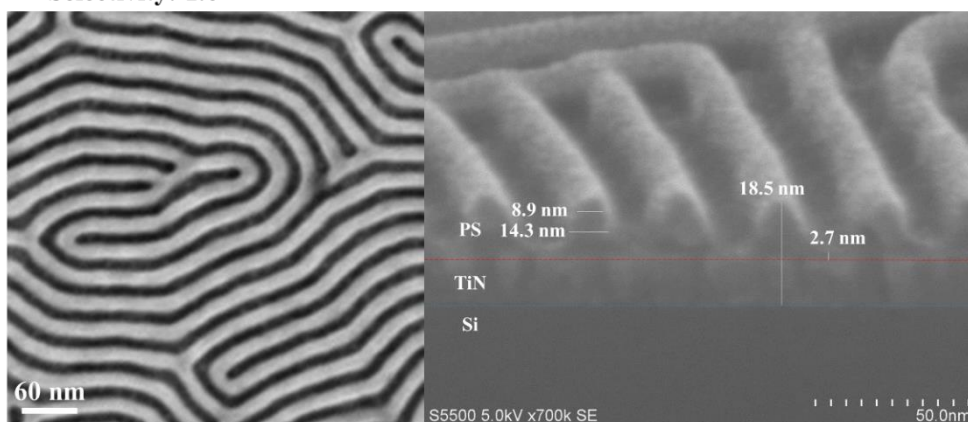


Figure IV-3: Top-view and cross-section SEM images of the (a) high- χ L32 and (b) standard L32 PS-*b*-PMMA block copolymer after PMMA removal using the $\text{CH}_3\text{F}/\text{Ar}/\text{SO}_2$ plasma for 12 seconds.

Therefore, we can conclude that, for the same pitch and initial thickness, the high- χ modified PS-*b*-PMMA chemistry does not present a significant impact on the PMMA plasma etching when compared to the standard PS-*b*-PMMA block copolymer.

It should also be noticed that the selectivity on free surface pattern wafers is lower compared to that of the homopolymer wafers presented in Table IV-2, which has already been observed in the literature and indicates that new etching mechanisms come into place when the two block copolymer's phases interact.

IV.2.2 Impact of pitch and film thickness on the etching of high- χ modified PS-*b*-PMMA

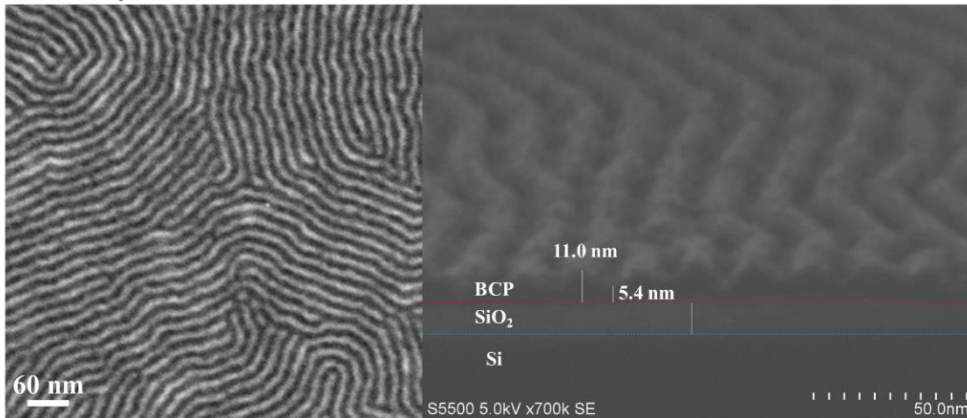
Now that we have shown that the high- χ modified PS-*b*-PMMA chemistry does not present a significant impact on the PMMA etching, our goal is to verify the impact of the reduced pitch and film thickness of the high- χ PS-*b*-PMMA on the PMMA removal. In order to do so, we shall apply the CH₃F/Ar/SO₂ and CH₄/N₂ plasma chemistries, selected in section IV.1.2 for their good PMMA:PS selectivity, on the high- χ PS-*b*-PMMA with two different pitch and initial thickness: L18 and L32. As we have seen before, the high- χ L18 presents a pitch of 18 nm and initial thickness of 16 nm, leading to a total BCP+NL initial thickness of 21 nm. As for the high- χ L32, it presents a pitch of 32 nm and a total BCP+NL initial thickness of 44 nm.

For the etching of the high- χ PS-*b*-PMMA, we have estimated that there should remain at least 15 nm of PS plus neutral layer after PMMA removal to ensure the correct pattern transfer into the SiO₂ hard mask. For the high- χ L32, this means a selectivity superior to 1.5. However, for the high- χ L18, due to its reduced initial thickness of 21 nm, the desired selectivity is around 3.5. Therefore, the BCP with smaller pitch requires higher selectivity when compared to the same BCP with larger pitch. This increases the importance of developing a plasma etching process that allows for high selectivity between both phases of the high- χ BCP.

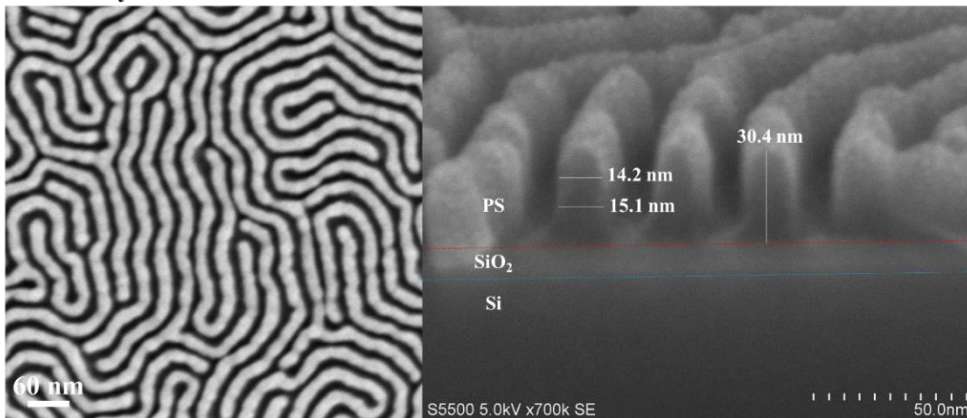
Figure IV-3(a) already presented the results for high- χ L32 after CH₃F/Ar/SO₂, which leads to a PMMA:PS selectivity of 1.6 and a PS+NL remaining thickness of 18.8 nm after 12 seconds of etching. Figure IV-4(a) presents the SEM images for the high- χ L18 after CH₃F/Ar/SO₂ for 6 seconds. In this case, the PMMA has almost been completely removed and around 5.4 nm of PMMA + neutral layer remain, which translates to a total PMMA + NL consumed thickness of 15.6 nm. Moreover, the PS + NL remaining thickness is around 11 nm, meaning 10 nm of PS have been consumed. Therefore, the PMMA:PS selectivity for the high- χ L18, determined by the ratio between consumed PMMA+NL (15.6 nm) and consumed PS (10 nm) is approximately 1.6, similar to the selectivity obtained for the high- χ L32 using the same chemistry.

As for the oxygen-free PMMA removal based on CH₄/N₂, Figure IV-4(b) shows that, for the high- χ L32, the PMMA and its subjacent neutral layer have both been completely removed after 60 seconds of etching. This translates to a total PMMA + NL consumed thickness of 44 nm. Moreover, the PS + NL remaining thickness is around 30.4 nm, meaning 13.6 nm of PS have been consumed. Therefore, the PMMA:PS selectivity for the high- χ L32 with the oxygen-free chemistry is approximately 3.2. Finally, for the same chemistry applied to high- χ L18, Figure IV-4(c) shows that 13.3 nm of PMMA and 5.1 nm of PS have been consumed after 30 seconds of etching, leading to a PMMA:PS selectivity of 2.6, which is slightly inferior when compared to the L32.

a) CH₃F/Ar/SO₂ on high- χ L18
Selectivity: 1.6



b) CH₄/N₂ on high- χ L32
Selectivity: 3.2



c) CH₄/N₂ on high- χ L18
Selectivity: 2.6

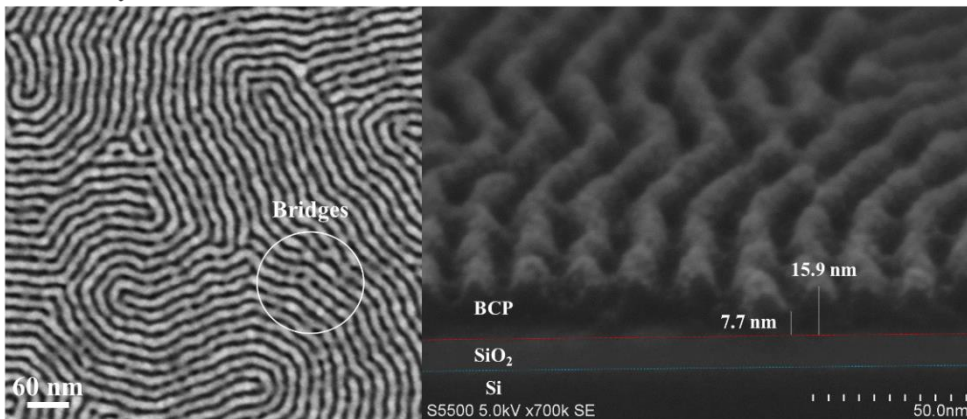


Figure IV-4: Top-view and cross-section SEM images of the (a, c) high- χ L18 and (b) high- χ L32 PS-*b*-PMMA block copolymers after PMMA removal using two different plasma chemistries: (a) CH₃F/Ar/SO₂ and (b, c) CH₄/N₂. It should be noticed that the cross-section SEM measurements are approximations, due to the tool's lower precision when using higher magnification.

Many conclusions can be drawn based on these results. It is important to notice that, once again, for both plasma chemistries investigated, the selectivity on free surface pattern wafers is lower compared to that of the homopolymer wafers presented in Table IV-2. For example, the CH₄/N₂ selectivity decreases from infinite on homopolymers to around 3.0 on free surface

wafers, confirming that new etching mechanisms come into place when the two block copolymer's phases interact. As we have seen on the XPS analysis of the PMMA homopolymers presented in section IV.1.1, PMMA presents C-O and C=O bonds. During plasma etching of the PS-*b*-PMMA BCP, these C-O simple and double bonds are broken, forming volatile oxygen-containing by-products, which probably interact with the PS phase and induce its consumption.

It should also be noticed that, for the same CH₄/N₂ etching, the high- χ L18 BCP presents lower selectivity compared to the high- χ L32. This might be due to the fact that the etching time is shorter for the BCP with smaller thickness, and thus indicates a dependence of the PMMA:PS selectivity on the etching duration for this chemistry. However, it is important to highlight that the cross-section SEM measurements are approximations, due to the tool's lower precision when using higher magnification. Therefore, we cannot determine the degree of significance of the difference in selectivity between both pitch.

In order to better evaluate the results for the high- χ L18, we proceeded to the pattern transfer into the SiO₂ hard mask after removing the PMMA with the two different plasma chemistries. For the SiO₂ etching, we used a CHF₃/CF₄ plasma for 8 seconds with the following parameters: 50/50 sccm, pressure 4 mTorr, RF power 625 W and RF bias 110 V. The results can be found in Figure IV-5.

Regarding the CH₃F/Ar/SO₂ etching, we have seen that it leads to a PMMA:PS selectivity of 1.6. However, while for the high- χ L32, the low 1.6 selectivity is still enough to ensure the pattern transfer into the SiO₂ layer, the same cannot be said for the high- χ L18. Indeed, with a selectivity of 1.6, Figure IV-5(a) shows that the same chemistry cannot allow the pattern transfer when applied to the BCP with 18-nm pitch.

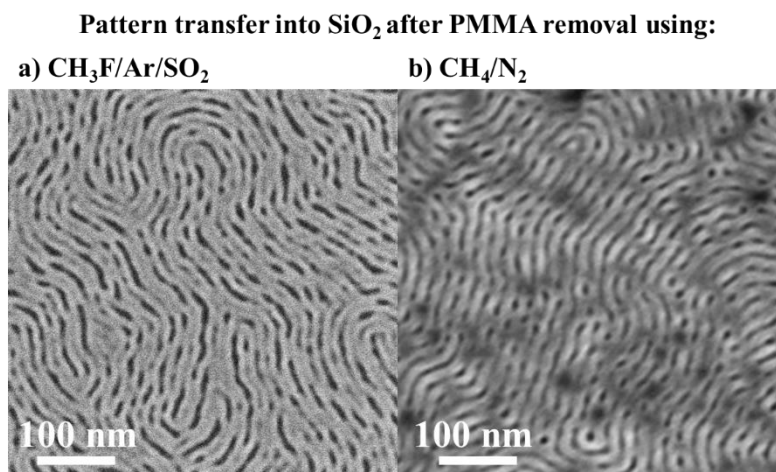


Figure IV-5: Top-view SEM images of the high- χ L18 PS-*b*-PMMA block copolymer after pattern transfer into the SiO₂ hard mask. The PMMA removal was conducted using two different plasma chemistries: (a) CH₃F/Ar/SO₂, and (b) CH₄/N₂.

As for the CH₄/N₂ etching, the top-view image in Figure IV-4(c) highlights the formation of bridges between the PS lines for the high- χ L18, which were not present on the high- χ L32 PS-*b*-PMMA shown in Figure IV-4(b). Figure IV-5(b) shows that these bridges prevent the complete pattern transfer of the PS lines into the SiO₂ hard mask. The origin of these bridges will be further explored in section IV.3.3.

In this section, we have characterized the impact of the modified chemistry, pitch and initial thickness on the etching of the high- χ modified PS-*b*-PMMA.

When comparing a modified and a standard PS-*b*-PMMA BCP with the same pitch and initial thickness, we conclude that, for the same plasma etching chemistry, the high- χ modified PS-*b*-PMMA chemistry does not present a significant impact on the PMMA plasma etching when compared to the standard PS-*b*-PMMA block copolymer.

However, when comparing the high- χ modified PS-*b*-PMMA with two different pitch (18 and 32 nm) and two different initial thickness (16 and 36 nm, respectively), for the high- χ L18 BCP, the same etching chemistries that were validated for larger pitch (32 nm) present different problems that prevent pattern transfer into the SiO₂ hard mask for the smaller BCP. When using CH₃F/Ar/SO₂ plasma, there is probably not enough PS budget remaining for L18 pattern transfer and, when using the CH₄/N₂ plasma, bridges are formed between the PS lines, preventing L18 pattern transfer.

Therefore, we can conclude that the main high- χ L18 PS-*b*-PMMA plasma etching difficulties come from its small dimensions, namely the pitch and initial thickness.

IV.3 Alternatives for the etching of high- χ PS-*b*-PMMA films with 18-nm pitch

We have seen in the previous section that, for the high- χ L18 BCP, two main types of difficulties can be identified: (1) not enough PS budget remaining for pattern transfer and (2) formation of bridges between the PS lines. The first one is quite evident for highly reactive chemistries, such as CH₃F/Ar/SO₂ and Ar/O₂ (not represented), that present lower PMMA:PS selectivity due to the reactivity between oxygen and both organic blocks of the high- χ L18 BCP. The second one is observed for highly passivating chemistries, such as CH₄/N₂ and CO/H₂ (not represented), whose selectivity mechanism is mostly based on the deposition of carbon-based passivating layers over the PS [Sarrazin 2017].

This next section shall present different approaches explored throughout this PhD thesis with the goal of increasing the PMMA:PS selectivity for the high- χ L18 PS-*b*-PMMA in order to validate the pattern transfer into the SiO₂ and Si subjacent layers, while also avoiding the formation of defects, such as bridges.

IV.3.1 First approach: argon-based PMMA removal

The first approach that shall be presented focuses on optimizing the BKM recipe, based on CH₃F/Ar/SO₂, which presents low selectivity (around 1.6) for the high- χ L18, but no bridge formation after PMMA removal. First, a process window for this recipe will be determined by varying some plasma parameters, such as the RF bias and the gas flow. Then, the impact of increasing the block copolymer thickness will be evaluated. Finally, a cyclic approach with argon-based steps shall be explored.

IV.3.1.1 Process window for high- χ L18 with argon-based PMMA removal

For this study, one of the main challenges is to characterize the high- χ L18 block copolymer after the PMMA removal step, namely due to the small dimensions of the copolymer (pitch and

remaining PS thickness) coupled with the charging effects typical of polymeric materials during cross-section SEM observations. For example, when observing the top-view SEM images after PMMA removal using the CH₃F/Ar/SO₂ plasma for 6 seconds, which are presented in Figure IV-4(a), it may seem as though we have succeeded in completely removing the PMMA. However, when we proceed to the pattern transfer into the silicon oxide, presented in Figure IV-5(a), we observe that the lines pattern is not conserved. Indeed, these images indicate that the pattern transfer is not complete, which means the PMMA removal step's duration was not enough.

We then started by varying the etch time of the CH₃F/Ar/SO₂ plasma while conserving the other parameters presented in Table IV-1. The SEM images are not presented here because, for shorter durations ($\Delta t = 5$ seconds), the results are similar to the ones observed in Figure IV-4(a), while for longer durations ($\Delta t = 7$ seconds) the lines pattern is no longer discernible, which means the PS has probably been completely consumed and there is no more budget for pattern transfer. These results indicate that the CH₃F/Ar/SO₂ plasma presents a very narrow process window, mostly due to the high PMMA and PS etch rates when compared to the other chemistries evaluated (Table IV-2). A narrow process window is undesired for manufacturing processes in a microelectronics fab, since the smallest variation in the process can lead to very different results.

Therefore, in order to reduce the etch rate of both blocks and obtain a larger process window, we have decided to reduce the RF bias voltage of the recipe, which was set at 325V instead of the original 650V. Indeed, the RF bias, also known as self-bias voltage, is the main responsible for the ion acceleration inside the plasma reactor chamber. Since the argon ions – which are inert and do not react with the BCP blocks – are accelerated by the self-bias voltage and thus participate on the physical sputtering of the BCP, the RF bias voltage is one of the parameters that influence the etch rate. To verify the reduction of the etch rate with the lower RF bias, modified PS and PMMA homopolymer thickness was measured before and after etching with CH₃F/Ar/SO₂ 325V for 10 seconds. The etch rates for PS and PMMA were calculated at 0.7 nm/s and 2.3 nm/s, respectively, which means the etch rate for both materials is reduced by half with the lower bias when compared to the original values for 650V presented in Table IV-2.

The results for the CH₃F/Ar/SO₂ plasma with reduced bias are presented in Figure IV-6. Figures IV-6(a, b, c) present the top-view images after PMMA removal for different etching durations (Δt between 11 and 17 seconds), while Figures IV-6(d, e, f) present the SEM images after pattern transfer into the SiO₂ in order to verify whether the PMMA has been completely removed. Based on the top-view SEM images after SiO₂ etching, we can observe that, for the PMMA removal for 11 and 14 seconds, the etch duration was not enough to ensure the complete removal of the PMMA and therefore the correct pattern transfer, leading to wiggling and eventual pattern collapse. On the other hand, for the PMMA removal during 17 seconds, there was not enough PS budget remaining for pattern transfer and the lines pattern was no longer discernible. These results indicate that the CH₃F/Ar/SO₂ process window is still very narrow even with the lower bias.

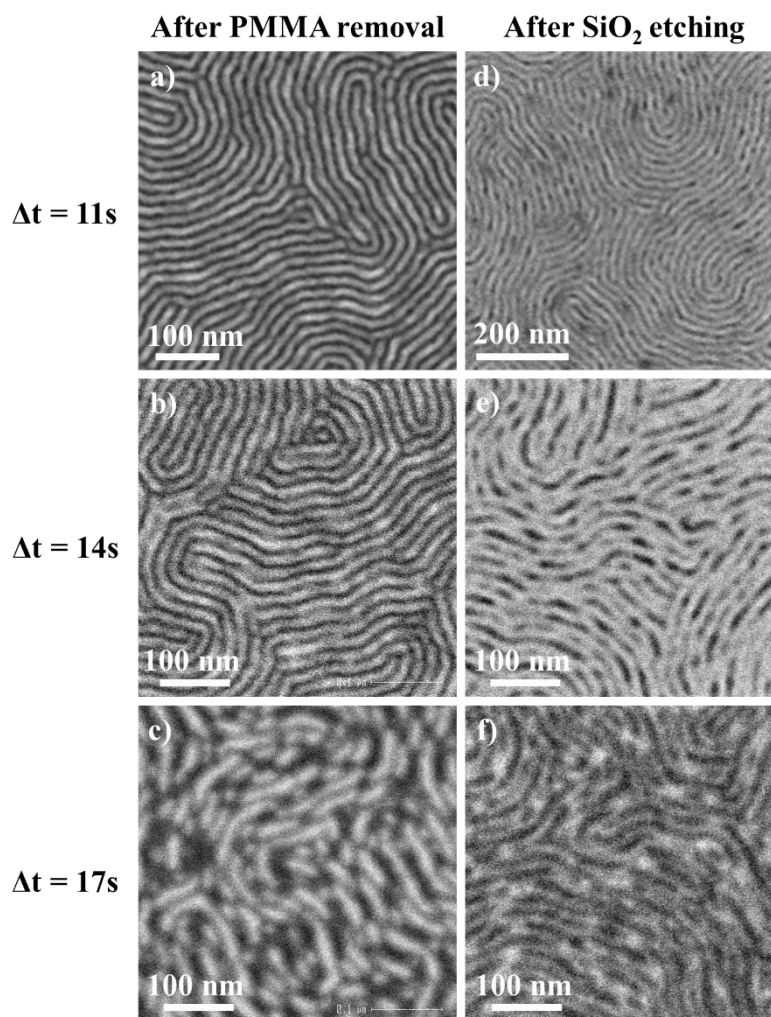


Figure IV-6: Top-view SEM images of the high- χ L18 block copolymer (a, b, c) after PMMA removal using $\text{CH}_3\text{F}/\text{Ar}/\text{SO}_2$ with reduced bias and (d, e, f) after pattern transfer into the SiO_2 hard mask using CHF_3/CF_4 plasma for 8s. The PMMA removal duration was varied and is indicated on the left by Δt : (a, d) 11s; (b, e) 14s; and (c, f) 17s.

Since the $\text{CH}_3\text{F}/\text{Ar}/\text{SO}_2$ recipe presents some carbon passivation in the form of CH_3F , we then tried removing the CH_3F from the recipe to verify if it was blocking the PMMA removal by depositing a fluorocarbon (C_xF_y) compound on the PS sidewalls. The results are not represented because they were similar to the ones obtained in Figure IV-6. For an etch duration of 14 seconds, the etch duration was not enough to ensure the correct pattern transfer, leading to pattern collapse, while for the PMMA removal during 17 seconds, there was not enough PS budget remaining for pattern transfer.

These results led us to conclude that the process window for the $\text{CH}_3\text{F}/\text{Ar}/\text{SO}_2$ plasma is very narrow due to the small dimensions – pitch and thickness – of the high- χ L18 BCP film.

In order to overcome the dimensional limitation and therefore increase the available PS budget after etching, we tried increasing the initial thickness of the high- χ L18 PS-*b*-PMMA film to 35 nm. However, Figure IV-7 shows that some pattern wiggling is observed after PMMA removal using the $\text{CH}_3\text{F}/\text{Ar}/\text{SO}_2$ plasma with the same parameters from Table IV-1. This is probably due to the high aspect ratio of the lines, which is superior to 2.0 after PMMA removal. Therefore, we can conclude that, while increasing the initial thickness could be

interesting to increase the PS budget available after etching, mechanical stability problems lead to pattern wiggling due to the high aspect ratio of the lines. Therefore, the smaller CD of the high- χ block copolymer limits the maximum initial thickness allowed for the BCP film in order to avoid pattern wiggling or collapse.

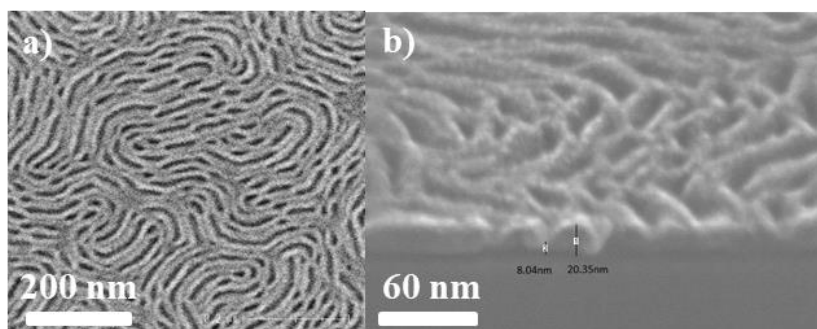


Figure IV-7: (a) Top-view and (b) cross-section SEM images after PMMA removal for the high- χ L18 PS-*b*-PMMA with 35-nm initial thickness, showing the wiggling phenomena.

IV.3.1.2 Cyclic approach on high- χ PS-*b*-PMMA

In section IV.1.2, we have seen that a pure argon (Ar) plasma allows for good PMMA:PS selectivity, but the resulting PS domains have a rough surface and wider CD than expected. Therefore, pure Ar does not allow the conservation of the patterns [Ting 2008]. From these results, a cyclic approach based on alternating Ar and Ar/O₂ steps have been developed by Chan *et al.* and present higher selectivity than Ar/O₂ only [Chan 2014]. We have tried a similar approach based on alternating CH₃F/Ar/SO₂ and Ar steps. Our goal is to improve the PMMA:PS selectivity, thanks to the highly selective argon step, and have better control of etching process window by using the CH₃F/Ar/SO₂ plasma with reduced bias (325V).

We started by evaluating the impact of the pure argon step on PS and PMMA modified homopolymers. The pure argon step was conducted in the Kiyō FX® ICP reactor from LamResearch® with the following plasma parameters: Ar flow 100 sccm, pressure 10 mTorr, RF power at 220W and RF bias at -100V. The etch rate of the Ar step applied to modified PS and PMMA homopolymers for 10 seconds was calculated as 0.03 and 2.0 nm/s, respectively. This leads to an excellent PMMA:PS selectivity on homopolymers of approximately 66.7.

We then evaluated the impact of this step on lamellar block copolymers. We chose to use the high- χ L32 BCP, because it is easier to characterize using cross-section SEM, allows for a larger process window due to its greater thickness compared to L18, and presented a similar selectivity to high- χ L18 for the CH₃F/Ar/SO₂ plasma (around 1.6 for both pitch). Figure IV-8 is a graphic representation of the PMMA and PS consumption, as well as the PMMA:PS selectivity, as a function of the pure Ar etching time when applied to the high- χ L32 BCP. We observe in Figure IV-8(a) that, for an etch duration of 5 seconds, less than 3 nm of PS have been consumed while around 13 nm of PMMA were consumed, leading to a high PMMA:PS selectivity of 4.4 represented in Figure IV-8(b). However, starting from an etch duration of 10 seconds, we observe a saturation phenomenon, also known as etch stop, for both PS and PMMA. Indeed, the pure argon step seems to stop etching the PS and PMMA after a consumption of 18 and 29 nm, respectively. Therefore, for etch durations equal or superior to 10 seconds, the PMMA:PS selectivity decreases to 1.6 and is no longer of interest to the cyclic

application. We have thus selected the duration of the argon step for the cyclic approach as 5 seconds, since it presents higher PMMA:PS selectivity and no etch stop on lamellar high- χ L32.

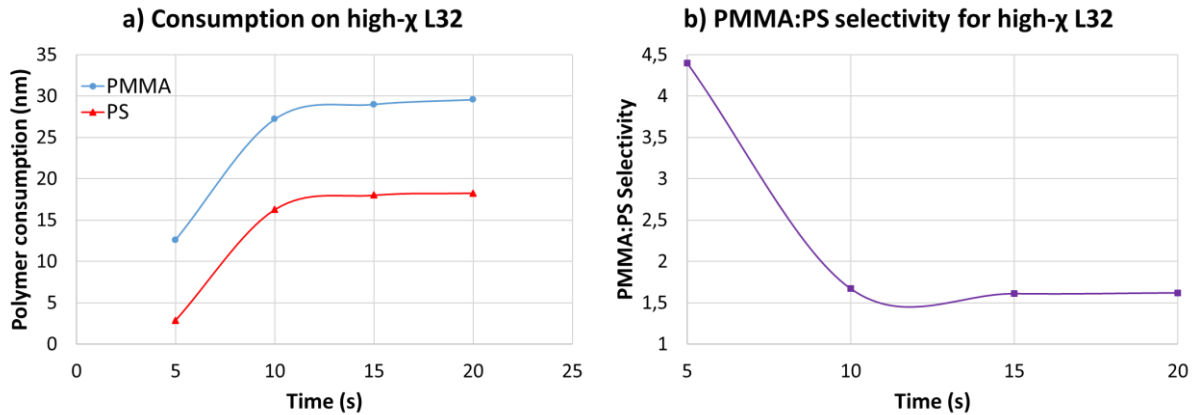
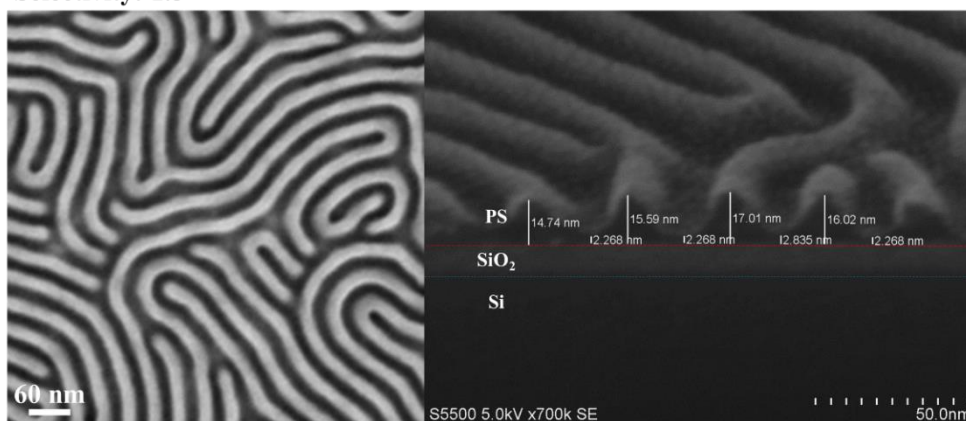


Figure IV-8: (a) PS and PMMA consumption and (b) PMMA:PS selectivity as a function of the argon etching time when applied to the high- χ L32 BCP.

Figure IV-9 presents the top-view and cross-section SEM images after the cyclic $\text{CH}_3\text{F}/\text{Ar}/\text{SO}_2 + \text{Ar}$ approach was applied to the high- χ L32 BCP for three complete cycles. The $\text{CH}_3\text{F}/\text{Ar}/\text{SO}_2$ 325V step duration was also set at 5 seconds to minimize the PS consumption. The results for the complete PMMA removal using only the $\text{CH}_3\text{F}/\text{Ar}/\text{SO}_2$ plasma with reduced bias during 25 seconds were also presented for comparison purposes. Figure IV-9(4) shows that the PMMA has been completely removed after 25 seconds of etching with the $\text{CH}_3\text{F}/\text{Ar}/\text{SO}_2$ plasma and around 2.4 nm of neutral layer remain. This translates to a total PMMA + NL consumed thickness of 41.6 nm. Moreover, the PS + NL remaining thickness is around 15.8 nm, meaning 29.2 nm of PS have been consumed. Therefore, the PMMA:PS selectivity for the high- χ L32 with the non-cyclic approach is approximately 1.5. As for the cyclic $\text{CH}_3\text{F}/\text{Ar}/\text{SO}_2 + \text{Ar}$ approach, Figure IV-9(b) shows that approximately 40.3 nm of PMMA and 27.6 nm of PS have been consumed after 3 complete cycles – which corresponds to a total of 30 seconds of etching –, leading to a PMMA:PS selectivity of 1.5, which is similar to the one calculated for the non-cyclic approach. Therefore, the cyclic approach based on alternating $\text{CH}_3\text{F}/\text{Ar}/\text{SO}_2$ and Ar steps does not present an improvement to the PMMA:PS selectivity.

a) After $\text{CH}_3\text{F}/\text{Ar}/\text{SO}_2$ for 25s
Selectivity: 1.5



b) After 3 cycles $\text{CH}_3\text{F}/\text{Ar}/\text{SO}_2$ 5s + Ar 5s
Selectivity: 1.5

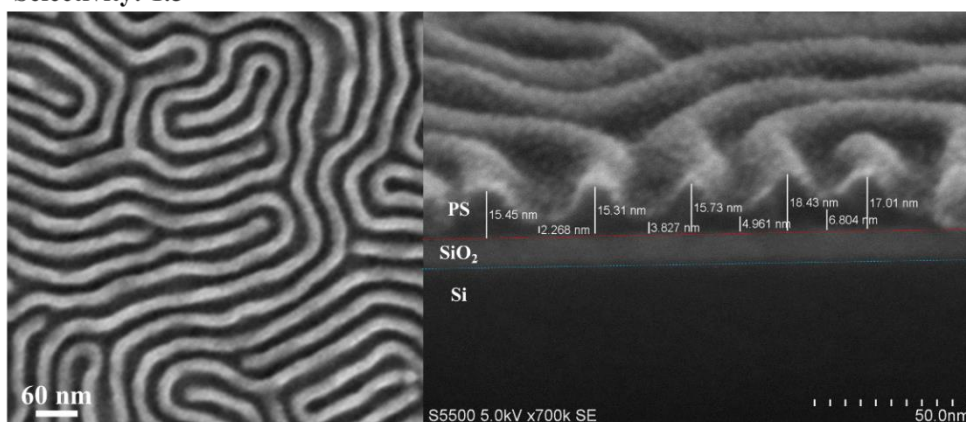


Figure IV-9: Top-view and cross-section SEM images of the high- χ L32 PS-*b*-PMMA after PMMA removal using: (a) $\text{CH}_3\text{F}/\text{Ar}/\text{SO}_2$ with reduced bias for 25 seconds and (b) 3 cycles of alternating $\text{CH}_3\text{F}/\text{Ar}/\text{SO}_2$ and Ar steps for 5 seconds each.

These results can be explained by the analysis of the extreme surface composition of the modified PS and PMMA homopolymers after etching with the $\text{CH}_3\text{F}/\text{Ar}/\text{SO}_2$ plasma, obtained through XPS with an incident angle of 76.25° , which analyzes approximately the first 3 nm of the surface. The etching time was set at 10 seconds to better evaluate the changes in surface composition of the modified PS and PMMA. When comparing the modified PS before etching presented in Figure IV-10(a) with the PS after etching presented in Figure IV-10(b), we observe that after etching the shake-up $\pi \rightarrow \pi^*$ peak disappears, which is characteristic of PS etching. Furthermore, C=O and C-O bonds represent around 67% of the final extreme surface composition after etching. Given the significant percentage of oxygen after etching, we may assume that it comes from both the oxygen present in the $\text{CH}_3\text{F}/\text{Ar}/\text{SO}_2$ plasma and from the air exposure between the etching and XPS tools. C-F bonds are also identified after etching, but cannot be differentiated from the C=O bonds due to the spectral resolution (C=O peak at 288.8 eV and C-F peak at 289.5 eV), hence being represented as “C=O, C-F” [Worley 1986]. Finally, around 12% of sulfur is identified after etching, represented by a $\text{S}2p_{3/2}$ peak at 164.4 eV, which may correspond to sulfur bound to the aromatic ring and is represented as $\text{S}(\text{C}_6\text{H}_5)$ [Riga 1978].

As for the modified PMMA after etching with $\text{CH}_3\text{F}/\text{Ar}/\text{SO}_2$ plasma, presented in Figure IV-10(d), we observe that the extreme surface composition is quite similar to that of the PS after

etching, except for the presence of sulfur, which is not observed for PMMA. The absence of sulfur is compensated by a 7% increase in the C-C bonds percentage and a slight increase (around 1 or 2%) for the other bonds. Therefore, the similar surface composition between PS and PMMA after etching with $\text{CH}_3\text{F}/\text{Ar}/\text{SO}_2$ could explain why adding an argon step does not improve the selectivity. Thus, this approach is not appropriate to improve the PMMA:PS selectivity for the high- χ PS-*b*-PMMA.

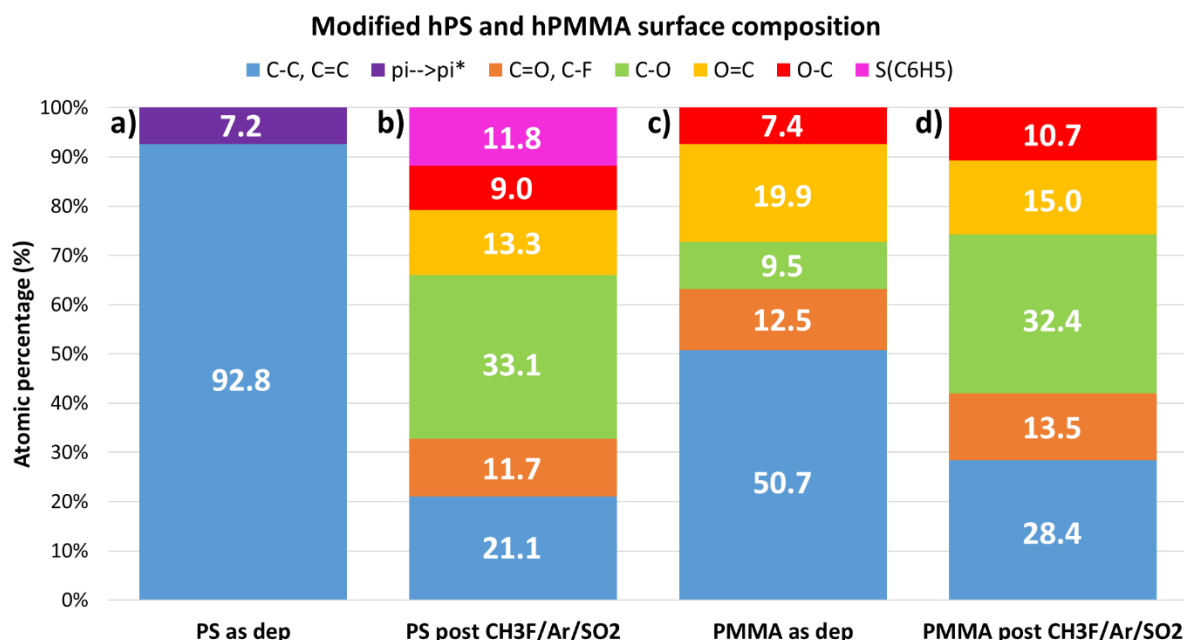


Figure IV-10: Surface composition of modified (a, b) PS and (c, d) PMMA homopolymers obtained by *ex-situ* XPS: (a, c) before and (b, d) after etching with $\text{CH}_3\text{F}/\text{Ar}/\text{SO}_2$ for 10 seconds. The results correspond to an incident angle of 76.25° .

In this section, we have tried to optimize the PMMA:PS selectivity for the $\text{CH}_3\text{F}/\text{Ar}/\text{SO}_2$ plasma, which presents low selectivity (around 1.6) for the high- χ L18, but no bridge formation. We observed that the $\text{CH}_3\text{F}/\text{Ar}/\text{SO}_2$ plasma presents a very narrow process window regarding the etch duration. Indeed, the etch duration was either not enough to completely remove the PMMA and neutral layer, and therefore the pattern transfer into the SiO_2 hard mask was not correct; or the etch duration was long enough to remove the PMMA and neutral layer, but there was not enough PS budget remaining for pattern transfer and the lines pattern was no longer discernible. Reducing the RF bias to decrease the etch rate did not improve the results. Thus, we concluded that the process window for the $\text{CH}_3\text{F}/\text{Ar}/\text{SO}_2$ plasma was very narrow due to the small dimensions – pitch and thickness – of the high- χ L18 BCP film.

In order to overcome the dimensional limitation and therefore increase the available PS budget after etching, we tried increasing the initial thickness of the high- χ L18 film. However, mechanical stability problems led to pattern wiggling due to the high aspect ratio of the lines. Therefore, the smaller CD of the high- χ block copolymer limits the maximum initial thickness allowed for the BCP film in order to avoid pattern wiggling or collapse.

Finally, we tried a cyclic approach based on alternating CH₃F/Ar/SO₂ and Ar steps. Our goal was to improve the PMMA:PS selectivity thanks to the highly selective argon step. While the results were promising on modified PS and PMMA homopolymers, no significant improvement was observed on high- χ L32, which might be explained by the similar surface composition for both PS and PMMA after CH₃F/Ar/SO₂ etching, which would decrease the selectivity of the argon step.

Therefore, we have concluded that this approach is not appropriate to improve the PMMA:PS selectivity for the high- χ PS-b-PMMA.

IV.3.2 Second approach: UV exposure followed by plasma etching

The use of UV exposure before wet removal is known to improve the selectivity between PMMA and PS. Indeed, UV radiation causes the degradation of the covalent bond between PS and PMMA and of the PMMA block through PMMA chain scissions. Moreover, it can also strengthen the PS bonds and thus reduce their solubility [Thurn-Albrecht 2000] [Gharbi 2015].

Thus, our second approach is based on an UV exposure followed by plasma etching. The goal is to break the PMMA chains and harden the PS block before plasma removal of the remaining PMMA and of the neutral layer. This should allow us to obtain higher PMMA:PS selectivity and also avoid wiggling and pattern collapse, since the PS mechanical stability would be improved.

IV.3.2.1 Effect of UV exposure on modified PS and PMMA homopolymers

We started by evaluating the impact of UV exposure on modified PS and PMMA homopolymers. The UV exposure was conducted on the 300 mm SOKUDO DUO tool with a wavelength of 172 nm. Two different doses were evaluated: 30 and 150 mJ/cm².

Table IV-3 presents the modified PS and PMMA homopolymer thickness reduction (Δe) determined by ellipsometry after UV exposure for the two different doses. For both doses, there is almost no change in PS thickness. As for the PMMA, Table IV-3 shows that the higher the dose the higher the PMMA thickness reduction after UV exposure, which corresponds to approximately 5.7 nm for an UV dose of 30 mJ/cm² and a significant 17-nm shrink for a higher UV dose of 150 mJ/cm².

We then measured the PS and PMMA consumption after etching with CH₃F/Ar/SO₂ for 8 seconds, with and without UV exposure. We observe that the PS consumption does not vary significantly when applying an UV exposure prior to the etching, remaining around 10 nm for the three conditions evaluated. However, the PMMA consumption is reduced for higher doses, varying between 35 nm without previous exposure and 24 nm with the higher UV dose of 150 mJ/cm². Finally, the PS and PMMA etch rates, as well as the corresponding PMMA:PS selectivity, were also calculated for the three different conditions evaluated. While the PS etch rate does not vary, the PMMA etch rate – and therefore the PMMA:PS selectivity – is significantly reduced for higher UV doses applied prior to etching.

Table IV-3: Modified PS and PMMA homopolymer thickness reduction (Δe) determined by ellipsometry after UV exposure for two different doses (30 and 150 mJ/cm²) and after etching with CH₃F/Ar/SO₂ for 8 seconds. The modified PS and PMMA etch rates, as well as the corresponding hPMMA:hPS selectivity, were calculated for the different UV exposure doses.

Homopolymer	UV exposure (mJ/cm ²)	Δe after UV exposure (nm)	Δe after etching (nm)	ER (nm/s)	PMMA:PS selectivity
PS	No	-	10.32	1.29	3.53
PMMA		-	35.31	4.55	
PS	30	0.06	10.40	1.30	3.09
PMMA		5.71	32.18	4.02	
PS	150	0.38	10.20	1.28	2.36
PMMA		17.05	24.08	3.01	

In order to understand the results obtained, we used Fourier-Transform Infrared (FTIR) spectroscopy, which was presented in Chapter II.3.1.4. By detecting absorbance lines characteristic of chemical functions, this technique provides information on the film composition. The results for the modified PS and PMMA homopolymers before and after UV exposure are presented in Figure IV-11(a) and (b), respectively.

For the hPS before UV exposure, the absorption bands from 700 to 827 cm⁻¹ correspond to the hydrogen bound to the aromatic ring. The band at 1109 cm⁻¹ corresponds to the oxygen in the interstices of Si (Si-O bonds), which is characteristic of the silicon substrate and unrelated to the PS. The band at 1245 cm⁻¹ might correspond to oxygen bound to carbon (C-O), which probably comes from air exposure. Next, the absorption band from 1450 to 1606 cm⁻¹ correspond to the phenyl ring stretching vibrations. The band at 2339 cm⁻¹ is characteristic of the CO₂ from air exposure. The bands at 2854 and 2923 cm⁻¹ characterize the C-H bond stretching vibrations of the -CH₂- groups. Finally, the band at 3028 cm⁻¹ represents the C-H aromatic stretching vibration (HC=CH) [Nakanishi 1977].

For the hPS results after UV exposure, no significant difference is observed between the three conditions evaluated, except for a decrease of the C-O band at 1245 cm⁻¹, which is attributed to a shorter air exposure. Therefore, these results are consistent with the ellipsometry results, which show neither a significant consumption of PS nor a change in its etch rate after UV exposure.

Figure IV-11(b) shows the results for the hPMMA. For the as deposited hPMMA, the band at 752 cm⁻¹ can be attributed to the α -methyl (α -CH₃) group vibrations. There is also a distinct absorption band from 1122 to 1245 cm⁻¹, which can be attributed to the C-O-C stretching vibration. The band at 1728 cm⁻¹ shows the presence of the acrylate carboxyl group (C=O) stretching vibration. The band from 1452 to 1488 cm⁻¹ can be attributed to the bending vibration of the C-H bonds of the -CH₃ and -CH₂- groups, while the two bands at 2952 and 2999 cm⁻¹ can be assigned to the C-H bond stretching vibrations of the same groups. Finally, the weak

absorption band at 3446 cm^{-1} can be attributed to the $-\text{OH}$ group stretching vibration of physisorbed moisture [Nakanishi 1977].

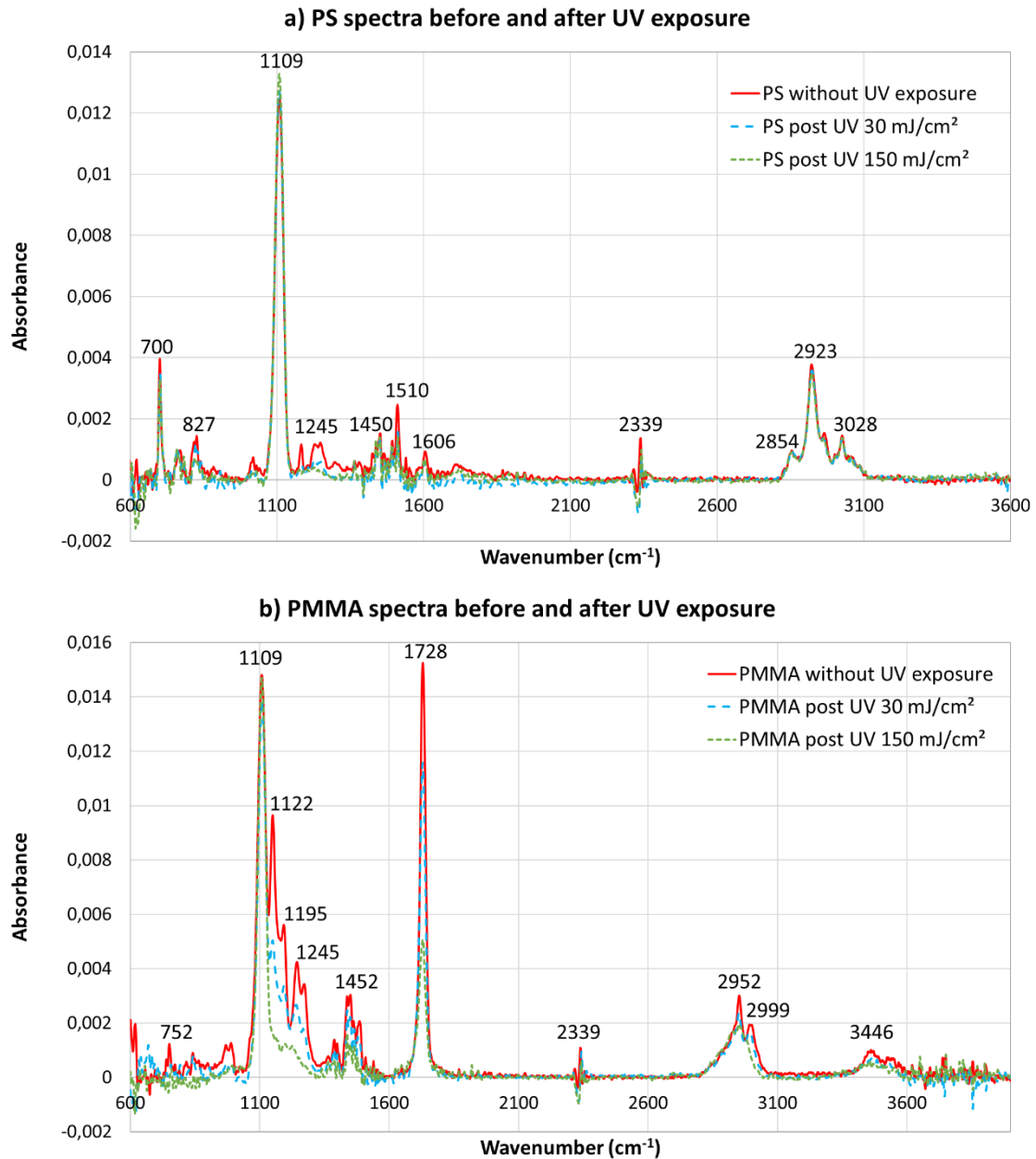


Figure IV-11: FTIR spectra of modified (a) PS and (b) PMMA homopolymers before and after UV exposure with two different doses: 30 mJ/cm^2 and 150 mJ/cm^2 .

After UV exposure, Figure IV-11(b) shows that, for a dose of 30 mJ/cm^2 , both the absorption band from 1122 to 1245 cm^{-1} attributed to the $\text{C}-\text{O}-\text{C}$ group and the band at 1728 cm^{-1} attributed to the $\text{C}=\text{O}$ group are reduced. For a higher UV exposure dose of 150 mJ/cm^2 , these same bands have decreased even more. This indicates that the UV exposure leads to the scission of the simple and double bonds between carbon and oxygen in the PMMA chain. The loss of $\text{C}-\text{O}$ and $\text{C}=\text{O}$ groups during UV exposure explains the decrease of the hPMMA etch rate, since hPMMA usually presents a higher plasma etch rate when compared to the hPS due to the presence of $\text{C}-\text{O}$ and $\text{C}=\text{O}$ groups, which exhibit much higher sputter yields than pure carbon materials according to the Ohnishi parameter.

Therefore, we can conclude that, by eliminating these oxygen-containing groups during UV exposure, the etch rate of PMMA during $\text{CH}_3\text{F}/\text{Ar}/\text{SO}_2$ plasma approaches that of the PS, and therefore the selectivity between both materials decreases. In summary, the higher the UV exposure dose, the lower the PMMA etch rate and PMMA:PS selectivity.

IV.3.2.2 Effect of UV exposure on high- χ PS-*b*-PMMA

Nevertheless, it should be observed in Table IV-3 that, for a UV exposure dose of 150 mJ/cm^2 , hPMMA presents a thickness reduction of 17 nm during exposure. This corresponds approximately to the initial thickness of the high- χ L18 PS-*b*-PMMA film. This led us to wonder if the loss in PMMA etch rate for a higher UV exposure dose could be compensated by the 17-nm thickness reduction of the PMMA caused by the UV exposure only.

In order to verify this hypothesis, the high- χ L32 BCP film was then exposed to the 150 mJ/cm^2 dose in the same conditions of the previous section. From the results presented in Figure IV-12, we observe a thickness loss of 10 nm for PMMA and 4 nm for PS, leading to a difference between the thicknesses for both blocks of only 6 nm. Thus, the PMMA thickness reduction during UV exposure on pattern wafers is less important than expected based on the homopolymer results and cannot compensate the PMMA etch rate reduction caused by the UV exposure. Therefore, we can conclude that the approach based on an UV exposure followed by a dry removal is not adapted to increase the PMMA:PS selectivity.

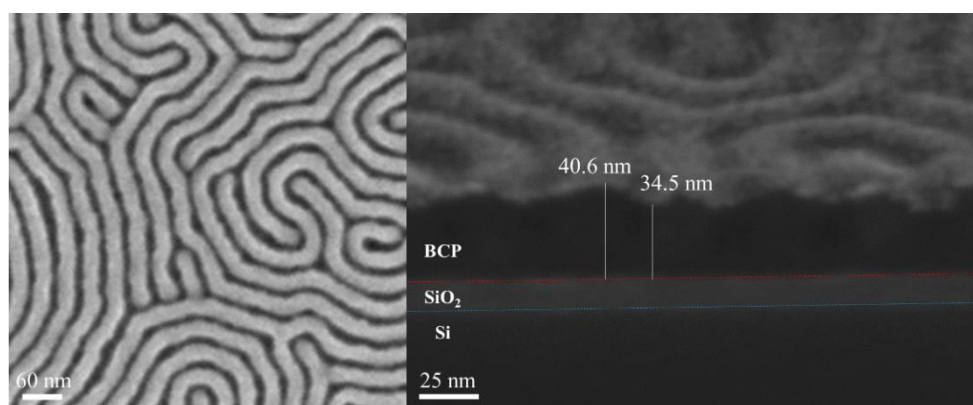


Figure IV-12: Top-view and cross-section SEM images of the high- χ L32 PS-*b*-PMMA after UV exposure with a dose of 150 mJ/cm^2 and a wavelength of 172 nm.

In this section, we have tried to optimize the PMMA:PS selectivity using an approach based on an UV exposure followed by plasma etching. The goal was to break the PMMA chains and harden the PS block before plasma removal of the remaining PMMA and of the neutral layer.

The impact of UV exposure on modified PS and PMMA homopolymers was evaluated. The UV exposure had no effect in the hPS thickness, etch rate during $\text{CH}_3\text{F}/\text{Ar}/\text{SO}_2$ plasma nor structure. However, for the hPMMA, the higher UV exposure dose led to a thickness reduction of 17 nm and decreased the hPMMA etch rate and the PMMA:PS selectivity by about 30%. FTIR analysis allowed us to conclude that the loss of C–O and C=O groups during UV exposure was responsible for the decrease of the hPMMA etch rate. Therefore, we concluded that, by eliminating these oxygen-containing groups during UV exposure, the

etch rate of hPMMA during CH₃F/Ar/SO₂ plasma approaches that of the hPS, and therefore the selectivity between both materials decreases. In summary, the higher the UV exposure dose, the lower the PMMA etch rate and PMMA:PS selectivity.

Nevertheless, the 17-nm thickness loss of hPMMA during UV exposure corresponds approximately to the initial thickness of the high- χ L18 PS-*b*-PMMA film. Thus, the high- χ L32 BCP was used to verify if the loss in PMMA etch rate for a higher UV exposure dose could be compensated by the 17-nm thickness reduction of the PMMA caused by the UV exposure only. However, after an UV exposure with a dose of 150 mJ/cm², the difference between the thicknesses of both blocks with the lamellar BCP was only 6 nm, which does not compensate the PMMA etch rate reduction. Therefore, we concluded that the approach based on an UV exposure followed by a dry removal was not adapted to increase the PMMA:PS selectivity.

IV.3.3 Third approach: oxygen-free PMMA removal

In section IV.2.2 we have seen that the oxygen-free PMMA removal based on CH₄/N₂ presents the best PMMA:PS selectivity for the high- χ PS-*b*-PMMA among the evaluated plasma processes. In this section, we propose to explore this CH₄/N₂ PMMA removal as the third approach for optimizing the PMMA:PS selectivity while also avoiding bridge formation.

We shall begin by varying the CH₄/N₂ ratio applied to modified PS and PMMA homopolymers in order to evaluate the process window of this dry etch chemistry. The etch mechanisms shall also be determined thanks to X-ray photoelectron spectroscopy (XPS). Then, the results obtained for the 18-nm pitch high- χ PS-*b*-PMMA will be presented, highlighting the challenges encountered due to its smaller dimensions.

IV.3.3.1 Application to modified PS and PMMA homopolymers

Figure IV-13 summarizes the high- χ modified PS and PMMA homopolymer consumption as a function of plasma process time for different CH₄/N₂ ratios. All of the experiments were performed in the 300 mm Kiyof FX® ICP reactor from LamResearch®. The pressure, RF bias and RF power are the ones presented in Table IV-1. Ratio 1:1 corresponds to the recipe presented in said table, with the CH₄/N₂ flow corresponding to 50/50 sccm. Ratio 1:2 corresponds to CH₄/N₂ 25/50 sccm, while ratio 2:1 corresponds to CH₄/N₂ 50/25 sccm.

The graph in Figure IV-13 shows that, for the ratio 1:2, both materials consumptions are linear. After 60 seconds of etching, around 42 nm of PMMA and 9 nm of PS are etched, corresponding to a selectivity of 4.7, approximately. As for the ratio 1:1, after 60 seconds, 16 nm of PMMA are etched while a deposition of around 5 nm is observed on top of PS, which means the ratio 1:1 presents infinite selectivity on blanket wafers. Finally, ratio 2:1 presents the same tendencies as ratio 1:1. However, for the PMMA consumption, it seems to reach a plateau after 25 seconds of etching.

These results indicate that CH₄ is the major passivating component of this etching chemistry, since the ratio 1:2, which presents less CH₄ (25 sccm) when compared to the other two ratios

(50 sccm), is also the one that presents higher etch rate for both PS and PMMA. Thus, nitrogen (N_2) seems to be the main etching component.

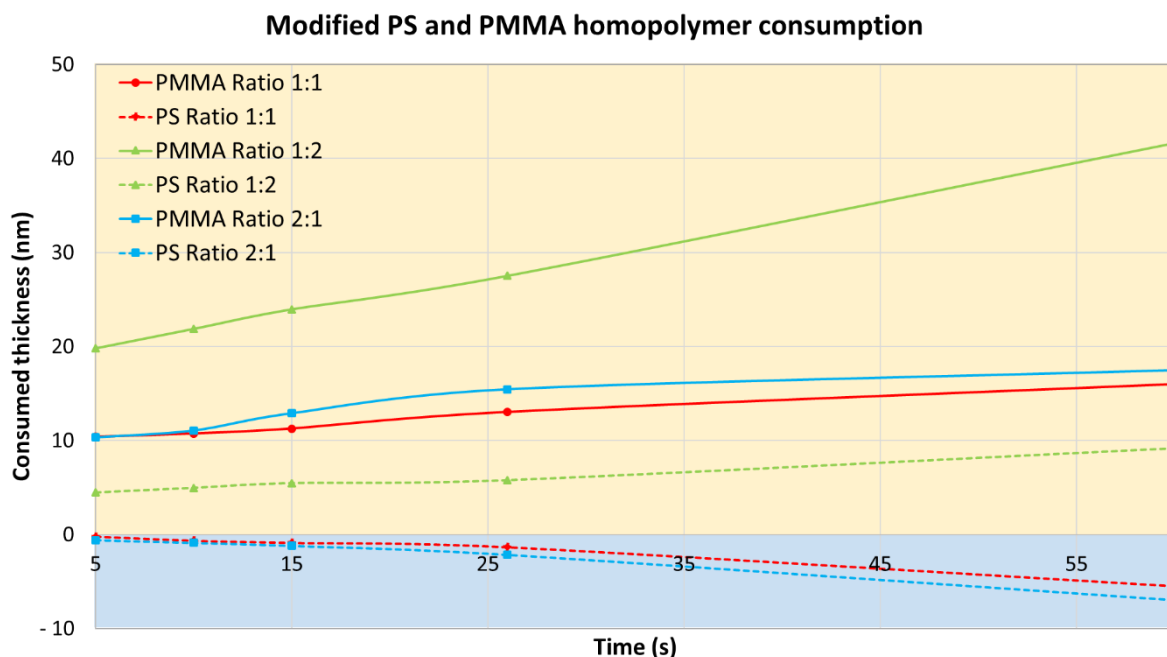


Figure IV-13: Modified PS and PMMA homopolymer consumption for different CH_4/N_2 ratios. The yellow zone corresponds to the etching zone while the blue zone corresponds to the deposition zone.

In order to understand the etching mechanisms and plasma/surface interactions involved, *quasi in-situ* XPS analysis were carried out on these blanket high- χ homopolymers for ratios 1:1 and 1:2 with different etching times. The results for the surface composition of hPS and hPMMA after etching are shown in Figure IV-14. The as deposited composition is also presented for comparison purposes.

First, it should be reminded that the composition of the as deposited high- χ PS and PMMA homopolymers has already been detailed in section IV.1.1 (Figure IV-2) and that they present a composition very similar to that of the standard PS and PMMA. After etching, Figures IV-14(a) and (c) represent the ratio 1:1, while Figures IV-14(b) and (d) represent the ratio 1:2. These results correspond to an angle of 76.25° from the normal incidence, meaning it represents mostly the first 2 nm of the surface. It is important to notice the presence of two new peaks on both materials after etching. A C-N peak appears at 286 eV which, due to spectral resolution, cannot be differentiated from C-O (286.5 eV) bonds and is thus represented together as C-O/C-N. The presence of this bond is confirmed by the apparition of an N-C peak on the N1s spectra at 399.4 eV [Beamson 1992]. We should also notice that, for the two different CH_4/N_2 ratios, the surface composition of both polymers is already modified from the first seconds of etching.

When we observe the results after CH_4/N_2 plasma with ratio 1:1 for the PS surface presented in Figure IV-14(a), the $\pi \rightarrow \pi^*$ shake-up peak is no longer present for all the etching durations. Moreover, as we increase the etching duration, there is an increase in the percentage of C-N and N-C bonds and decrease of C-C/C=C bonds. This indicates that a CN-type deposit forms on the PS surface and increases in thickness over time, preventing the etching of the PS layer. Therefore, N_2 also participates on the passivation of PS. Moreover, thanks to the *quasi in-situ*

XPS technique, almost no oxygen is detected after etching and its atomic percentage is represented together for both O-C and O=C.

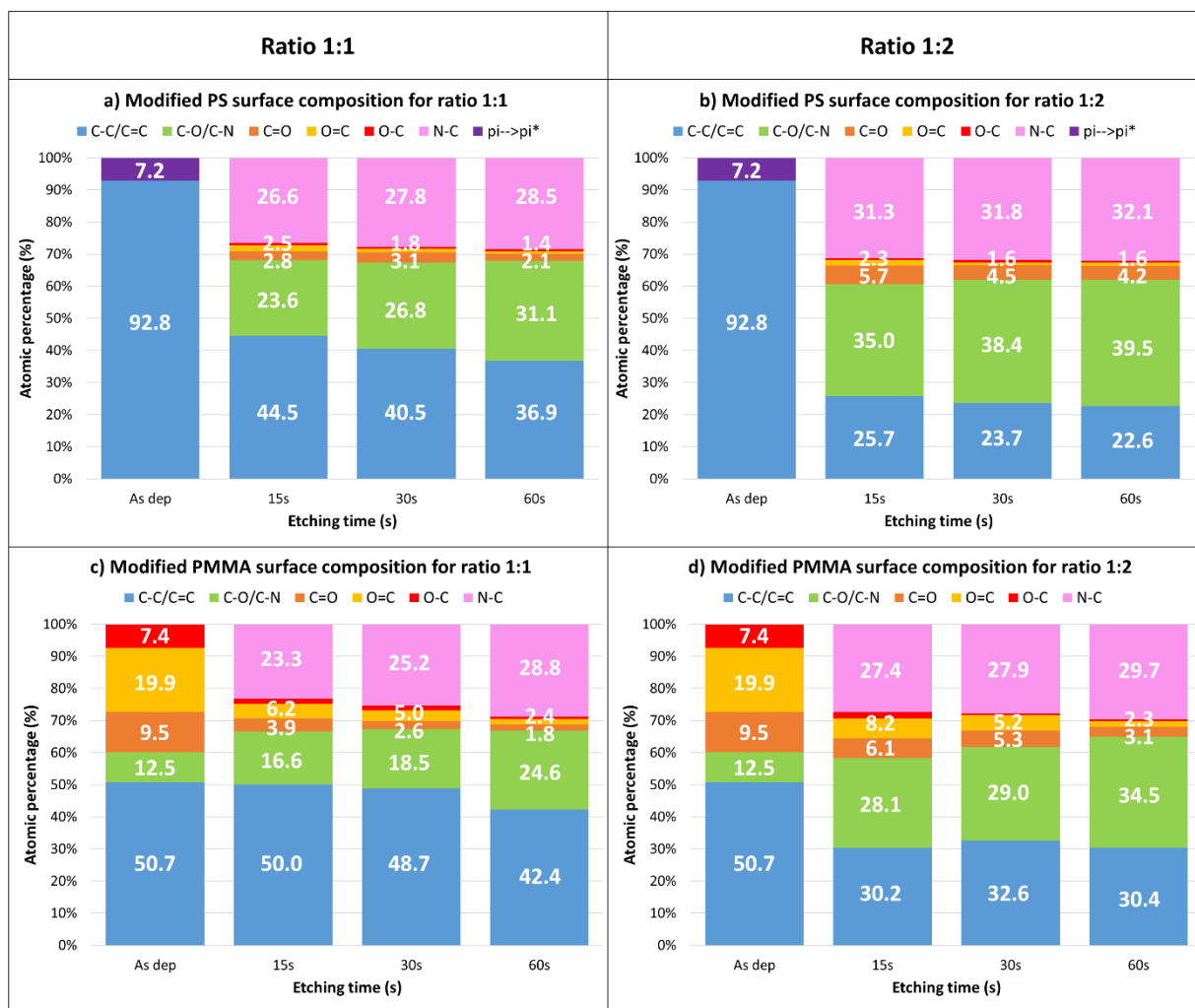


Figure IV-14: Surface composition of modified (a, b) PS and (c, d) PMMA homopolymers obtained by *quasi in-situ* XPS for two different ratios: (a, c) ratio 1:1, and (b, d) ratio 1:2. The results correspond to an incident angle of 76.25° .

As for the PMMA after CH_4/N_2 plasma with ratio 1:1, Figure IV-14(c) shows a loss of O-C and O=C bonds, which goes from a total atomic percentage of oxygen of 27.3% to 2.4% after 60 seconds of etching. The C=O C1s peak is also reduced from 9.5% to 1.8% after the same etching duration. This loss of carbon-oxygen simple and double bonds is characteristic of PMMA consumption. We also observed the presence of the C-N bonds after etching, which could explain the decrease of the PMMA etch rate with time. Indeed, from the graph in Figure IV-13, we see that, after 5 seconds of PMMA etching with ratio 1:1, around 10 nm of PMMA were consumed, while for 60 seconds only 16 nm were etched. This confirms our observation that, depending on the CH_4/N_2 ratio and etching duration, N_2 participates in both the etching and passivation of PMMA and PS.

For the CH_4/N_2 plasma with ratio 1:2, we can observe on Figures IV-14(b) and (d) that the etching presents the same tendencies as the ratio 1:1 with a higher C-N content, which is to be expected from the increase of the N_2 flow. These same etching mechanisms were observed for standard PS-*b*-PMMA in previous works [Sarrazin 2019].

IV.3.3.2 Application to PS-*b*-PMMA films with lamellar morphology

The oxygen-free PMMA removal based on a CH₄/N₂ plasma was first validated using a standard PS-*b*-PMMA with intrinsic period L₀ = 38 nm supplied by Arkema. The BCP solution is spin-coated and annealed on 300 mm wafers using the Sokudo DUO™ DSA-dedicated track. As we have seen for the other block copolymers, a thin neutral layer composed of PS-*r*-PMMA random copolymer is spin-coated on the substrate before the BCP deposition in order to neutralize the surface and obtain the vertical lamellae morphology. The neutral and BCP layer thicknesses are around 8 and 52 nm, respectively. Figure IV-15 presents the cross-section and top-view SEM images post PMMA removal, as well as the calculated selectivity for the different CH₄/N₂ ratios applied to this block copolymer in order to compare the PMMA:PS selectivity of free surface and blanket wafers.

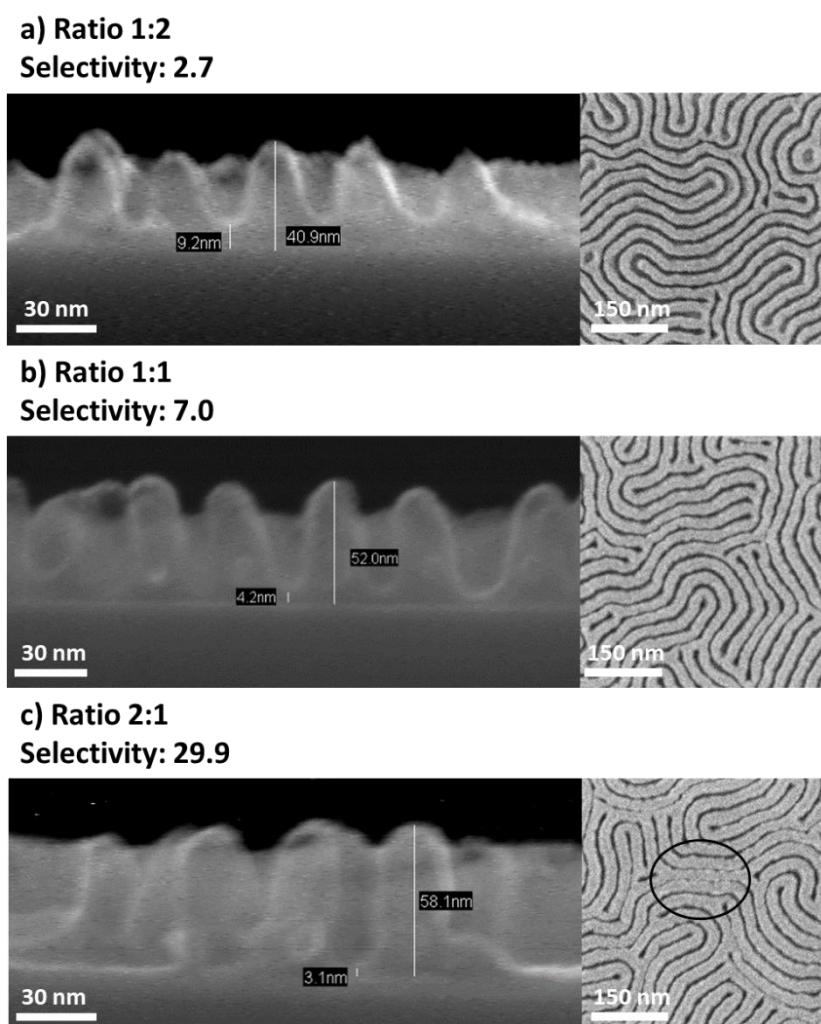


Figure IV-15: Cross-section and top-view SEM images of standard PS-*b*-PMMA with 38-nm pitch after etching with different CH₄/N₂ ratios: (a) ratio 1:2; (b) ratio 1:1; and (c) ratio 2:1. The calculated PMMA:PS selectivity is also indicated for each ratio.

As expected, the greater the CH₄ content, the better the selectivity since CH₄ is the major passivating component of this etching chemistry. However, Figure IV-15(c) shows that when the CH₄/N₂ ratio is too important, the PS lines thickness is increased due to too much carbon passivation on the PS flanks. The highlighted section on the top-view image in Figure IV-15(c) presents the consequent pattern collapse caused by the lines thickening, which will prevent the

correct pattern transfer into the hard mask. Therefore, we selected the ratios 1:2 and 1:1, which present a PMMA:PS selectivity of 2.7 and 7.0, respectively, to continue our studies for the high- χ PS-*b*-PMMA.

It is also important to notice that, for all CH₄/N₂ ratios studied, the selectivity on free surface is lower compared to that of blanket wafers. For example, the ratio 1:1 PMMA:PS selectivity decreases from infinite on homopolymers to around 7.0 for the standard PS-*b*-PMMA with 38-nm pitch. This difference between block copolymer and homopolymer etching regarding the PS consumption has already been observed in section IV.2.2 and indicates that the oxygen-containing by-products of the PMMA etching probably interact with the PS phase, inducing its consumption.

For the etching of the 18-nm pitch high- χ PS-*b*-PMMA, we have estimated at the beginning of this chapter that there should be at least 15 nm of PS plus neutral layer left after PMMA removal to ensure the correct pattern transfer into the silicon oxide hard mask. This means that the high- χ L18 BCP requires a higher selectivity than the standard PS-*b*-PMMA that we have just evaluated due to the L18's reduced initial thickness (16 nm). Since the initial thickness of the PS-*b*-PMMA and neutral layer stack is approximately 21 nm, this translates to a desired selectivity of around 3.5.

Figure IV-16 presents the cross-section and top-view SEM images after PMMA removal using CH₄/N₂ with ratio 1:2 and 1:1 for the high- χ L18 BCP, as well as the calculated selectivity for each ratio. First, it is important to notice that, for the same dry process, the 18-nm pitch high- χ BCP presents lower selectivity compared to the 38-nm pitch standard PS-*b*-PMMA, which we had already observed in Figure IV-4 for the 32-nm pitch high- χ BCP. We have seen in Figure IV-3 that, for two PS-*b*-PMMA with the same intrinsic period but different chemistry, there is no difference in selectivity for the same plasma etching chemistry between both BCPs. Thus, this difference observed in selectivity between the high- χ L18 and the standard L38 is probably not caused by the modified chemistry of the high- χ BCP. However, it might be due to the fact that the etching time is shorter for smaller thickness. It should also be noticed that the cross-section SEM measurements are approximations, due to the tool's low precision when using higher magnification.

Figure IV-16(a) shows the results for the CH₄/N₂ plasma with ratio 1:2, which presents a selectivity of around 1.4. As we have established before, with the block copolymer's reduced 21-nm initial thickness, such low selectivity means there is not enough PS budget for pattern transfer. However, the results in Figure IV-7 have shown us that, when the PS-*b*-PMMA initial thickness is increased to 35 nm, pattern wiggling is observed after PMMA removal due to the high aspect ratio of the lines.

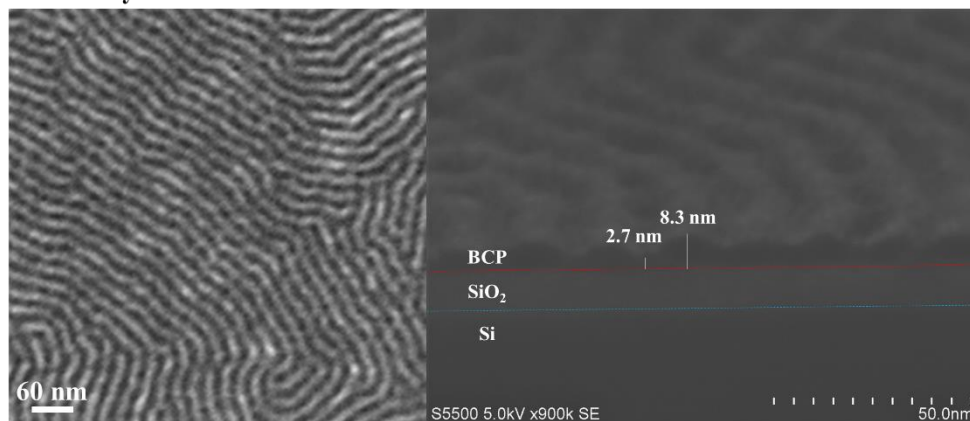
As for the CH₄/N₂ plasma with ratio 1:1, the results have already been presented in Figure IV-4 and detailed in section IV.2.2. They have been reproduced again in Figure IV-16(b) to highlight the formation of bridges on top of the lines pattern, which prevents correct pattern transfer into the SiO₂ hard mask, as we have seen in Figure IV-5. These bridges were not present on the 38-nm pitch standard PS-*b*-PMMA shown in Figure IV-15(b). They might have come from the modified PS-*b*-PMMA chemistry of the high- χ BCP, except they were not observed after CH₃F/Ar/SO₂ plasma in Figures IV-4 nor IV-6. Therefore, they are probably formed due to intensive sidewalls passivation during the CH₄/N₂ plasma and to a species confinement

effect, both accentuated by the small 9-nm critical dimension (CD) of the lines for the high- χ L18.

Therefore, the main high- χ PS-*b*-PMMA dry etching key challenges come from the trade-off between obtaining a high PMMA:PS selectivity and avoiding bridge formation due to carbon passivation. This inspired the idea presented in the next section, which consists of alternating etching and deposition steps to avoid bridge formation and improve selectivity, using a cyclic approach based on different CH₄/N₂ ratios.

a) Ratio 1:2

Selectivity: 1.4



b) Ratio 1:1

Selectivity: 2.6

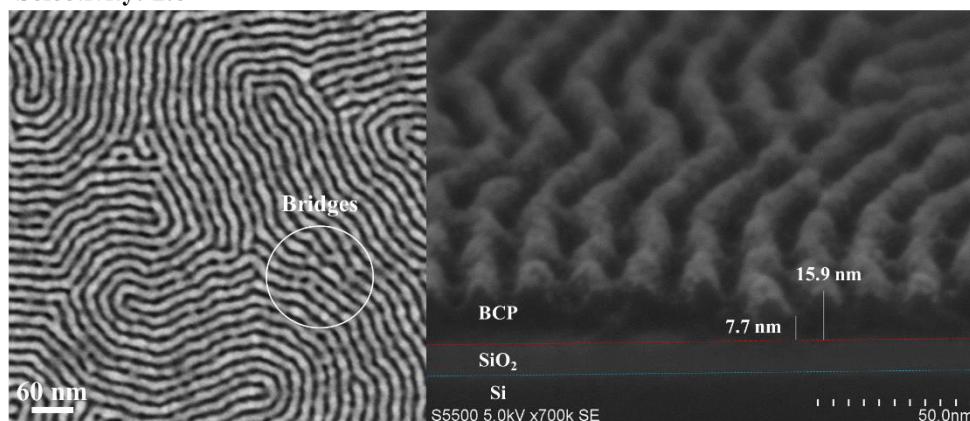


Figure IV-16: Top-view and cross-section SEM images of the high- χ L18 PS-*b*-PMMA block copolymer after PMMA removal using two different CH₄/N₂ ratios: (a) 1:2 and (b) 1:1. It should be noticed that the cross-section SEM measurements are approximations, due to the tool's lower precision when using higher magnification.

IV.3.3.3 Cyclic approach on high- χ L18 PS-*b*-PMMA

Figure IV-17 presents the schematics for the cyclic approach. The idea is to have a first step with a lower carbon content (ratio 1:2) to etch both PS and PMMA followed by a step with a higher carbon content (ratio 2:1) to etch the PMMA and form a CN-type deposit on the PS. These two steps together make one cycle and are then repeated until all PMMA has been removed and no PS has been consumed.

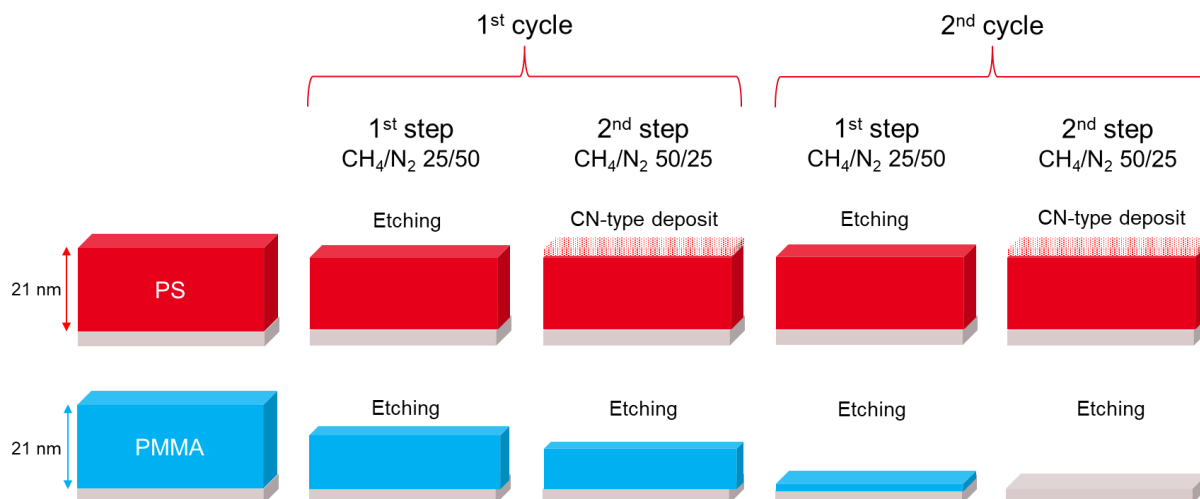


Figure IV-17: Schematics for the cyclic approach with different CH₄/N₂ ratios in order to completely remove the PMMA selectively to PS.

First, this cyclic approach was tested on modified PS and PMMA homopolymers. Figure IV-18 presents the homopolymer consumption for the cyclic approach with a first 5-seconds CH₄/N₂ step with ratio 1:2 followed by a second 5-seconds CH₄/N₂ step with ratio 2:1. The yellow zone corresponds to the etching zone while the blue zone corresponds to the deposition zone. The graph shows that the PMMA is continuously etched with the increasing number of cycles. After 4 cycles, around 23 nm of PMMA have been etched, which is greater than the initial thickness of the PMMA + neutral layer stack for the high- χ L18 BCP. Figure IV-18 also shows that the PS is not consumed after 4 cycles, thus validating the schematics presented in Figure IV-17 for PS and PMMA homopolymers.

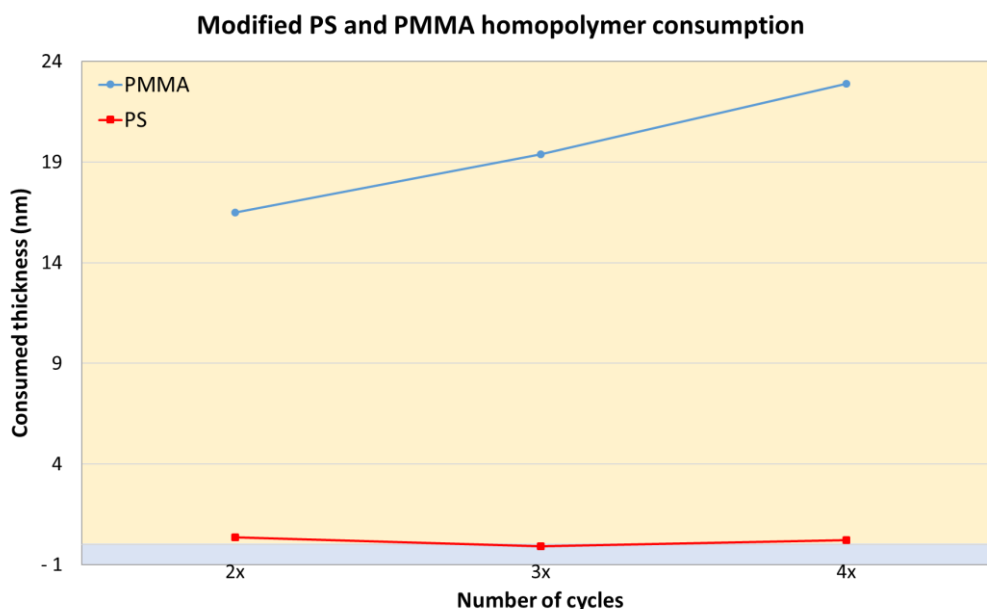


Figure IV-18: Modified PS and PMMA homopolymer consumption for the cyclic approach with a first 5-seconds CH₄/N₂ step with ratio 1:2 followed by a second 5-seconds CH₄/N₂ step with ratio 2:1. The yellow zone corresponds to the etching zone while the blue zone corresponds to the deposition zone.

However, as we can see in Figure IV-19, when the same cyclic etching approach is applied to free surface high- χ L18 PS-*b*-PMMA, there is no visible improvement of the PMMA:PS selectivity when compared to the non-cyclic approach presented in the previous section. Indeed, after 3 cycles, Figure IV-19(b) shows us that a selectivity of 2.5 is obtained, which is similar to the selectivity of 2.6 obtained for the CH₄/N₂ ratio 1:1 presented in Figure IV-16(b). Furthermore, some bridge formation is once again observed in Figure IV-19(b) after the third cycle. Finally, for both number of cycles presented in Figures IV-19(a) and (b), the PMMA plus neutral layer remaining thickness is approximately 6 nm, meaning there is a PMMA etch stop between the second and third cycles. Both phenomena indicate that the carbon passivation on the etching step is too important, which leads to an eventual saturation of PMMA etching and to bridge formation.

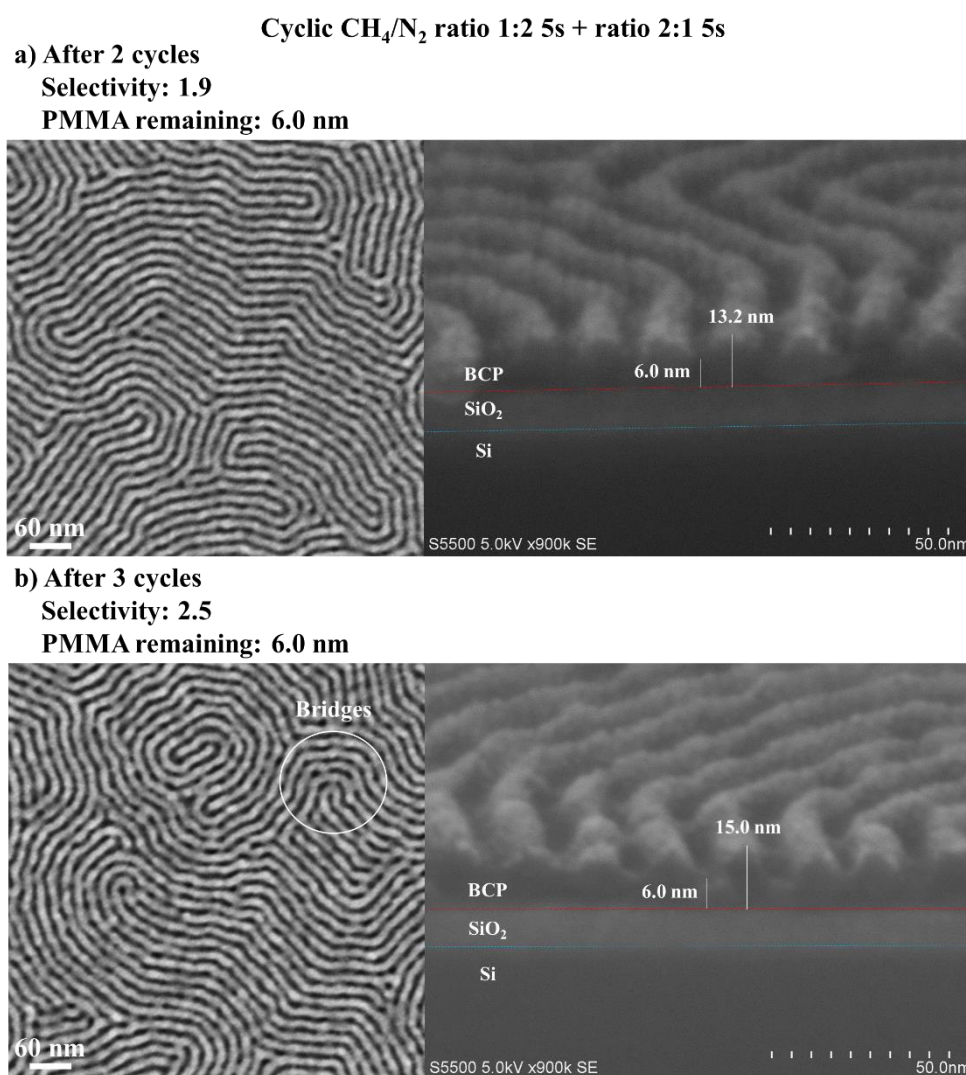


Figure IV-19: Top-view and cross-section SEM images of the high- χ L18 PS-*b*-PMMA block copolymer after PMMA removal using the cyclic approach with a first 5-seconds CH₄/N₂ step with ratio 1:2 followed by a second 5-seconds CH₄/N₂ step with ratio 2:1. Results after (a) 2 cycles and (b) 3 cycles.

Based on these results, a cyclic etching with lower CH₄ flow on the first step was also tested. By reducing the CH₄/N₂ flow on the first step to 10/50 (ratio 1:5) we expect to avoid the bridge formation and PMMA etch stop. The results are presented in Figure IV-20. After 4 cycles,

Figure IV-20(b) presents a PMMA:PS selectivity of around 1.6. This result is coherent with what was seen on the previous sections: the reduced CH_4 flow leads to lower PMMA:PS selectivity, which then prevents correct pattern transfer. Nevertheless, it should be noticed that no PMMA etch stop was observed thanks to the reduced carbon content on the etching step, confirming the hypothesis that the carbon passivation on the etching step was too important in the previous experiment (Figure IV-19). However, bridge formation is only slightly delayed in comparison to the previous approach, with bridges forming between third and fourth cycles, as can be seen in Figure IV-20(b).

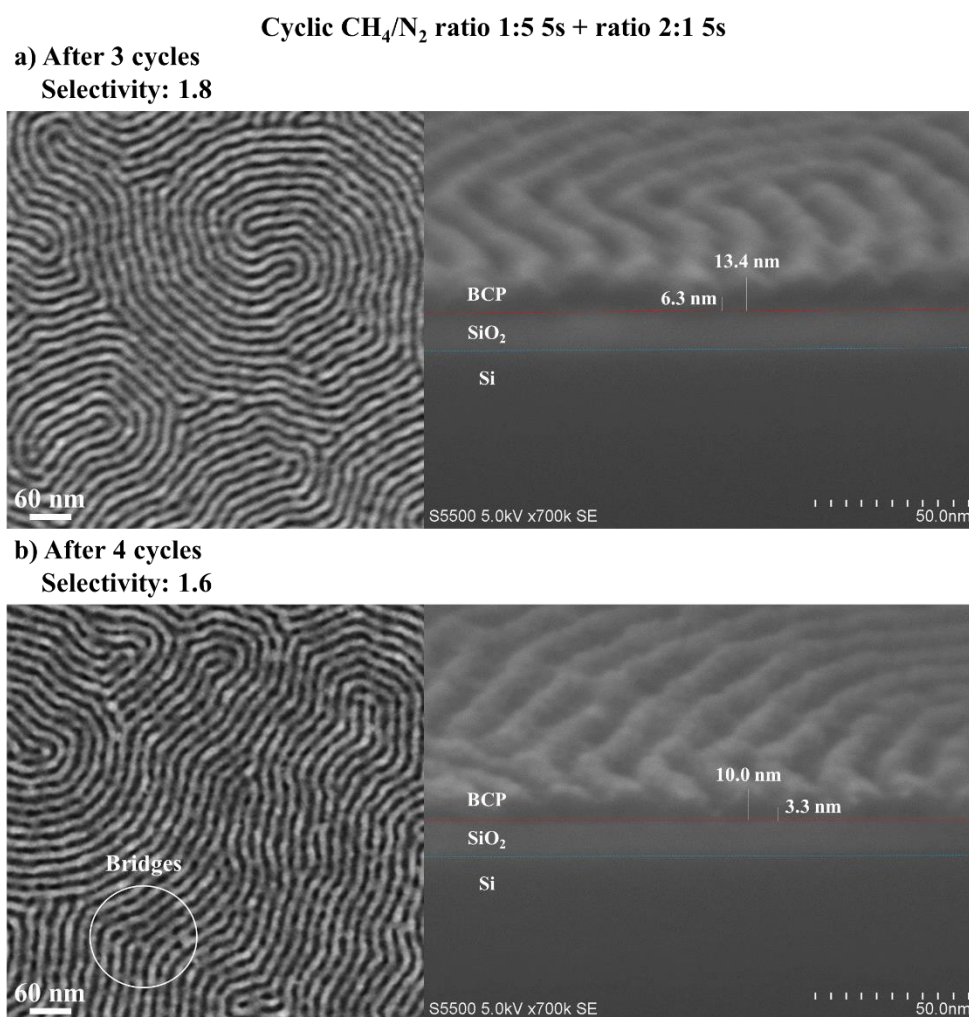


Figure IV-20: Results for the cyclic approach with a first 5-seconds CH_4/N_2 step with ratio 1:5 followed by a second 5-seconds CH_4/N_2 step with ratio 2:1. Cross-section and top-view SEM images of high- χ L18 PS-*b*-PMMA after (a) 3 cycles and (b) 4 cycles.

In order to avoid bridge formation altogether, a third cyclic approach was tested. It consisted of alternating short CH_4/N_2 and Ar/O_2 steps of 5 and 3 seconds each, respectively. As we have seen in section IV.1.2, Ar/O_2 is known to effectively remove the PMMA phase and present low LER and LWR. However, it presents very low selectivity (around 1.0 for the high- χ L18 PS-*b*-PMMA), which explains the presence of the CH_4/N_2 step to improve the PMMA:PS selectivity. The results for 3 and 4 cycles applied to the high- χ L18 BCP can be found in Figure IV-21. It can be observed that no bridge is formed with these cycles, which confirms the theory that bridge formation comes from too much carbon deposit on the PS lines. After 4 cycles, Figure

IV-21(b) shows that the PMMA is completely removed, however there is not enough PS remaining (around 7 nm) for pattern transfer into the SiO₂ hard mask.

Therefore, we conclude that the cyclic approach still presents the same etching difficulties that we observed for the non-cyclic process. This means the full dry etching approach cannot find the right balance between high selectivity and bridge formation for the high- χ L18 PS-*b*-PMMA, mostly due to its small dimensions, namely its initial thickness and pitch.

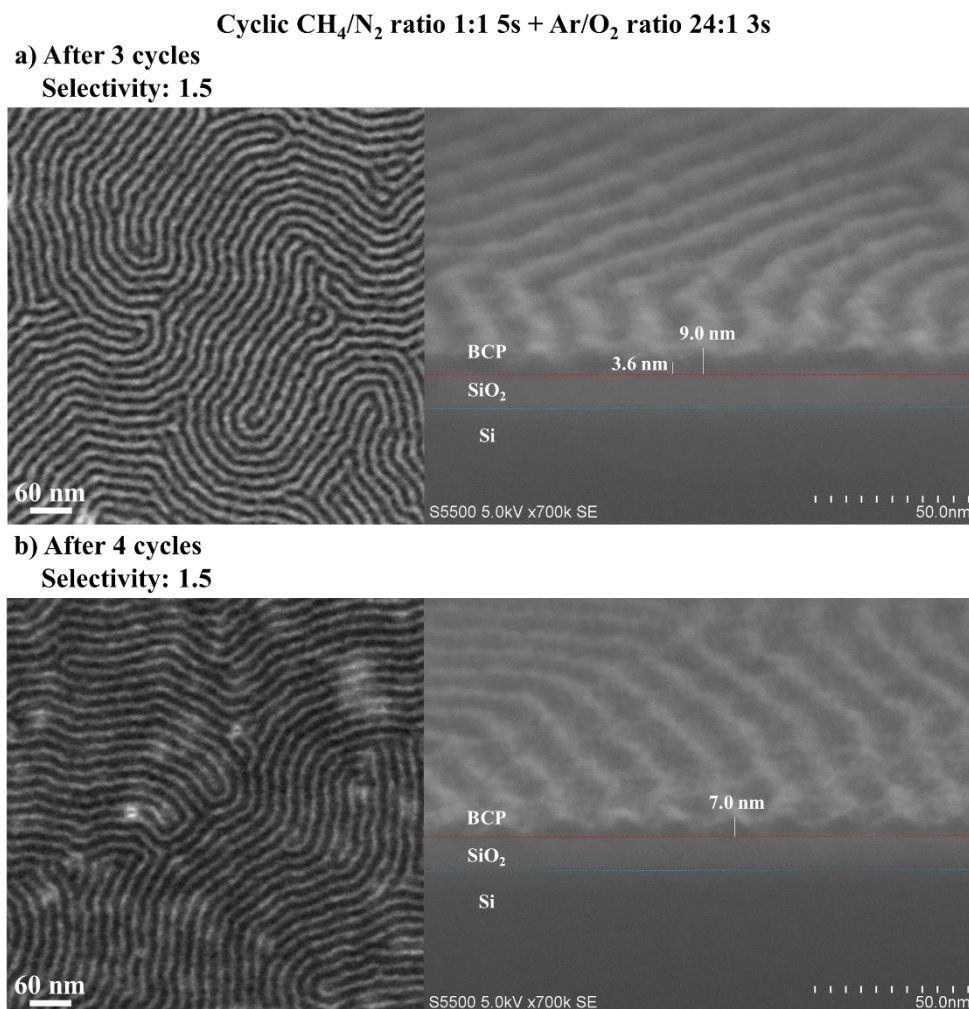


Figure IV-21: Results for the cyclic approach with a first 5-seconds CH₄/N₂ step with ratio 1:1 followed by a second 3-seconds Ar/O₂ step with ratio 24:1. Cross-section and top-view SEM images of high- χ L18 PS-*b*-PMMA after (a) 3 cycles and (b) 4 cycles.

In this section, we have tried to optimize the oxygen-free PMMA removal based on CH₄/N₂, which presented the best selectivity for the high- χ L18, but also some bridge formation on top of the lines.

The impact of the CH₄/N₂ ratio variation was evaluated on PS and PMMA homopolymers. For ratios 1:1 and 2:1, the PMMA was etched and a deposited layer was formed over the PS, leading to an infinite PMMA:PS selectivity. The etching and deposition mechanisms were determined by XPS. For the PS, a CN-type deposit forms on the PS surface and increases in thickness over time, preventing the etching of the PS layer. For the PMMA, a loss of C-O and C=O bonds was observed, which is characteristic of PMMA etch.

We also observed the presence of the C-N bonds after etching, which explains the decrease of the PMMA etch rate with time.

When applying this chemistry on the lamellar BCP, we observed that, the greater the CH₄ content, the better the PMMA:PS selectivity, indicating that CH₄ is the major passivating component of this etching chemistry. However, for the ratio 2:1, the PS lines thickness was increased due to too much carbon passivation on the PS flanks, which led to pattern collapse. Ratio 1:2 presented a selectivity of around 1.4 for the high- χ L18. Such low selectivity means there is not enough PS budget for pattern transfer. Finally, ratio 1:1 presented a selectivity of 2.6, but bridges were formed on top of the lines pattern, which prevented correct pattern transfer into the SiO₂ hard mask. These bridges were probably formed due to intensive sidewalls passivation during the CH₄/N₂ plasma and to a species confinement effect, both accentuated by the small 9-nm critical dimension (CD) of the lines for the high- χ L18.

Therefore, we concluded that the main high- χ PS-*b*-PMMA dry etching key challenges come from the trade-off between obtaining a high PMMA:PS selectivity and avoiding bridge formation due to carbon passivation.

We then tried using a cyclic approach based on different CH₄/N₂ ratios, which consisted of alternating etching and deposition steps to avoid bridge formation and improve selectivity. However, the results showed that the cyclic approach still presents the same etching difficulties observed for the non-cyclic process. Therefore, the full dry etching approach cannot find the right balance between high selectivity and bridge formation for the high- χ L18 PS-*b*-PMMA, mostly due to its small dimensions, namely its initial thickness and pitch.

IV.3.4 Fourth approach: mixed wet and dry etching

The PMMA removal by aqueous solution has been considered an interesting approach in order not to damage the PS. The principle is to use a solvent for which one of the blocks of the BCP is soluble while the other is insoluble. Thus, the soluble polymer dissolves in the presence of the solvent while the other phase is not altered by it.

Gharbi *et al.* have evaluated the interest of UV exposure as well as the impact of the dose used on cylindrical PS-*b*-PMMA. In their study, they have shown that, when acetic acid is used without UV exposure, a surface reconstruction of the block copolymer occurs: PMMA chains migrate from the cylindrical domains to the top surface and remain tethered to the PS chains. This leads to an increase of the BCP thickness and surface roughness. They conclude that certain covalent bonds between the two blocks of the copolymer were not broken during acetic acid rinsing, and therefore the use of the solvent alone does not allow the scission of the chains, leading to the addition of an UV exposure step. They then show that, depending on the UV exposure dose used, the thickness of the polymer after acetic acid rinsing may be greater than the initial thickness (low doses) or lower (high doses). Therefore, when an UV exposure is conducted with a sufficient dose before acetic acid rinsing, a flat surface is obtained and the BCP thickness decreases. This shows that UV exposure leads to the degradation of the PMMA block via chains scission and the cleavage of the PS/PMMA covalent bonds, so that PMMA

can be completely removed after the wet development. It also reportedly permits the cross-linking of PS and the reduction of its solubility [Gharbi 2015].

Based on the results obtained in the previous sections with the full dry approach, in this section we have proposed a mixed wet and dry etching approach in order to successfully remove the PMMA and open the neutral layer, conserving enough PS budget for pattern transfer. This approach consists of a wet PMMA removal in order to obtain an infinite PMMA:PS selectivity, followed by a dry neutral layer opening step to allow for pattern transfer into the SiO₂ layer. The schematics for this approach is presented in Figure IV-22. The main difference between this approach and the full dry approach is that the UV exposure + wet removal does not remove the neutral layer, which has to be removed through dry etching.

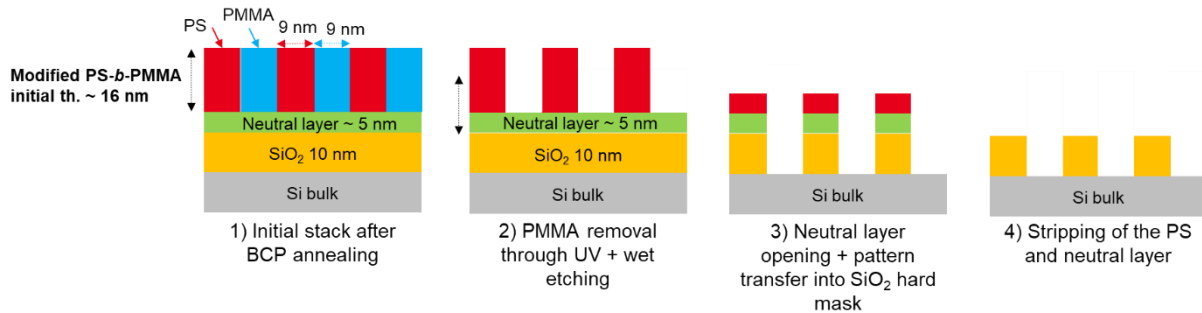


Figure IV-22: Schematics for the flow used in the mixed wet and dry etching approach for the 18-nm pitch high- χ PS-*b*-PMMA block copolymer.

IV.3.4.1 PMMA removal through UV exposure followed by wet rinsing

The wet PMMA removal for the high- χ L18 PS-*b*-PMMA consists of two steps: an UV exposure followed by a solvent rinse. With the appropriate dose, the UV exposure is responsible for both breaking the PMMA chains and the PS/PMMA covalent bond, which allows these broken chains to be later removed by the solvent rinse, and hardening the PS lines, which helps avoid possible pattern collapse due to capillary forces. The optimal dose was found by the lithography team to be 30 mJ/cm² with a 172 nm wavelength. Similarly to section IV.3.2, the UV exposure was conducted in the Sokudo DUO tool. As for the second step, the solvent chosen was isopropyl alcohol (IPA), which dissolves the PMMA without modifying the PS. The rinse time is set at 30 seconds.

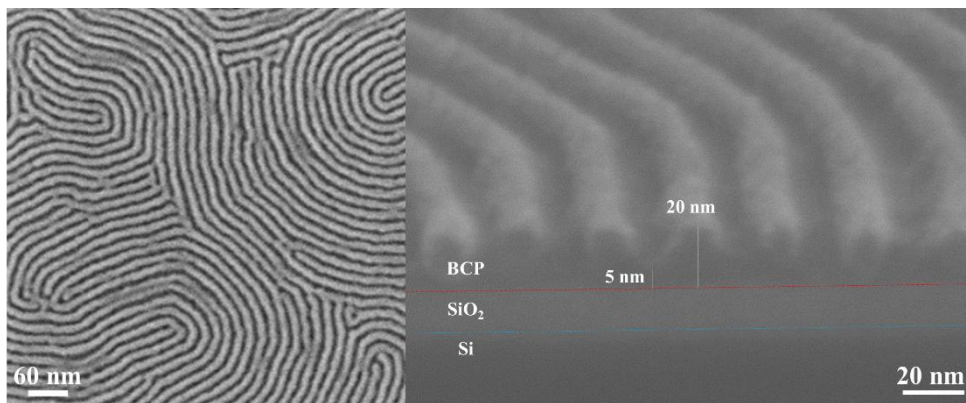


Figure IV-23: Top-view and cross-section SEM images of high- χ L18 PS-*b*-PMMA after PMMA removal through UV exposure followed by IPA rinsing.

The cross-section and top-view SEM images after wet PMMA removal are presented in Figure IV-23. They confirm that the PMMA is completely removed while no PS nor neutral layer are consumed. The top-view image shows some pattern collapse, which is to be expected due to the high aspect ratio of the PS lines (around 2.2).

In order to understand the etching mechanisms of the wet PMMA removal, we must determine the role of UV exposure and IPA rinsing. The impact of UV exposure on modified PS and PMMA homopolymers was already investigated in section IV.3.2.1. In summary, UV exposure had no significant impact on the PS structure nor thickness. However, for the PMMA, it led to the loss of C–O and C=O groups and to a decrease in the PMMA film thickness.

To evaluate the impact of IPA rinsing on the PS-*b*-PMMA BCP, two experiments were conducted. The first one consisted in performing an IPA rinse without UV exposure, while the second one consisted in performing an IPA etching in vapor phase instead of liquid. Both experiments presented the same results, which are represented in Figure IV-24. The top-view SEM image presented in Figure IV-24 shows almost no contrast between both blocks and the cross-section image confirms that both PMMA and PS have not been removed by either experiments. These results indicate that UV exposure and aqueous rinsing are both necessary for PMMA removal and that there is no chemical reaction between IPA and PMMA. Thus, the role of the IPA aqueous solution in the wet PMMA removal process shown in Figure IV-23 consists of rinsing and removing the PMMA chains that were degraded by the UV exposure.

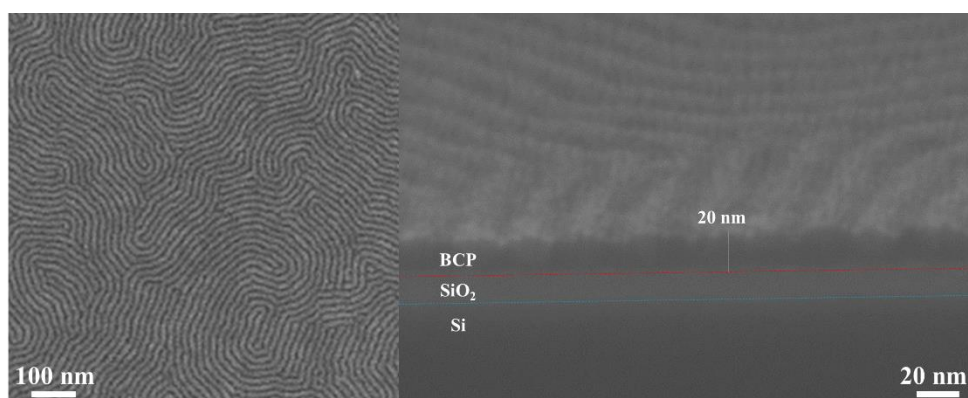


Figure IV-24: Top-view and cross-section SEM images of high- χ L18 PS-*b*-PMMA after IPA rinsing without UV exposure. The results for IPA etching in vapor phase are not represented, since they were similar to the ones presented here.

IV.3.4.2 Development of dry etching step for neutral layer opening

Once the PMMA has been removed, the second step necessary in order to proceed to pattern transfer is the neutral layer opening plasma etching step. For this step, two different chemistries were proposed: CF₄ and Ar/O₂. In order to evaluate these chemistries and validate their interest, we proceeded to the pattern transfer into the SiO₂ subjacent layer using the same CHF₃/CF₄ plasma for both experiments. Table IV-4 presents the plasma parameters of each chemistry studied for neutral layer opening and hard mask etching.

Figure IV-25 shows the results obtained after wet PMMA removal, neutral layer opening and transfer into the SiO₂ layer. We observe in Figure IV-25(a) that the CF₄ neutral layer opening plasma leads to some wiggling. This might come from the fluorocarbon redeposit on the PS flanks, affecting the mechanical stability of the PS lines. Figure IV-25(b), on the other

hand, shows that the Ar/O₂ plasma was too aggressive and, while completely removing the neutral layer, it also consumed too much PS. Therefore, it did not conserve enough PS + neutral layer budget for complete pattern transfer into the silicon oxide hard mask.

Table IV-4. Plasma parameters of the chemistries tested for the dry etching of the neutral and SiO₂ layers.

Etching	Pressure (mTorr)	Power (W)	Bias (V)	Flow (sccm)	Time (s)
CF ₄	10	625	-70	150	5
Ar/O ₂	10	220	-200	50/5	5
CHF ₃ /CF ₄	4	625	-110	50/50	8

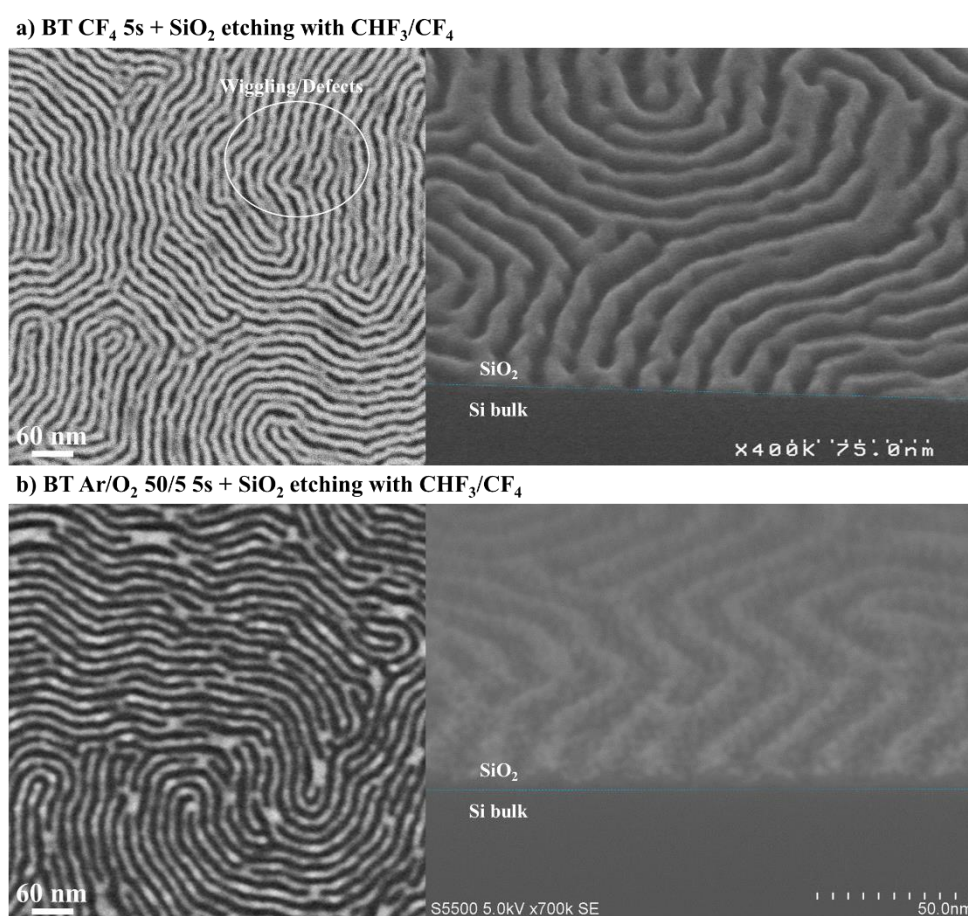


Figure IV-25: Top-view and cross-section SEM images of high- χ L18 PS-*b*-PMMA after the wet PMMA removal, the neutral layer dry opening (represented as “BT” for breakthrough step) and the SiO₂ etching. Two different neutral layer opening plasmas are presented: (a) CF₄ and (b) Ar/O₂ with ratio 10:1.

The Ar/O₂ ratio was then improved to 24:1 (120/5 sccm) instead of 10:1 (50/5 sccm) while conserving the other parameters presented in Table IV-4. This ratio improvement is expected to provide a less isotropic etching and to conserve more PS budget. Figure IV-26(a) presents the top-view and cross-section SEM images after wet PMMA removal, neutral layer opening with Ar/O₂ ratio 24:1, SiO₂ etching with CHF₃/CF₄ and PS stripping with an oxygen plasma. It

confirms what was expected: increasing the argon content improved the neutral layer:PS selectivity and allowed for complete pattern transfer into the SiO₂.

Finally, Figure IV-26(b) presents the results after the complete stack etching: wet PMMA removal with UV exposure followed by IPA rinsing, dry neutral layer opening using the optimized Ar/O₂ plasma, SiO₂ etching using the CHF₃/CF₄ plasma, Si bulk layer etching with an HBr/O₂ plasma, and remaining PS stripping with an O₂ plasma. The lines pattern has been transferred into 13.8 nm of silicon bulk with a CD of 11 nm (CD bias ~ 2 nm). Therefore, we demonstrate the pattern transfer of an 18-nm pitch high- χ organic block copolymer into SiO₂ and silicon bulk layers using a mixed wet and dry etching removal process.

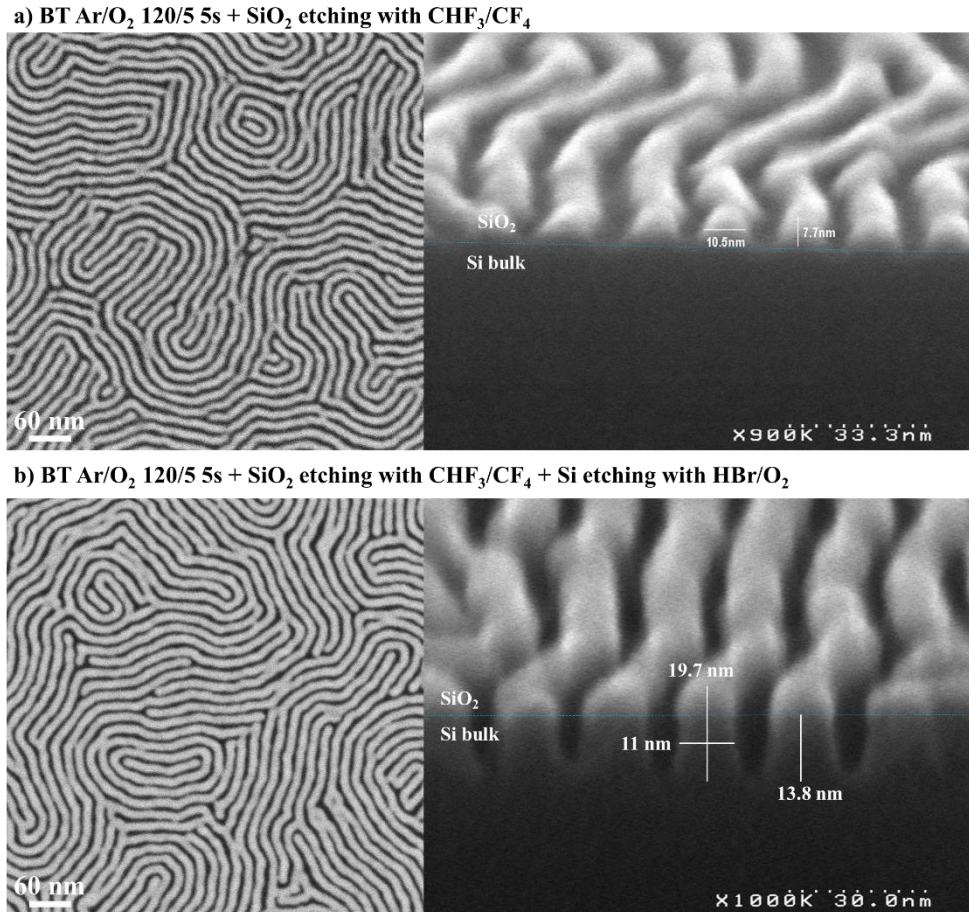


Figure IV-26: Top-view and cross-section SEM images of high- χ L18 PS-*b*-PMMA (a) after the wet PMMA removal, the neutral layer dry opening with Ar/O₂ ratio 24:1 and the SiO₂ etching; and (b) the partial transfer into the silicon bulk. For both cross-section images, the PS has been stripped with an oxygen plasma before imaging.

In this section, we have explored a mixed wet and dry etching approach for the PMMA removal and transfer into the hard mask. This approach consisted of a wet PMMA removal in order to obtain an infinite PMMA:PS selectivity, followed by a dry neutral layer opening step to allow for pattern transfer into the SiO₂ layer.

The wet PMMA removal was validated using an UV exposure with wavelength 172 nm and dose 30 mJ/cm². The UV exposure is responsible for the degradation of the PMMA block via chains scission and the cleavage of the PS/PMMA covalent bonds. After UV, an

IPA rinsing is conducted to remove the PMMA chains that were degraded by the UV exposure. This process was shown to completely remove the PMMA while conserving the PS and the neutral layer.

The next step consisted in the neutral layer dry opening. An Ar/O₂ breakthrough step was developed to open the neutral layer while conserving enough PS budget to validate the pattern transfer into the silicon oxide hard mask. Finally, the transfer into 13.8 nm of silicon bulk was also performed, leading to line patterns with a CD of 11 nm (CD bias ~ 2 nm), and therefore demonstrating the pattern transfer of an 18-nm pitch high- χ organic block copolymer into SiO₂ and silicon bulk layers using a mixed wet and dry etching removal process.

IV.4 Conclusions

In this chapter, we have studied the PMMA removal selectively to PS on high- χ PS-*b*-PMMA films with an 18-nm pitch. We started by characterizing the composition of the modified PS and PMMA homopolymers that compose the high- χ modified PS-*b*-PMMA block copolymer, which led us to conclude that the modified PS-*b*-PMMA presents a composition similar to that of standard PS-*b*-PMMA. Then, we selected different plasma chemistries and we evaluated their etch rate, and consequent selectivity, on modified PS and PMMA homopolymers, therefore selecting two different chemistries that fulfill our selectivity requirement: CH₃F/Ar/SO₂ and CH₄/N₂.

We then characterized the impact of the modified chemistry, pitch and initial thickness on the etching of the high- χ modified PS-*b*-PMMA. When comparing a modified and a standard PS-*b*-PMMA BCP with the same pitch and initial thickness, we concluded that, for the same plasma etching chemistry, the high- χ modified PS-*b*-PMMA chemistry does not present a significant impact on the PMMA plasma etching when compared to the standard PS-*b*-PMMA block copolymer. However, when comparing the high- χ modified PS-*b*-PMMA with two different pitch (18 and 32 nm) and two different initial thicknesses (16 and 36 nm, respectively), for the high- χ L18 BCP, the same etching chemistries that were validated for larger pitch (32 nm) present different problems that prevent pattern transfer into the SiO₂ hard mask for the smaller BCP. Therefore, we concluded that the main high- χ L18 PS-*b*-PMMA plasma etching challenges come from its small dimensions, namely the pitch and initial thickness.

The next sections focused on developing different approaches in order to improve the PMMA:PS selectivity. The first approach focused on optimizing the CH₃F/Ar/SO₂ plasma, which presented low selectivity (around 1.6) for the high- χ L18, but no bridge formation. However, we concluded that this plasma presents a very narrow process window regarding the etch duration due to the small dimensions – pitch and thickness – of the high- χ L18 BCP film. Varying the etching parameters did not improve the results, nor did the cyclic approach based on alternating CH₃F/Ar/SO₂ and Ar steps. Increasing the initial thickness of the high- χ L18 film led to mechanical stability problems and to pattern wiggling due to the high aspect ratio of the lines, showing that the smaller CD of the high- χ block copolymer limits the maximum initial thickness allowed for the BCP film in order to avoid pattern wiggling or collapse. Therefore, we concluded that the CH₃F/Ar/SO₂ plasma was not appropriate for the high- χ PS-*b*-PMMA etching.

The second approach was based on an UV exposure followed by plasma etching. The goal was to break the PMMA chains and harden the PS block before plasma removal of the remaining PMMA and of the neutral layer. We showed that the UV exposure had no effect in the PS. However, for the PMMA, the higher UV exposure dose led to a consumption of 17 nm and decreased the PMMA etch rate and the PMMA:PS selectivity by about 30%. FTIR analysis allowed us to conclude that the loss of C–O and C=O groups during UV exposure was responsible for the decrease of the PMMA etch rate. Therefore, we concluded that, by eliminating these oxygen-containing groups during UV exposure, the etch rate of PMMA during CH₃F/Ar/SO₂ plasma approaches that of the PS, and therefore the selectivity between both materials decreases. In summary, the higher the UV exposure dose, the lower the PMMA etch rate and PMMA:PS selectivity. Thus, this approach was not adapted to increase the PMMA:PS selectivity.

The third approach consisted on optimizing the CH₄/N₂. While for PS and PMMA homopolymers we succeeded in etching the PMMA without consuming the PS thanks to a CN-type deposition layer formed on the PS surface, the same could not be applied to the high- χ PS-*b*-PMMA block copolymer assembled on a free surface. The results showed that high- χ BCP requires higher selectivity than standard PS-*b*-PMMA due to its smaller thickness. Moreover, the ratio 1:1, while presenting the best PMMA:PS selectivity without pattern collapse, also presented some bridge formation on top of the lines, which were formed due to intensive sidewalls passivation and to a species confinement effect accentuated by the small CD (9 nm). We then concluded that the main high- χ PS-*b*-PMMA dry etching difficulties come from the trade-off between obtaining high selectivity and avoiding bridge formation.

The fourth approach proposed was a mixed wet and dry etching process. The wet PMMA removal presents infinite selectivity on high- χ modified PS-*b*-PMMA. The UV exposure causes the PMMA chains to break and the PS lines to harden, and the IPA rinse removes the broken PMMA chains without modifying the PS lines. A dry etching process to open the neutral layer using an Ar/O₂ plasma with high argon content was developed in order to obtain a highly anisotropic etching and to conserve more PS budget. With this mixed wet and dry etching approach, the complete pattern transfer of an 18-nm pitch high- χ organic block copolymer into the SiO₂ hard mask and silicon bulk layers was validated with CD bias \sim 2 nm.

CHAPTER V:

ETCHING AND PATTERN TRANSFER OF SILICON-BASED HIGH- χ BLOCK COPOLYMER

V. ETCHING AND PATTERN TRANSFER OF SILICON-BASED HIGH- χ BLOCK COPOLYMER

In Chapter I, we have seen that there are two main types of high- χ block copolymers: purely organic and inorganic. While Chapter IV focused on the purely organic high- χ PS-*b*-PMMA, Chapter V shall present the plasma etching of the silicon-containing high- χ poly(styrene-*b*-1,1-dimethylsilacyclobutane) (PS-*b*-PDMSB). This block copolymer was developed by Arkema, presents an intrinsic period L_0 of 18 nm and lamellar morphology.

Since the silicon-containing phase (PDMSB) presents higher affinity to the air than the organic phase (PS), a top coat layer with the same affinity for both blocks is added on top of the block copolymer to ensure the vertical orientation of the lamellae, as shown in Figure V-1. Therefore, the main objective of this study is to develop a plasma etching approach capable of removing the top coat layer and the PS block selectively to the PDMSB and adapted to the 18-nm pitch on 300 mm wafers.

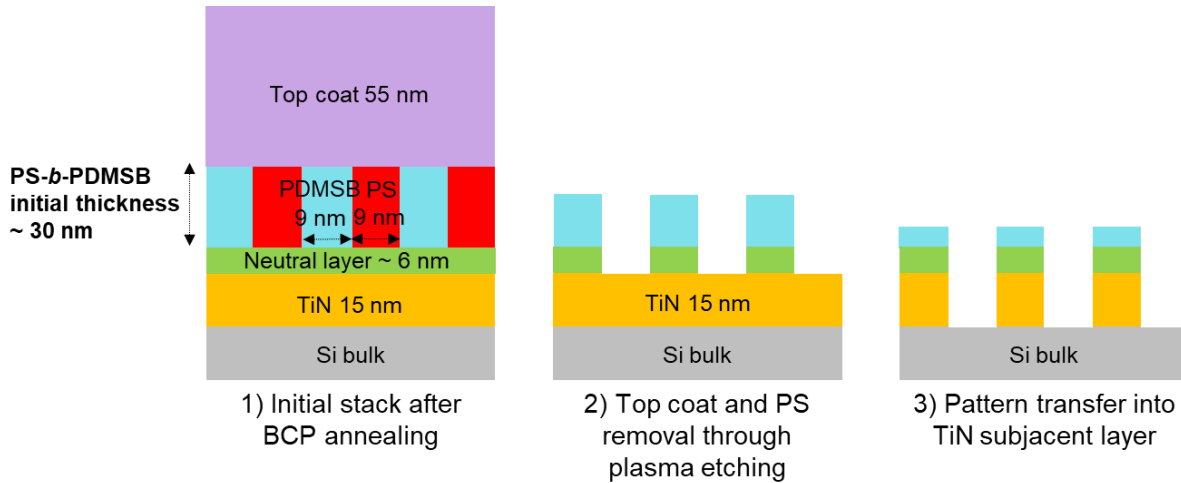


Figure V-1: Schematics for the flow used in the etching study of the 18-nm pitch high- χ PS-*b*-PMMA block copolymer.

Figure V-1 shows the etching flow for this high- χ PS-*b*-PDMSB. The initial stack consists of a 15-nm titanium nitride (TiN) hard mask layer deposited over the silicon substrate through physical vapor deposition (PVD). To neutralize the hard mask surface and obtain a vertical alignment of the block copolymer, a thin neutral layer with a thickness of around 6 nm is grafted to the hard mask. The PS-*b*-PDMSB solution is then deposited with a thickness of approximately 30 nm. Next, the cross-linkable top coat is also deposited, presenting a final thickness of around 55 nm. Our goal is to conserve enough PDMSB budget after top coat and PS removal to transfer the line patterns into the 15-nm TiN layer.

We shall start by characterizing the top coat and high- χ PS-*b*-PDMSB composition before etching, as well as the Top coat:PS selectivity for different plasma etching chemistries. Once the plasma chemistries that achieve good selectivity between top coat, PS and PDMSB have been identified, they shall be evaluated on high- χ PS-*b*-PDMSB patterned wafers with fingerprint-like morphology.

Part of the work presented in this Chapter has been published at the *Journal of Vacuum Science & Technology B* and was selected as an Editor's Pick [Gusmão 2021B].

V.1 Characterization of pristine top coat and PS-*b*-PDMSB

In order to propose etching solutions capable of removing the top coat layer and the PS block selectively to the PDMSB and adapted to the 18-nm pitch, it is important to characterize both the top coat and the PS-*b*-PDMSB block copolymer before etching. Our goal is to confirm that the formulas given in Figure II-2 of Chapter II.1.1.2 corresponded well to the materials on which we worked during this thesis. The surface composition of the different materials was characterized by *ex-situ* X-ray photoelectron spectroscopy (XPS).

The results for the PS homopolymer have already been presented in Chapter IV.1.1. Before etching, PS consists of only carbon and hydrogen. Its C1s spectra shows two peaks: one at 284.8 eV, assigned to C-C/C=C, corresponds to two different bonds (aliphatic carbon at 284.7 eV and carbon from phenyl cycle at 285.0 eV) that cannot be dissociated due to the spectral resolution. The second one is observed at 291.5 eV and represents a shake-up peak characteristic of the aromatic cycle, being therefore identified as $\pi \rightarrow \pi^*$ [Beamson 1992].

For the top coat characterization, the top coat solution was spin-coated on 300 mm silicon blanket wafers and then annealed to obtain a 55-nm homogeneous film. The XPS results presented in Figure V-2 for the top coat correspond to an incident angle of 23.75°, which inspects the first 10 nm of the top coat surface. Since the film is homogeneous, the XPS surface analysis should accurately represent the bulk of the film. However, for the PDMSB characterization, the PDMSB homopolymer is not available. Therefore, in order to characterize its composition, the PS-*b*-PDMSB block copolymer is deposited over a silicon wafer without top coat and *ex-situ* XPS analysis are conducted. Since there is not a top coat layer, the top of the BCP layer will consist of horizontal PDMSB and PS lamellae, with the PDMSB on the interface with the air. This means that for the XPS analysis with an angle of 76.25°, which inspects around 2 or 3 nm of the top surface, it is mostly the PDMSB that will be analyzed.

Figure V-2(a) shows a comparison of the full survey spectra (binding energies between 0 and 1000 eV) for both materials. The top coat and the PDMSB lamellae on top of the PS-*b*-PDMSB present only one peak in common, which is detected around 285 eV and corresponds to the carbon C1s peak. The two peaks detected around 100 and 150 eV correspond to the silicon Si2p and Si2s peaks, respectively. They are only observed for the PS-*b*-PDMSB, as expected, since it is a silicon-containing BCP. The peaks detected around 533 and 978 eV corresponds to the oxygen O1s and Auger KL₂₃L₂₃ peaks, respectively, and is only observed for the top coat. Finally, the peaks around 688 and 832 eV represent the fluorine F1s and Auger KL₂₃L₂₃ peaks, respectively, and are once again only present in the top coat spectra [Beamson 1992]. It is important to notice that hydrogen cannot be detected by XPS. Therefore, we can conclude that PS-*b*-PDMSB consists only of carbon, hydrogen and silicon, while the top coat consists of carbon, oxygen, fluorine and hydrogen. These observations correspond to the top coat and PS-*b*-PDMSB structures presented in Figures II-5 and II-2, respectively, of Chapter II.

Once the main elements present in each material were identified, we then obtained the spectra for each element. From Chapter II.1.1.3, we have seen that the top coat consists of a poly(2,2,2-trifluoroethylmethacrylate-*r*-glycidylmethacrylate-*r*-2-hydroxyethylmethacrylate) statistical terpolymer [Chevalier 2021]. The C1s spectra for the top coat, presented in Figure V-2(b), shows four different peaks: one at 285.0 eV also identified as C-C/CHCOOH, which represents both the carbon at CH₂ and CH₃ bonds (at 284.7 eV) and the carbon from the acrylate

compounds (at 285.5 eV). The second peak appears at 286.5 eV and represents the carbon in the methyl ester (C-O) bonds. The third one, at 288.8 eV, corresponds to the carbon in the carboxyl group (C=O). Finally, the fourth one, at 292.7 eV, corresponds to carbon bound to three fluorine atoms (CF₃) [Beamson 1992].

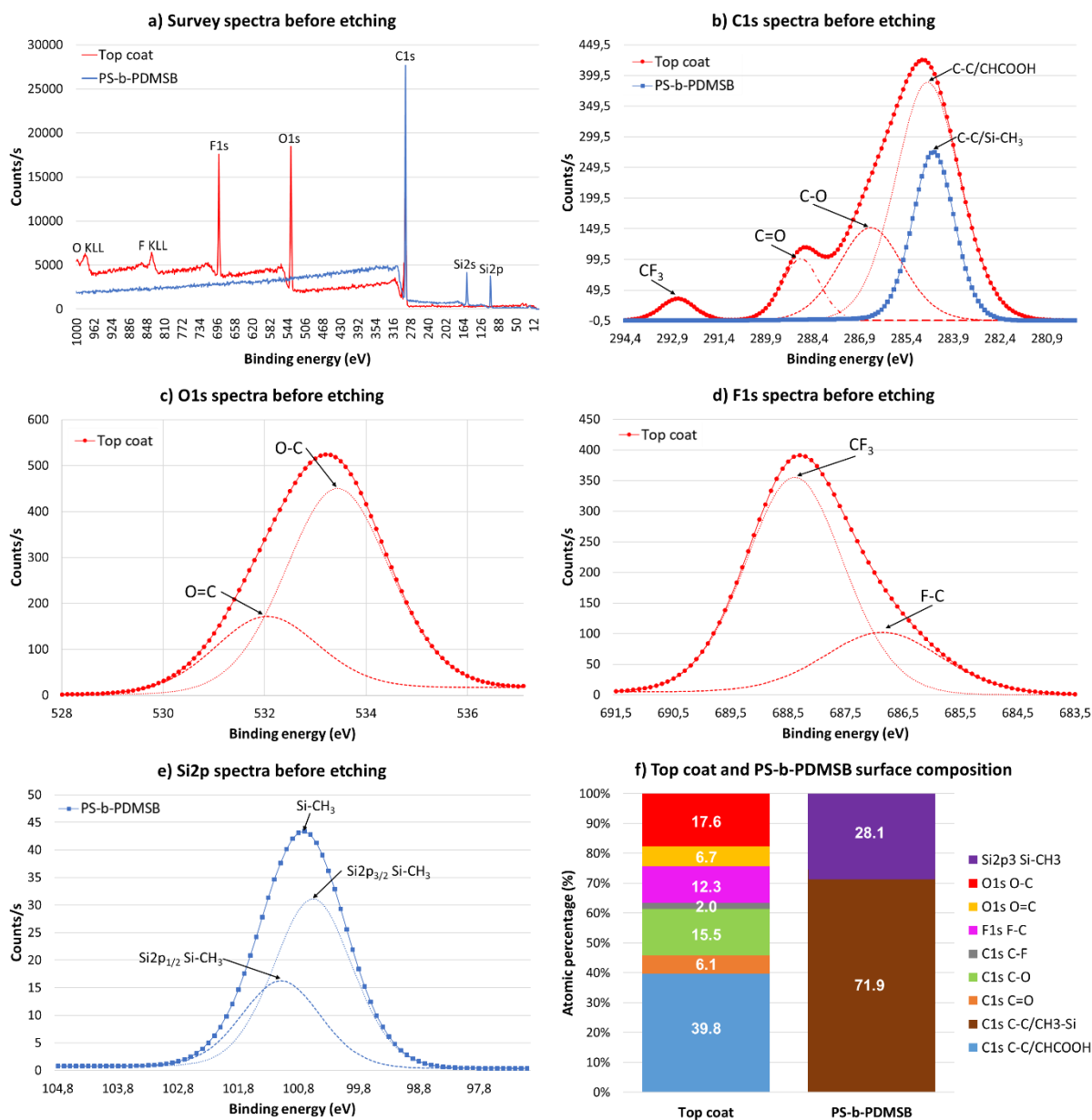


Figure V-2: Surface composition of the top coat and PS-*b*-PDMSB block copolymer obtained by *ex-situ* XPS: (a) survey spectra; (b) C1s spectra; (c) O1s spectrum; (d) F1s spectrum; (e) Si2p spectrum; and (f) atomic percentage of each peak identified on the different spectra. The results for the top coat and PS-*b*-PDMSB correspond to an incident angle of 23.75° and 76.25°, respectively.

The atomic percentage of each of these peaks is presented in Figure V-2(f) and leads to a total carbon percentage of 63.4%. The as deposited top coat also presents around 24.3% of oxygen and the O1s peaks in Figure V-2(c) confirm the observations already made: one at 532.0 eV and the other at 533.5 eV corresponding to O=C and O-C bonds, respectively. Finally, Figure V-2(d) shows the fluorine F1s spectra for the top coat. The main peak is attributed to two different contributions: a F-C peak at 686.8 eV and a CF₃ peak at 688.4 eV. These peaks

contributions are represented together as “F-C” in Figure V-2(f) and correspond to 12.3% of the top coat surface composition [Beamson 1992].

As we can see in Figures V-2(a) and (f), the PDMSB lamellae on top of the PS-*b*-PDMSB BCP consist of carbon (71.9%) and silicon (28.1%). Figure V-2(b) presents the carbon C1s scan for the PDMSB lamellae, where one peak is identified as C-C/Si-CH₃ at 284.5 eV: it represents both the carbon at CH₂ and CH₃ bonds (at 284.7 eV) and the carbon from Si-CH₃ bonds (at 284 eV). The Si2p spectra in Figure V-2(e) confirms the presence of Si-CH₃ bonds, which are represented by doublet Si2p_{3/2} and Si2p_{1/2} peaks at 100.5 and 101.1 eV, respectively [Beamson 1992].

Finally, following the analysis of the various contributions present in the top coat and PDMSB lamellae on top of the PS-*b*-PDMSB, we can quantify each of them and thus define the composition of these two polymers. Figure V-2(f) shows that the PS-*b*-PDMSB is only composed of carbon-carbon, carbon-hydrogen and carbon-silicon bonds, as expected by the known formula of the material presented in Figure II-2 of Chapter II.1.1.2. Regarding the top coat, we observe a composition very similar to that of the PMMA presented in the previous chapter, with only the addition of 12.2% of fluorine. This result is consistent with the composition of the top coat presented in Chapter II.1.1.3, which consists of different methacrylate-based monomers.

Therefore, we can conclude that the top coat and PS-*b*-PDMSB materials studied throughout this PhD correspond to the known formulas for these materials. This shall help us propose etching solutions adapted to these polymers.

V.2 Top coat removal selectively to PS-*b*-PDMSB

We have seen in Chapter IV that, for the PS-*b*-PMMA block copolymer, a variety of etching chemistries have been investigated for the selective PMMA removal. Most of them are based on O₂, Ar/O₂, CO/H₂ and CH₄/N₂ [Liu 2007] [Chan 2014] [Sarrazin 2018]. The O₂-based chemistries present low PMMA:PS selectivity (around 1.6) due to their high reactivity, while oxygen-free chemistries such as CH₄/N₂ obtain high selectivity but present bridge formation for smaller pitch. Since the top coat's composition consists of different methacrylate-based monomers, it should present etching mechanisms and selectivity similar to the PMMA with these same chemistries.

For the PS removal selectively to a silicon-containing phase such as PDMSB, we have seen in Chapter I.5.2 that the most commonly used approaches are oxygen-based plasmas. Oxygen is known to etch the organic block while oxidizing the silicon-containing block, replacing Si-CH₃ bonds by Si-O_x bonds, with good selectivity [Zhang 2014] [Girardot 2014] [Aissou 2015].

In this section, we propose to evaluate a top coat and PS removal approach which consists of removing the top coat selectively to the BCP with a first etching step and then removing the PS phase in a separate step. We shall start by evaluating two different chemistries for the top coat removal: an Ar/O₂ plasma, which has been largely used in the literature, and the CH₃F/Ar/SO₂ plasma that was investigated in Chapter IV for the selective removal of PMMA. Once the top coat removal has been validated, we shall proceed to the PS removal selectively to PDMSB. For that, both oxidizing and reducing chemistries that have already been explored

in the previous chapter will be investigated and the results obtained for the high chi PS-*b*-PDMSB will be presented.

V.2.1 Development of a top coat removal plasma etching process

V.2.1.1 Application to blanket wafers

To evaluate the top coat removal selectively to the PS for the two-step approach, 300 mm silicon blanket wafers with either the top coat or the PS homopolymer deposited on top were used. Both materials presented a thickness of around 55 nm. All plasma etching experiments for the two-step approach were conducted on the 300-mm KiyO FX® ICP reactor from LamResearch. For the two-step approach, two oxygen-containing plasma etching are selected to investigate the top coat removal: Ar/O₂ and CH₃F/Ar/SO₂. The plasma parameters for these chemistries are recalled in Table V-1. Just like in Chapter IV, the CH₃F/Ar/SO₂ recipe presents a RF bias pulsing mode with the following conditions: duty cycle at 31% and pulsing frequency at 300 Hz. These parameters shall not be varied during our studies.

Table V-1: Plasma parameters for the different chemistries tested for the top coat removal.

Chemistry	Pressure (mTorr)	Power (W)	Bias (V)	Flow (scm)
CH ₃ F/Ar/SO ₂	10	250	-650 (pulsed)	30/200/150
Ar/O ₂	10	220	-100 (continuous)	50/5

The top coat and PS etch rates and top coat:PS selectivity are presented in Table V-2 for an etching duration of 10 seconds. The CH₃F/Ar/SO₂ plasma presents faster etch rate for both materials, probably due to the much higher RF bias (-650V) when compared to the Ar/O₂ plasma (-100V). Nevertheless, both chemistries present similar top coat:PS selectivity, which ranges between 3.2 and 3.5. Therefore, both chemistries shall be applied to the top coat removal for patterned wafers.

Table V-2: Top coat and PS homopolymer etch rates, as well as the corresponding Top coat:PS selectivity, calculated for the different etching chemistries. Etching duration was 10 seconds.

Chemistry	Etch rate PS (nm/s)	Etch rate top coat (nm/s)	Top coat:PS selectivity
CH ₃ F/Ar/SO ₂	1.3	4.1	3.2
Ar/O ₂	0.8	2.8	3.5

V.2.1.2 Application to patterned wafers

In this section, we shall apply the selected plasma chemistries from the previous section to the top coat removal for patterned wafers. All experiments were conducted on 300 mm silicon wafers with a 15-nm TiN layer. To neutralize the hard mask surface and obtain a vertical alignment of the block copolymer, a thin neutral layer is spin-coated and annealed at 200°C for 75 seconds in order to be grafted to the hard mask. After a propylene glycol methyl ether acetate (PGMEA) rinse, it presents a thickness of around 6 nm. The PS-*b*-PDMSB solution is then spin-

coated and annealed at 60°C for 60 seconds to obtain a thickness of approximately 30 nm. Next, the cross-linkable top coat is also spin-coated and then annealed at 90°C for 180 seconds, presenting a final thickness of around 55 nm. Finally, the whole stack goes through a final annealing at 200°C for 5 minutes in order to assemble the block copolymer into vertical lamellae with period $L_0 = 18$ nm and CD = 9 nm.

Figure V-3 presents the results for the top coat removal using the $\text{CH}_3\text{F}/\text{Ar}/\text{SO}_2$ plasma for etching durations between 15 and 25 seconds. First, it should be noticed that it was not possible to obtain a top-view SEM image for the top coat removal during 15 seconds, because there was no contrast. This indicates that the top coat was not completely removed and, therefore, the block copolymer's fingerprint-like pattern cannot be seen. This is confirmed by the thickness measurements obtained through ellipsometry. The values presented in Figure V-3 for the different etching durations correspond to the mean value for 25 different points throughout the 300 mm wafer's surface. After 15 seconds of top coat removal with the $\text{CH}_3\text{F}/\text{Ar}/\text{SO}_2$ plasma, the average polymer thickness is around 36.5 nm, which is greater than the block copolymer initial thickness (30 nm). Therefore, an etching duration of 15 seconds is not enough to completely remove the top coat layer.

For an etching duration of 20 seconds, however, the top-view SEM images and thickness measurements show that the top coat layer has been completely removed and that the block copolymer was not significantly etched by the $\text{CH}_3\text{F}/\text{Ar}/\text{SO}_2$ plasma. Finally, for a longer etch duration of 25 seconds, the decrease in polymer thickness shows that the block copolymer has been partially etched. Furthermore, the increase of the standard deviation (represented by 3σ) indicates that one of the blocks (namely, the organic PS block) has probably been more consumed than the other. Therefore, the etching duration of 20 seconds has been retained as ideal for a top coat removal selectively to the block copolymer with the $\text{CH}_3\text{F}/\text{Ar}/\text{SO}_2$ plasma.

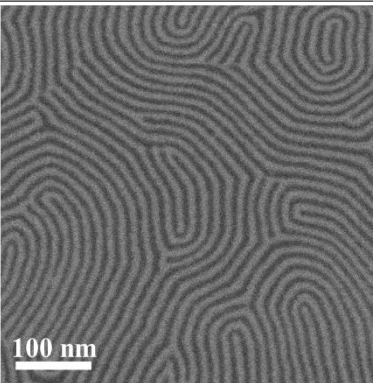
Time (s)	15s	20s	25s
Top-view SEM	/		
Thickness (nm)	36.45	29.85	26.23
3σ (nm)	0.89	0.71	1.06

Figure V-3: Results for the top coat removal using $\text{CH}_3\text{F}/\text{Ar}/\text{SO}_2$ for three different etching durations (15, 20 and 25 seconds).

Figure V-4 presents the results for the top coat removal using the Ar/O_2 plasma for etching durations between 30 and 50 seconds. The results for 30 seconds of top coat removal are similar to the ones for the $\text{CH}_3\text{F}/\text{Ar}/\text{SO}_2$ plasma for 15 seconds: there was no contrast during the top-view SEM inspection and the thickness measurement values are greater than the block

copolymer's initial thickness. However, when we extend the etching duration to 40 or 50 seconds, we observe some brighter spots where no line/space patterns are visible. Where the bright spots are not present, the lines are mostly interrupted and present an apparently smaller CD. Ellipsometry measurements indicate a block copolymer average thickness of 27 nm after 40 seconds of etching, which indicates that the top coat has been fully removed and the Ar/O₂ plasma began to etch the block copolymer.

A possible explanation for these results is that the top coat has not been completely removed in some places, but it is not detectable by the ellipsometer, which gives us an average value over the entire film. Indeed, there may be something at the top coat and BCP interface that does not etch in Ar/O₂ plasma (for example, a non-homogeneous PDMSB interface or non-volatile etching by-products), therefore explaining the etch stop in certain places. These results indicate that the top coat removal using an Ar/O₂ plasma is not adapted to this PS-*b*-PDMSB stack.

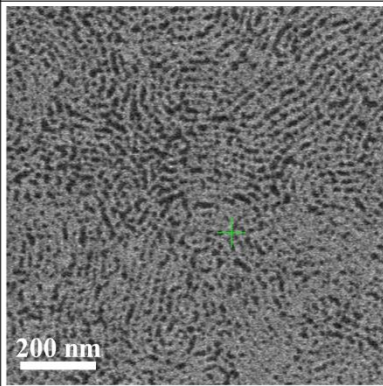
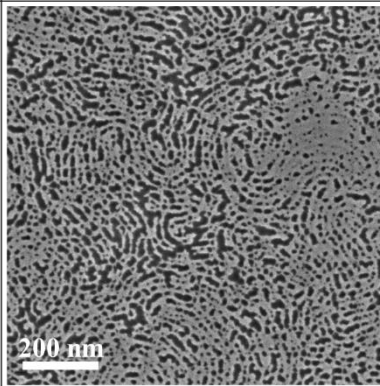
Time (s)	30s	40s	50s
Top-view SEM	/		
Thickness (nm)	33.95	27.04	22.09
3 σ (nm)	0.51	0.66	1.40

Figure V-4: Results for the top coat removal using Ar/O₂ for three different etching durations (30, 40 and 50 seconds).

In this section, two oxygen-containing plasma etching were selected to investigate the top coat removal: Ar/O₂ and CH₃F/Ar/SO₂. For blanket top coat and PS homopolymer wafers, both chemistries presented similar top coat:PS selectivity, which ranged between 3.2 and 3.5. Thus, both chemistries were selected for application with patterned wafers.

However, when the Ar/O₂ plasma was applied to the patterned wafers with the complete PS-*b*-PDMSB and top coat stack, we observed some brighter spots where no line/space patterns were visible. Moreover, where the bright spots were not present, the lines were mostly interrupted and presented a smaller CD. This etch stop of the top coat in certain areas of the wafer could be explained by the presence of something at the top coat and BCP interface that does not etch in Ar/O₂ plasma (for example, a non-homogeneous PDMSB interface or non-volatile etching by-products).

Finally, using the CH₃F/Ar/SO₂ plasma during 20 seconds, the top-view SEM images and thickness measurements show that the top coat layer was completely removed without significantly etching the block copolymer. Therefore, this process has been selected as the process of reference for the top coat removal.

V.2.2 Development of PS removal step selectively to PDMSB

V.2.2.1 Application to PS-*b*-PDMSB patterned wafers

Now that we have selected the best process for the top coat removal, we shall evaluate different etching chemistries for the PS removal. We have seen before that, for the PS removal selectively to a silicon-containing phase such as PDMSB, the most commonly used approaches are oxygen-based plasma, which are capable of etching the organic block while oxidizing the silicon-containing block, replacing Si-CH₃ bonds by Si-O_x bonds. Thus, one of the plasma etching options that shall be investigated in this section is the Ar/O₂ plasma that was validated for the neutral layer opening in Chapter IV.3.4.2. Furthermore, we have also chosen to evaluate an oxygen-free chemistry, which corresponds to the CH₄/N₂ etching explored in Chapter IV.3.3 for the selective PMMA removal. The goal of the oxygen-free chemistry is to avoid further oxidation of the TiN hard mask, thus possibly facilitating the pattern transfer. Finally, the third chemistry explored is a CH₄/N₂/O₂ plasma, which presents the same plasma parameters as the CH₄/N₂ etching with the addition of 5 sccm of oxygen to ensure the PS etching and prevent bridge formation.

The plasma parameters for the three etching chemistries are presented in Table V-3, as well as the PS etch rate calculated through ellipsometry measurements of PS homopolymer blanket wafers before and after etching. Since the PDMSB homopolymer is not available, it is not possible to estimate the PS:PDMSB selectivity for blanket wafers.

Table V-3: Plasma parameters and PS homopolymer etch rate (ER) for the different chemistries tested for the PS removal.

Chemistry	Pressure (mTorr)	Power (W)	Bias (V)	Flow (sccm)	hPS ER (nm/s)
Ar/O ₂	10	220	-200	120/5	1.0
CH ₄ /N ₂	10	500	-200	10/50	0.7
CH ₄ /N ₂ /O ₂	10	500	-200	10/50/5	1.0

We then proceeded to the application on patterned wafers with the complete PS-*b*-PDMSB and top coat stack. The top coat was removed with the CH₃F/Ar/SO₂ plasma during 20 seconds and then the three different plasma chemistries from Table V-3 were conducted for PS removal. The top-view and cross-section SEM images after top coat and PS removal are presented in Figure V-5. For these samples, different TiN thickness were used, but it does not impact the results, since we use the contrast between TiN and BCP to define the interface (highlighted in red). More importantly, the top coat, BCP and neutral layer initial thicknesses are always the same as the ones presented in Figure V-1: 55, 30 and 6 nm, respectively.

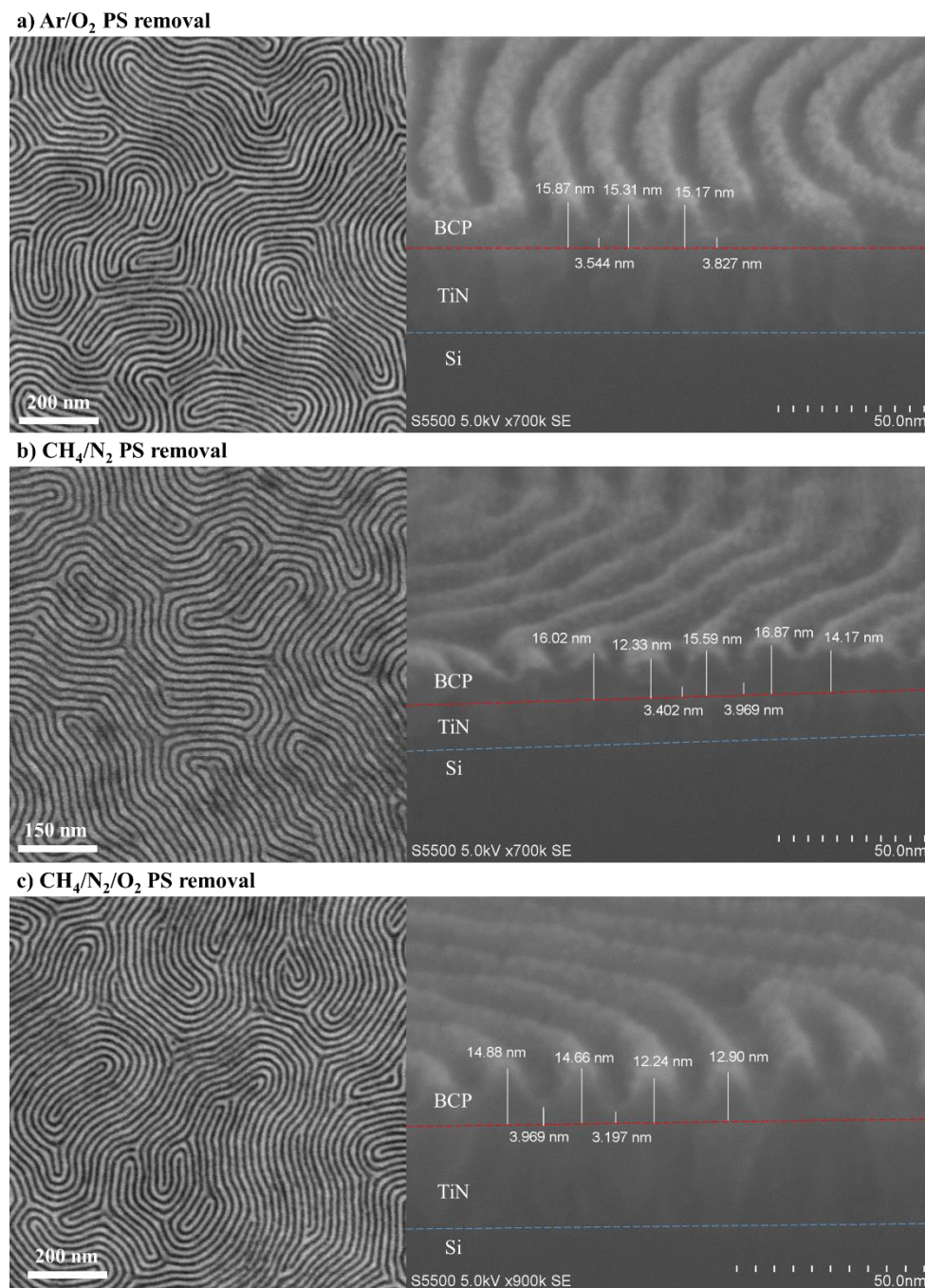


Figure V-5: Top-view and cross-section SEM images for the PS-*b*-PDMSB block copolymer after top coat removal using the CH₃F/Ar/SO₂ plasma and PS removal with three different plasma chemistries: (a) Ar/O₂ during 20 seconds; (b) CH₄/N₂ during 60 seconds; and (c) CH₄/N₂/O₂ during 30 seconds.

After 20 seconds of Ar/O₂ plasma, Figure V-5(a) shows that the PS has been completely removed and there are around 3.7 nm of neutral layer left. The PDMSB budget remaining after etching is around 15.5 nm, which translates to a PS:PDMSB selectivity of 1.8. Figure V-5(b) indicates that the CH₄/N₂ plasma presents similar results: after 60 seconds of etching, the PS has been completely etched. The remaining neutral layer and PDMSB thickness correspond to 3.7 and 15 nm, respectively, once again leading to a PS:PDMSB selectivity of 1.8. Finally, Figure V-5(c) shows the results for the CH₄/N₂/O₂ plasma, which presents a slightly lower

selectivity of 1.6, due to the lower PDMSB remaining budget of 13.7 nm after 30 seconds of PS removal.

For the pattern transfer of the 18-nm pitch high- χ PS-*b*-PDMSB into the 18-nm hard mask (15 nm of TiN and approximately 3 nm of native titanium oxide, TiO_x), we estimate that there should be at least 18 nm of PDMSB plus neutral layer left after top coat and PS removal to ensure the correct pattern transfer. Since the BCP plus neutral layer thickness after top coat removal is around 30 nm, this means the minimum PS:PDMSB selectivity desired during PS removal is around 2.5.

Therefore, none of these plasma processes allows us to obtain the desired minimum PS:PDMSB selectivity. It should also be noticed that, for the Ar/O₂ and CH₄/N₂/O₂ plasmas, the PDMSB lines present a faceted profile after PS removal, which is probably caused by the more chemical (isotropic) aspect of the oxygen-based etching. The CH₄/N₂ plasma, on the other hand, leads to a larger CD based on the top-view image in Figure V-5(b), indicating the presence of a flank passivation mechanism, which shall be further explored in section V.2.2.3.

V.2.2.2 Increasing the block copolymer's initial thickness

In order to increase the PDMSB budget after top coat and PS removal and relax the PS:PDMSB selectivity constraints, we have decided to increase the block copolymer's initial thickness. This is achieved by reducing the rotational speed during spin coating from 2000 rpm (process of reference) to 1000 rpm (increased thickness). All the other deposition parameters for the neutral layer, block copolymer and top coat remained the same and were presented in section V.2.1.2. The SEM and ellipsometry results for the block copolymer with increased thickness are presented in Figure V-6.

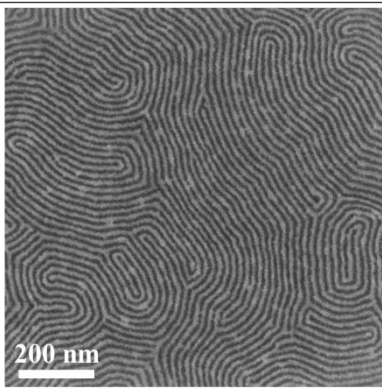
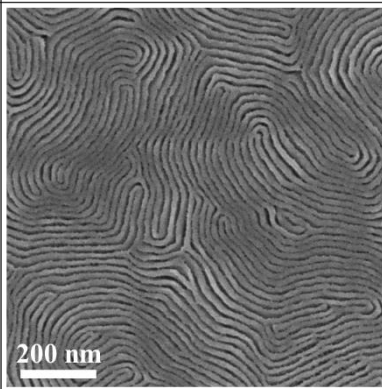
Step	As dep	After top coat removal	After PS removal
Top-view SEM	/		
Thickness (nm)	100.8	42.8	22.3
3 σ (nm)	1.0	0.9	1.9

Figure V-6: Results for the PS-*b*-PDMSB block copolymer with increased thickness before etching, after top coat removal with the CH₃F/Ar/SO₂ plasma during 20 seconds and after PS removal with the Ar/O₂ plasma during 25 seconds.

First, it should be noticed that it was not possible to obtain a top-view SEM image for the as deposited initial stack because there is no contrast before top coat removal. However, the ellipsometry measurements indicate a total thickness of approximately 100.8 nm, which

indicates an increase of around 10 nm when compared to the results for the process of reference (initial thickness for the complete stack of approximately 91 nm).

After top coat removal using the CH₃F/Ar/SO₂ plasma during 20 seconds, the top-view images confirms the complete removal of the top coat layer, while the ellipsometry measurements indicate a remaining BCP thickness of approximately 42.8 nm. This indicates a consumption of around 58 nm of polymeric materials, thus corresponding to the complete removal of the top coat layer (55 nm) and a slight consumption of the block copolymer (3 nm). Despite the slight 3-nm BCP consumption, the BCP budget has been increased by 13 nm when compared to the results of Figure V-3, in which the BCP thickness after top coat removal was approximately 29.9 nm. As a consequence, for the block copolymer with increased initial thickness, the desired PS:PDMSB selectivity in order to conserve 18 nm of PDMSB after PS removal is around 1.7, which corresponds to the selectivity values obtained for the different PS removal chemistries in Figure V-5.

After PS removal with the Ar/O₂ plasma during 25 seconds, the thickness measurements indicate a remaining BCP average thickness of 22.3 nm, which is superior to the desired thickness of 18 nm. However, the top-view SEM image shows significant pattern collapse, thus preventing any possibility of pattern transfer into the hard mask. This pattern collapse is probably caused by the high aspect ratio of the PDMSB lines, which is around 2.5.

Therefore, even though increasing the block copolymer's initial thickness allows us to increase the available PDMSB budget after top coat and PS removal, it also leads to pattern collapse due to the high aspect ratio of the lines. Thus, it is not a viable solution and all further experiments shall be conducted using the process of reference: block copolymer spin coating at 2000 rpm and initial thickness for the complete stack of approximately 91 nm.

V.2.2.3 Understanding the etching and passivation mechanisms

In order to understand the etching mechanisms and plasma/surface interactions involved during PS removal, *ex-situ* XPS analysis were carried out on the PDMSB lines with patterned wafers after top coat and PS removal using the three different etching chemistries evaluated in section V.2.2.1. Even though the results obtained cannot be considered quantitatively accurate, they can still be used for qualitative evaluation and compared amongst each other. Figure V-7 presents a schematic representation of the XPS analysis for the PDMSB lines after top coat and PS removal, using an incident angle of 76.25° from the normal. The theoretical depth of the analyzed area for this incident angle, represented by the red *y* segment, can be calculated by Equation V-1. This means that, for this incident angle, the XPS analysis mostly observes the top 2 nm of the PDMSB lines.

$$\tan(90^\circ - 76.25^\circ) = \frac{y}{9 \text{ nm}} \Rightarrow y = 9 \text{ nm} \times \tan(13.75^\circ) = 2.2 \text{ nm}$$

Equation V-1: Theoretical depth of the analyzed area for an incident angle of 76.25° from the normal.

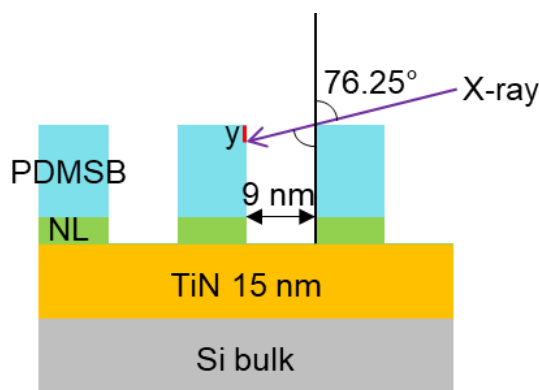


Figure V-7: Schematics for the XPS analysis with an incident angle of 76.25° for the PDMSB lines after top coat and PS removal. The red segment (y) represents the theoretical depth of the analyzed area for this incident angle.

The results for the block copolymer's surface composition after top coat and PS removal are shown in Figures V-8 and V-9. The as deposited composition (without top coat) is also presented for comparison purposes. We have seen in section V.1 that the as deposited PS-*b*-PDMSB consists of carbon (71.9%) and silicon (28.1%) with a C1s peak representing C-C and Si-CH₃ bonds at 284.5 eV and a Si2p doublet peak centered on 100.7 eV representing the Si-CH₃ bonds.

After top coat removal using CH₃F/Ar/SO₂ and PS removal using Ar/O₂, Figure V-8(a) shows a significant decrease of the C-C peak, which has also been shifted of around 0.5 eV. It is now situated around 285 eV, indicating that the Si-CH₃ bonds are no longer present and, therefore, the peak at 285 eV corresponds only to the carbon at CH₂ and CH₃ bonds. This observation is confirmed by the Si2p spectra in Figure V-8(b), which shows that the Si-CH₃ doublet peak at 100.7 eV is replaced by a Si-O doublet peak at 103.6 eV (Si2p_{3/2} at 103.3 eV and Si2p_{1/2} at 103.9 eV). Furthermore, the C1s spectra in Figure V-8(a) also shows the presence of C-O and C=O bonds after PS removal, which come from both the oxygen present in the plasma and from the air exposure before XPS analysis. Finally, Figure V-9(b) shows the atomic percentage of each bond observed. It allows us to conclude that the PDMSB lines are mostly composed of Si-O bonds, which is confirmed by the significant atomic percentage of O1s Si-O (peak at 533 eV) and Si2p Si-O, which are around 37.8% and 34.8%, respectively [Beamson 1992]. Therefore, for the Ar/O₂ etching, we conclude that the oxygen consumes the PS very quickly by forming volatile CO_x species and, at the same time, it transforms the Si-CH₃ bonds of the PDMSB into Si-O bonds.

For the PS removal based on CH₄/N₂ plasma, Figure V-8(a) presents the same phenomena already observed for the C1s spectra after Ar/O₂: the C-C peak is significantly reduced and a 0.5 eV shift is observed, indicating the loss of Si-CH₃ bonds. Moreover, a C-N peak appears at 286 eV which, due to spectral resolution, cannot be differentiated from C-O (286.5 eV) bonds and is thus represented together as C-O/C-N. The presence of this bond is confirmed by Figure V-9(c), in which a N-C peak contribution related to the N1s spectra (peak at 399 eV) represents around 19.7% of the PS-*b*-PDMSB surface composition. C-O and C=O bonds are also observed after PS removal, which come from the air exposure before XPS analysis. As for the Si2p spectra after CH₄/N₂ plasma, Figure V-8(b) shows a main peak at 103 eV, which is composed of two doublet peaks: Si-O at 103.6 eV (Si2p_{3/2} at 103.3 eV and Si2p_{1/2} at 103.9 eV) and a smaller Si-N peak at 102.3 eV (Si2p_{3/2} at 102 eV and Si2p_{1/2} at 102.6 eV) [Beamson 1992].

Thus, we may conclude that, for the CH₄/N₂ plasma, SiO_xN_y bonds replace the Si-CH₃ bonds from the PDMSB and a CN-type deposit forms over the PDMSB lines.

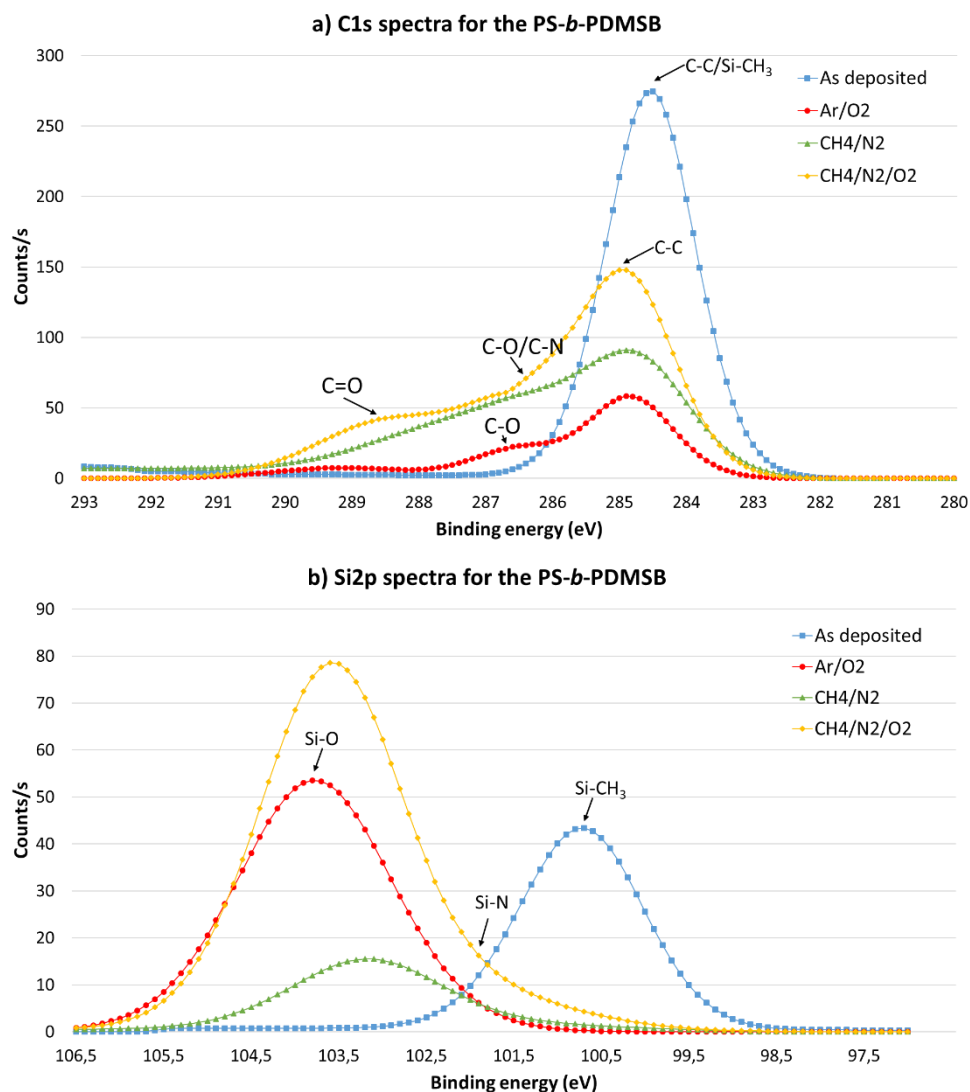


Figure V-8: PS-*b*-PDMSB (a) C1s and (b) Si2p spectra determined by *ex-situ* XPS on patterned wafers as deposited (without top coat) and after top coat and PS removal. The top coat was removed using a CH₃F/Ar/SO₂ plasma during 20 seconds, while three different chemistries were evaluated for the PS removal: Ar/O₂, CH₄/N₂ and CH₄/N₂/O₂. The results correspond to an incident angle of 76.25°.

Finally, for the PS removal based on CH₄/N₂/O₂ plasma, Figure V-8(a) shows that the C1s spectra results are similar to the ones for the CH₄/N₂ plasma. Indeed, the Si-CH₃ bonds are no longer present, thus shifting the C-C peak to 285 eV. Moreover, C-O, C-N and C=O bonds are observed, which come from both the plasma chemistry and the air exposure after etching. Figure V-9(d) shows that the presence of 5 sccm of oxygen on the plasma, however, leads to a lower C-N content (both for the C1s and N1s peaks) when compared to the oxygen-free CH₄/N₂. The Si2p spectra in Figure V-8(b) shows a main peak at 103.5 eV, which corresponds mostly to the Si-O bonds at 103.6 eV, but is slightly wider when compared to the Si-O peak for the Ar/O₂ plasma, due to the presence of a small Si-N peak at 102.3 eV. Therefore, we can conclude that the CH₄/N₂/O₂ plasma presents an etching and passivation mechanism in-between the ones for the Ar/O₂ and CH₄/N₂ plasmas: Si-O bonds replace the Si-CH₃ bonds from the PDMSB and a

CN-type deposit forms over the PDMSB lines. However, this deposit is thinner when compared to the CH_4/N_2 plasma probably due to the addition of oxygen to the plasma, which consumes both the PS and the CN-type deposit.

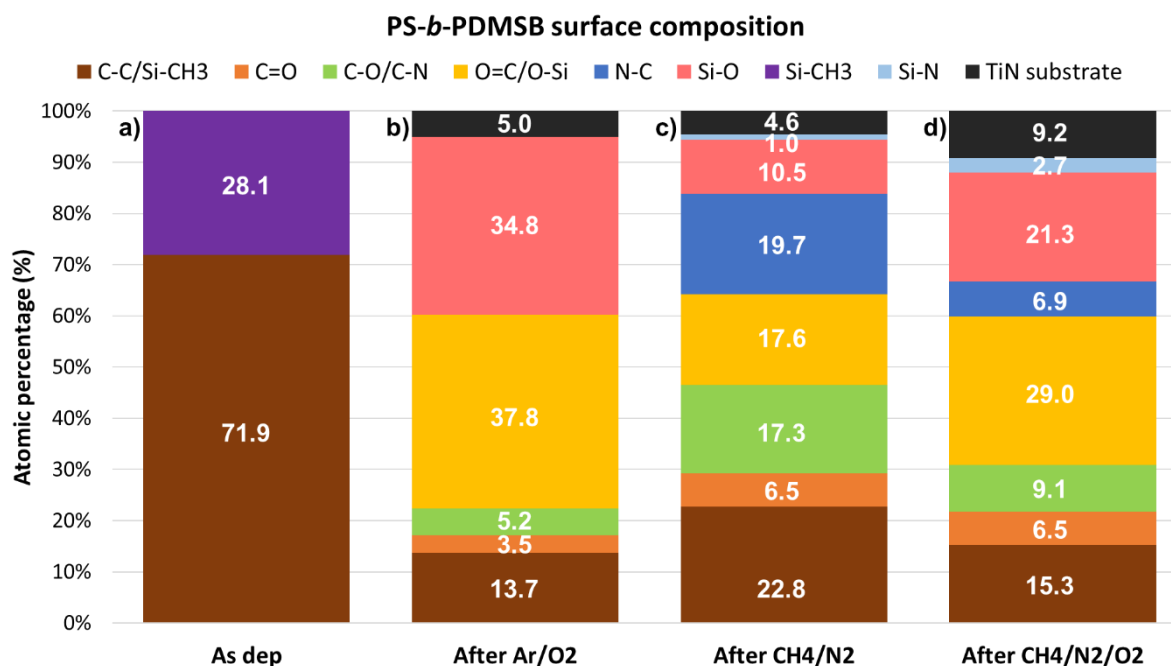


Figure V-9: PS-*b*-PDMSB surface composition determined by *ex-situ* XPS on patterned wafers (a) as deposited without top coat and (b, c, d) after top coat and PS removal. The top coat was removed using a $\text{CH}_3\text{F}/\text{Ar}/\text{SO}_2$ plasma during 20 seconds, while three different chemistries were evaluated for the PS removal: (b) Ar/O_2 ; (c) CH_4/N_2 ; and (d) $\text{CH}_4/\text{N}_2/\text{O}_2$. The results correspond to an incident angle of 76.25° .

In this section, three different etching chemistries were evaluated for the PS removal selectively to the PDMSB: Ar/O_2 , CH_4/N_2 and $\text{CH}_4/\text{N}_2/\text{O}_2$. For the pattern transfer of the PS-*b*-PDMSB into the TiN hard mask, we estimated that there should be at least 18 nm of PDMSB plus neutral layer left after top coat and PS removal, which translates to a PS:PDMSB selectivity ≥ 2.5 . However, the three PS removal chemistries evaluated led to a maximum selectivity of 1.8, which was not enough for complete pattern transfer.

We then tried increasing the block copolymer's initial thickness to relax the selectivity constraints. While it did allow us to increase the available PDMSB budget after top coat and PS removal, it also led to pattern collapse due to the high aspect ratio of the lines.

Next, XPS analysis were conducted to understand the etching and passivation mechanisms for the three different plasma approaches. For the Ar/O_2 etching, we concluded that the oxygen consumes the PS by forming volatile CO_x species while at the same time transforming the Si- CH_3 bonds of the PDMSB into Si-O bonds. For the CH_4/N_2 plasma, SiO_xN_y bonds replace the Si- CH_3 bonds from the PDMSB and a CN-type deposit forms over the PDMSB lines, thus forming a passivation layer and explaining its larger CD when compared to the other two approaches. Finally, the $\text{CH}_4/\text{N}_2/\text{O}_2$ plasma presents an etching and passivation mechanism in-between the ones for the Ar/O_2 and CH_4/N_2 plasmas: Si-O bonds replace the Si- CH_3 bonds from the PDMSB and a CN-type deposit forms over the

PDMSB lines. However, this deposit is thinner when compared to the CH_4/N_2 plasma probably due to the addition of oxygen to the plasma, which consumes both the PS and the CN-type deposit.

Therefore, none of these plasma processes are compatible with the 18-nm pitch high- χ PS-*b*-PDMSB and a new approach that allows for higher PS:PDMSB selectivity without pattern collapse must be developed.

V.3 One step top coat and PS removal selectively to PDMSB

In this section, we propose to evaluate a one-step top coat and PS removal approach which consists of removing the top coat and the PS selectively to the PDMSB in a single plasma etching step. For that, we have selected both oxidizing and reducing chemistries that have already been explored in the two previous chapters as well-known solutions to etch purely organic materials. We shall start by evaluating two oxygen-based chemistries: the Ar/O₂ plasma detailed in Table V-3 and the CH₃F/Ar/SO₂ plasma detailed in Table V-1. We then shall evaluate a reducing H₂/N₂ plasma, which has already been presented in Chapter III.3.1 as an alternative for the SOC removal.

Once the best top coat and PS removal approach has been identified, the pattern transfer into the titanium nitride (TiN), silicon oxide (SiO₂) and silicon (Si) underlayers shall be evaluated in order to confirm this approach's compatibility with the 18-nm pitch high- χ PS-*b*-PDMSB.

V.3.1 Comparison between oxidizing and reducing plasma chemistries for top coat and PS removal

V.3.1.1 Top coat and PS removal with two different oxidizing plasmas

Both the Ar/O₂ and CH₃F/Ar/SO₂ plasmas are applied to the PS-*b*-PDMSB patterned wafers with the complete stack from Figure V-1 during 50 seconds and the results are presented in Figure V-10. For the Ar/O₂ plasma, the cross-section SEM image in Figure V-10(a) shows that there is only around 9.6 nm of PDMSB and neutral layer left after etching, which is not enough for pattern transfer. Moreover, the top-view SEM image shows some spots where the lines have been interrupted and the CD is apparently smaller. This is reminiscent of the results obtained during top coat removal with the Ar/O₂ plasma with smaller ratio presented in Figure V-4. Thus, it could be further indication of a non-homogeneous top coat/PS-*b*-PDMSB interface. Varying the etching time or Ar/O₂ ratio did not eliminate these defects. These results indicate that the one-step oxidizing approach using an Ar/O₂ plasma is not adapted to this PS-*b*-PDMSB stack.

For the top coat and PS removal using the CH₃F/Ar/SO₂ plasma, both top-view and cross-section SEM images presented in Figure V-10(b) indicate a significant increase in the CD of the PDMSB lines. It can be explained by the presence of CH₃F and SO₂ as passivating agents for the PDMSB, thus forming a passivation layer on the sidewalls of the PDMSB lines and effectively increasing their CD. This probably leads to the very low selectivity between PS and PDMSB, which present almost the same thickness after 50 seconds of etching according to the cross-section SEM in Figure V-10(b). Therefore, the CH₃F/Ar/SO₂ plasma is not adapted to the one-step top coat and PS removal approach.

Furthermore, the formation of a thicker TiO_x layer on the surface of the TiN hard mask using the oxidizing plasma may induce some difficulties during pattern transfer due to the limited PDMSB budget available. Therefore, we decided to investigate a reducing plasma based on H_2/N_2 , which has been shown in Chapter III.3 to etch organic layers with good selectivity to silicon-containing materials without further modification of TiN hard mask composition.

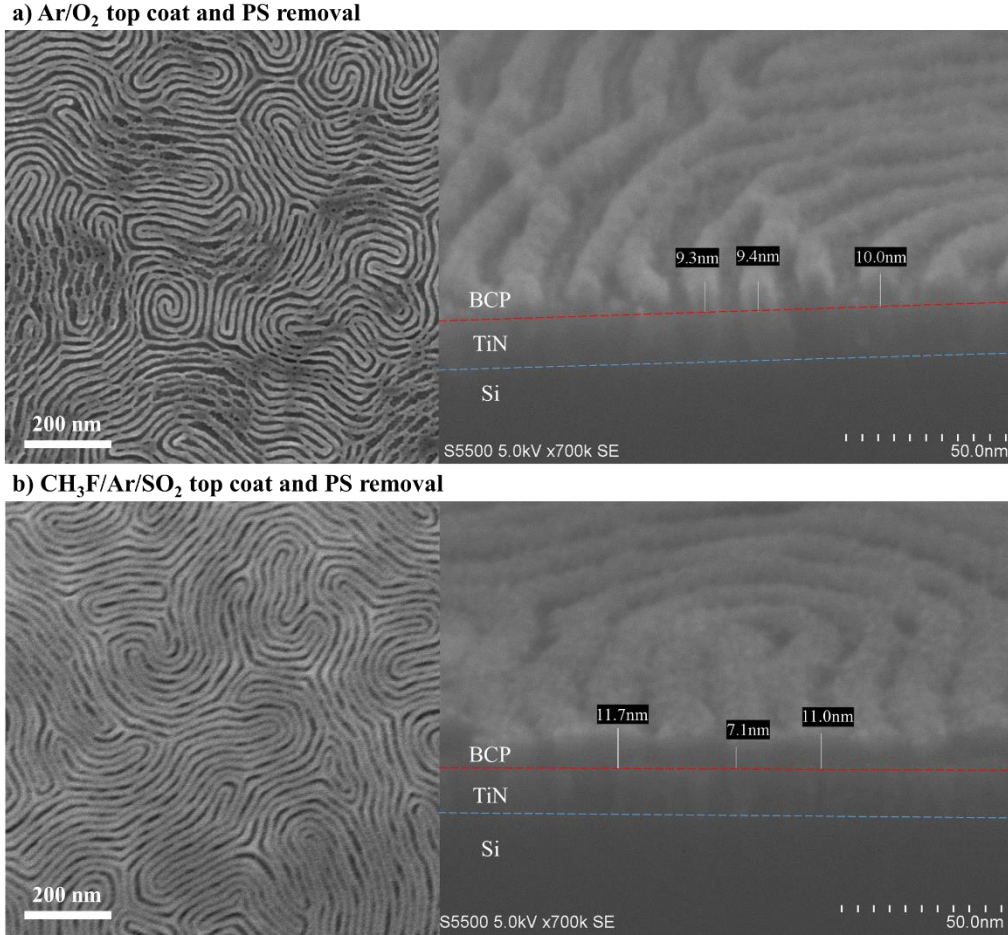


Figure V-10: Top-view and cross-section SEM images for the PS-*b*-PDMSB block copolymer after top coat and PS removal with (a) Ar/O_2 or (b) $\text{CH}_3\text{F}/\text{Ar}/\text{SO}_2$ during 50 seconds.

V.3.1.2 Top coat and PS removal with a reducing plasma

The reducing approach based on H_2/N_2 is evaluated on a FLEX CFE® capacitively coupled plasma (CCP) reactor, which has been detailed in Chapter II.2.1.1, due to the H_2 not being available in the ICP reactor. The details of the plasma parameters are presented in Table V-4. The top coat and PS etch rates on blanket wafers are 5.5 and 2.0 nm/s, respectively. Thus, etching times varying from 10 to 30 seconds have been applied on patterned wafers in order to find the best etch durations on PS-*b*-PDMSB films.

Table V-4: Plasma parameters for the H_2/N_2 plasma evaluated for top coat and PS removal.

Chemistry	Pressure (mTorr)	RF 2MHz (W)	RF 27MHz (W)	Flow (sccm)
H_2/N_2	160	0	1000	150/500

The top-view and cross-section SEM images after top coat and PS removal for the studied etching times can be found in Figure V-11. After 10 seconds, Figure V-11(a) shows that the top coat has been completely removed and that around 6 nm of PS have been etched, while the PDMSB is not consumed.

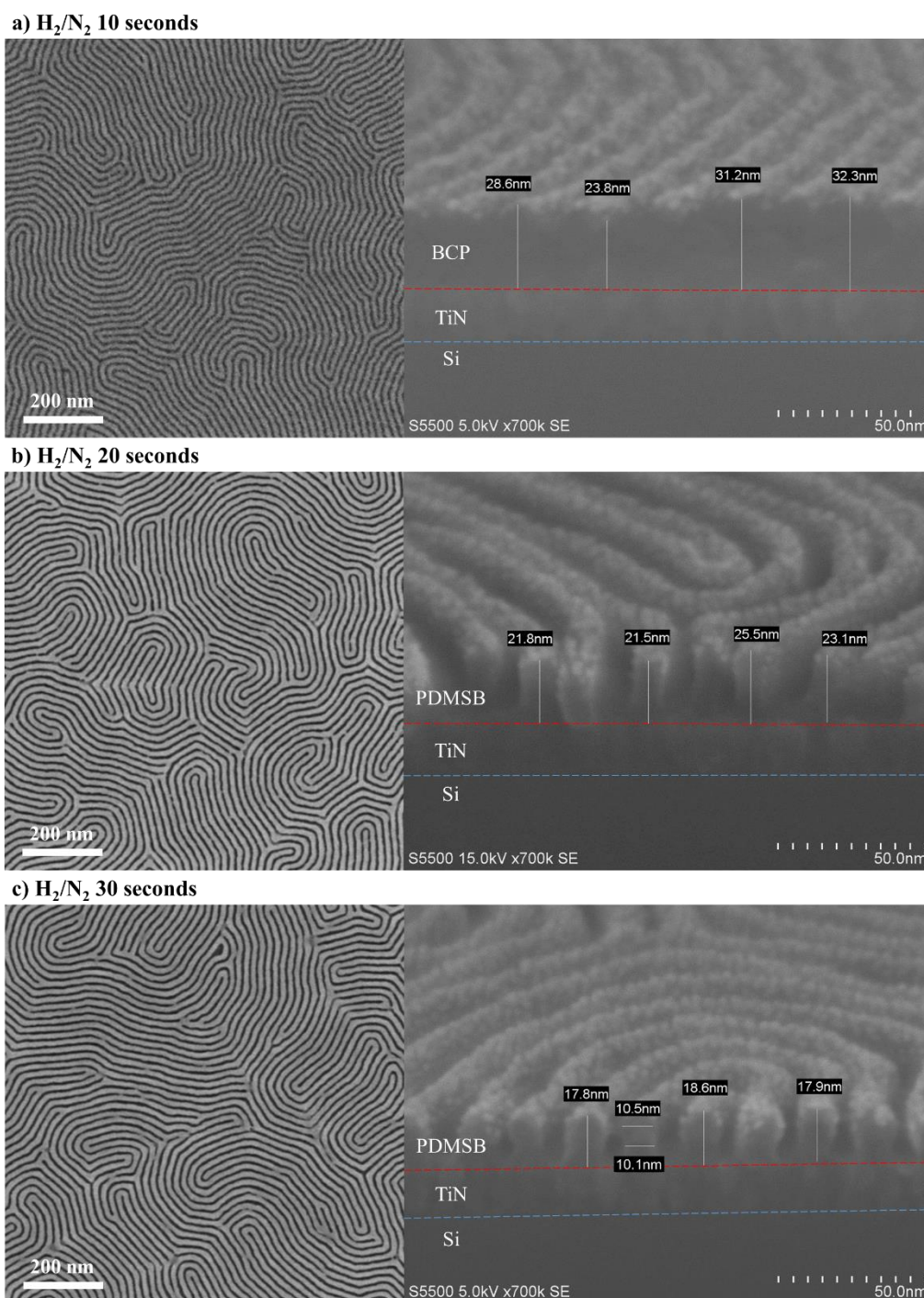


Figure V-11: Top-view and cross-section SEM images of PS-*b*-PDMSB block copolymer after top coat and PS removal using H_2/N_2 with ratio 150/500 for: (a) 10 seconds; (b) 20 seconds; and (c) 30 seconds.

After 20 seconds, Figure V-11(b) indicates that the PS has also been completely removed and around 23 nm of PDMSB remain, which means a PS:PDMSB minimum selectivity of 4.3. Indeed, since the PS has been completely removed, it is possible that the PS:PDMSB selectivity

is greater than 4.3 for shorter etching durations. However, some collapsing of the PDMSB lines can be observed in the cross-section image in Figure V-11(b), probably due to the high aspect ratio of the lines, which is around 2.5 due to the small CD of 9 nm.

Finally, after 30 seconds, based on Figure V-11(c), we observe that the PDMSB presents an average thickness of 18 nm while the PS has been completely removed, translating to a PS:PDMSB selectivity of 2.5. No pattern collapse is observed after 30 seconds due to the lower aspect ratio of 2. Moreover, the line patterns after the reducing plasma present an anisotropic profile and a CD of approximately 10 nm, which means a CD bias of 1 nm when compared to the as deposited material. However, there is some bridge formation between the lines, which has already been observed for such small and dense pitch in Chapter IV and has been attributed to intensive sidewalls passivation and to a species confinement effect accentuated by the small 18-nm pitch [Gusmão 2020].

Therefore, 30 seconds has been selected as the etching duration of reference for the H₂/N₂ plasma with ratio 150/500 since it is able to obtain the minimum desired PS:PDMSB selectivity of 2.5 without leading to pattern collapse due to the high aspect ratio of the PDMSB lines.

In order to understand the role of the H₂ and N₂ on the top coat and PS-*b*-PDMSB etching and passivation mechanisms, the gas ratio has been varied while the other plasma parameters remained the same as the ones presented in Table V-4. The top-view and cross-section SEM images after top coat and PS removal during 30 seconds are presented in Figure V-12 for the following H₂/N₂ flow: 150/50, 150/150, 150/300 and 0/500 (indicated as N₂ only). The results for H₂/N₂ 150/500 have already been presented in Figure V-11(c). The estimated remaining PS and PDMSB thickness as well as the calculated PS:PDMSB selectivity for each H₂/N₂ ratio can be found in Table V-5. Once again, it should be noticed that, since the PS has been completely removed, the PS:PDMSB selectivity presented corresponds to the minimum value and could be greater for shorter etching durations. As we can see, the lower the N₂ content, the lower the PS:PDMSB selectivity, thus indicating that N₂ plays an important role on PDMSB passivation and protection.

Table V-5. Estimated remaining PS and PDMSB thickness as well as the calculated minimum PS:PDMSB selectivity for each H₂/N₂ ratio. These values were obtained by averaging the measured values on the SEM images presented in Figures V-11 and V-12.

H ₂ /N ₂ flow (sccm)	PS remaining (nm)	PDMSB remaining (nm)	PS:PDMSB Selectivity
150/50	0	12.7	1.7
150/150	0	16.3	2.2
150/300	0	16.7	2.3
150/500	0	18.0	2.5
0/500	21.6	21.6	1.0

Figure V-12(a) shows the results for H₂/N₂ 150/50, which has the lower N₂ content and lower PS:PDMSB selectivity (1.7) when compared to the other ratios. It should be noticed that no

bridges are observed on the top-view SEM image, probably because this ratio is less passivating and has a smaller CD of around 8 nm. A few lines have collapsed, which might be related to the smaller CD as well as the slight difference in CD between the top and the bottom of the line that is shown in the cross-section SEM image.

This difference in CD between top and bottom of the line pattern is even more significant for the ratio 1.0 (150/150), presented in Figure V-12(b). The CD different corresponds to 3 nm, which also explains the many collapsing lines visible in the top-view SEM image. The bigger gap in CD might be caused by the combination of two simultaneous phenomena. First, the larger CD observed on top of the line is probably due to the higher N₂ content, which preferably passivates the top sidewall. Second, the smaller bottom CD may correspond to the lateral etching of the neutral layer under the PDMSB block, since this layer is purely organic and etches faster than the silicon-containing PDMSB.

As we observe the two next H₂/N₂ ratios – 150/300 in Figure V-12(c) and 150/500 in Figure V-11(c) –, as expected, the greater the N₂ content, the better the selectivity since N₂ seems to be the major passivating component of this etching chemistry. For both ratios, the CD difference between top and bottom of the patterns still exist, but is less significant than the one observed for the 150/150 ratio and leads to less pattern collapse. The higher N₂ content, and therefore passivation, also leads to the reappearance of bridges, which are visible in the top-view SEM image in Figure V-12(c).

However, when attempting to etch the top coat and PS with N₂ only, we observe in Figure V-12(d) and Table V-5 that, while the top coat is completely removed, there is no selectivity between PS and PDMSB. This indicates that H₂ is necessary to etch the PS selectively to the PDMSB.

Therefore, the 150/500 sccm is the most interesting ratio in terms of PS:PDMSB selectivity (2.5) while 150/50 sccm presents as an advantage the absence of bridging on top of the PDMSB lines. Both ratios present a slight pattern collapse due to the high aspect ratio of the lines. They shall be evaluated for pattern transfer into the titanium nitride hard mask in section V.3.3.1.

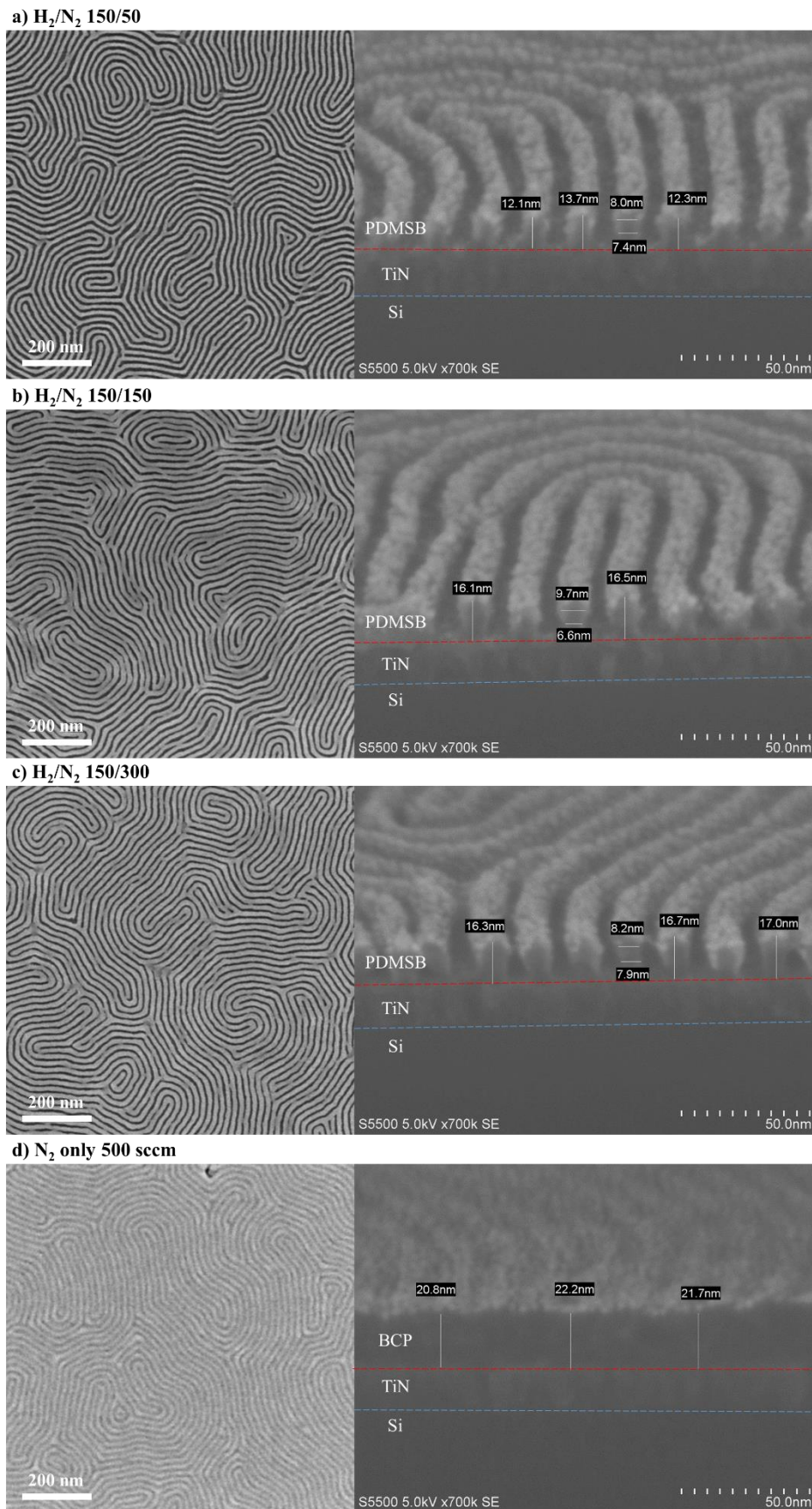


Figure V-12: Top-view and cross-section SEM images of PS-*b*-PDMSB block copolymer after top coat and PS removal using H₂/N₂ with different ratios for 30 seconds: (a) 150/50 sccm; (b) 150/150 sccm; (c) 150/300 sccm; and (d) only N₂ (500 sccm).

In this section, a one-step top coat and PS removal approach has been evaluated with three different plasma chemistries.

The Ar/O₂ plasma presented low PS:PDMSB selectivity and, in some spots, the PDMSB lines were interrupted and presented smaller CD, which could be further indication of a non-homogeneous top coat/PS-*b*-PDMSB interface. The Ar/O₂ plasma was therefore considered not appropriate for the one-step top coat and PS removal.

The CH₃F/Ar/SO₂ plasma led to a significant increase in the CD of the PDMSB lines, which was explained by the presence of CH₃F and SO₂ as passivating agents, thus forming a passivation layer on the sidewalls of the PDMSB lines and increasing their CD. As a consequence of the very low PS:PDMSB selectivity due to too much passivation, the CH₃F/Ar/SO₂ plasma was also not adapted to the one-step top coat and PS removal.

We then decided to evaluate a reducing top coat and PS removal approach based on H₂/N₂ plasma, which led to good PS:PDMSB selectivity and lines profile. By varying the etching duration, we observed that for shorter etching times (20 seconds), even though the PS was completely removed and the PS:PDMSB selectivity was good (4.3), the high aspect ratio of the lines (2.5) led to pattern collapse. Therefore, a longer etching duration of 30 seconds, despite leading to lower PS:PDMSB selectivity (2.5), was selected as the reference etching time due to the slightly lower aspect ratio of the lines, thus avoiding pattern collapse.

Next, we evaluated the impact of gas ratio variation. On one hand, with lower N₂ content (50 sccm instead of 500 sccm), even though lower PS:PDMSB selectivity was obtained when compared to the process of reference, there was no bridge formation. On the other hand, when only N₂ is applied to the top coat and PS removal, there is an etch stop. These results indicate that N₂ is the main passivating agent in the plasma, while H₂ is the main etching agent.

Therefore, the 150/500 sccm is the most interesting ratio in terms of PS:PDMSB selectivity (2.5) while 150/50 sccm presents as an advantage the absence of bridging on top of the PDMSB lines. Both ratios present a slight pattern collapse due to the high aspect ratio of the lines. They shall be evaluated for pattern transfer into the titanium nitride hard mask in a later section.

V.3.2 Understanding the etching and passivation mechanisms

In order to understand the etching and passivation mechanisms involved in the top coat and PS removal, *ex-situ* XPS analysis were carried out on blanket top coat and PS homopolymers before and after etching with the H₂/N₂ plasma with ratio 150/500. The results are shown in Figures V-13 and V-14. Figure V-13 presents the atomic percentage for each element in the different samples while Figure V-14 presents the evolution of the C1s and N1s spectra for the top coat and PS before and after etching.

The surface composition for the as deposited top coat and PS has already been detailed in section V.1. The PS homopolymer C1s spectra presented in Figure V-14(b) shows two peaks: one at 284.8 eV, assigned to C-C/C=C, and the other at 291.5 eV, identified as $\pi \rightarrow \pi^*$. The as deposited top coat consists of a poly(2,2,2-trifluoroethylmethacrylate-*r*-glycidylmethacrylate-*r*-2-hydroxyethylmethacrylate) statistical terpolymer. The C1s spectra for the as deposited top coat in Figure V-14(a) presents four different peaks: one at 285.0 eV, identified as C-

C/CHCOOH, which represents both the carbon at CH₂ and CH₃ bonds (at 284.7 eV) and the carbon from the acrylate compounds (at 285.7 eV). The second peak appears at 286.5 eV and represents the carbon in the methyl ester (C-O) bonds. The third one, at 288.8 eV, corresponds to the carbon in the carboxyl group (C=O). Finally, the fourth one, at 292.7 eV, corresponds to carbon bound to three fluorine atoms (CF₃).

Figures V-13 and V-14 also present the XPS results after etching these materials with H₂/N₂ plasma. For both materials, a C-N peak appears at 399 eV on the N1s spectra in Figure V-14(c) and at 286 eV on the C1s spectra – in which, due to spectral resolution, it cannot be differentiated from C-O (286.5 eV) bonds and is thus fitted together as C-O/C-N in Figures V-14(a) and (b) [Beamson 1992]. For the PS, this C-N bond formation has already been observed with CH₄/N₂ plasma in Chapter IV.3.3.1 and indicates that a CN-type deposit forms on the PS surface. This CN_x layer then probably reacts with the hydrogen in the plasma to form HCN as a volatile product.

As for the top coat after H₂/N₂ etching, represented in Figures V-13(b) and V-14(a), a decrease in percentage of CF₃ and C-O simple and double bonds is observed, indicating that they are preferentially etched by the reactive species present in the H₂/N₂ plasma. The loss of C-O and C=O bonds is characteristic of methacrylate-based polymers etching and similar to what is observed for PMMA etching with CH₄/N₂ in Chapter IV.3.3.1, as expected given that both materials present similar characteristic groups in their composition.

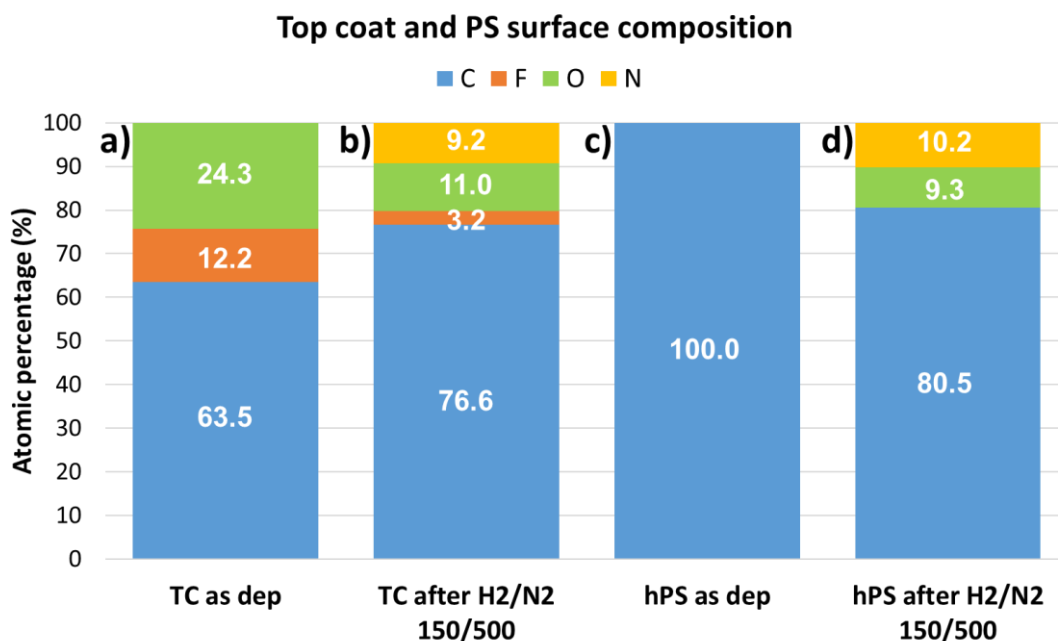


Figure V-13: Surface composition of (a, b) Top coat and (c, d) PS homopolymer determined by *ex-situ* XPS with an incident angle of 23.75° (a, c) before and (b, d) after etching with H₂/N₂ ratio 150/500 for 5 seconds.

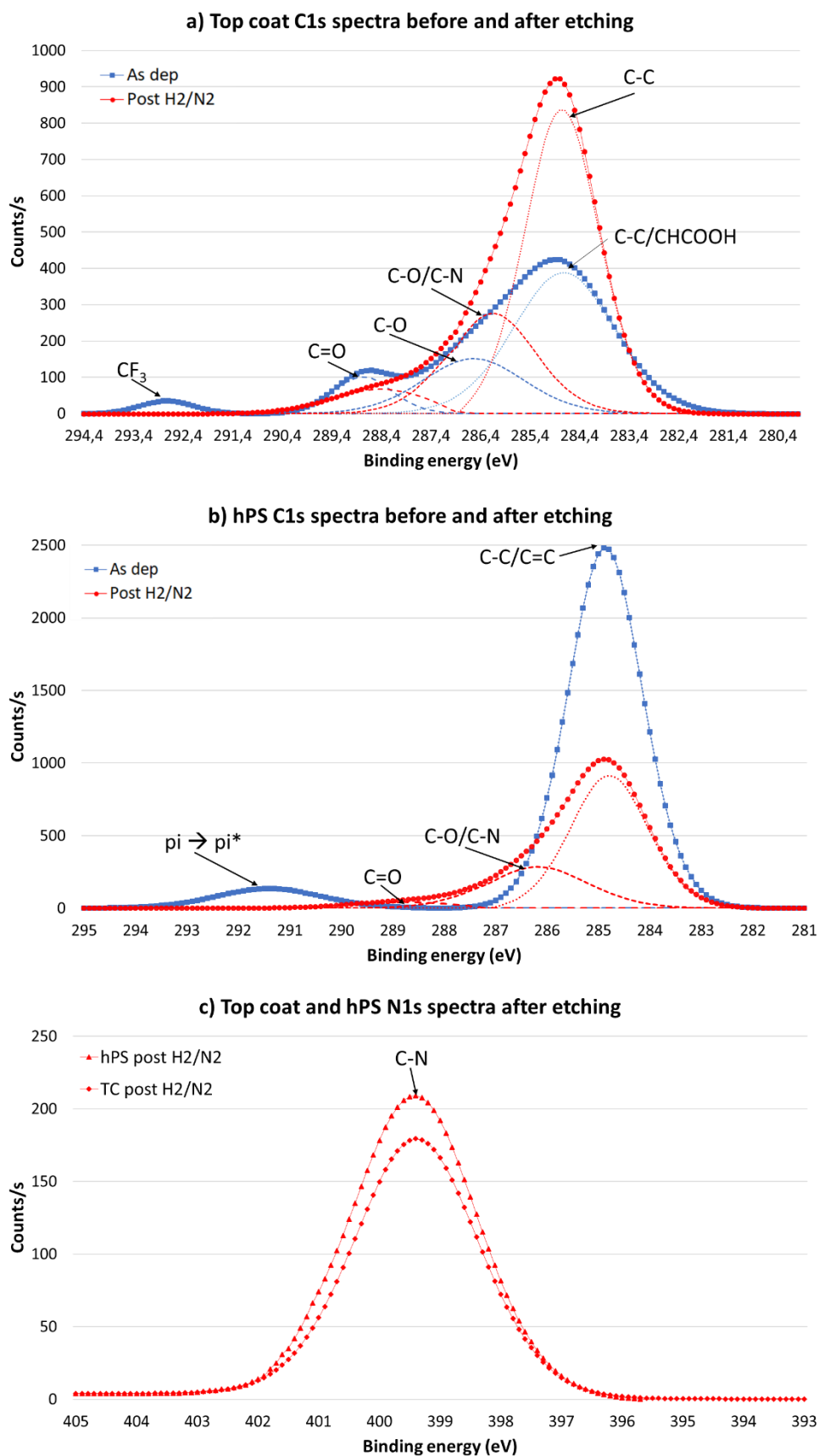


Figure V-14: (a, b) C1s and (c) N1s spectra for (a, c) Top coat and (b, c) hPS determined by *ex-situ* XPS with an incident angle of 23.75° before and after etching with H₂/N₂ ratio 150/500 for 5 seconds.

As we have seen in section V.1, since the PDMSB homopolymer is not available, the PS-*b*-PDMSB as deposited surface composition was determined with patterned wafers, by depositing the block copolymer over a silicon wafer without top coat and conducting *ex-situ* XPS analysis. The results have been presented in detail in section V.1. A schematic view of the horizontal PDMSB lamellae on top of the as deposited PS-*b*-PDMSB without top coat to vertically assemble the BCP is presented in Figure V-15(a). Figure V-15(b) shows that these top PDMSB lamellae consist of carbon (71.9%) and silicon (28.1%). Figure V-16(a) presents the C1s scan for the PDMSB lamellae on top of the as deposited PS-*b*-PDMSB, where one peak is identified as C-C/Si-CH₃ at 284.5 eV: it represents both the carbon at CH₂ and CH₃ bonds (at 284.7 eV) and the carbon from Si-CH₃ bonds (at 284 eV). The Si2p spectra in Figure V-15(b) confirms the presence of Si-CH₃ bonds with a doublet peak centered around 100.7 eV [Beamson 1992].

In order to understand the etching and passivation mechanisms of the PDMSB lines during the reducing plasma, both *ex-situ* and *quasi in-situ* XPS analysis have been conducted using patterned wafers after top coat and PS removal with an H₂/N₂ (150/500) plasma for 30 seconds. The surface composition of patterned wafers after complete top coat and PS etching is presented in Figures V-15 and V-16. Even though the results obtained cannot be considered quantitatively accurate, they can still be compared to mechanisms proposed by other authors and amongst each other. As we have seen in Figure V-7, for this incident angle of 76.25°, the XPS analysis mostly observes the top 2 nm of the PDMSB lines after top coat and PS removal.

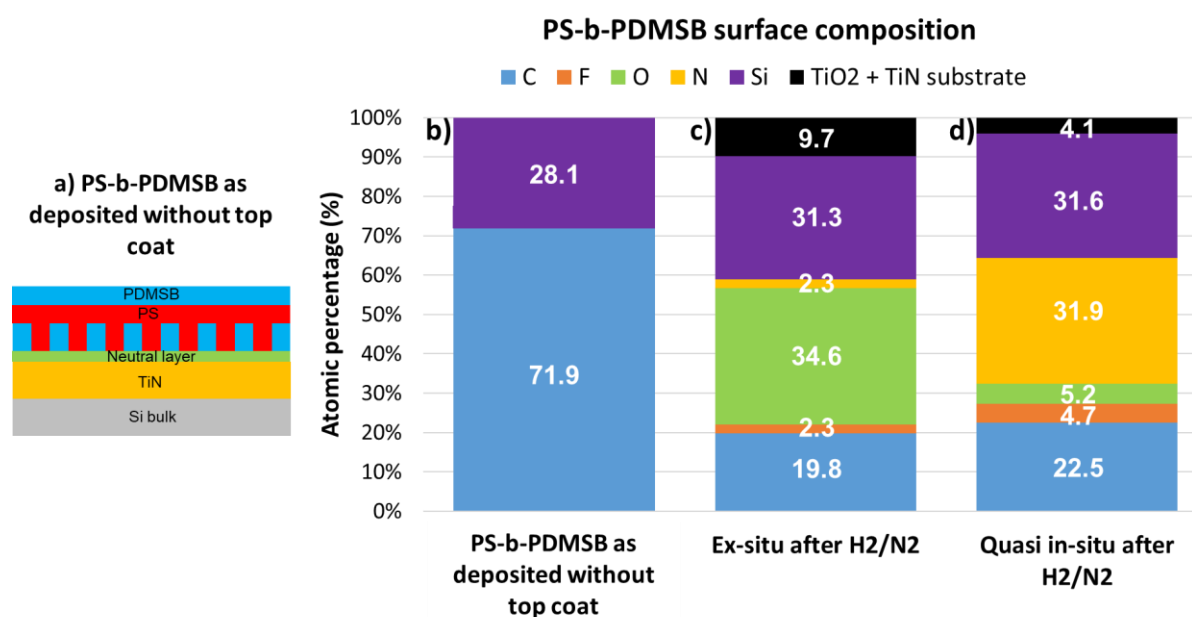


Figure V-15: (a) Schematics for the PS-*b*-PDMSB as deposited without top coat, highlighting the horizontal lamellae on top of the BCP; and PS-*b*-PDMSB surface composition determined by (b, c) *ex-situ* and (d) *quasi in-situ* XPS with an incident angle of 76.25° on patterned wafers (b) as deposited without top coat and (c, d) after top coat and PS removal with H₂/N₂ ratio 150/500 for 30 seconds.

Posseme *et al.* [Posseme 2007] propose the following reaction mechanism during downstream H₂/N₂ or reactive ion etching (RIE) NH₃ plasma for Si-CH₃ bonds:



For our PDMSB lines, the presence of Si-N bonds after top coat and PS removal using H₂/N₂ plasma is confirmed by the *quasi in-situ* XPS analysis. Indeed, Figure V-16(b) presents the Si2p spectra after etching, which shows that the Si-CH₃ peak is no longer present and a new doublet peak at 102.3 eV (Si2p_{3/2} at 102 eV and Si2p_{1/2} at 102.6 eV), representing Si-N bonds, appears [Beamson 1992]. Moreover, Figure V-16(c) also confirms the presence of the N-Si peak on the N1s spectra, which appears at a binding energy of 398.5 eV [Ingo 1989]. These results indicate that the Si-CH₃ bonds in PDMSB are probably turned into Si-NH₂ during top coat and PS removal, as proposed in reaction 1.

It is also important to notice that the oxygen and nitrogen atomic percentages presented in Figures V-15(c) and V-15(d) are the only ones that present a significant variation between *quasi in-situ* and *ex-situ* XPS analysis. Indeed, their values are almost inverted: for the *quasi in-situ* XPS, there is around 32% of nitrogen and 5% of oxygen, while for the *ex-situ* XPS, there is approximately 35% of oxygen and 2% of nitrogen. This difference can be explained by the reaction of the Si-NH₂ bonds with water molecules when the wafer is exposed to the atmosphere. The Si-NH₂ bonds are replaced by Si-OH bonds, according to the reaction:

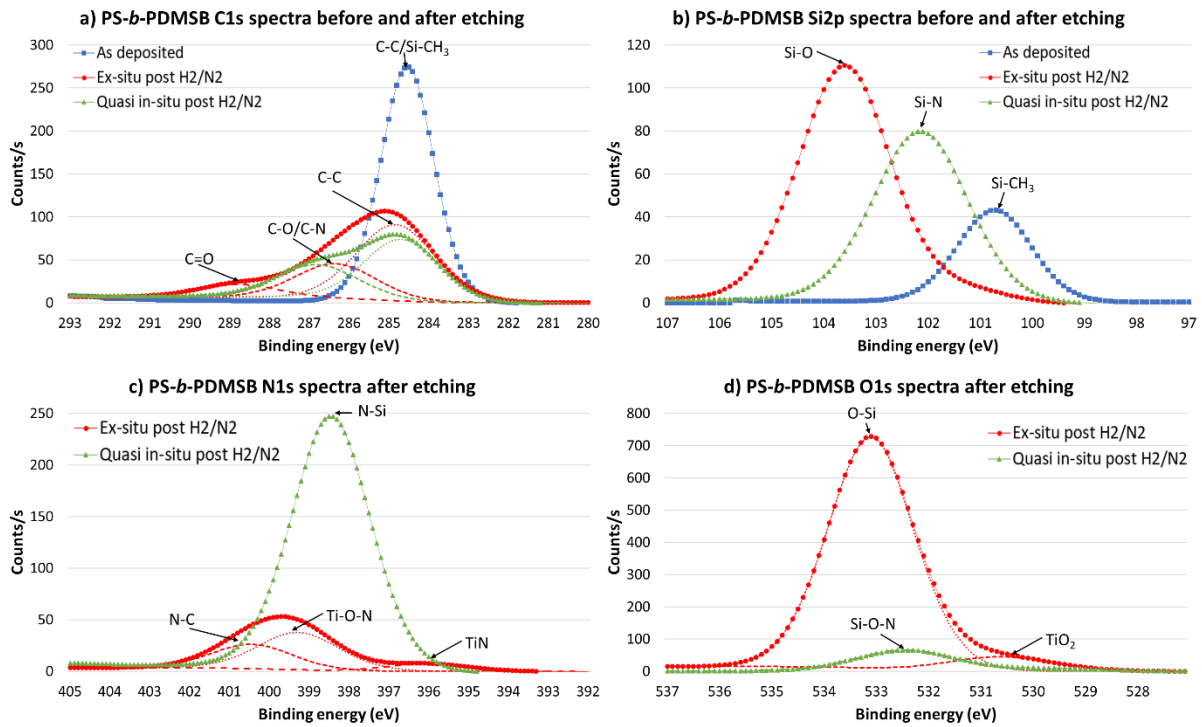


Figure V-16: (a) C1s, (b) Si2p, (c) N1s and (d) O1s spectra determined by *ex-situ* and *quasi in-situ* XPS with an incident angle of 76.25° for the as deposited PS-b-PDMSB (without top coat) and for the PDMSB lines after top coat and PS removal with H₂/N₂ ratio 150/500 for 30 seconds.

This reaction is confirmed by the XPS analysis for the *ex-situ* samples. Figure V-16(b) shows that the Si-N peak that was present for the *quasi in-situ* sample has been shifted to a higher binding energy of 103.6 eV, which is characteristic of the doublet peak for the Si-O bonds (Si2p_{3/2} at 103.3 eV and Si2p_{1/2} at 103.9 eV). Furthermore, the O1s spectra presented in Figure V-16(d) shows the presence of an O-Si peak at 533 eV [Beamson 1992], thus confirming that Si-N bonds are replaced by Si-O bonds after air exposure. Also according to Posseme *et al.*,

these different reactions lead to the formation of a modified passivation layer composed of $\text{SiO}_x\text{N}_y\text{H}_z$, which is denser and carbon depleted [Posseme 2007]. This layer is observed for the PDMSB according to *quasi in-situ* XPS analysis in Figure V-16(d), which presents a peak at 532.4 eV that corresponds to Si-O-N bonds [Bois 1996].

In order to minimize the oxidation of the TiN surface after top coat and PS removal, all experiments of pattern transfer into the TiN layer that shall be presented in the next section are conducted without air exposure between the top coat and PS removal step and the TiN etching step. Therefore, we may conclude that the formation of Si-NH₂ and $\text{SiO}_x\text{N}_y\text{H}_z$ over the PDMSB lines is responsible for their passivation during top coat and PS removal with H₂/N₂ plasma.

In this section, we conducted XPS analysis in order to understand the etching and passivation mechanisms involved in the top coat and PS removal for the 18-nm pitch high- χ PS-*b*-PDMSB.

For the PS homopolymer after top coat and PS removal using H₂/N₂ (150/500 sccm), a CN-type deposit was formed on the PS surface. This CN_x layer then probably reacted with the hydrogen in the plasma to form HCN as a volatile product. For the top coat after H₂/N₂ etching, a decrease in percentage of CF₃ and C-O simple and double bonds was observed, indicating that they were preferentially etched by the reactive species present in the H₂/N₂ plasma.

Finally, for the PS-*b*-PDMSB patterned wafers, both *ex-situ* and *quasi in-situ* XPS analysis were conducted. *Quasi in-situ* analysis indicated that the Si-CH₃ bonds in PDMSB were probably turned into Si-NH₂ during top coat and PS removal, while *ex-situ* analysis showed that these Si-NH₂ bonds reacted with water molecules when the wafer was exposed to the atmosphere, thus being replaced by Si-OH bonds. Furthermore, these different reactions led to the formation of a modified layer composed of $\text{SiO}_x\text{N}_y\text{H}_z$, which is denser and carbon depleted. Therefore, we concluded that the formation of Si-NH₂ and $\text{SiO}_x\text{N}_y\text{H}_z$ over the PDMSB lines was responsible for their passivation during top coat and PS removal with H₂/N₂ plasma.

V.3.3 Pattern transfer of the 18-nm pitch high- χ PS-*b*-PDMSB

V.3.3.1 Pattern transfer into the titanium nitride hard mask

For the pattern transfer of the 18-nm pitch high- χ PS-*b*-PDMSB into the 18-nm hard mask (15 nm of TiN and around 3 nm of native titanium oxide, TiO_x), we have selected three different combinations of H₂/N₂ ratio and etching times to evaluate the impact of high selectivity, aspect ratio and bridge formation. These combinations are 150/50 sccm during 20 seconds, 150/500 sccm during 20 seconds and 150/500 sccm during 30 seconds. The 150/50 ratio for 20 seconds, while not shown here, presents a PS:PDMSB selectivity of 3.7 with around 21.9 nm of PDMSB remaining, as well as a straight line profile with a CD of 8 nm and no bridge formation.

Pattern transfer into the TiN hard mask is conducted in a Kiyō[®] CX ICP reactor from LamResearch without air exposure after the top coat and PS removal through H₂/N₂, in order to avoid further oxidation of the TiN and PDMSB exposed surfaces. The TiN etching consists of two steps: a breakthrough (BT) step using Cl₂/BCl₃ to remove the TiO_x on the surface and

initiate the TiN etching. This BT step is followed by a main etch (ME) using $\text{Cl}_2/\text{CH}_4/\text{N}_2$, which presents better selectivity to the PDMSB thanks to the presence of CH_4 and N_2 as passivating agents. Both steps have been validated for other applications at CEA Leti. The plasma parameters can be found in Table V-6.

Table V-6. Plasma parameters of the chemistries used for the dry etching of the TiN hard mask.

Plasma	Pressure (mTorr)	Power (W)	Bias (V)	Flow (ratio)	Time (s)
BT: Cl_2/BCl_3	8	400	-100	2:1	5
ME: $\text{Cl}_2/\text{CH}_4/\text{N}_2$	10	350	-200	4:1:3	5

Figure V-17 shows the results for the pattern transfer of the high- χ PS-*b*-PDMSB into the TiN hard mask using the three top coat and PS removal conditions evaluated. For H_2/N_2 with ratio 150/500 for 20 seconds, which is the condition with higher selectivity, and therefore higher aspect ratio, we observe from the results in Figure V-17(b) that the line patterns have mostly collapsed. The cross-section SEM image shows that, because of PDMSB collapse, pattern transfer into the TiN hard mask is not initiated.

Based on the results presented in Figure V-17(a) for the 150/50 ratio during 20 seconds, which presents an intermediate PDMSB remaining thickness among the three conditions studied and no bridge formation, pattern collapse is still observed although in smaller intensity when compared to the previous condition presented in Figure V-17(b). Pattern transfer into the TiN hard mask is initiated: the TiO_x layer has been opened and around 5 nm of TiN have been etched. However, pattern collapse probably prevented further TiN etching.

Finally, the best result is obtained with the third condition, H_2/N_2 with ratio 150/500 for 30 seconds, which is presented in Figure V-17(c). For this combination, the TiO_x layer has been opened and around 10 nm of TiN have been etched. Moreover, no pattern collapse is observed. However, the PDMSB mask has been completely etched, which is confirmed when we extend the main etch time to 10 seconds (not depicted) instead of 5 seconds and observe that the line patterns are no longer present because the TiN has been overetched.

These results lead to the conclusion that, while good PS:PDMSB selectivity is desired in order to conserve enough PDMSB budget to completely transfer the line patterns into the hard mask, mechanical stability problems cause pattern collapse due to the high aspect ratio of the lines. Therefore, the smaller CD of the high- χ block copolymer limits the maximum PDMSB budget allowed for pattern transfer, which in its turn limits the TiN thickness that can be etched using this block copolymer as a mask. Herein we are able to transfer 18-nm pitch PDMSB lines into a TiN thickness of 10 nm.

Further investigation into solutions to improve the block copolymer's mechanical stability would be necessary in order to increase the etching process window for the TiN hard mask.

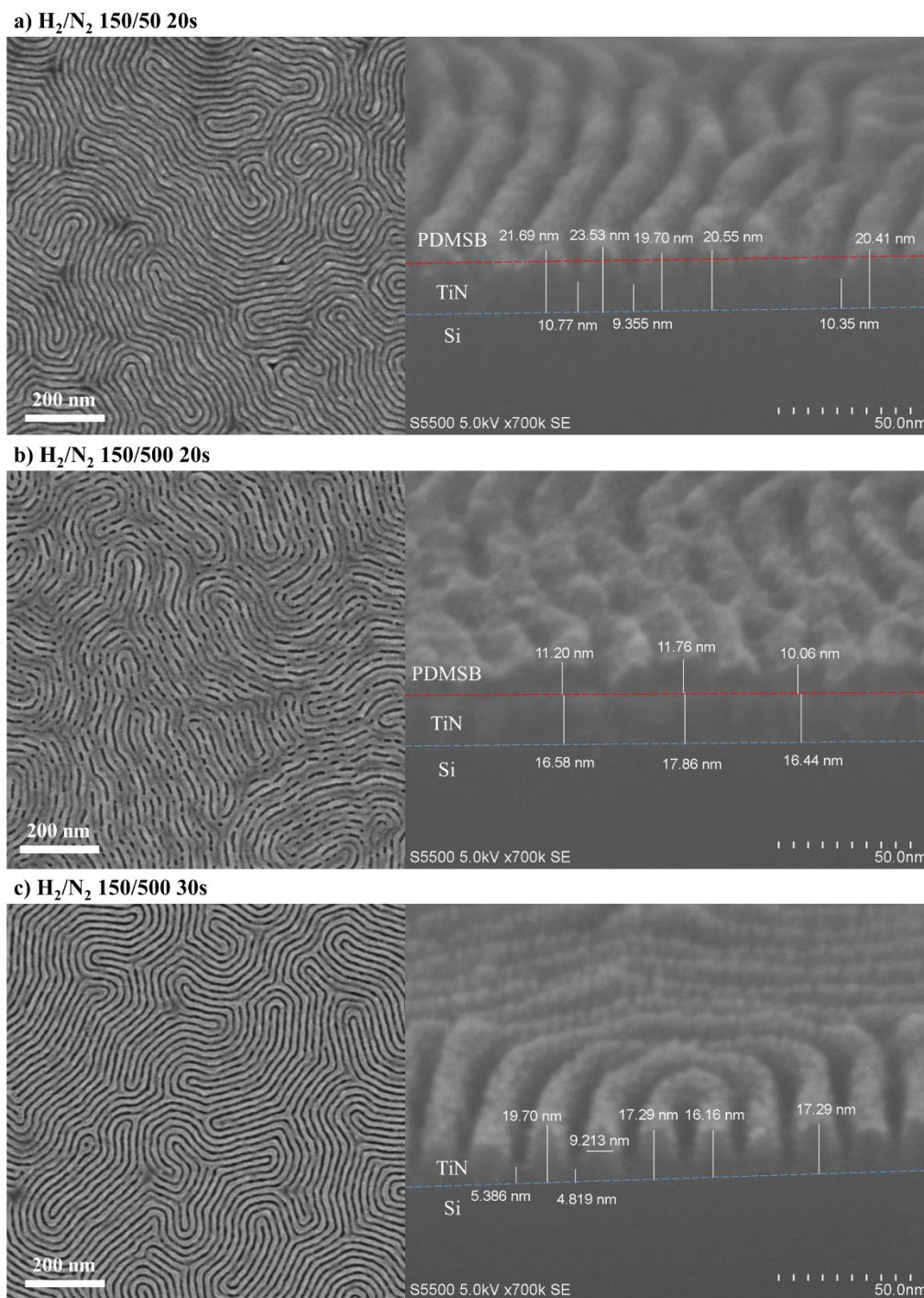


Figure V-17: Top-view and cross-section SEM images of the pattern transfer of high- χ PS-*b*-PDMSB into the TiN hard mask using three different conditions for the top coat and PS removal with H_2/N_2 : (a) 150/50 sccm during 20 seconds; (b) 150/500 sccm during 20 seconds; and (c) 150/500 sccm during 30 seconds.

V.3.3.2 Pattern transfer into the silicon oxide hard mask and silicon bulk

Due to the limits imposed by the PDMSB budget to the TiN etching, we decided to adapt the stack studied by replacing the TiN hard mask by a 10-nm SiO_2 hard mask. Just as it was shown in Chapter IV, the goal is to demonstrate a proof-of-concept pattern transfer for this high- χ BCP. The top coat and PS are removed using the best result from the previous section:

H_2/N_2 with ratio 150/500 for 30 seconds. The SiO_2 etching is conducted in the same CCP reactor as the top coat and PS removal, with the following parameters: $CF_4/H_2/Ar$ with ratio 3.6:1:14, pressure of 50 mTorr, RF 2 MHz at 600W and RF 27 MHz at 300W for 7 seconds. Next, the silicon is partially etched in the Kiyoo[®] CX ICP reactor without air exposure in between. The plasma parameters for Si etching are: $CH_2F_2/SF_6/N_2/He$ with ratio 3:2:3:7, pressure of 5 mTorr, RF power at 450W and RF bias at -70V for 11 seconds. Both plasma chemistries have been previously validated for other applications within CEA Leti.

After SiO_2 etching, Figure V-18(a) shows no pattern collapse, however some bridges are present, probably originated from the top coat and PS removal step. The cross-section SEM image shows that the pattern transfer into the 10-nm SiO_2 layer is complete and that there are around 7 nm of PDMSB left. Moreover, the lines present a good, straight profile and a CD slightly larger than the initial one (10 nm instead of 9 nm).

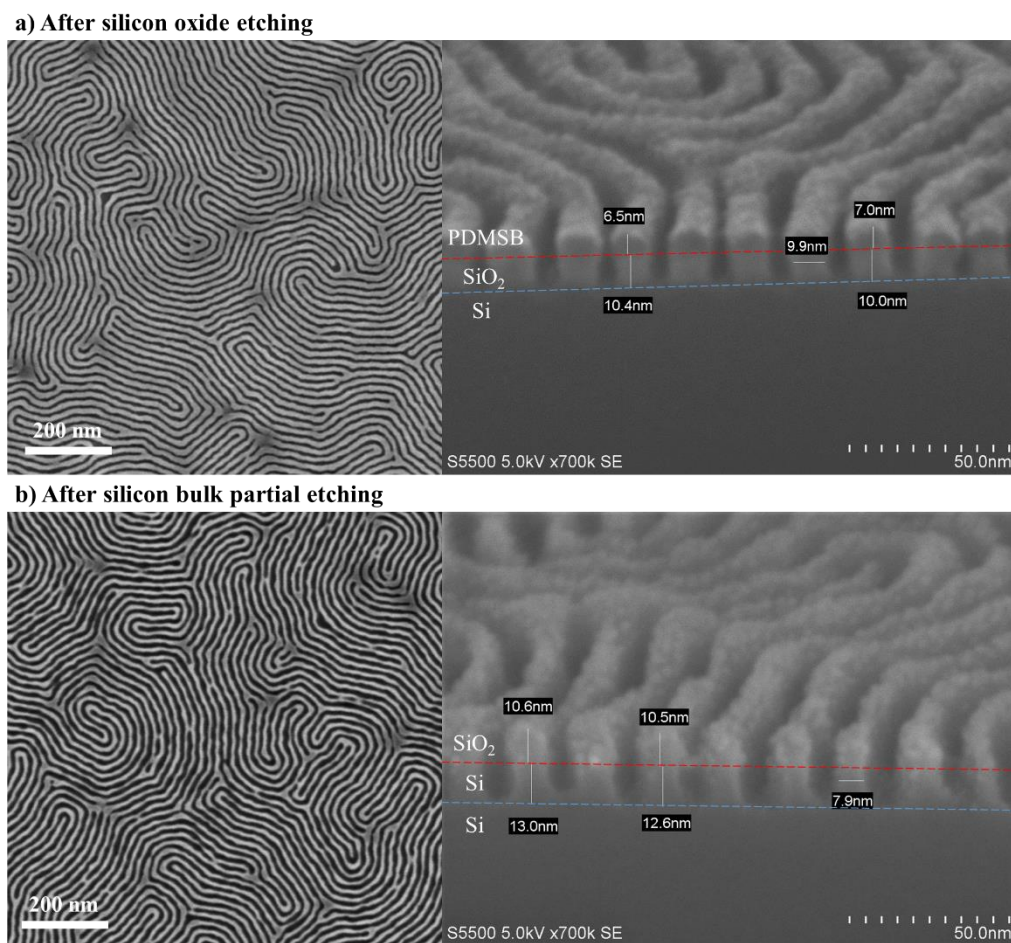


Figure V-18: Top-view and cross-section SEM images of the pattern transfer of high- χ PS-*b*-PDMSB (a) into the SiO_2 hard mask and (b) Si bulk using H_2/N_2 150/500 during 30 seconds for the top coat and PS removal.

After partially etching the Si bulk, the top-view and cross-section SEM images presented in Figure V-18(b) show that the line pattern has been transferred into 13 nm of Si and there are approximately 10 nm of SiO_2 left, thus indicating the possibility to obtain very high aspect ratio silicon features with a plasma etching with good Si: SiO_2 selectivity. Moreover, the good mechanical stability of silicon should prevent pattern collapse. The CD bias between the silicon oxide and silicon bulk etching steps is 2 nm and the final CD is around 8 nm, thus respecting

the CD bias ≤ 2 nm condition. Some bridges are still present, having been transferred from the previous etching steps. Furthermore, no pattern collapse is observed, though a slight wiggling of the lines may be observed with the top-view SEM image in Figure V-18(b). The silicon etching step could be optimized in order to better conserve the CD, possibly avoiding the wiggling effect.

Therefore, we demonstrate the pattern transfer of an 18-nm pitch high- χ silicon-containing block copolymer into a 23-nm thick SiO₂ and silicon stack using a reducing H₂/N₂ plasma etching for top coat and PS removal.

In this section, we started by evaluating the pattern transfer of the high- χ PS-*b*-PDMSB into the TiN hard mask. Three different top coat and PS removal conditions were explored and the results led to the conclusion that, while good PS:PDMSB selectivity is desired in order to conserve enough PDMSB budget to completely transfer the line patterns into the hard mask, mechanical stability problems caused pattern collapse due to the high aspect ratio of the lines. Therefore, the smaller CD of the high- χ block copolymer limited the maximum PDMSB budget allowed for pattern transfer, which in turn limited the TiN thickness that could be etched using this block copolymer as a mask. Nevertheless, we were able to transfer the 18-nm pitch PDMSB lines into a TiN thickness of 10 nm, which could allow for pattern transfer into other subjacent layers using the 10 nm of TiN as hard mask.

Furthermore, a proof of concept for the pattern transfer into a 10-nm SiO₂ hard mask was also validated. After complete pattern transfer into the silicon oxide layer with good profile and CD, there were around 7 nm of PDMSB left. We then demonstrated the partial pattern transfer into approximately 13 nm of the silicon bulk layer while conserving the SiO₂ hard mask, thus indicating the possibility to obtain very high aspect ratio silicon features with a plasma etching with good Si:SiO₂ selectivity. Therefore, we validated the pattern transfer of an 18-nm pitch high- χ silicon-containing block copolymer into a 23-nm thick SiO₂ and silicon stack using a reducing H₂/N₂ plasma etching for top coat and PS removal.

V.4 Conclusions

Throughout this chapter, we investigated two different approaches for the top coat and PS removal selectively to the PDMSB. The first one was based on a top coat removal selectively to the block copolymer, followed by the PS removal selectively to the PDMSB in a separate step. The second one, on the other hand, consisted of a top coat and PS removal in a single step.

For the two-step approach, two oxygen-containing plasma etching were selected to investigate the top coat removal: Ar/O₂ and CH₃F/Ar/SO₂. When the Ar/O₂ plasma was applied to the patterned wafers with the complete PS-*b*-PDMSB and top coat stack, we observed some brighter spots where no line/space patterns were visible. Moreover, where the bright spots were not present, the lines were mostly interrupted and presented a smaller CD. This etch stop of the top coat in certain areas of the wafer could be explained by the presence of something at the top coat and BCP interface that does not etch in Ar/O₂ plasma (for example, a non-homogeneous PDMSB interface or non-volatile etching by-products). On the other hand, when using the CH₃F/Ar/SO₂ plasma during 20 seconds, the top coat layer was completely removed without

significantly etching the block copolymer. Therefore, this process was selected as the process of reference for the top coat removal.

Once the top coat removal process was validated, three different etching chemistries were evaluated for the PS removal selectively to the PDMSB: Ar/O₂, CH₄/N₂ and CH₄/N₂/O₂. For the pattern transfer of the PS-*b*-PDMSB into the TiN hard mask, we estimated that a PS:PDMSB selectivity ≥ 2.5 was necessary. However, the three PS removal chemistries evaluated led to a maximum selectivity of 1.8, which was not enough for complete pattern transfer. We then tried increasing the block copolymer's initial thickness to relax the selectivity constraints. While it did allow us to increase the available PDMSB budget after top coat and PS removal, it also led to pattern collapse due to the high aspect ratio of the lines. Therefore, none of these plasma processes were compatible with the 18-nm pitch high- χ PS-*b*-PDMSB.

We then explored the one-step top coat and PS removal approach with three different plasma chemistries. The Ar/O₂ plasma presented low PS:PDMSB selectivity and, in some spots, the PDMSB lines were interrupted and presented smaller CD, which could be further indication of a non-homogeneous top coat/PS-*b*-PDMSB interface. The Ar/O₂ plasma was therefore considered not appropriate for the one-step top coat and PS removal. The CH₃F/Ar/SO₂ plasma led to a significant increase in the CD of the PDMSB lines, which was explained by the presence of CH₃F and SO₂ as passivating agents, thus forming a passivation layer on the sidewalls of the PDMSB lines and increasing their CD. As a consequence of the very low PS:PDMSB selectivity due to too much passivation, the CH₃F/Ar/SO₂ plasma was also not adapted to the one-step top coat and PS removal.

We then investigated a reducing plasma based on H₂/N₂ to etch the organic phase (PS) of the block copolymer with good selectivity to the silicon-containing phase (PDMSB) while avoiding further oxidation of the titanium nitride hard mask. For a H₂/N₂ ratio of 150/500, after 20 seconds the PS was completely removed with a PS:PDMSB selectivity of 4.3, but some pattern collapse was observed due to the high aspect ratio of the lines. Prolonging the etching time to 30 seconds led to a PDMSB remaining thickness of 18 nm (PS:PDMSB selectivity = 2.5) and no pattern collapse was observed due to the lower aspect ratio of 2. However, some bridges were formed between the lines, which was attributed to intensive sidewalls passivation and to a species confinement effect accentuated by the small and dense pitch.

The gas ratio was varied in order to understand the role of the H₂ and N₂ on the top coat and PS-*b*-PDMSB etching and passivation mechanisms. We showed that higher N₂ content leads to higher selectivity but also more bridge formation, indicating that N₂ is the main passivating agent in this reducing plasma. Higher H₂ content, on the other hand, led to lower selectivity and to an undercutting of the lines due to the neutral layer's lateral etching. However, when attempting to etch the top coat and PS with N₂ only, while the top coat was completely removed, there was no selectivity between PS and PDMSB. This indicated that H₂ is necessary to etch the PS selectively to the PDMSB.

Ex-situ and *quasi in-situ* XPS analysis were conducted to further understand the etching and passivation mechanisms. After etching, the top coat presented a loss of C-O simple and double bonds as well as CF₃ bonds, which is characteristic of other methacrylate-based polymers etching, such as PMMA. As for PS, the formation of a CN_x layer was observed on the surface, which was then removed by hydrogen reactive species by forming HCN as a volatile by-

product. As for the PDMSB, the formation of Si-NH₂ and SiO_xN_yH_z was responsible for the PDMSB passivation during top coat and PS removal with H₂/N₂ plasma.

Finally, we proceeded to the pattern transfer of the PDMSB lines into 10 nm of the 18-nm TiN hard mask. The results led to the conclusion that, while good PS:PDMSB selectivity is desired in order to conserve enough PDMSB budget to completely transfer the line patterns into the hard mask, mechanical stability problems caused pattern collapse due to the high aspect ratio of the lines. Therefore, the smaller CD of the high- χ block copolymer limited the maximum PDMSB budget allowed for pattern transfer (and therefore the PS:PDMSB selectivity), which in its turn limited the TiN thickness that could be etched using this block copolymer as a mask. We then replaced the TiN hard mask by a 10-nm SiO₂ hard mask for a proof of concept of pattern transfer. After complete pattern transfer into the silicon oxide layer with good profile and CD, there were around 7 nm of PDMSB left. Next, we demonstrated the partial pattern transfer into approximately 13 nm of the silicon bulk layer while conserving the SiO₂ hard mask, thus indicating the possibility to obtain very high aspect ratio silicon features with a plasma etching with good Si:SiO₂ selectivity. Therefore, we validated the pattern transfer of an 18-nm pitch high- χ silicon-containing block copolymer into a 23-nm thick SiO₂ and silicon stack using a reducing H₂/N₂ plasma etching for top coat and PS removal.

CHAPTER VI:

CONCLUSION AND PERSPECTIVES

VI. CONCLUSION AND PERSPECTIVES

Chapter I presented the state-of-the-art of the various techniques used for pattern miniaturization in the transistor fabrication process. For decades, optical lithography has been used, but resolution limits prevent this technique from being considered for patterns with critical dimensions inferior to 20 nm. Therefore, to continue pattern scaling, new lithography techniques have been explored throughout the years, such as spacer patterning (or SADP), Extreme Ultraviolet (EUV), Nanoimprint (NIL) and others. Of the various lithography techniques that emerged, the Directed Self-Assembly (DSA) of block copolymers was the one retained for this PhD thesis, namely for line/space applications.

In the introduction chapter, we have also seen that one of the critical steps for the integration of DSA in the microelectronics industry is the alignment of the block copolymers in long range distance, that is, obtaining straight, narrow lines throughout the wafer. To do so, two main techniques were developed, known as grapho-epitaxy and chemo-epitaxy. The chapter detailed some of the different alignment flows developed these last couple decades. At CEA Leti, the main integration flow studied is the “ACE” (for Arkema-CEA) chemo-epitaxy flow. This process aims to align high- χ block copolymers using spacer lithography to form very narrow guiding lines, thus inducing the block copolymer’s alignment due to chemical affinity constraints.

Chapter I also introduced the high- χ block copolymers, which present smaller pitch due to the higher interaction parameter (χ) between the two blocks. Indeed, a higher χ allows us to reduce the value of the degree of polymerization (N) – and thus also reduce the BCP’s period (L_0) – without violating the condition of the order-disorder transition ($\chi N > 10.5$). Moreover, the increase in χ leads to an increase in repulsion between the blocks, and therefore the domains are better defined, and present better roughness compared to larger-pitch block copolymers such as PS-*b*-PMMA.

We then established the state-of-the-art of another important step in the integration of block copolymers, which consists of removing one phase of the block copolymer selectively to the other through to etching, while conserving enough of the remaining block to correctly transfer the patterns into the subjacent layers.

Therefore, this PhD focused on the etching of both purely organic and silicon-containing high- χ lamellar block copolymers, having as goal to successfully remove one block and transfer the line/space patterns into the desired subjacent layers. It also investigated the impact of plasma etching on the ACE process in order to optimize the flow for a PS-*b*-PMMA BCP and a future application with high- χ block copolymers.

Chapter II detailed the characteristics of the different polymeric materials studied throughout this PhD, namely their composition and deposition parameters. It also presented the properties of the different etching reactors, both ICP and CCP, used to study the plasma etching of the high- χ block copolymers; as well as the wet etching tool used for understanding the interaction between plasma etching, the hard mask and the neutral layer during the ACE chemo-epitaxy process. Finally, it explained the principle of several characterization tools used during this thesis to determine the physicochemical and morphological properties of the materials studied before and after etching, detailing the experimental setup and data analysis.

Chapter III focused on evaluating the impact that the different etching steps of the ACE flow have on the surface properties (composition and surface energy) of the TiN hard mask,

and thus on the final self-assembly of the block copolymer over it. We applied the non-optimized process of reference to patterned wafers, which led us to realize that different types of defects could be seen in the top-view image of the block copolymer's alignment after the DSA step, such as dark spots and alignment defects. To understand the origin of the defects and evaluate the hard mask's capability to align the block copolymer, we studied the effect of the sequence of etching and deposition steps on the TiN surface and neutral layer adherence using blanket wafers. We then concluded that the dark spots and alignment defects were caused by a lift-off phenomenon, confirming the inadequacy of the non-optimized flow to align the BCP.

By investigating the effect of each etching step on the TiN surface, we observed that all of them induced significant surface energy and composition modifications when compared to the pristine TiN hard mask. Furthermore, to verify the adherence of the neutral layer to the TiN surface modified by the different etching steps, the neutral layer thickness was measured before and after HF wet etching. Ellipsometry measurements showed that the neutral layer is completely removed for the samples after trilayer etching and SOC removal, which were both based on SO₂/O₂/He plasma. Further investigation on the effect of the RF bias and each gas (SO₂, O₂ and He) separately showed that the SO₂ molecule was the main responsible for this recipe's inadequacy to the ACE flow. Thus, our goal was to understand the interaction mechanisms between the SO₂ plasma, the TiN surface, the xNL deposition and the HF wet etching that led to the lift-off of the neutral layer. Several hypotheses were proposed and the one retained as the most probable was: SO₄²⁻ ions interact with the neutral layer's cross-linking agent, disrupting its complete cross-linking and allowing the HF to pass through. The HF then removes the modified TiO₂/TiO_xS_y layer formed on the TiN surface, which reduces the neutral layer adherence to the TiN hard mask and allows its consequent lift-off.

Finally, we proposed two different alternatives for the SOC removal: replacing the SO₂/O₂/He plasma or adding a post-treatment step. To replace the SO₂/O₂/He, two plasma chemistries were explored (O₂ and H₂/N₂). The O₂ etching modifies the surface composition and energy of the TiN hard mask, but allows the xNL to be conserved during HF wet etching and presents several different process windows for patterned wafers. However, due to a microloading effect on patterned wafers, it does not allow complete SOC removal for smaller pitch and CD_{SOC}, leading to a hybrid chemo/grapho-epitaxy alignment as a function of the multiplication factor. The H₂/N₂ etching conserves the surface energy and composition of the as deposited TiN, and therefore allows the xNL to resist the HF wet etching. Similarly to the O₂ etching, microloading effects during etching of patterned wafers lead to SOC residues for smaller patterns and to a hybrid chemo/grapho-epitaxy alignment. While the H₂/N₂ approach presents the best defectivity result for a single {CD_{SOC}/pitch} pair, with 0 def/100μm² for a lithography pitch of 128 nm, it presents fewer process windows compared to O₂ etching.

In order to further optimize the block copolymer's alignment with the ACE flow, the second approach consisted in a two-step SOC removal: SO₂/O₂/He plasma followed by the H₂/N₂ plasma. This approach exhibits the best alignment results when compared to the other approaches investigated. Indeed, the combination of both plasmas allows for all the prerequisites to be met: the SOC layer is completely removed, the TiN surface properties are conserved, the xNL adheres to the TiN surface throughout the HF wet etching step, and the ACE process is determined mainly by chemo-epitaxy.

Chapter IV focused on the PMMA removal selectively to PS on high- χ modified PS-*b*-PMMA films with an 18-nm pitch and 21-nm initial thickness. By characterizing the

composition of the modified PS and PMMA homopolymers that compose the modified PS-*b*-PMMA block copolymer, we concluded that the modified PS-*b*-PMMA presents a composition similar to that of standard PS-*b*-PMMA. Then, we selected different plasma chemistries and we evaluated their etch rate, and consequent selectivity, on modified PS and PMMA homopolymers, therefore selecting two different chemistries that fulfilled our selectivity requirement: CH₃F/Ar/SO₂ and CH₄/N₂.

We then characterized the impact of the modified chemistry, pitch and initial thickness on the etching of the high- χ modified PS-*b*-PMMA. When comparing a modified and a standard PS-*b*-PMMA BCP with the same pitch and initial thickness, we concluded that, for the same plasma etching chemistry, the high- χ modified PS-*b*-PMMA chemistry does not present a significant impact on the PMMA plasma etching when compared to the standard PS-*b*-PMMA block copolymer. However, when comparing the high- χ modified PS-*b*-PMMA with two different pitch (18 and 32 nm) and two different initial thicknesses (16 and 36 nm, respectively), for the high- χ L18 BCP, the same etching chemistries that were validated for larger pitch (32 nm) present different problems that prevent pattern transfer into the SiO₂ hard mask for the smaller-pitch BCP. Therefore, we concluded that the main high- χ L18 PS-*b*-PMMA plasma etching challenges come from its small dimensions, namely the pitch and initial thickness.

Different approaches were tested to improve the PMMA:PS selectivity and increase the remaining PS budget after PMMA removal. Increasing the initial thickness of the high- χ L18 film led to mechanical stability problems and to pattern wiggling due to the high aspect ratio of the lines, showing that the smaller CD of the high- χ block copolymer limits the maximum initial thickness allowed for the BCP film in order to avoid pattern wiggling or collapse. We also varied the CH₄/N₂ ratio to find a good compromise between etching and carbon passivation. While for PS and PMMA homopolymers we succeeded in etching the PMMA without consuming the PS thanks to a CN-type deposition layer formed on the PS surface, the same could not be applied to the high- χ PS-*b*-PMMA block copolymer assembled on a free surface. The results showed that high- χ BCP requires higher selectivity than standard PS-*b*-PMMA due to its smaller thickness. Moreover, the CH₄/N₂ ratio 1:1, while presenting the best PMMA:PS selectivity without pattern collapse, also presented some bridge formation on top of the lines, which were probably formed due to intensive sidewalls passivation and to a species confinement effect accentuated by the small CD (9 nm). We then concluded that the main high- χ PS-*b*-PMMA dry etching difficulties come from the trade-off between obtaining high selectivity and avoiding bridge formation.

The final approach proposed was a mixed wet and dry etching process. The wet PMMA removal presents infinite selectivity on high- χ modified PS-*b*-PMMA. The UV exposure with a dose of 30 mJ/cm² and a wavelength of 172 nm causes the PMMA chains to break by scission of the C=O and C-O bonds. The IPA rinse then removes the broken PMMA chains without modifying the PS lines. A dry etching process to open the neutral layer using an Ar/O₂ plasma with high argon content (120/5 sccm) was developed to obtain a highly anisotropic etching and to conserve more PS budget. With this mixed wet and dry etching approach, the complete pattern transfer of an 18-nm pitch high- χ organic block copolymer into the 10-nm SiO₂ hard mask and around 14 nm of the silicon bulk layer was validated with CD bias \sim 2 nm.

Chapter V focused on the top coat and PS removal selectively to PDMSB on high- χ silicon-containing PS-*b*-PDMSB films with an 18-nm pitch and 30-nm initial thickness. To do so, two different approaches were investigated and the second one, which consisted of a top coat and

PS removal in a single step, was selected as the best result. This approach was based on a reducing H_2/N_2 plasma to etch the organic phase (PS) of the block copolymer with good selectivity to the silicon-containing phase (PDMSB) while avoiding further oxidation of the titanium nitride hard mask. For a H_2/N_2 ratio of 150/500, after 20 seconds, the PS was completely removed with a PS:PDMSB selectivity of 4.3, but some pattern collapse was observed due to the high aspect ratio of the lines. Prolonging the etching time to 30 seconds led to a PDMSB remaining thickness of 18 nm (PS:PDMSB selectivity = 2.5) and no pattern collapse was observed due to the lower aspect ratio of 2. However, some bridges were formed between the lines, which was attributed to intensive sidewalls passivation and to a species confinement effect accentuated by the small and dense pitch, as seen in Chapter IV for the high- χ PS-*b*-PMMA.

The gas ratio was varied in order to understand the role of the H_2 and N_2 on the top coat and PS-*b*-PDMSB etching and passivation mechanisms. We showed that higher N_2 content leads to higher selectivity but also more bridge formation, indicating that N_2 is the main passivating agent in this reducing plasma. Higher H_2 content, on the other hand, led to lower selectivity and to an undercutting of the lines due to the neutral layer's lateral etching. However, when attempting to etch the top coat and PS with N_2 only, while the top coat was completely removed, there was no selectivity between PS and PDMSB. This indicated that H_2 is necessary to etch the PS selectively to the PDMSB. *Ex-situ* and *quasi in-situ* XPS analysis were conducted to further understand the etching and passivation mechanisms. After etching, the top coat presented a loss of C-O, C=O and CF_3 bonds, which is characteristic of other methacrylate-based polymers etching, such as PMMA. As for PS, the formation of a CN_x layer was observed on the surface, which was then removed by hydrogen reactive species by forming HCN as a volatile by-product. As for the PDMSB, the formation of Si-NH₂ and SiO_xN_yH_z was responsible for the PDMSB passivation during top coat and PS removal with H_2/N_2 plasma.

Finally, we proceeded to the pattern transfer of the PDMSB lines into 10 nm of the 18-nm TiN hard mask. The results led to the conclusion that, while good PS:PDMSB selectivity is desired in order to conserve enough PDMSB budget to completely transfer the line patterns into the hard mask, mechanical stability problems caused pattern collapse due to the high aspect ratio of the lines – a difficulty that we also saw for the high- χ PS-*b*-PMMA in Chapter IV. Therefore, the smaller CD of the high- χ block copolymer limited the maximum PDMSB budget allowed for pattern transfer (and therefore the PS:PDMSB selectivity), which in its turn limited the TiN thickness that could be etched using this block copolymer as a mask. We then replaced the TiN hard mask by a 10-nm SiO₂ hard mask for a proof of concept of pattern transfer. After complete pattern transfer into the silicon oxide layer with good profile and CD, there were around 7 nm of PDMSB left. Next, we demonstrated the partial pattern transfer into approximately 13 nm of the silicon bulk layer while conserving the SiO₂ hard mask, thus indicating the possibility to obtain very high aspect ratio silicon features with a plasma etching with good Si:SiO₂ selectivity. Therefore, we validated the pattern transfer of an 18-nm pitch high- χ silicon-containing block copolymer into a 23-nm thick SiO₂ and silicon stack using a reducing H_2/N_2 plasma etching for top coat and PS removal.

The results obtained with the ACE flow in Chapter III show a good improvement of alignment and defectivity after the optimization of the SOC removal step. Thus, this thesis presented the development and optimization of a chemo-epitaxy method more resolving than those existing to date. Indeed, thanks to the ACE flow, the integration of high- χ block copolymers with pitch inferior to 20 nm using optical immersion lithography is made possible.

Two high- χ block copolymers with pitch 18 nm, one purely organic (modified PS-*b*-PMMA) and the other silicon-containing (PS-*b*-PDMSB), were studied in Chapters IV and V, respectively. The removal of one block selectively to the other led to some similar conclusions in both cases. First, we have seen that high- χ BCPs demand higher selectivity during block removal due to their lower initial thickness when compared to large-pitch block copolymers such as standard PS-*b*-PMMA. However, due to the small CD of these BCPs (CD ~ 9 nm), high selectivity may lead to mechanical stability problems, which cause pattern collapse because of the high aspect ratio of the lines. Indeed, a remaining BCP budget superior to 25 nm, while ideal for complete pattern transfer into the subjacent layers, also leads to an aspect ratio of the BCP lines superior to 2.5, thus increasing the risk of pattern collapse. Therefore, the smaller CD of the high- χ block copolymer limits the maximum BCP budget allowed for pattern transfer, which in turn limits the hard mask thickness that can be etched using this block copolymer as a mask.

Furthermore, a bridge formation phenomenon on top of the lines was also observed for more passivating plasma chemistries. They were probably formed due to intensive sidewalls passivation and to a species confinement effect accentuated by the small CD (9 nm). All of these results led to the conclusion that the main high- χ block copolymer dry etching challenges come from the trade-off between obtaining high selectivity, avoiding bridge formation and avoiding pattern collapse.

Nevertheless, we were able to transfer both 18-nm pitch high- χ block copolymers into a 10-nm SiO₂ hard mask. After complete pattern transfer into the silicon oxide layer with good profile and CD, we then demonstrated the partial pattern transfer into approximately 13 nm of the silicon bulk layer while conserving the SiO₂ hard mask, thus indicating the possibility to obtain high aspect ratio silicon features.

Perspectives

1) Alignment of high- χ PS-*b*-PMMA with pitch 18 nm using the optimized ACE chemo-epitaxy flow.

Now that the ACE process flow has been optimized and presents good alignment and low defectivity for a standard PS-*b*-PMMA block copolymer, the goal is to align the high- χ modified PS-*b*-PMMA with pitch $L_0 = 18$ nm.

Figure VI-1 shows a first CD-SEM image of the L18 high- χ PS-*b*-PMMA aligned using the ACE flow. Since we have shown in Chapter IV that the standard and modified PS-*b*-PMMA present similar compositions, the neutral layer and guiding layer used when applying the ACE flow to the L18 high- χ PS-*b*-PMMA are the same ones from the standard PS-*b*-PMMA studied throughout Chapter III. Therefore, the SOC removal step is well-adapted to the cross-linkable neutral layer (xNL) used and does not cause its lift-off during HF wet etching. The blocks of

L18 are aligned for multiplication factors (MF) 2 and 3. However, Figure VI-1 indicates that the L18 high- χ BCP presents higher LER and LWR when compared to the results obtained for the standard L32 PS-*b*-PMMA in Chapter III. This may be caused by either an aging effect of the BCP or by the non-optimized spacer CD, which does not correspond to the block copolymer's CD (9 nm). Thus, an optimization of the spacer CD and a study of the modified PS-*b*-PMMA aging may be necessary to improve the alignment and roughness results.

Furthermore, the software used for measuring the number of defects developed at CEA Leti – also known as Deboara – must be optimized for the smaller dimensions of the high- χ BCP. For the moment, the measurement of the number of defects is subject to detection errors that do not allow the establishment of defectivity maps to determine precise process windows. The experimental details of the defectivity measurements using the Deboara software can be found in [Le Pennec 2021].

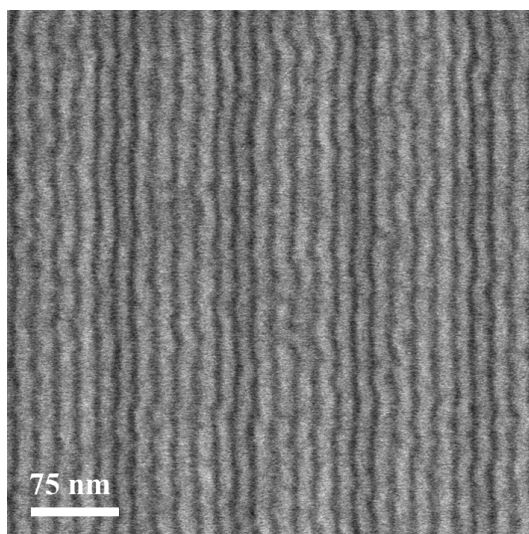


Figure VI-1: Top-view SEM image of high- χ modified PS-*b*-PMMA with pitch 18 nm aligned using the ACE chemo-epitaxy flow.

2) Alignment of high- χ PS-*b*-PDMSB with pitch 18 nm using the optimized ACE chemo-epitaxy flow.

The ACE chemo-epitaxy flow can also be used to align the silicon-containing high- χ PS-*b*-PDMSB block copolymer. As we have seen in Chapter II, this BCP requires a graftable neutral layer based on poly(2-ethylhexyl methacrylate) (PEHMA) homopolymer. To verify the neutral layer's compatibility with the TiN surface after SOC removal, a study similar to the one conducted in Chapter III for the PS-*b*-PMMA cross-linkable neutral layer (xNL) was conducted for the PEHMA homopolymer.

First, the neutral layer was deposited on the pristine TiN surface to measure its initial thickness and water contact angle (WCA) using ellipsometry and contact angle measurements, respectively. The results are presented in Table VI-1: the neutral layer presents an initial thickness of around 6 nm and a WCA of 92.2° before HF. Then, the neutral layer was deposited over the TiN surface after SOC removal using either the non-optimized process (SO₂/O₂/He) or the optimized process (SO₂/O₂/He + H₂/N₂) to compare the results. The measured thickness and WCA before and after 60 seconds of HF wet etching are presented in Table VI-1 for the different samples.

Table VI-1 shows that, for the TiN after SOC removal with the non-optimized plasma ($\text{SO}_2/\text{O}_2/\text{He}$), the neutral layer is almost completely removed after HF wet etching and the WCA decreases approximately in half (46.8°). However, for the TiN as deposited and after SOC removal using the optimized plasma ($\text{SO}_2/\text{O}_2/\text{He} + \text{H}_2/\text{N}_2$), after HF wet etching there is a slight reduction of the neutral layer's thickness of around 2 nm but the water contact angle remains unchanged (around 92.2°).

Table VI-1. Neutral layer thickness measured by ellipsometry before and after HF wet etching for 60 seconds when deposited over the TiN surface before and after each etching step, as well as the water contact angle (WCA) before and after HF.

Neutral layer deposited on	Before HF 60s		After HF 60s	
	Thickness (nm)	WCA ($^\circ$)	Thickness (nm)	WCA ($^\circ$)
TiN as deposited	5.9 ± 0.4	92.2 ± 0.3	4.1 ± 0.6	92.5 ± 0.4
TiN after $\text{SO}_2/\text{O}_2/\text{He}$	7.0 ± 0.4	92.3 ± 0.4	0.4 ± 0.3	46.8 ± 5.6
TiN after $\text{SO}_2/\text{O}_2/\text{He} + \text{H}_2/\text{N}_2$	7.1 ± 0.4	92.2 ± 0.2	5.2 ± 0.5	92.2 ± 0.4

CD-SEM images of the neutral layer before and after HF wet etching were also obtained to verify the presence of lift-off spots. Figure VI-2(a) shows the neutral layer's surface before HF, which is completely uniform and free of dark spots. Figures VI-2(b), (c) and (d) represent the NL surface after 60 seconds of HF wet etching when deposited over the different TiN surfaces. On one hand, we first notice that Figure VI-2(c), which corresponds to the TiN after $\text{SO}_2/\text{O}_2/\text{He}$ plasma, presents many lift-off spots (dark areas), which confirms the results already observed in Table VI-1. On the other hand, Figures VI-2(b) and (d), which correspond to the TiN as deposited and after SOC removal using the $\text{SO}_2/\text{O}_2/\text{He} + \text{H}_2/\text{N}_2$ plasma respectively, present fewer lift-off spots when compared to Figure VI-2(c), which is expected given the slight reduction in the neutral layer's thickness (around 2 nm) observed in Table VI-1 for these two samples. This thickness reduction observed even for the as deposited TiN – which was not the case for the cross-linkable neutral layer (xNL) in Chapter III – indicates that the graftable NL of the PS-*b*-PDMSB block copolymer may not be fully compatible with the TiN hard mask.

Nevertheless, the next step should be to apply the ACE chemo-epitaxy flow to the PS-*b*-PDMSB block copolymer using the graftable PEHMA neutral layer and the optimized SOC removal plasma. This would allow us to verify if this thickness reduction of 2 nm after HF wet etching would affect the BCP's alignment or if the fact that the water contact angle remains unchanged after HF means the neutral layer retains its ability to align the block copolymer.

If the PEHMA graftable neutral layer cannot provide a good BCP alignment, another alternative would be to use the top coat layer, which is composed of a poly(2,2,2-trifluoroethylmethacrylate-*r*-glycidylmethacrylate-*r*-2-hydroxyethylmethacrylate) statistical terpolymer. Since this layer is cross-linkable, it should present a better resistance to the HF wet etching step when using the optimized SOC removal plasma ($\text{SO}_2/\text{O}_2/\text{He} + \text{H}_2/\text{N}_2$). To do so, the dilution percentage of the top coat solution must be reduced to obtain a thinner layer (around 6 nm) instead of the actual solution, which provides a 55 nm layer.

Finally, similarly to the high- χ PS-*b*-PMMA presented in Perspective 1, the Deboara software [Le Pennec 2021] used for measuring the number of defects must be optimized for the smaller dimensions of the high- χ BCP.

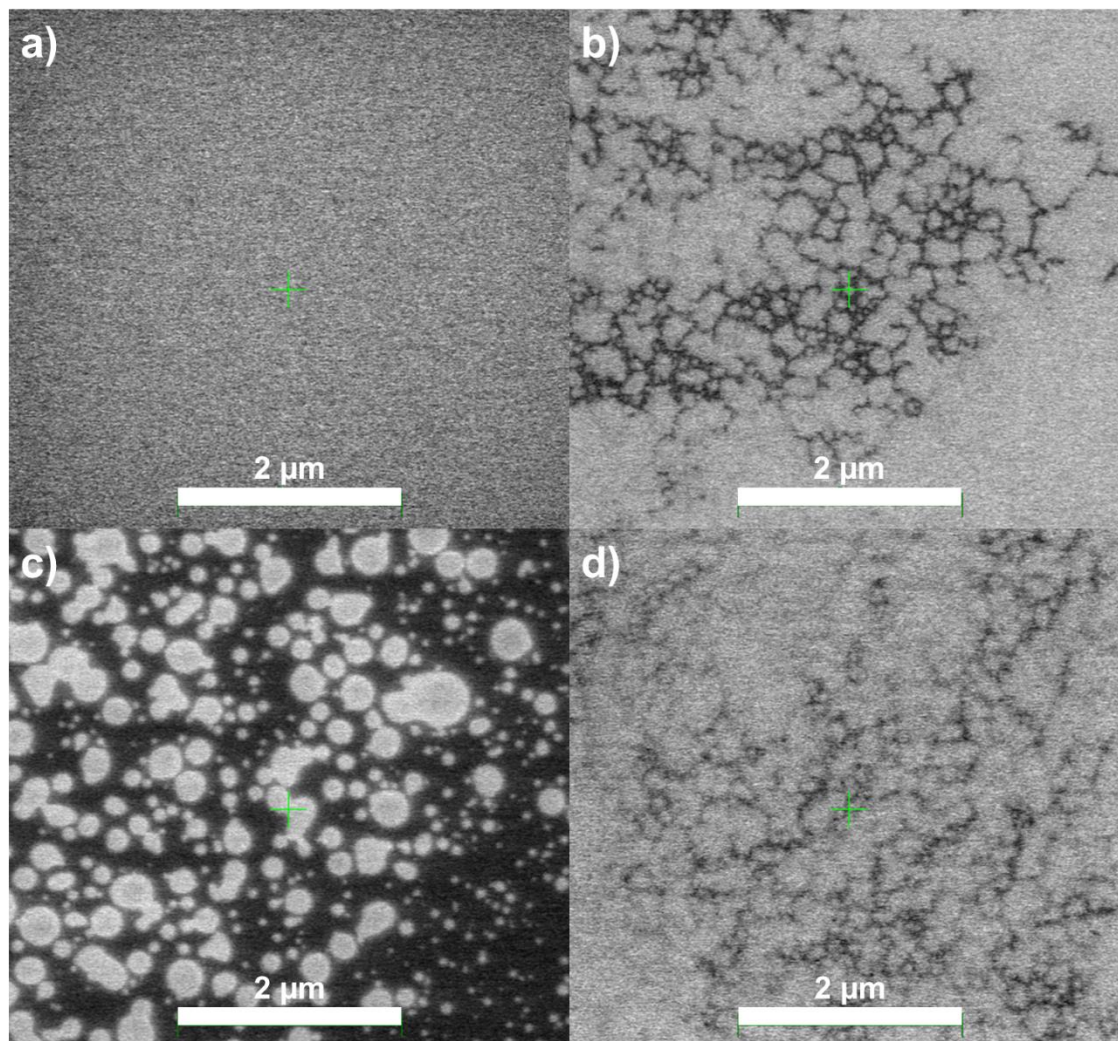


Figure VI-2: Top-view SEM images of the PS-*b*-PDMSB graftable neutral layer (a) before and (b, c, d) after HF wet etching for 60 seconds when deposited over (a, b) TiN as deposited; (c) TiN after SOC removal with SO₂/O₂/He plasma; and (d) TiN after SOC removal with SO₂/O₂/He + H₂/N₂ plasma.

3) Obtain high PS:PMMA selectivity using Sequential Infiltration Synthesis (SIS) for the L18 high- χ PS-*b*-PMMA.

Sequential infiltration synthesis (SIS) is a vapor phase infiltration technique that allows the growth of inorganic materials into polymeric films by penetration of gaseous precursors into the polymer. Thus, it offers the possibility to enhance the mechanical properties of the final film, to improve its chemical etch resistance, and to fabricate inorganic nanostructures when infiltrating in patterned polymer films or in self-assembled block copolymers.

A typical SIS process consists of a controlled sequence of metal–organic precursor and co-reactant vapor exposure cycles of the polymer films in an atomic layer deposition (ALD) reactor, intercalating appropriate purging cycles of inert gas to remove unreacted molecules or reaction by-products. E. Cianci *et al.* have demonstrated the infiltration of trimethylaluminum (TMA) in combination with H₂O for the synthesis of Al₂O₃ into PS-*b*-PMMA films. They have

shown that TMA has a high reactivity at low temperature and interacts selectively with the carbonyl (C=O) groups in the PMMA units. Indeed, FTIR analysis of PMMA films evidenced that the interaction between TMA and C=O and C-O bonds forms a reversible adduct $C=O \cdots Al(CH_3)_3$ for the subsequent nucleation of Al_2O_3 . Furthermore, for the PS-*b*-PMMA BCP, TMA infiltration process discriminates PMMA with respect to PS domains, where no TMA-phylic groups are available, allowing to selectively grow alumina only in the PMMA volume. By applying an O_2 plasma to remove the organic materials (PS and remaining PMMA), it is then possible to create inorganic Al_2O_3 nanostructures used as hard masks for pattern transfer [Cianci 2018] [Caligiore 2019].

A partnership between the DSA team at CEA Leti and the SIS team at IMM-CNR (Italy) is ongoing in order to study the sequential infiltration synthesis of alumina in the PMMA phase of the high- χ L18 PS-*b*-PMMA. The goal is to improve the PS:PMMA selectivity by increasing the etching contrast between the purely organic phase (PS) and the hybrid organic-inorganic phase (Al_2O_3 in PMMA).

4) Increase the mechanical stability of the high- χ PS-*b*-PDMSB.

As we have seen in Chapter V, the main challenge for the etching of the silicon-containing high- χ PS-*b*-PDMSB is the trade-off between obtaining high selectivity and avoiding pattern collapse due to the high aspect ratio of the lines. Thus, a solution to avoid pattern collapse, and therefore conserve a thicker PDMSB budget for pattern transfer, would be to improve the mechanical stability of the PDMSB lines.

For example, A. Legrain *et al.* have shown that vacuum UV (VUV) irradiation during 75 seconds with a 172-nm wavelength in the presence of oxygen can improve the mechanical stability of PS-*b*-PDMSB lamellae. Indeed, UV treatment is known to enhance the thermal and mechanical stability of PS through cross-linking. For the PDMSB, X-ray photoelectron spectrometry (XPS) indicates that carbon atoms are replaced by oxygen atoms during VUV irradiation, gradually forming Si-O bonds to replace the Si-CH₃ bonds. Consequently, the VUV treatment of PDMSB cross-links the polymer, improving its resistance to the etching of the organic phase and its mechanical stability during PS removal and pattern transfer. Therefore, the mechanical properties of both PS and PDMSB are improved through VUV treatment, and no pattern collapse is observed during pattern transfer [Legrain 2017].

BIBLIOGRAPHY

[Adcock 1954] W. A. Adcock, M. E. Jones, J. W. Thornhill and E. D. Jackson, Silicon transistor, Proceedings of the IRE. 42, 1192 (1954).

[Agarwal 2009] A. Agarwal *et al.*, Effect of simultaneous source and bias pulsing in inductively coupled plasma etching, Journal of Applied Physics. 106, 103305 (2009). <https://doi.org/10.1063/1.3262616>

[Aissou 2015] K. Aissou *et al.*, Sub-10 nm Features Obtained from Directed Self-Assembly of Semicrystalline Polycarbosilane-Based Block Copolymer Thin Films, Advanced Materials. 27, 2 (2015). <https://doi.org/10.1002/adma.201404077>

[Argoud 2014] M. Argoud *et al.*, 300mm pilot line DSA contact hole process stability, Proceedings of SPIE. 9049, 904929 (2014). <https://doi.org/10.1117/12.2046315>

[Austin 2004] M. D. Austin *et al.*, Fabrication of 5 nm linewidth and 14 nm pitch features by nanoimprint lithography, Applied Physics Letters. 84, 5299 (2004). <https://doi.org/10.1063/1.1766071>

[Azarnouche 2012] L. M. Azarnouche, Défis liés à la réduction de la rugosité des motifs de résine photosensible 193 nm. Université Grenoble Alpes. Grenoble, 2012. Français. <https://tel.archives-ouvertes.fr/tel-00767820>

[Baravelli 2007] E. Baravelli *et al.*, Impact of Line-Edge Roughness on FinFET Matching Performance, IEEE Transactions on Electron Devices. 54, 9 (2007). <https://doi.org/10.1109/TED.2007.902166>

[Bardeen 1948] J. Bardeen and W. H. Brattain, The Transistor, A Semi-Conductor Triode, Physics Review. 74, 230 (1948). <https://doi.org/10.1103/PhysRev.74.230>

[Bates 1999] F. S. Bates and G. H. Fredrickson, Block Copolymers—Designer Soft Materials, Physics Today. 52, 2, 32 (1999). <https://doi.org/10.1063/1.882522>

[Bates 2012] C. M. Bates *et al.*, Polarity-Switching Top Coats Enable Orientation of Sub-10-nm Block Copolymer Domains, Science. 338, 6108 (2012). <https://doi.org/10.1126/science.1226046>

[Bates 2014] S. Kim, P. F. Nealey and F. S. Bates, Directed Assembly of Lamellae Forming Block Copolymer Thin Films near the Order–Disorder Transition, Nano Letters. 14, 1, 148-152 (2014). <https://doi.org/10.1021/nl403628d>

[Beamson 1992] G. Beamson and D. Briggs, High Resolution XPS of Organic Polymers: The Scienta ESCA300 Database. Published by Wiley. Chichester, 1992.

[Bezard 2018] P. Bézard *et al.*, Graphoepitaxy integration and pattern transfer of lamellar silicon-containing high-chi block copolymers, Proceedings of SPIE. 10589, 105890C (2018). <https://doi.org/10.1117/12.2299337>

[Blachut 2016] G. Blachut *et al.*, A Hybrid Chemo-/Grapho-Epitaxial Alignment Strategy for Defect Reduction in Sub-10 nm Directed Self-Assembly of Silicon-Containing Block Copolymers, Chemistry of Materials. 28, 24, 8951–8961 (2016). <https://doi.org/10.1021/acs.chemmater.6b03633>

[Black 2005] C. T. Black, Self-aligned self assembly of multi-nanowire silicon field effect transistors, Applied Physics Letters. 87, 163116 (2005). <https://doi.org/10.1063/1.2112191>

[Bois 1996] L. Bois *et al.*, Characterization of a boro-silicon oxynitride prepared by thermal nitridation of a polyborosiloxane, *Journal of Alloys and Compounds*. 232, 1–2, 244-253 (1996). [https://doi.org/10.1016/0925-8388\(95\)01982-0](https://doi.org/10.1016/0925-8388(95)01982-0)

[Caligiore 2019] F. E. Caligiore *et al.*, Effect of the Density of Reactive Sites in P(S-r-MMA) Film during Al₂O₃ Growth by Sequential Infiltration Synthesis, *Advanced Materials Interfaces*. 6, 12 (2019). <https://doi.org/10.1002/admi.201900503>

[Chan 2014] B. T. Chan *et al.*, 28 nm pitch of line/space pattern transfer into silicon substrates with chemo-epitaxy Directed Self-Assembly (DSA) process flow, *Microelectronic Engineering*. 123, 180–186 (2014). <https://doi.org/10.1016/j.mee.2014.07.028>

[Chang 2009] L-W. Chang, T. L. Lee, C. H. Wann, C. Y. Chang and H-S. P. Wong, Top-gated FETs/inverters with diblock copolymer self-assembled 20 nm contact holes, *IEEE International Electron Devices Meeting (IEDM)*. Baltimore, MD, USA. 1-4 (2009). <https://doi.org/10.1109/IEDM.2009.5424272>

[Cheng 2004] J. Y. Cheng, A. M. Mayes and C. A. Ross, Nanostructure engineering by templated self-assembly of block copolymers, *Nature Materials*. 3, 823–828 (2004). <https://doi.org/10.1038/nmat1211>

[Cheng 2010] J. Y. Cheng *et al.*, Simple and Versatile Methods To Integrate Directed Self-Assembly with Optical Lithography Using a Polarity-Switched Photoresist, *ACS Nano*. 4, 8, 4815–4823 (2010). <https://doi.org/10.1021/nn100686v>

[Chernyy 2017] S. Chernyy *et al.*, Synthesis and Characterization of Ferrocene Containing Block Copolymers, *Journal of Polymer Science, Part A: Polymer Chemistry*. 55, 3, 495–503 (2017). <https://doi.org/10.1002/pola.28435>

[Chevalier 2021] X. Chevalier *et al.*, Lithographically Defined Cross-Linkable Top Coats for Nanomanufacturing with High- χ Block Copolymers, *ACS Applied Materials & Interfaces*. 13, 9, 11224–11236 (2021). <https://doi.org/10.1021/acsami.1c00694>

[Chevillon 2012] Nicolas Chevillon. Etude et modélisation compacte du transistor FinFET ultime. Université de Strasbourg. Strasbourg, 2012. Français. <https://tel.archives-ouvertes.fr/tel-00750928>

[Choi 2010] E. Kim *et al.*, Transition behavior of PS-b-PMMA films on the balanced interfacial interactions, *Polymer*. 51, 26, 6313-6318 (2010). <https://doi.org/10.1016/j.polymer.2010.10.055>

[Chou 1995] S. Y. Chou, P. R. Krauss and P. J. Renstrom, Imprint of sub-25 nm vias and trenches in polymers. *Applied Physics Letters*. 67, 21, 3114 (1995). <https://doi.org/10.1063/1.114851>

[Cianci 2018] E. Cianci, D. Nazzari, G. Seguíni and M. Perego, Trimethylaluminum Diffusion in PMMA Thin Films during Sequential Infiltration Synthesis: In Situ Dynamic Spectroscopic Ellipsometric Investigation, *Advanced Materials Interfaces*. 5, 20 (2018). <https://doi.org/10.1002/admi.201801016>

[Claveau 2016] G. Claveau *et al.*, Surface affinity role in graphoepitaxy of lamellar block copolymers, *Journal of Micro/Nanolithography, MEMS, and MOEMS*. 15, 3, 031604 (2016). <https://doi.org/10.1117/1.JMM.15.3.031604>

[Claveau 2017] G. Claveau, Etude d'une lithographie ligne/espace innovante par auto-assemblage dirigé d'un copolymère à blocs pour la réalisation de dispositifs CMOS sub-20nm. Université Grenoble Alpes. Grenoble, 2017. Français.

[Coburn 2002] J.W. Coburn, The Evolution of Plasma Etching in Integrated Circuit Manufacturing, Invited Paper at AVS 49th International Symposium. November 4, 2002. Available at https://www2.avs.org/symposium2002/Papers/Paper_PS-MoM1.html (accessed on 02/01/2021)

[Cochran 2006] E. W. Cochran, C. J. Garcia-Cervera and G. H. Fredrickson, Stability of the Gyroid Phase in Diblock Copolymers at Strong Segregation, *Macromolecules*. 39, 7, 2449–2451 (2006). <https://doi.org/10.1021/ma0527707>

[Correia 2019] C. Gomes Correia, Directed self-assembly strategies for orientation-controlled block copolymers in advanced lithography. Université de Bordeaux. Bordeaux, 2019. English.

[Courtland 2016] R. Courtland, The Next High-Performance Transistor Could Be Made From Lateral Nanowires. 28 September 2016. Available at <https://spectrum.ieee.org/semiconductors/nanotechnology/the-next-highperformance-transistor-could-be-made-from-lateral-nanowires> (accessed on 02/04/2021)

[Craighead 1984] H. G. Craighead, 10-nm resolution electron-beam lithography, *Journal of Applied Physics*. 55, 4430 (1984). <https://doi.org/10.1063/1.333015>

[Danglad-Flores 2018] J. Danglad-Flores, S. Eickelmann and H. Riegler, Deposition of polymer films by spin casting: A quantitative analysis, *Chemical Engineering Science*. 179, 257-264 (2018). <https://doi.org/10.1016/j.ces.2018.01.012>

[Delachat 2018] F. Delachat *et al.*, An embedded neutral layer for advanced surface affinity control in grapho-epitaxy directed self-assembly, *Nanoscale*. 10, 10900-10910 (2018). <https://doi.org/10.1039/C8NR00123E>

[De Marchi 2014] M. De Marchi *et al.*, Top-Down Fabrication of Gate-All-Around Vertically Stacked Silicon Nanowire FETs With Controllable Polarity, *IEEE Transactions on Nanotechnology*. 13, 6, 1029-1038 (2014). <https://doi.org/10.1109/TNANO.2014.2363386>

[Dhindsa 2008] R. Dhindsa *et al.*, Multiple frequency plasma processor method and apparatus, US Patent n° 7405521 (29 July 2008).

[Doise 2017] J. Doise, B. T. Chan, M. Hori, and R. Gronheid, Dual brush process for selective surface modification in graphoepitaxy directed self-assembly, *Journal of Micro/Nanolithography, MEMS, and MOEMS*. 16, 3, 033503 (2017). <https://doi.org/10.1117/1.JMM.16.3.033503>

[Durand 2015] W. J. Durand *et al.*, Design of High- χ Block Copolymers for Lithography, *Journal Of Polymer Science, Part A: Polymer Chemistry*. 53, 2, 344–352 (2015). <https://doi.org/10.1002/pola.27370>

[Emslie 1958] A.G. Emslie, F.T. Bonner and L.G. Peck, Flow of a viscous liquid on a rotating disk, *Journal of Applied Physics*. 29, 858 (1958). <https://doi.org/10.1063/1.1723300>

[Feng 2017] H. Feng, X. Lu, W. Wang, N-G. Kang and J. W. Mays, Block Copolymers: Synthesis, Self-Assembly, and Applications, *Polymers*. 9, 10, 494 (2017). <https://doi.org/10.3390/polym9100494>

[Fitrianto 2011] Fitrianto, Method for reworking a silicon-containing arc layer on a substrate, Patent n° WO 2011/041268 A1 (7 April 2011).

[Fowkes 1964] F. M. Fowkes, Attractive Forces at Interfaces, *Industrial and Engineering Chemistry*. 56, 12, 40–52 (1964). <https://doi.org/10.1021/ie50660a008>

[Gharbi 2015] A. Gharbi *et al.*, PMMA removal options by wet development in PS-*b*-PMMA block copolymer for nanolithographic mask fabrication, *Journal of Vacuum Science & Technology B*. 33, 051602 (2015). <https://doi.org/10.1116/1.4929548>

[Girardot 2014] C. Girardot *et al.*, Pulsed Transfer Etching of PS–PDMS Block Copolymers Self-Assembled in 193 nm Lithography Stacks, *ACS Applied Materials & Interfaces*. 6, 18, 16276–16282 (2014). <https://doi.org/10.1021/am504475q>

[Gonbeau 1991] D. Gonbeau *et al.*, XPS study of thin films of titanium oxysulfides, *Surface Science*. 254, 1-3, 81-89 (1991). [https://doi.org/10.1016/0039-6028\(91\)90640-E](https://doi.org/10.1016/0039-6028(91)90640-E)

[Griffiths 2007] P. R. Griffiths and J. A. de Haseth, *Fourier Transform Infrared Spectrometry*. Published by John Wiley & Sons, Inc. Hoboken, New Jersey. 2nd edition, 2007.

[Gu 2012] X. Gu *et al.*, High Aspect Ratio Sub-15 nm Silicon Trenches From Block Copolymer Templates, *Advanced Materials*. 24, 42, 5688–5694 (2012) <https://doi.org/10.1002/adma.201202361>

[Guerrero 2017] D. J. Guerrero *et al.*, A track process for solvent annealing of high- χ BCPs, *Proceedings of SPIE*. 10146, 101460W (2017). <https://doi.org/10.1117/12.2261094>

[Gusmão 2020] M. G. Gusmão Cacho *et al.*, Etching of sub-10 nm half-pitch high chi block copolymers for directed self-assembly (DSA) application, *Microelectronic Engineering*. 230, 111369 (2020). <https://doi.org/10.1016/j.mee.2020.111369>

[Gusmão 2021] M. G. Gusmão Cacho *et al.*, Study of plasma etching impact on chemoepitaxy directed self-assembly, *Journal of Vacuum Science & Technology A*. 39, 033004 (2021). <https://doi.org/10.1116/6.0000850>

[Gusmão 2021B] M. G. Gusmão Cacho *et al.*, Selective plasma etching of silicon-containing high chi block copolymer for directed self-assembly (DSA) application, *Journal of Vacuum Science & Technology B*. 39, 042801 (2021). <https://doi.org/10.1116/6.0001102>

[Haisma 1996] J. Haisma, M. Verheijen, K. van den Heuvel and J. van den Berg, Mold-assisted nanolithography: A process for reliable pattern replication. *Journal of Vacuum Science & Technology B*. 14, 4124 (1996). <https://doi.org/10.1116/1.588604>

[Han 2008] E. Han, K. O. Stuen, Y-H. La, P. F. Nealey and P. Gopalan, Effect of Composition of Substrate-Modifying Random Copolymers on the Orientation of Symmetric and Asymmetric Diblock Copolymer Domains, *Macromolecules*. 41, 23, 9090–9097 (2008). <https://doi.org/10.1021/ma8018393>

[Handy 2014] J. Handy, How Many Transistors Have Ever Shipped?, *Forbes* (May 26, 2014). Available at <https://www.forbes.com/sites/jimhandy/2014/05/26/how-many-transistors-have-ever-shipped/#673320484425> (accessed on 05/20/20)

[Hashimoto 1980] T. Hashimoto, M. Shibayama and H. Kawai, Domain-Boundary Structure of Styrene-Isoprene Block Copolymer Films Cast from Solution. 4. Molecular-Weight Dependence of Lamellar Microdomains, *Macromolecules*. 13, 5, 1237–1247 (1980). <https://doi.org/10.1021/ma60077a040>

[Hedlund 1994] C. Hedlund, H-O. Blom and S. Berg, Microloading effect in reactive ion etching, *Journal of Vacuum Science & Technology A*. 12, 1962 (1994). <https://doi.org/10.1116/1.578990>

[Hirahara 2016] E. Hirahara *et al.*, Directed Self-Assembly Materials for High Resolution beyond PS-*b*-PMMA, *Journal of Photopolymer Science and Technology*. 29, 5 (2016). <https://doi.org/10.2494/photopolymer.29.679>

[Hoffman 1998] D. M. Hoffman, B. Singh and J. H. Thomas III, *Handbook of Vacuum Science and Technology*. Published by Elsevier, 1998. <https://doi.org/10.1016/B978-0-12-352065-4.X5040-8>

[Hu 2014] H. Hu, M. Gopinadhan and C. O. Osuji, Directed self-assembly of block copolymers: a tutorial review of strategies for enabling nanotechnology with soft matter, *Soft Matter*. 10, 3867-3889 (2014). <https://doi.org/10.1039/C3SM52607K>

[Ingo 1989] G. M. Ingo, N. Zacchetti, D. della Sala and C. Coluzza, X-ray photoelectron spectroscopy investigation on the chemical structure of amorphous silicon nitride (a-SiN_x), *Journal of Vacuum Science & Technology A*. 7, 3048 (1989). <https://doi.org/10.1116/1.576314>

[Intel 2011] M. Bohr and K. Mistry, Intel's Revolutionary 22 nm Transistor Technology. May, 2011. Available at https://download.intel.com/newsroom/kits/22nm/pdfs/22nm-Details_Presentation.pdf (accessed on 02/04/2021)

[IRDS 2016] “What Is the IRDS™?”. Available at <https://irds.ieee.org/> (accessed on 06/15/20)

[IRDS 2020] “International Roadmap for Devices and Systems 2020 Edition Lithography”. Available at <https://irds.ieee.org/editions/2020> (accessed on 06/15/20)

[Isono 2018] T. Isono, B. J. Ree, K. Tajima, R. Borsali and T. Satoh, Highly Ordered Cylinder Morphologies with 10 nm Scale Periodicity in Biomass-Based Block Copolymers, *Macromolecules*. 51, 2, 428–437 (2018). <https://doi.org/10.1021/acs.macromol.7b02279>

[ITRS 2009] “International Technology Roadmap for Semiconductors 2009 Edition Lithography”. Available at <https://www.semiconductors.org/wp-content/uploads/2018/09/Litho.pdf> (accessed on 06/15/20)

[Ji 2016] S. Ji, L. Wan, C-C. Liu and P. F. Nealey, Directed self-assembly of block copolymers on chemical patterns: A platform for nanofabrication, *Progress in Polymer Science*. 54–55, 76-127 (2016). <https://doi.org/10.1016/j.progpolymsci.2015.10.006>

[Jiang 2013] X. Jiang, R. Wang, T. Yu, J. Chen and R. Huang, Investigations on Line-Edge Roughness (LER) and Line-Width Roughness (LWR) in Nanoscale CMOS Technology: Part I—Modeling and Simulation Method, *IEEE Transactions on Electron Devices*. 60, 11, 3669-3675 (2013). <https://doi.org/10.1109/TED.2013.2283518>

[Kahng 1963] D. Kahng, Electric Field Controlled Semiconductor Device, U. S. Patent n^o 3102230A (27 August 1963).

[Kanarik 2015] K. J. Kanarik *et al.*, Overview of atomic layer etching in the semiconductor industry, *Journal of Vacuum Science & Technology A*. 33, 020802 (2015). <https://doi.org/10.1116/1.4913379>

[Karouta 2014] F. Karouta, A practical approach to reactive ion etching, *Journal of Physics D: Applied Physics*. 47, 233501 (2014). <https://doi.org/10.1088/0022-3727/47/23/233501>

[Kelly 2005] J. J. Kelly and H. G. G. Philipsen, Anisotropy in the wet-etching of semiconductors, *Current Opinion in Solid State and Materials Science*. 9, 1-2, 84–90 (2005). <https://doi.org/10.1016/j.cossms.2006.04.003>

[Kennemur 2014] J. G. Kennemur, L. Yao, F. S. Bates and M. A. Hillmyer, Sub-5 nm Domains in Ordered Poly(cyclohexylethylene)-*block*-poly(methyl methacrylate) Block Polymers for Lithography, *Macromolecules*. 47, 4, 1411–1418 (2014). <https://doi.org/10.1021/ma4020164>

[Khaira 2014] G. S. Khaira *et al.*, Evolutionary Optimization of Directed Self-Assembly of Triblock Copolymers on Chemically Patterned Substrates, *ACS Macro Letters*. 3, 8, 747–752 (2014). <https://doi.org/10.1021/mz5002349>

[Kilby 1964] Jack S. Kilby, Miniaturized Electronic Circuits, US Patent n° 3138743A (23 June 1964).

[Kim 2010] H-C. Kim, S-M. Park and W. D. Hinsberg, Block Copolymer Based Nanostructures: Materials, Processes, and Applications to Electronics, *Chemical Reviews*. 110, 1, 146–177 (2010). <https://doi.org/10.1021/cr900159v>

[Kim 2013] J. Kim *et al.*, The SMART™ Process for Directed Block Co-polymer Self-Assembly, *Journal of Photopolymer Science and Technology*. 26, 5, 573-579 (2013). <https://doi.org/10.2494/photopolymer.26.573>

[Kim 2014] E. Kim, W. Kim, K. H. Lee, C. A. Ross and J. G. Son, A Top Coat with Solvent Annealing Enables Perpendicular Orientation of Sub-10 nm Microdomains in Si-Containing Block Copolymer Thin Films. *Advanced Functional Materials*. 24, 44, 6981–6988 (2014). <https://doi.org/10.1002/adfm.201401678>

[Kim 2015] J. Kim *et al.*, Toward high-performance quality meeting IC device manufacturing requirements with AZ SMART DSA process, *Proceedings of SPIE*. 9423, 94230R (2015). <https://doi.org/10.1117/12.2086160>

[Knotter 2000] D. M. Knotter, Etching Mechanism of Vitreous Silicon Dioxide in HF-Based Solutions, *Journal of the American Chemical Society*. 122, 18, 4345–4351 (2000). <https://doi.org/10.1021/ja993803z>

[Knotter 2001] D. M. Knotter and T. J. J. Denteneer, Etching Mechanism of Silicon Nitride in HF-Based Solutions, *Journal of The Electrochemical Society*. 148, 3, F43-F46 (2001). <https://doi.org/10.1149/1.1348262>

[Koo 2013] K. Koo, H. Ahn, S-W. Kim, D. Y. Ryu and T. P. Russell, Directed self-assembly of block copolymers in the extreme: guiding microdomains from the small to the large, *Soft Matter*. 9, 9059-9071 (2013). <https://doi.org/10.1039/C3SM51083B>

[Lane 2017] A. P. Lane *et al.*, Directed Self-Assembly and Pattern Transfer of Five Nanometer Block Copolymer Lamellae, *ACS Nano*. 11, 8, 7656–7665 (2017). <https://doi.org/10.1021/acsnano.7b02698>

[Legrain 2017] A. Legrain *et al.*, Straightforward Integration Flow of a Silicon-Containing Block Copolymer for Line–Space Patterning, *ACS Applied Materials & Interfaces*. 9, 49, 43043–43050 (2017). <https://doi.org/10.1021/acsaami.7b12217>

Bibliography

[Le Pennec 2021] A. Le Pennec, Développement de procédés de lithographie avancée par auto-assemblage de copolymères à blocs de haute résolution. Université Grenoble Alpes. Grenoble, 2021. Français.

[Levinson 2010] H. J. Levinson, Principles of Lithography. Published by SPIE Press. 3rd edition. Bellingham, Wash, 2010.

[Liu 2007] C-C. Liu, P. F. Nealey, Y-H. Ting and A. E. Wendt, Pattern transfer using poly(styrene-*block*-methyl methacrylate) copolymer films and reactive ion etching, Journal of Vacuum Science & Technology B. 25, 1963 (2007). <https://doi.org/10.1116/1.2801884>

[Liu 2011] C-C. Liu *et al.*, Fabrication of Lithographically Defined Chemically Patterned Polymer Brushes and Mats, Macromolecules. 44, 7, 1876–1885 (2011). <https://doi.org/10.1021/ma102856t>

[Liu 2013] C-C. Liu *et al.*, Chemical Patterns for Directed Self-Assembly of Lamellae-Forming Block Copolymers with Density Multiplication of Features, Macromolecules. 46, 4, 1415–1424 (2013). <https://doi.org/10.1021/ma302464n>

[Luo 2015] Y. Luo *et al.*, Poly(dimethylsiloxane-*b*-methyl methacrylate): A Promising Candidate for Sub-10 nm Patterning, Macromolecules. 48, 11, 3422–3430 (2015). <https://doi.org/10.1021/acs.macromol.5b00518>

[Mansky 1996] P. Mansky, C. K. Harrison, P. M. Chaikin, R. A. Register and N. Yao, Nanolithographic templates from diblock copolymer thin films. Applied Physics Letters. 68, 2586 (1996). <https://doi.org/10.1063/1.116192>

[Mansky 1997] P. Mansky *et al.*, Interfacial Segregation in Disordered Block Copolymers: Effect of Tunable Surface Potentials, Physical Review Letters. 79, 237 (1997). <https://doi.org/10.1103/PhysRevLett.79.237>

[Matsushita 1990] Y. Matsushita *et al.*, Molecular weight dependence of lamellar domain spacing of diblock copolymers in bulk, Macromolecules. 23, 19, 4313–4316 (1990). <https://doi.org/10.1021/ma00221a019>

[Mele 1984] T. C. Mele, J. Nulman and J. P. Krusius, Selective and anisotropic reactive ion etch of LPCVD silicon nitride with CHF₃ based gases, Journal of Vacuum Science & Technology B. 2, 684 (1984). <https://doi.org/10.1116/1.582863>

[Miyazoe 2017] H. Miyazoe, A. V. Jagtiani, H-Y. Tsai, S. U. Engelmann and E. A. Joseph, Highly selective dry etching of polystyrene-poly(methyl methacrylate) block copolymer by gas pulsing carbon monoxide-based plasmas, Journal of Physics D: Applied Physics. 50, 204001 (2017). <https://doi.org/10.1088/1361-6463/aa68c6>

[Mizoguchi 2017] H. Mizoguchi, High Power LPP-EUV Source With Long Collector Mirror Lifetime For High Volume Semiconductor Manufacturing, 2nd EUV-FEL Workshop. Japan (2017). Available at http://pfwww.kek.jp/PEARL/EUV-FEL_Workshop2/Proceedings/07_Mizoguchi.pdf (accessed on 01/21/21)

[Mokarian-Tabari 2014] P. Mokarian-Tabari *et al.*, Study of the kinetics and mechanism of rapid self-assembly in block copolymer thin films during solvo-microwave annealing, Langmuir. 30, 35, 10728–10739 (2014). <https://doi.org/10.1021/la503137q>

[Moore 1965] G. Moore, Cramming More Components onto Integrated Circuits, Electronics. 38, 8 (1965).

Bibliography

[**Moore 1975**] G. Moore, Progress in digital integrated electronics, Electron Devices Meeting. 21, 11-13 (1975).

[**Morris 2015**] M. A. Morris, Directed self-assembly of block copolymers for nanocircuitry fabrication, Microelectronic Engineering. 132, 207–217 (2015). <https://doi.org/10.1016/j.mee.2014.08.009>

[**Nakanishi 1977**] K. Nakanishi and P. H. Solomon, Infrared Absorption Spectroscopy. Published by Holden-Day, Inc. 2nd edition. San Francisco, 1977.

[**NIST 2021**] National Institute of Standards and Technology (NIST) website, “Time-of-Flight Secondary Ion Mass Spectrometry”. Available at <https://www.nist.gov/programs-projects/time-flight-secondary-ion-mass-spectrometry> (accessed on 05/05/2021)

[**Nobel Prize 1956**] The Nobel Prize in Physics 1956. NobelPrize.org. Nobel Media AB 2020. Available at <https://www.nobelprize.org/prizes/physics/1956/summary/> (accessed on 05/20/2020)

[**Nobel Prize 1981**] The Nobel Prize in Physics 1981. NobelPrize.org. Nobel Media AB 2021. Available at <https://www.nobelprize.org/prizes/physics/1981/summary/> (accessed on 05/03/2021)

[**Nobel Prize 2000**] The Nobel Prize in Physics 2000. NobelPrize.org. Nobel Media AB 2020. Available at <https://www.nobelprize.org/prizes/physics/2000/summary/> (accessed on 05/19/2020)

[**Nojiri 2015**] K. Nojiri, Dry Etching Technology for Semiconductors. Published by Springer International Publishing. Switzerland, 2015. <https://doi.org/10.1007/978-3-319-10295-5>

[**Noyce 1961**] R. N. Noyce, Semiconductor device-and-lead structure, US Patent n^o 2981877A (25 April 1961).

[**Ohnishi 1983**] H. Gokan, S. Esho and Y. Ohnishi, Dry Etch Resistance of Organic Materials, Journal of The Electrochemical Society. 130, 143 (1983). <https://iopscience.iop.org/article/10.1149/1.2119642>

[**Oktay 2015**] S. Oktay, Z. Kahraman, M. Urgen and K. Kazmanli, XPS investigations of tribolayers formed on TiN and (Ti,Re)N coatings, Applied Surface Science. 328, 255-261 (2015). <https://doi.org/10.1016/j.apsusc.2014.12.023>

[**OWRK 1969**] D. K. Owens and R. C. Wendt, Estimation of the surface free energy of polymers, Journal of Applied Polymer Science. 13, 8, 1741-1747 (1969). <https://doi.org/10.1002/app.1969.070130815>

[**Oyama 2014**] K. Oyama *et al.*, Robust Complementary technique with Multiple-Patterning for sub-10 nm node device, Proceedings of SPIE. 9051, 90510V (2014). <https://doi.org/10.1117/12.2046236>

[**Paquet 2019**] A. Paquet *et al.*, Spacer patterning lithography as a new process to induce block copolymer alignment by chemoepitaxy, Proceedings of SPIE. 10958, 109580M (2019). <https://doi.org/10.1117/12.2514960>

[**Park 2009**] S-M. Park, B. C. Berry, E. Dobisz and H-C. Kim, Observation of surface corrugation-induced alignment of lamellar microdomains in PS-b-PMMA thin films, Soft Matter. 5, 957–961 (2009). <https://doi.org/10.1039/B813749H>

[Pimenta-Barros 2018] P. Pimenta-Barros *et al.*, Precise control of template affinity achieved by UV-assisted graphoepitaxy approach on silicon nanowires applications, Proceedings of SPIE. 10584, 105840C (2018). <https://doi.org/10.1117/12.2297407>

[Posseme 2007] N. Posseme *et al.*, Mechanisms of porous dielectric film modification induced by reducing and oxidizing ash plasmas, Journal of Vacuum Science & Technology B. 25, 1928 (2007). <https://doi.org/10.1116/1.2804615>

[Posseme 2010] N. Posseme *et al.*, Residue growth on metallic-hard mask after dielectric etching in fluorocarbon-based plasmas. I. Mechanisms, Journal of Vacuum Science & Technology B. 28, 809 (2010). <https://doi.org/10.1116/1.3456182>

[Posseme 2014] N. Posseme, O. Pollet and S. Barnola, Alternative process for thin layer etching: Application to nitride spacer etching stopping on silicon germanium, Applied Physics Letters. 105, 051605 (2014). <https://doi.org/10.1063/1.4892543>

[Pourteau 2016] M. L. Pourteau *et al.*, Non-CAR resists and advanced materials for Massively Parallel E-Beam Direct Write process integration, Proceedings of SPIE. 9777, 977713 (2016). <https://doi.org/10.1117/12.2218884>

[Rademaker 2020] G. J. Rademaker *et al.*, Establishing a sidewall image transfer chemo-epitaxial DSA process using 193 nm immersion lithography, Proceedings of SPIE. 11326, 113260Z (2020). <https://doi.org/10.1117/12.2552003>

[Riga 1978] J. Riga, J. J. Verbist, F. Wudl and A. Kruger, The electronic structure and conductivity of tetrathiotetracene, tetrathionaphthalene, and tetraselenotetracene studied by ESCA, The Journal of Chemical Physics. 69, 3221 (1978). <https://doi.org/10.1063/1.436972>

[Rodwogin 2010] M. D. Rodwogin, C. S. Spanjers, C. Leighton and M. A. Hillmyer, Poly(lactide)-Poly(dimethylsiloxane)-Poly(lactide) Triblock Copolymers as Multifunctional Materials for Nanolithographic Applications, ACS Nano. 4, 2, 725–732 (2010). <https://doi.org/10.1021/mn901190a>

[Roser 2020] M. Roser and H. Ritchie, Technological Progress. Published online at OurWorldInData.org (2020). Available at <https://ourworldindata.org/technological-progress> (accessed on 05/20/20)

[Salim 2011] N. Tjitra Salim *et al.*, The effect of post-treatments on the powder morphology of titanium dioxide (TiO₂) powders synthesized for cold spray, Surface and Coatings Technology. 206, 2-3, 366-371 (2011). <https://doi.org/10.1016/j.surfcoat.2011.07.030>

[Samsung 2019] “Samsung Successfully Completes 5nm EUV Development to Allow Greater Area Scaling and Ultra-low Power Benefits”. Available at <https://news.samsung.com/global/samsung-successfully-completes-5nm-euv-development-to-allow-greater-area-scaling-and-ultra-low-power-benefits> (accessed on 01/21/21)

[Sanders 2010] D. P. Sanders, Advances in Patterning Materials for 193 nm Immersion Lithography, Chemical Reviews. 110, 1, 321–360 (2010). <https://doi.org/10.1021/cr900244n>

[Sarrazin 2016] A. Sarrazin *et al.*, PMMA removal selectivity to polystyrene using dry etch approach, Journal of Vacuum Science & Technology B. 34, 061802 (2016). <https://doi.org/10.1116/1.4964881>

[Sarrazin 2017] A. Sarrazin, Développement de techniques de patterning avancées pour les filières CMOS-sub 10nm. Université de Nantes. Nantes, 2017. Français.

Bibliography

[Sarrazin 2018] A. Sarrazin *et al.*, Block copolymer selectivity: A new dry etch approach for cylindrical applications, *Journal of Vacuum Science & Technology B*. 36, 041803 (2018). <https://doi.org/10.1116/1.5034133>

[Sarrazin 2019] A. Sarrazin *et al.*, New CH₄-N₂ dry etch chemistry for PMMA removal without consuming PS, *Journal of Vacuum Science & Technology B*. 37, 030601 (2019). <https://doi.org/10.1116/1.5090395>

[Schaller 2004] R. Schaller, *Technological Innovation in the Semiconductor Industry: A Case Study of the International Technology Roadmap for Semiconductors (ITRS)*. George Mason University. Fairfax County, Virginia, USA, 2004. English.

[Scofield 1976] J. H. Scofield, Hartree-Slater subshell photoionization cross-sections at 1254 and 1487 eV, *Journal of Electron Spectroscopy and Related Phenomena*. 8, 2, 129-137 (1976). [https://doi.org/10.1016/0368-2048\(76\)80015-1](https://doi.org/10.1016/0368-2048(76)80015-1)

[Segalman 2001] R. A. Segalman, H. Yokoyama and E. J. Kramer, Graphoepitaxy of Spherical Domain Block Copolymer Films, *Advanced Materials*. 13, 15, 1152-1155 (2001). [https://doi.org/10.1002/1521-4095\(200108\)13:15<1152::AID-ADMA1152>3.0.CO;2-5](https://doi.org/10.1002/1521-4095(200108)13:15<1152::AID-ADMA1152>3.0.CO;2-5)

[Shilov 2020] A. Shilov, TSMC Places Massive EUV Tools Order to Boost Capacity. Published November 13, 2020. Available at <https://www.tomshardware.com/news/tsmc-euv-tools-order> (accessed on 01/21/21)

[Sivaniah 2008] E. Sivaniah *et al.*, Symmetric Diblock Copolymer Thin Films on Rough Substrates: Microdomain Periodicity in Pure and Blended Films, *Macromolecules*. 41, 7, 2584–2592 (2008). <https://doi.org/10.1021/ma702465t>

[Somervell 2012] M. Somervell *et al.*, Comparison of directed self-assembly integrations, *Proceedings of SPIE*. 8325, 83250G (2012). <https://doi.org/10.1117/12.916406>

[Stoykovich 2006] M. P. Stoykovich and P. F. Nealey, Block copolymers and conventional lithography, *Materials Today*. 9, 9, 20-29 (2006). [https://doi.org/10.1016/S1369-7021\(06\)71619-4](https://doi.org/10.1016/S1369-7021(06)71619-4)

[Takeishi 2015] H. Takeishi and S. V. Sreenivasan, Nanoimprint system development and status for high volume semiconductor manufacturing, *Proceedings of SPIE*. 9423, 94230C (2015). <https://doi.org/10.1117/12.2087017>

[Thermo 2021] Thermo Scientific XPS website. Available at <https://xpssimplified.com/elements/silicon.php> (accessed on 05/03/2021)

[Thurn-Albrecht 2000] T. Thurn-Albrecht *et al.*, Nanoscopic templates from oriented block copolymer films, *Advanced Materials*. 12, 11, 787–791 (2000). [https://doi.org/10.1002/\(SICI\)1521-4095\(200006\)12:11<787::AID-ADMA787>3.0.CO;2-1](https://doi.org/10.1002/(SICI)1521-4095(200006)12:11<787::AID-ADMA787>3.0.CO;2-1)

[Ting 2008] Y-H. Ting *et al.*, Plasma etch removal of poly(methyl methacrylate) in block copolymer lithography, *Journal of Vacuum Science & Technology B*. 26, 1684 (2008). <https://doi.org/10.1116/1.2966433>

[Tiron 2012] R. Tiron *et al.*, Pattern density multiplication by direct self assembly of block copolymers: toward 300mm CMOS requirements, *Proceedings of SPIE*. 8323, 83230O (2012). <https://doi.org/10.1117/12.916400>

[Tsai 2014] H. Tsai *et al.*, Two-dimensional pattern formation using graphoepitaxy of PS-b-PMMA block copolymers for advanced FinFET device and circuit fabrication, ACS Nano. 8, 5, 5227-5232 (2014). <https://doi.org/10.1021/nn501300b>

[Tsai 2016] H. Tsai *et al.*, High chi block copolymer DSA to improve pattern quality for FinFET device fabrication, Proceedings of SPIE. 9779, 977910 (2016). <https://doi.org/10.1117/12.2219544>

[Tseng 2010] Y-C. Tseng and S. B. Darling, Block Copolymer Nanostructures for Technology, Polymers. 2, 4, 470-489 (2010). <https://doi.org/10.3390/polym2040470>

[Vickerman 2001] J. C. Vickerman and D. Briggs, ToF-SIMS: surface analysis by mass spectrometry. Published by SurfaceSpectra (Manchester, UK) and IM Publications (Chichester, West Sussex, UK). 2001.

[Vora 2016] A. Vora *et al.*, Orientation Control of Block Copolymers Using Surface Active, Phase-Preferential Additives, ACS Applied Materials & Interfaces. 8, 43, 29808–29817 (2016). <https://doi.org/10.1021/acsami.6b11293>

[Wadley 2012] M. L. Wadley, I-F. Hsieh, K. A. Cavicchi and S. Z. D. Cheng, Solvent Dependence of the Morphology of Spin-Coated Thin Films of Polydimethylsiloxane-Rich Polystyrene-*block*-Polydimethylsiloxane Copolymers, Macromolecules. 45, 13, 5538–5545 (2012). <https://doi.org/10.1021/ma300044d>

[Wagner 1982] C. D. Wagner and J. A. Taylor, Contributions to screening in the solid state by electron systems of remote atoms: Effects to photoelectron and Auger transitions, Journal of Electron Spectroscopy and Related Phenomena. 28, 2, 211-217 (1982). [https://doi.org/10.1016/0368-2048\(82\)85044-5](https://doi.org/10.1016/0368-2048(82)85044-5)

[Wang 2011] X. Wang, A. R. Brown, B. Cheng and A. Asenov, Statistical variability and reliability in nanoscale FinFETs, 2011 International Electron Devices Meeting. Washington, DC, USA. 5-7 December 2011. <https://doi.org/10.1109/IEDM.2011.6131494>

[Williamson 2016] L. D. Williamson *et al.*, Three-Tone Chemical Patterns for Block Copolymer Directed Self-Assembly, ACS Applied Materials & Interfaces. 8, 4, 2704–2712 (2016). <https://doi.org/10.1021/acsami.5b10562>

[Wong 2012] H-S. P. Wong, C. Bencher, H. Yi, X-Y. Bao and L-W. Chang, Block copolymer directed self-assembly enables sublithographic patterning for device fabrication, Proceedings of SPIE. 8323, 832303 (2012). <https://doi.org/10.1117/12.918312>

[Worley 1986] S. D. Worley *et al.*, Analyses of spacecraft polymeric materials, Journal of Spacecraft and Rockets. 23, 3, 350 (1986). <https://doi.org/10.2514/3.25810>

[Yamashita 2012] F. Yamashita, E. Nishimura, K. Yatsuda, H. Mochiki and J. Bannister, Exploration of suitable dry etch technologies for directed self-assembly, Proceedings of SPIE. 8328, 83280T (2012). <https://doi.org/10.1117/12.916349>

[Yang 2009] G. Yang, P. Tang, Y. Yang and J. T. Cabral, Self-Assembly of AB Diblock Copolymers under Confinement into Topographically Patterned Surfaces, The Journal of Physical Chemistry B. 113, 43, 14052–14061 (2009). <https://doi.org/10.1021/jp9033613>

[Yeap 2019] G. Yeap *et al.*, 5nm CMOS Production Technology Platform featuring full-fledged EUV, and High Mobility Channel FinFETs with densest 0.021 μ m² SRAM cells for Mobile SoC and High Performance Computing Applications, 2019 IEEE International Electron

Bibliography

Devices Meeting (IEDM). San Francisco, CA, USA. 7-11 December 2019. <https://doi.org/10.1109/IEDM19573.2019.8993577>

[Zalusky 2002] A. S. Zalusky, R. Olayo-Valles, J. H. Wolf and M. A. Hillmyer, Ordered Nanoporous Polymers from Polystyrene–Polylactide Block Copolymers, *Journal of the American Chemical Society*. 124, 43, 12761–12773 (2002). <https://doi.org/10.1021/ja0278584>

[Zhang 2010] X. Zhang *et al.*, Solvent Retention in Thin Spin-Coated Polystyrene and Poly(methyl methacrylate) Homopolymer Films Studied By Neutron Reflectometry, *Macromolecules*. 43, 2, 1117–1123 (2010). <https://doi.org/10.1021/ma902168w>

[Zhang 2014] J. Zhang *et al.*, New Materials for Directed Self-Assembly for Advanced Patterning, *Proceedings of SPIE*. 9051, 905111 (2014). <https://doi.org/10.1117/12.2046328>

[Zhang 2016] J. Zhang *et al.*, Orientation Control in Thin Films of a High- χ Block Copolymer with a Surface Active Embedded Neutral Layer, *Nano Letters*. 16, 1, 728–735 (2016). <https://doi.org/10.1021/acs.nanolett.5b04602>

[Zhou 2016] S. X. Zhou, D. W. Janes, C. B. Kim, C. G. Willson and C. J. Ellison, Designing Intrablock Attractions To Increase the χ Parameter of a Symmetric Diblock Copolymer, *Macromolecules*. 49, 21, 8332–8340 (2016). <https://doi.org/10.1021/acs.macromol.6b01382>

[Zisman 1964] W. A. Zisman, Relation of the Equilibrium Contact Angle to Liquid and Solid Constitution, *Advances in Chemistry*. Volume 43, Chapter I of Contact Angle, Wettability, and Adhesion. Published in 1964 by the American Chemical Society. <http://dx.doi.org/10.1021/ba-1964-0043.ch001>

RÉSUMÉ EN FRANÇAIS

Le **chapitre I** présente l'état de l'art des différentes techniques utilisées pour la miniaturisation des motifs dans les procédés de fabrication des transistors. Depuis des décennies, la lithographie optique est utilisée, mais les limites de résolution empêchent d'envisager cette technique pour des motifs de dimensions critiques inférieures à 20 nm. Par conséquent, pour continuer la miniaturisation des motifs, de nouvelles techniques de lithographie ont été explorées au fil des ans, telles que le « spacer patterning » (ou SADP), l'extrême ultraviolet (EUV), la nano-impression (NIL) parmi d'autres. L'une d'entre elle, l'auto-assemblage dirigé (DSA) de copolymères à blocs est l'objet de cette thèse ; plus précisément les applications ligne/espace.

Dans le chapitre d'introduction, nous avons vu que l'une des étapes critiques pour l'intégration du DSA dans l'industrie de la microélectronique est l'alignement des copolymères à blocs à longue distance, c'est-à-dire l'obtention de lignes droites et étroites tout au long de la plaque. Pour ce faire, deux techniques principales ont été développées, la grapho-épitaxie et la chemo-épitaxie. Le chapitre I détaille certains des différents procédés d'alignement développés au cours des deux dernières décennies. Au CEA Leti, le principal procédé d'intégration étudié est le procédé de chemo-épitaxie « ACE » (pour Arkema-CEA). Ce procédé vise à aligner des copolymères à blocs de haute résolution (dits « high- χ ») en utilisant le « spacer patterning » pour former des lignes de guidage très étroites, induisant ainsi l'alignement du copolymère à blocs grâce à des contraintes d'affinité chimique.

Le chapitre I introduit également les copolymères blocs à haut χ (« high- χ »), qui présentent un espacement (« pitch ») entre les motifs formés plus petit en raison du paramètre d'interaction de Flory-Huggins (χ) plus élevé entre les deux blocs. En effet, un χ plus élevé permet de diminuer la valeur du degré de polymérisation (N) – et donc aussi de réduire la période du BCP (L_0) – tout en respectant la condition de la transition ordre-désordre ($\chi N > 10,5$). De plus, l'augmentation du χ entraîne une augmentation de la répulsion entre les blocs. Par conséquent, les domaines sont mieux définis et présentent une meilleure rugosité par rapport aux copolymères à blocs de plus grand « pitch » comme le polystyrène-*b*-poly(méthacrylate de méthyle) (PS-*b*-PMMA). Nous avons ensuite établi l'état de l'art d'une autre étape importante dans l'intégration des copolymères à blocs, qui consiste à retirer sélectivement une phase du copolymère à blocs grâce à la gravure, tout en conservant suffisamment du bloc restant pour transférer correctement les motifs dans les couches sous-jacentes.

Cette thèse se concentre donc sur la gravure de copolymères à blocs lamellaires de haute résolution (« high- χ »), dans le but de retirer avec succès un bloc et de transférer les motifs de lignes/espaces dans les couches sous-jacentes souhaitées. Nous avons également étudié l'impact de la gravure plasma sur le procédé ACE afin d'optimiser ce procédé pour un copolymère à blocs PS-*b*-PMMA de « pitch » 32 nm, et pour une future application avec des copolymères à blocs high- χ . Les objectifs de cette thèse peuvent être séparés en trois parties principales :

1) Première partie : impact de la gravure sur le procédé ACE.

Lorsque le procédé ACE non optimisé est appliqué à un copolymère à blocs PS-*b*-PMMA de « pitch » 32 nm, différents types de défauts peuvent être observés, comme des taches sombres et des défauts d'alignement du copolymère à blocs, ce qui indique que les propriétés de surface du masque dur de nitrure de titane (TiN) sont modifiées au cours des différentes étapes de gravure et, ainsi, deviennent moins favorables à l'alignement du copolymère à blocs.

Par conséquent, l'objectif principal de la première partie de cette thèse était d'étudier et de comprendre l'origine de ces défauts et l'impact que les différentes étapes de gravure du procédé ACE ont sur les propriétés de surface du masque dur TiN, et donc sur l'auto-assemblage du copolymère à blocs. Leur effet sur l'adhérence de la couche neutre et donc sa résistance à l'étape de gravure humide à l'acide fluorhydrique (HF) est également évaluée.

2) Deuxième partie : gravure d'un copolymère à blocs high- χ purement organique.

Dans le cadre de cette thèse, le copolymère à blocs high- χ purement organique étudié est un PS-*b*-PMMA modifié avec un pitch de 18 nm et une morphologie lamellaire. Il a été développé par Brewer Science Inc. et Arkema. Les modifications apportées au PS-*b*-PMMA standard pour obtenir cette version modifiée avec un plus petit espacement entre les lignes sont confidentielles. L'objectif principal de cette étude est de développer un procédé de retrait du PMMA sélectif au PS et adapté au « pitch » de 18 nm sur des plaques de 300 mm en explorant différentes chimies et approches, telles que la gravure cyclique et l'exposition aux UV.

Nous estimons qu'il devrait y avoir au moins 15 nm de PS plus la couche neutre après le retrait du PMMA pour assurer le transfert des motifs dans la couche d'oxyde de silicium (SiO₂) sous-jacente, ce qui signifie que le copolymère à blocs high- χ nécessite une sélectivité PMMA:PS supérieure à 3,5 en raison de son épaisseur initiale réduite (environ 21 nm). Une fois le PMMA complètement éliminé, le transfert des motifs dans la couche sous-jacente de SiO₂ permet de valider l'approche de gravure développée.

3) Troisième partie : gravure d'un copolymère à blocs high- χ contenant du silicium.

Dans le cadre de cette thèse, le copolymère à blocs high- χ contenant du silicium étudié est un poly(styrène-*b*-1,1-diméthylsilacyclobutane) (PS-*b*-PDMSB) développé par Arkema. Il présente un « pitch » de 18 nm, une morphologie lamellaire et un paramètre de Flory-Huggins (χ) compris entre 0,08 et 0,1 à température ambiante. La phase contenant du silicium (PDMSB) présentant une affinité à l'air plus élevée que la phase organique (PS), ce copolymère à blocs nécessite donc le dépôt d'une surcouche supérieure (appelée « top coat »), qui a une affinité neutre pour les deux phases, afin de s'auto-assembler en lamelles verticales. Notre objectif est de retirer sélectivement le top coat et le PS vis-à-vis du PDMSB, en conservant suffisamment d'épaisseur de PDMSB pour ensuite transférer les motifs ligne/espace dans le masque dur de 18 nm (15 nm de TiN et environ 3 nm d'oxyde de titane natif, TiO_x). Pour ce faire, différentes chimies sont évaluées pour obtenir une sélectivité élevée et un bon contrôle des dimensions (variation de dimension critique inférieure à 2 nm).

Le **chapitre II** détaille les caractéristiques des différents matériaux polymères étudiés tout au long de cette thèse, à savoir leur composition et leurs paramètres de dépôt. Il présente également les propriétés des différents réacteurs de gravure, à la fois de couplage inductif (ICP) et capacitif (CCP), utilisés pour étudier la gravure plasma des copolymères à blocs high- χ ; ainsi que l'équipement de gravure humide utilisé pour comprendre l'interaction entre la gravure plasma, le masque dur et la couche neutre lors du procédé de chemo-épitaxie ACE. Enfin, ce chapitre explique le principe de plusieurs techniques de caractérisation utilisées au cours de cette thèse pour déterminer les propriétés physico-chimiques et morphologiques des matériaux étudiés avant et après gravure, en détaillant le dispositif expérimental.

Ensuite, le **chapitre III** se concentre sur l'évaluation de l'impact des différentes étapes de gravure du procédé ACE sur les propriétés de surface (composition et énergie de surface) du masque dur TiN, et donc sur l'auto-assemblage final du copolymère à blocs sur celui-ci. En

appliquant le procédé de référence non optimisé aux plaques avec des motifs, nous avons observé différents types de défauts dans l'image en vue de dessus après l'étape d'alignement du copolymère à blocs, tels que des taches sombres et des défauts d'alignement. Pour comprendre l'origine des défauts et évaluer la capacité du masque dur à aligner le copolymère à blocs, nous avons étudié l'effet de la séquence d'étapes de gravure et de dépôt sur la surface de TiN et l'adhérence de la couche neutre. Nous avons alors conclu que les taches sombres et les défauts d'alignement étaient dus à un phénomène de décollement (appelée « lift-off »), confirmant l'incompatibilité du procédé non optimisé pour aligner le copolymère à blocs.

En étudiant l'effet de chaque étape de gravure séparément sur la surface du TiN, nous avons observé que toutes les étapes induisaient des modifications significatives de l'énergie de surface et de la composition par rapport au masque dur TiN tel que déposé. De plus, pour vérifier l'adhérence de la couche neutre à la surface du TiN modifiée par les différentes étapes de gravure, l'épaisseur de la couche neutre a été mesurée avant et après gravure humide par HF. Les mesures d'ellipsométrie ont montré que la couche neutre est complètement éliminée pour deux échantillons : celui après gravure du tri-couche Résine/SiARC/SOC et celui après retrait SOC, tous deux s'arrêtant sur TiN avec un plasma $\text{SO}_2/\text{O}_2/\text{He}$. Une enquête plus approfondie sur l'effet de la tension d'auto-polarisation (RF bias) et de chaque gaz (SO_2 , O_2 et He) séparément a montré que la molécule de SO_2 était la principale responsable de l'inadéquation de ce plasma au procédé ACE. Ainsi, notre objectif était de comprendre les mécanismes d'interaction entre le plasma de SO_2 , la surface de TiN, le dépôt de la couche neutre et la gravure humide HF qui ont conduit au lift-off de la couche neutre. Plusieurs hypothèses ont été proposées et celle retenue comme la plus probable est : les ions SO_4^{2-} sur la surface du TiN interagissent avec l'agent de réticulation de la couche neutre, empêchant sa réticulation complète et laissant passer le HF. Le HF retire ensuite la couche de $\text{TiO}_2/\text{TiO}_x\text{S}_y$ modifiée formée sur la surface de TiN, ce qui réduit l'adhérence de la couche neutre au masque dur de TiN et entraîne son décollement.

Enfin, nous avons proposé deux alternatives différentes pour le retrait du SOC : remplacer le plasma $\text{SO}_2/\text{O}_2/\text{He}$ ou ajouter une étape de post-traitement. Pour remplacer le $\text{SO}_2/\text{O}_2/\text{He}$, deux chimies de plasma ont été explorées (O_2 et H_2/N_2). La gravure O_2 modifie la composition de surface et l'énergie du masque dur TiN, mais permet de conserver la couche neutre lors de la gravure humide par HF et présente plusieurs fenêtres d'alignement différentes pour les plaques avec des motifs. Sur ces plaques avec motifs, plusieurs types de lignes sont disponibles et sont réalisées avec différentes tailles et densités (différents couples CD/pitch). Or, le plasma O_2 ne permet pas un retrait complet du SOC pour les lignes les plus petites et les plus denses (faible « pitch » et CD_{SOC}), conduisant à un alignement hybride chemo/grapho-épitaxie en fonction du facteur de multiplication. On assiste ici à un phénomène de « micro-loading », qui correspond à une différence de performances pour la gravure plasma selon la densité et/ou la taille des motifs. La gravure H_2/N_2 conserve l'énergie de surface et la composition du TiN tel que déposé, et permet donc à la couche neutre de résister à la gravure humide par HF. De la même manière que pour la gravure O_2 , les effets de « micro-loading » lors de la gravure de plaques avec des motifs conduisent à des résidus de SOC pour des motifs plus petits et à un alignement hybride chemo/grapho-épitaxie. Alors que l'approche H_2/N_2 présente le meilleur résultat de défektivité pour une seule paire $\{\text{CD}_{\text{SOC}}/\text{pitch}\}$, avec 0 def/100 μm^2 pour un « pitch » de lithographie de 128 nm, elle présente moins de fenêtres d'alignement par rapport à la gravure O_2 .

Afin d'optimiser davantage l'alignement du copolymère à blocs avec le procédé ACE, la deuxième approche présentée consiste en un retrait SOC en deux étapes : plasma $\text{SO}_2/\text{O}_2/\text{He}$ suivi du plasma H_2/N_2 . Cette approche présente les meilleurs résultats d'alignement par rapport aux autres approches étudiées. En effet, la combinaison des deux plasmas permet de réunir tous les prérequis : la couche de SOC est totalement retirée, les propriétés de surface du TiN sont conservées, la couche neutre adhère à la surface du TiN tout au long de l'étape de gravure humide par HF, et le procédé ACE est déterminé principalement par chemo-épitaxie.

Le **chapitre IV** se concentre sur le retrait sélectif du PMMA vis-à-vis du PS pour un copolymère à blocs high- χ composé de PS-*b*-PMMA modifié, avec un « pitch » de 18 nm et une épaisseur initiale de 21 nm. En caractérisant la composition des homopolymères PS et PMMA modifiés qui composent le copolymère à blocs PS-*b*-PMMA modifié, nous avons conclu que le PS-*b*-PMMA modifié présente une composition similaire à celle du PS-*b*-PMMA standard. Ensuite, nous avons sélectionné différentes chimies de plasma et nous avons évalué leur vitesse de gravure, et la sélectivité qui en résulte, sur des homopolymères PS et PMMA modifiés, sélectionnant ainsi deux chimies différentes qui remplissaient notre exigence de sélectivité : $\text{CH}_3\text{F}/\text{Ar}/\text{SO}_2$ et CH_4/N_2 .

Nous avons ensuite caractérisé l'impact de la chimie modifiée, du « pitch » et de l'épaisseur initiale sur la gravure du PS-*b*-PMMA modifié high- χ . En comparant des copolymères à blocs PS-*b*-PMMA modifié et standard avec le même « pitch » (32 nm) et la même épaisseur initiale, nous avons conclu que, pour la même chimie de gravure plasma, la chimie du PS-*b*-PMMA modifié high- χ ne présente pas d'impact significatif sur la gravure plasma du PMMA par rapport au copolymère à blocs PS-*b*-PMMA standard. Cependant, lorsque l'on compare le PS-*b*-PMMA modifié high- χ avec deux « pitch » différents (18 et 32 nm) et deux épaisseurs initiales différentes (16 et 36 nm, respectivement), pour le copolymère à blocs avec un « pitch » de 18 nm, les mêmes chimies de gravure qui ont été validées pour un « pitch » plus grand (32 nm) présentent différents problèmes qui empêchent le transfert des motifs dans le masque dur SiO_2 pour le copolymère à blocs à « pitch » plus petit. Par conséquent, nous avons conclu que les principaux défis de la gravure plasma du PS-*b*-PMMA high- χ avec « pitch » 18 nm proviennent de ses petites dimensions, à savoir le « pitch » et l'épaisseur initiale.

Différentes approches ont été testées pour améliorer la sélectivité PMMA:PS et augmenter l'épaisseur de PS restant après retrait du PMMA. L'augmentation de l'épaisseur initiale du film high- χ avec pitch 18 nm a conduit à des problèmes de stabilité mécanique et à une ondulation des lignes (un phénomène connu comme « wiggling ») en raison du rapport d'aspect élevé des lignes. Ces résultats montrent que le CD plus petit du copolymère à blocs high- χ limite l'épaisseur initiale maximale autorisée pour le film polymérique afin d'éviter que le motif ne s'ondule ou ne s'effondre. Nous avons également fait varier le ratio CH_4/N_2 pour trouver un bon compromis entre gravure et passivation à base d'hydrocarbures. Alors que pour les homopolymères PS et PMMA modifiés nous avons réussi à graver le PMMA sans consommer le PS grâce à une couche de dépôt de type CN formée à la surface du PS, il n'en a pas été de même pour le copolymère à blocs PS-*b*-PMMA high- χ . Les résultats ont montré que le copolymère high- χ nécessite une sélectivité plus élevée que le PS-*b*-PMMA standard en raison de sa plus petite épaisseur. De plus, le ratio CH_4/N_2 1:1, tout en présentant la meilleure sélectivité PMMA:PS sans effondrement de motif, présentait également des ponts au sommet des lignes, qui se sont probablement formés en raison d'une passivation intensive des flancs et d'un effet de confinement des espèces accentué par le petit CD des motifs (9 nm). Nous avons

alors conclu que les principales difficultés de gravure plasma du PS-*b*-PMMA high- χ proviennent du compromis entre obtenir une sélectivité élevée et éviter la formation de ponts.

L'approche finale proposée est un procédé mixte de gravure humide et plasma. Le retrait du PMMA par gravure humide, qui consiste en une exposition aux UV suivi par un rinçage en IPA, présente une sélectivité infinie pour le PS-*b*-PMMA modifié high- χ . L'exposition aux UV avec une dose de 30 mJ/cm² et une longueur d'onde de 172 nm provoque la rupture des chaînes de PMMA par scission des liaisons C=O et C-O. Le rinçage IPA enlève alors les chaînes de PMMA cassées sans modifier les lignes de PS. Ensuite, un procédé de gravure sèche pour ouvrir la couche neutre à l'aide d'un plasma Ar/O₂ à haute teneur en argon (120/5 sccm) a été développé pour obtenir une gravure fortement anisotrope et conserver plus de budget PS. Avec cette approche mixte de gravure humide et sèche, le transfert des motifs d'un copolymère à blocs high- χ purement organique avec un « pitch » de 18 nm a été validé dans 10 nm du masque dur de SiO₂ et dans environ 14 nm du substrat en Si avec une variation de CD inférieure à 2 nm.

Le **chapitre V** se concentre sur le retrait sélectif du top coat et du PS vis-à-vis du PDMSB pour un copolymère à blocs high- χ à base de silicium composé de PS-*b*-PDMSB, avec un « pitch » de 18 nm et une épaisseur initiale de 30 nm. Pour ce faire, deux approches différentes ont été étudiées et la deuxième, qui consiste en un retrait du top coat et du PS en une seule étape, a été sélectionnée comme le meilleur résultat. Cette approche se base sur un plasma réducteur H₂/N₂ pour graver le top coat et la phase organique (PS) du copolymère à blocs avec une bonne sélectivité par rapport à la phase contenant du silicium (PDMSB), tout en évitant une oxydation supplémentaire du masque dur en nitrure de titane (TiN). Pour un rapport H₂/N₂ de 150/500, après 20 secondes, le PS a été complètement retiré avec une sélectivité PS:PDMSB de 4,3, mais un effondrement des motifs a été observé en raison du rapport d'aspect élevé des lignes (2,5). Prolonger le temps de gravure à 30 secondes a conduit à une épaisseur restante de PDMSB de 18 nm (sélectivité PS:PDMSB = 2,5) et aucun effondrement des motifs n'a été observé en raison du rapport d'aspect inférieur (2,0) à celui de 20 secondes. Cependant, quelques ponts se sont formés entre les lignes, ce qui a été attribué à une passivation intensive des flancs et à un effet de confinement des espèces accentué par la densité des lignes, comme vu au chapitre IV pour le PS-*b*-PMMA high- χ .

Nous avons fait varier le ratio de gaz afin de comprendre le rôle de l'H₂ et du N₂ sur les mécanismes de gravure et de passivation du top coat et du PS-*b*-PDMSB. Nous avons montré qu'une teneur plus élevée en N₂ conduit à une plus grande sélectivité mais également à plus de formation de ponts, indiquant que le N₂ est le principal agent de passivation dans ce plasma réducteur. Un ratio H₂/N₂ plus élevé d'autre part, a conduit à une sélectivité plus faible et à une perte de CD des lignes en raison de la gravure latérale de la couche neutre. Cependant, lors de la tentative de gravure du top coat et du PS avec du N₂ uniquement, alors que le top coat était complètement retiré, il n'y avait pas de sélectivité entre le PS et le PDMSB. Cela indique que le H₂ est nécessaire pour graver le PS sélectivement au PDMSB. Des analyses XPS *ex-situ* et *quasi in-situ* ont été menées pour mieux comprendre les mécanismes de gravure et de passivation. Après gravure, le top coat présente une perte de liaisons C-O, C=O et CF₃, ce qui est caractéristique de la gravure de polymères à base de méthacrylate, comme le PMMA. Quant au PS, la formation d'une couche de CN_x a été observée à la surface, qui a ensuite été éliminée par des espèces réactives à base d'hydrogène, en formant du HCN comme sous-produit volatil. Pour le PDMSB, le remplacement des liaisons Si-CH₃ par Si-NH₂ et SiO_xN_yH_z est responsable de la passivation du PDMSB lors du retrait du top coat et du PS avec le plasma H₂/N₂.

Enfin, nous avons procédé au transfert des motifs des lignes PDMSB dans 10 nm du masque dur TiN, qui présente une épaisseur de départ de 18 nm (15 nm de TiN et 3 nm d'oxyde natif, TiO_x). Les résultats ont conduit à la conclusion que, bien qu'une bonne sélectivité PS:PDMSB soit souhaitée afin de conserver suffisamment de budget PDMSB pour transférer complètement les motifs de lignes dans le masque dur, des problèmes de stabilité mécanique ont provoqué l'effondrement des motifs en raison du rapport d'aspect élevé des lignes - difficulté que nous avons également vue pour le PS-*b*-PMMA high- χ au chapitre IV. Par conséquent, le plus petit CD du copolymère à blocs high- χ limite le budget maximum de PDMSB autorisé pour le transfert des motifs (et donc la sélectivité PS:PDMSB), ce qui à son tour limite l'épaisseur de TiN pouvant être gravée en utilisant ce copolymère à blocs comme masque de gravure. Nous avons ensuite remplacé le masque dur TiN par un masque dur SiO₂ de 10 nm pour une preuve de concept du transfert des motifs. Après un transfert complet dans la couche d'oxyde de silicium avec un profil droit, il restait environ 7 nm de PDMSB. Ensuite, nous avons démontré le transfert des motifs partiel dans environ 13 nm du substrat silicium, tout en conservant le masque dur SiO₂, indiquant ainsi la possibilité d'obtenir des lamelles de silicium à rapport d'aspect très élevé à l'aide d'une gravure plasma avec une bonne sélectivité Si:SiO₂. Par conséquent, nous avons validé le transfert des motifs d'un copolymère à blocs high- χ contenant du silicium avec un « pitch » de 18 nm dans un empilement de SiO₂ et de silicium de 23 nm de profondeur en utilisant une gravure plasma H₂/N₂ réductrice pour le retrait du top coat et du PS.

Les résultats obtenus avec le procédé ACE dans le chapitre III montrent une bonne amélioration de l'alignement et de la défektivité après l'optimisation de l'étape de retrait SOC. Ainsi, cette thèse a présenté le développement et l'optimisation d'une méthode de chemo-épitaxie plus résolvante que celles existantes à ce jour. En effet, grâce au procédé ACE, l'intégration de copolymères blocs high- χ avec un « pitch » inférieur à 20 nm par lithographie optique par immersion est rendue possible.

Deux copolymères à blocs high- χ , l'un purement organique (PS-*b*-PMMA modifié) et l'autre contenant du silicium (PS-*b*-PDMSB), ont également été étudiés. Le retrait sélectif d'un bloc par rapport à l'autre a conduit à des conclusions similaires dans les deux cas. Tout d'abord, nous avons vu que, en raison du faible CD d'environ 9 nm de ces copolymères, une sélectivité élevée lors du retrait d'un bloc peut entraîner un effondrement des motifs en raison du rapport d'aspect élevé des lignes. Par conséquent, le CD plus petit des copolymères à blocs high- χ limite le budget maximal autorisé pour le transfert des motifs, ce qui à son tour limite l'épaisseur du masque dur qui peut être gravé en utilisant ce copolymère comme masque. Ces résultats ont conduit à la conclusion que les principales difficultés de gravure sèche des copolymères à blocs high- χ proviennent du compromis entre obtenir une sélectivité élevée, éviter la formation de ponts et éviter l'effondrement du motif. Néanmoins, nous avons pu transférer les deux copolymères à blocs high- χ dans un empilement de SiO₂ et de silicium de 23 nm de profondeur, indiquant ainsi la possibilité d'obtenir des lamelles de silicium à rapport d'aspect élevé.

Titre: Gravure plasma de copolymères à blocs dit « high- χ »

Résumé: Pour les nœuds technologiques inférieurs à 10 nm, la lithographie conventionnelle a atteint ses limites en termes de résolution des motifs et de nouvelles techniques sont étudiées pour poursuivre la miniaturisation des transistors. Dans cette thèse, nous nous sommes intéressés à l'auto-assemblage dirigé (DSA) de copolymères à blocs, qui est une solution prometteuse à faible coût pour obtenir des motifs de haute densité avec des dimensions inférieures à 10 nm. Deux des aspects les plus importants de la technologie DSA sont le contrôle de l'orientation du copolymère à blocs et le retrait sélectif d'un bloc vis-à-vis de l'autre avant le transfert des motifs. Ainsi, dans le chapitre III, nous avons évalué et optimisé les différentes étapes de gravure du procédé d'alignement par chemo-épitaxie Arkema-CEA (ACE), notamment en ce qui concerne leur impact sur l'alignement et la défektivité des copolymères à blocs. Les résultats obtenus nous ont permis d'aligner un copolymère à blocs PS-*b*-PMMA en motifs ligne/espace sans aucun type de défaut d'alignement ou de décollement, ce qui se traduit par 0 défaut/100 μm^2 . Dans les chapitres IV et V, nous avons étudié la gravure plasma de copolymères à blocs dit « high- χ », qui présentent un espacement entre les motifs (« pitch ») plus petit en raison d'une plus forte ségrégation de phase. Deux types de copolymères à blocs « high- χ » ont été étudiés, l'un purement organique (PS-*b*-PMMA modifié) et l'autre contenant du silicium (PS-*b*-PDMSB), présentant tous deux un « pitch » de 18 nm et un CD de 9 nm. Pour les deux copolymères à blocs, nous avons développé différentes approches de gravure plasma pour retirer sélectivement une phase tout en conservant suffisamment de budget de l'autre bloc afin de transférer les motifs ligne/espace. En utilisant ces approches, le transfert des motifs dans différentes sous-couches est démontré pour les deux copolymères à blocs « high- χ ».

Mots clés: *Gravure plasma; Copolymères à blocs; Auto-assemblage guidé; High- χ ; Transfert des motifs*

Title: Plasma etching of high- χ block copolymers

Abstract: For the sub-10 nm technologic nodes, conventional lithography has achieved its limit in terms of pattern scaling and new patterning techniques are being studied to continue the miniaturization of the transistor's dimensions. In this PhD, we have focused on the directed self-assembly (DSA) of block copolymers, which is a promising low-cost solution to obtain high density sub-10 nm patterns. Two of the most important aspects of the DSA technology are the orientation control of the block copolymer, in order to obtain the line patterns aligned in long range order, and the removal of one block selectively to the other before pattern transfer. Therefore, in Chapter III, we have evaluated and optimized the different etching steps of the Arkema-CEA (ACE) chemo-epitaxy alignment flow, namely regarding their impact on the block copolymer alignment and defectivity. The results obtained allowed us to align a PS-*b*-PMMA block copolymer in line/space patterns without any type of alignment or lift-off defects, which translates to 0 defects/100 μm^2 . In Chapters IV and V, we have studied the plasma etching of high- χ block copolymers, which present a smaller pitch due to a stronger microphase segregation between the blocks. Two types of high- χ block copolymers were studied, one purely organic (modified PS-*b*-PMMA) and the other silicon-containing (PS-*b*-PDMSB), both presenting a pitch of 18 nm and a CD of 9 nm. For both block copolymers, we have developed different plasma etching approaches to selectively remove one phase while conserving enough budget of the other block in order to transfer the line/space patterns. Using these approaches, the pattern transfer into different underlayers is demonstrated for both high- χ block copolymers.

Keywords: *Plasma etching; Block copolymers; Directed Self-Assembly; High- χ ; Pattern transfer*

Unité de recherche

Laboratoire d'électronique et de technologie de l'information (CEA-Leti)

17 avenue de Martyrs, 38054 Grenoble, France